

VAPOR COMPRESSION REFRIGERATION IN MICROGRAVITY

by

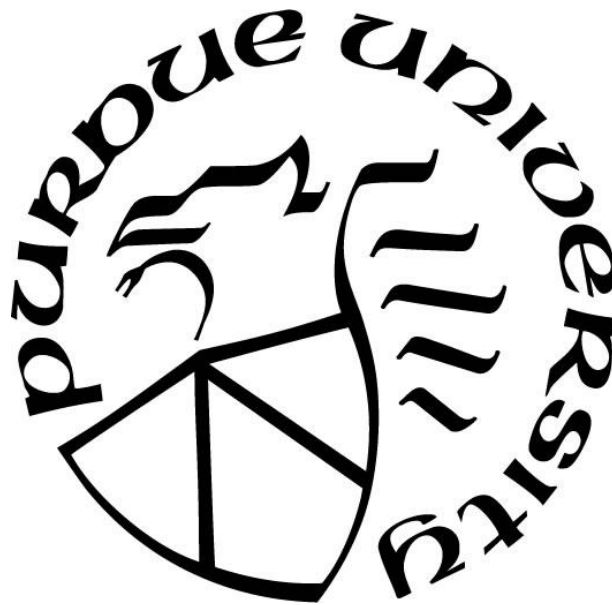
Leon P. M. Brendel

A Dissertation

Submitted to the Faculty of Purdue University

In Partial Fulfillment of the Requirements for the degree of

Doctor of Philosophy



School of Mechanical Engineering

West Lafayette, Indiana

December 2021

THE PURDUE UNIVERSITY GRADUATE SCHOOL
STATEMENT OF COMMITTEE APPROVAL

Dr. Eckhard A. Groll, Co-Chair

School of Mechanical Engineering

Dr. James E. Braun, Co-Chair

School of Mechanical Engineering

Dr. Justin A. Weibel

School of Mechanical Engineering

Dr. W. Travis Horton

School of Civil Engineering

Approved by:

Dr. Nicole L. Key

*This dissertation is dedicated to my parents.
For their unconditional love and support.*

ACKNOWLEDGMENTS

Thank you Eckhard and Jim for striking a balance between high expectations and a hands-off approach. There could not have been a more fertile ground for me to grow over the last four years. I felt respected not only when things went smoothly but also through challenges or critique. Last but not least, you provided an outstanding environment within the Herrick labs as well as a vast network outside which benefitted me greatly.

Thank you also Professor Weibel and Professor Horton for your availability, your curiosity and your very clear view for what matters. I took one class from each of you and enjoyed them from the beginning to the end. I am grateful to have you on my committee.

Frank, from the east wing all the way into a Boeing 727, half of my PhD is your creativity and skill. You made the compressors run and the refrigerant flow, and it would not all have been ready in Florida without your hard work. Thank you Charlie, for the inclinable structure and ample advice in various topics. Thank you Ryan, for being ready at any time to build custom fitted add-ons for the test stands. Thank you Rob, for the finest electrical connections. Your electrical slip ring-idea is still alive and under consideration.

Mike, where would I have started if you had not observed vapor compression cycles in microgravity for the past 30 years? You were essential in bringing together the first review paper on the topic, and it was the guidance from you and your colleagues at NASA that made this research meaningful.

Professor Mudawar and Professor Collicott, I am indebted to you for uncountable private consultations. Also, your classes ME506 and AAE597 taught me all I needed about two-phase flow and zero-G testing, respectively.

I want to thank you Stephen, for managing the project that allowed me to obtain a PhD. Your achievement of the project extension enabled our four parabolic flights. For my own benefit you kept me on my toes through a good two years of weekly meetings and by thorough reviews of numerous publications.

Thank you Alberto, for boosting this project by bringing in Whirlpool's funding and expertise.

Gene, Katy, Mojib, your perspective on two-phase flow from long careers at NASA influenced the course and pitch of this project regularly. I am grateful for all your feedback and guidance.

Paige, Smrithi, Skyler, thank you for letting me practice mentorship on you. I learned a lot, mostly how joyful it is to work with motivated students. Thank you for your many contributions in both modeling and experimental work. I could not have finished all this by myself.

Davide, from teaching me ACHP to having me as a TA in ME518, I was glad you helped me out in many situations. Thank you very much for being an always available, energetic, and inspiring colleague.

Francisco, you enabled my last semester as a digital nomad and simultaneously gave me a meaningful task and interesting insights through the GEARE program. Thank you for being a reliable constant in my social life, too.

Professor Hesse, Stefan, both of you hosted me in your laboratories for approximately 2 weeks in Dresden (Germany) and Buchs (Switzerland), respectively. Both were wonderful experiences and opportunities to acquire new perspectives on my work and learn about different approaches to run large research groups.

Jared and Kayla, thank you for the great videos and effective news releases. I am deeply impressed by your abilities to “spread the word”.

I came to the Herrick labs without knowing how to even wire up a pressure transducer. Thank you Jon, Orkan, Parveen, Riley and Vatsal for your patience with me and for shaping my learning curve. Thank you to numerous other HLAB members for help, inspiration and happy times: Akash, Andreas, Cai, Danielle, Fatih, Haotian, John, Jiacheng, Junyoung, Junyan, Li, Nick, Sourabh, Steven, Tayler, Trevor, Xinye and many others.

Also vital to my sanity and progress in the last four years were a bunch of family members and friends outside of the Herrick Laboratories.

TABLE OF CONTENTS

LIST OF TABLES	11
LIST OF FIGURES	12
NOMENCLATURE	18
ABSTRACT.....	24
1. INTRODUCTION	26
1.1 Motivation	26
1.1.1 Thermal management of spacecraft.....	27
1.1.2 Cooling technologies for microgravity applications.....	30
1.1.3 Mass penalty for power draw and occupied volume	31
1.2 Literature review	34
1.2.1 History of vapor compression cycles on orbit	34
1.2.2 Conceivable problems for vapor compression cycles in reduced and microgravity .	38
1.2.3 Microgravity testing opportunities	44
1.2.4 Direct condensing radiators	48
1.2.5 Gravity independence criteria.....	50
1.2.6 Thermal gravitational scaling	59
1.3 Summary	60
1.3.1 Conclusions from literature review	60
1.3.2 Research status and gaps	62
1.3.3 Increasing the TRL of vapor compression cycles in microgravity.....	64
1.4 Research goals.....	65
1.4.1 Goal 1: Quantifying cycle responses due to orientation changes	65
1.4.2 Goal 2: Quantifying cycle responses from hyper and microgravity.....	65
1.4.3 Goal 3: Assessing the threat of liquid flooding at cycle start-up.....	66
1.5 Organization of this thesis.....	67
2. INCLINABLE TEST STAND	68
2.1 Overview	68
2.2 Configurations	68
2.2.1 Configuration 1 – flat-plate evaporators.....	68

2.2.2	Configuration 2 – tube-in-tube evaporator	70
2.2.3	Configuration 3 – fin-tube evaporator	72
2.2.4	Configuration 3 – parabolic flight setup	73
2.3	Components	75
2.3.1	Heat exchangers	75
2.3.2	Compressors	81
2.3.3	Expansion valve	82
2.4	Inclination capability	83
2.4.1	Design and development	83
2.4.2	Component arrangement, angle convention and example inclination patterns	85
2.5	Instrumentation	87
2.6	Cameras	89
2.7	Instability quantifiers	89
2.7.1	mmx and 80% – quantifier	89
2.7.2	MDV and IIR quantifier	91
3.	START-UP TEST STAND	93
3.1	Overview	93
3.1.1	Test execution	95
3.2	Components	95
3.2.1	Evaporators	95
3.2.2	Compressor	96
3.2.3	Liquid tank	96
3.2.4	Hoses and valves	97
3.2.5	Fans	97
3.3	Instrumentation and data acquisition	97
3.4	Flooding quantifiers	98
4.	CYCLE OPERATION THROUGH 360°	100
4.1	Motivation	100
4.2	Anomalies during inclination testing	100
4.2.1	Dependence on charge distribution	100
4.2.2	Flat-plate evaporator flooding	101

4.2.3	Flooding against gravity	103
4.2.4	Impossible start-up at $\theta = -30^\circ$	104
4.3	First completed loop	106
4.4	Unstable steady-state conditions	107
4.5	Summary	110
5.	QUANTITATIVE IMPACT OF ORIENTATION CHANGES	111
5.1	Motivation	111
5.2	Classification of collected data.....	111
5.3	Low frequency orientation changes – steady-state testing	112
5.3.1	Experimental results	113
5.4	Medium frequency orientation changes – 6-angle testing.....	115
5.4.1	Overview.....	115
5.4.2	Instability results.....	117
5.4.3	Heat exchanger geometries.....	120
5.4.4	Compressor flooding during 6-angle testing	121
5.4.5	Vapor bubbles in liquid line	124
5.5	High frequency orientation changes – parabolic flight simulations.....	127
5.6	Summary	129
6.	IMPACT OF HYPER AND MICROGRAVITY	132
6.1	Motivation	132
6.2	Flight preparations.....	133
6.3	Quantity and quality of data	135
6.4	Repeatability of parabolas	137
6.5	Transient data	138
6.6	Thermodynamic stability.....	139
6.7	Evaporator outlet superheat.....	142
6.8	Flow visualizations.....	144
6.9	Flow oscillations.....	146
6.10	Clustering cycle responses to microgravity.....	147
6.11	Increase of condensation pressure at the onset of microgravity.....	151
6.12	Comparison of ground-based and parabolic flight data	153

6.12.1	Parabolic flights and high frequency inclination testing	154
6.12.2	All testing series	157
6.13	Summary	161
7.	ORIENTATION DEPENDENT HEAT EXCHANGER MODEL	163
7.1	Introduction	163
7.1.1	Motivation.....	163
7.1.2	General notes about the model	163
7.1.3	Model inputs	164
7.1.4	Disclaimer.....	165
7.2	Orientation dependence.....	166
7.2.1	Coil description.....	166
7.2.2	Equations for effective height.....	170
7.3	Heat transfer, pressure drop and charge modeling	170
7.4	Ratio of air outlet temperatures	174
7.5	Model tuning factors and validation.....	175
7.5.1	Heat transfer and pressure drop	175
7.5.2	Charge.....	177
7.6	Heat exchanger tables.....	179
8.	INSIGHTS FROM MODEL APPLICATION	182
8.1	Heat transfer coefficient	182
8.2	Pressure drop	183
8.3	Modelled and experimental charge migration.....	185
8.4	Summary	187
9.	START-UP FLOODING AT NORMAL VERSUS MICROGRAVITY.....	188
9.1	Motivation	188
9.2	Straight-tube testing	188
9.3	Vertical and horizontal ground-based testing.....	189
9.4	Parabolic flight testing.....	191
9.5	Microgravity flow visualizations.....	193
9.6	Summary	194
10.	CONCLUSIONS	195

10.1	Design recommendations for space-bound vapor compression cycles	195
10.1.1	Liquid ingestion by the compressor	195
10.1.2	Heat exchanger type	196
10.1.3	Heat exchanger sizing	196
10.1.4	Compressor type.....	197
10.1.5	Expansion device.....	198
10.1.6	Inclination testing.....	198
10.1.7	Microgravity testing	199
10.1.8	Gravity independence criteria	199
10.1.9	Thermal gravitational scaling.....	200
10.2	Recommendations for future work.....	200
10.2.1	In depth study of the potential mass savings.....	201
10.2.2	Insertion of vapor compression cycle into ISS or other orbital spacecraft	201
10.2.3	Orientation independent compressor lubrication	201
10.2.4	Pump down approach	202
10.2.5	Removal of condensed water from heat exchanger	202
10.3	Summary	202
REFERENCES		205
PUBLICATIONS.....		217
APPENDIX A. DESIGN OF SECONDARY LOOPS FOR AN INCLINABLE TEST STAND		220
APPENDIX B. MDV AND IIR FOR ARTIFICIAL DATASETS		221

LIST OF TABLES

Table 1: Examples of devices for refrigeration in space with temperature range and technology (Brendel et al., 2021g).	30
Table 2: Vapor compression technology that was documented to have operated in microgravity. More detailed table available in Brendel et al. (2021g).	36
Table 3: Examples of testing platforms. The information in the table provides specific examples and not limits or ranges for the testing platform characteristics. **Information not available. As published in Brendel et al. (2019a).	48
Table 4: Comparison of body-force and microgravity testing platforms on a "good", "medium" and "poor" scale for five aspects.	48
Table 5: Equations and parameters for example in Figure 14.	49
Table 6: Table of all compared gravity independence criteria and their functional form. Each criterion has been given a name for easier referencing (Brendel et al., 2021a).	56
Table 7: Overview of dimensionless numbers with different definitions employed by authors of gravity independence criteria (Brendel et al., 2021a).	56
Table 8: Research fields and their current status regarding vapor compression cycles in microgravity	64
Table 9: Types of sensors and associated uncertainties.	88
Table 10: Events and quantifiers during a typical test run.	99
Table 11: Collected data sets for steady-state investigation (from Brendel et al. (2022b)).	112
Table 12: Collected dataset according to the 6-angle inclination procedure.	117
Table 13: Overview of parabolas flown with inclinable test stand.	137
Table 14: Assignment of sets into groups (Brendel et al., 2022d).	149
Table 15: Evaporation temperature changes during microgravity.	151
Table 16: Evaporator data sets for validation.	176
Table 17: Experimental and modelled results for evaporator with tuning factors.	176
Table 18: Condenser data sets for validation.	177
Table 19: Experimental and modelled results for condenser with tuning factors.	177
Table 20: Experimental and modelled maximum charge migration.	186

LIST OF FIGURES

Figure 1: International Space Station with solar panels and radiators.....	28
Figure 2: Radiator panels of International Space Station.	29
Figure 3: Schematic of thermal management system of the ISS (Brendel et al., 2021g).	29
Figure 4: Illustration of mass and volume penalties in spacecraft design (Brendel et al., 2021f).32	
Figure 5: Mass benefit of a VCC due to energy savings as a function of the second law efficiency of an alternative technology (Brendel et al., 2021f).	33
Figure 6: Timeline of important events in the history of VCCs in zero-G (Brendel et al., 2021g).	36
Figure 7: LSLE refrigerators.....	37
Figure 8: Astronaut using Refrigerated Centrifuge (Image from NASA (2019))......	37
Figure 9: Vicious cycle for VCC in zero-G.	39
Figure 10: Aspects to consider for a vapor compression cycle operation in microgravity adapted from Brendel et al. (2022e).	39
Figure 11: Conventional oil-management with and without gravity.	42
Figure 12: Water drainage of evaporator coil with and without gravity.....	44
Figure 13: Earth gravity as a function of distance to the ISS (left) and the Moon (right).	45
Figure 14: Heat rejection capacity as a function of condensation temperature.	49
Figure 15: Ratio of heat transfer coefficient for different flow orientation as a function of flow velocity. Adapted from O'Neill et al. (2017).	51
Figure 16: Illustration of seven different flow velocities relevant in the slip-flow model for two-phase flow (Brendel et al., 2021a).	51
Figure 17: Generally expected trends of threshold flow velocity for gravity-independent two-phase flow with four different parameters.	52
Figure 18: Unconditionally and conditionally gravity independent two-phase flow based on Flow-regime criterion (Ungar, 1998) in Taitel and Dukler flow-map (Taitel & Dukler, 1976). Published in Brendel et al. (2021a).	54
Figure 19: Gravity independent region in Bond-Weber chart according to Bo-Fr-1 and Bo-Fr-2 criterion (Brendel et al., 2021a).	55
Figure 20: Example threshold flow-velocity for the CHF and Bo-Fr-1 criterion as a function of gravity.	55
Figure 21: Parametric studies on gravity independence criteria (Brendel et al., 2021a).	58

Figure 22: Illustration of the idea of thermal gravitational scaling.	60
Figure 23: Plumbing and instrumentation diagram of configuration 1.....	69
Figure 24: Picture of configuration 1 at an inclination angle of $+90^\circ$	70
Figure 25: Plumbing and instrumentation diagram of configuration 2.....	71
Figure 26: Picture of configuration 2.....	72
Figure 27: Plumbing and instrumentation diagram of configuration 3.....	74
Figure 28: Test stand shortly before parabolic flight testing.	74
Figure 29: Picture of tube-in-tube evaporator.....	76
Figure 30: Inner tube and annulus of tube-in-tube evaporator with heat transfer enhancements (Brendel et al., 2022c).....	76
Figure 31: Fin-tube evaporator with inlet, outlet and air-flow direction.	77
Figure 32: Installation of fin-tube evaporator in closed air-loop (side-view).....	78
Figure 33: Fin-tube condenser with inlet, outlet and air-flow direction.	79
Figure 34: Fin-tube heat exchanger capacities as a function of temperature driving potential for evaporator and condenser.	80
Figure 35: Fin-tube heat exchanger capacities as a function of LMTD for evaporator and condenser.	82
Figure 36: Flow coefficient of needle valve (Swagelok, 2007).....	83
Figure 37: Needle valve 5.2 turns open.	83
Figure 38: First schematic of inclinable VCC.	84
Figure 39: Sketch of strategy to organize wires on an inclinable test stand.	84
Figure 40: Modular fabrication of inclinable test setup.....	85
Figure 41: Approximate relative component positioning and refrigerant circuiting.	86
Figure 42: Example inclination patterns possible on an inclinable test stand.	87
Figure 43: Evaporation temperature through set of parabolas with maximum and minimum measured temperature (Brendel et al., 2022e).	90
Figure 44: Heat transfer rate as a function of time through 6-angle testing procedure compared to a constant heat transfer rate of 452 W (Brendel et al., 2022c).....	92
Figure 45: Schematic of start-up test stand (Brendel et al., 2022a).....	94
Figure 46: Completed assembly of start-up test rig (Brendel et al., 2022a).	94
Figure 47: Test sections (Brendel et al., 2022a).	96

Figure 48: Typical transient data for one test run (Brendel et al., 2022a).	99
Figure 49: Subcooling at the condenser outlet and the expansion valve inlet as a function of time (adapted from Brendel et al. (2020b)).	101
Figure 50: Loss of cooling capacity due to inclination of flat-plate evaporators (Brendel et al., 2021c).	102
Figure 51: Incomplete boil-off in flat-plate heat exchanger with spatially separated frost accumulation along flow direction (Brendel et al., 2021c).	103
Figure 52: Liquid flooding of the suction line upon lowering the evaporator relative to the compressor (Brendel et al., 2021c).	104
Figure 53: Successful and unsuccessful start-up at an inclination angle of $+30^\circ$ and -30° respectively.	105
Figure 54: Stable operation of cycle through 390° (Brendel et al., 2021c).	107
Figure 55: Marked shift in operating conditions after returning to a horizontal orientation (Brendel et al., 2021c).	109
Figure 56: Illustration of semi-stable and stable condition.	110
Figure 57: Various measurements from set 7 of the steady-state testing series.	114
Figure 58: Liquid and suction line mass flow rate during three sets of steady-state testing (Brendel et al., 2022b).	114
Figure 59: MDV and IIR for steady-state testing (from Brendel et al. (2022b)).	115
Figure 60: Inclination pattern for six-angle testing.	116
Figure 61: IIR of the heat source heat transfer rate as a function of the mass flow rate for configuration 2 (left) and configuration 3 (right). Adapted from Brendel et al. (2021e).	117
Figure 62: IIR for heat source heat transfer rate for both test stand configurations as a function of the mass flux.	118
Figure 63: IIR and mmx applied to various measurements and plotted as a function of the mass flux (compare with Figure 61 for the legend).	120
Figure 64: Schematic of coil routing for tube-in-tube and fin-tube heat exchanger (Brendel et al., 2021e).	121
Figure 65: Height as a function of tube length for tube-in-tube and fin-tube evaporator.	121
Figure 66: Time of no superheat (left (Brendel et al., 2022c)) and subcooling (right) as a function of the system charge (configuration 2).	123
Figure 67: Charge and subcooling levels for flooding test series (configuration 3).	124
Figure 68: Evaporator outlet superheat for 6-angle testing in air-to-air configuration.	125

Figure 69: Liquid line mass flow rate with oscillations due to vapor bubbles travelling upwards.	126
Figure 70: Gravity changes during parabolic flights and angle changes for parabolic flight simulations.	128
Figure 71: mmx/avg and mmx for flight simulations with R134a and R1234ze(E). Adapted from Brendel et al. (2021d).	129
Figure 72: Discussion slide about the best microgravity testing opportunity from May 2020...	133
Figure 73: Inclinal test stand installed on the parabolic flight aircraft (Brendel et al., 2022e).	134
Figure 74: Measurement of heater power and gravity level during set 18.	136
Figure 75: Gravity measurements through four sets of parabolic flights (Brendel et al., 2022d).	138
Figure 76: Transient temperature and pressure measurements from parabolic flights (sets 10 and 18).	140
Figure 77: Transient mass flow rate, superheat and subcooling data from parabolic flights (sets 10 and 18).	141
Figure 78: Maximum, minimum and average mmx or mmx/avg value for sets 2, 8-12, 15, 16, 18, 20, 22-24 for all or only the tightest 80% of the data. Adapted from Brendel et al. (2022e).	142
Figure 79: Superheat at the evaporator outlet in set 1 and set 20. Set 1 as shown in Brendel et al. (2022e).	143
Figure 80: Flow visualizations from the parabolic flights during cruise and in microgravity (Brendel et al., 2022d).	145
Figure 81: Oscillations in microgravity measured during set 8 (Brendel et al., 2022d).....	147
Figure 82: Patterns of cooling capacity response to microgravity (Brendel et al., 2022d).....	148
Figure 83: Plotting of operating conditions by superheat and mass flow rate (Brendel et al., 2022d).	149
Figure 84: Evaporation temperature changes due to microgravity.	150
Figure 85: Change of the evaporation temperature due to microgravity as a function of the average superheat through the set of parabolas.	152
Figure 86: Overlay plot of normalized condensation pressures (Brendel et al., 2022d).	153
Figure 87: Mass flow rate measurements, relative COP and relative η_{2nd} changes during parabolic flights and ground based flight simulations (Brendel et al., 2022e).	155
Figure 88: mmx/avg and mmx indicator plotted as a function of We_4 for ground-based flight simulations and parabolic flights.	156
Figure 89: mmx and mmx/avg quantifier for all testing series.	159

Figure 90: Maximum, minimum and average mmx and mmx/avg quantifier for all testing series.	160
Figure 91: Nomenclature for orientation dependent heat exchanger modeling.	168
Figure 92: Picture of inclined test rig with x- and z-axis of inner coordinate system. The y-axis goes through the test stand and is the axis of rotation.	168
Figure 93: Example of coil description with Length, θ_i and ϕ_i .	169
Figure 94: Evaporator geometry from a front and side view.	175
Figure 95: Transient measurement of pump down test number 5.	178
Figure 96: Experimentally evaluated evaporator charge plotted as a function of modelled evaporator charge.	178
Figure 97: Picture of evaporator with inlet and outlet and orientation of inner coordinate system as installed on the inclinable test stand.	180
Figure 98: Tabular description of evaporator (part 1).	180
Figure 99: Tabular description of evaporator (part 2).	181
Figure 100: Picture of condenser with inlet and outlet and orientation of inner coordinate system as installed on the inclinable test stand.	181
Figure 101: Two-phase heat transfer tuning coefficients for steady-state testing (adapted from Brendel et al. (2022b)).	183
Figure 102: Total experimental and modelled gravitational pressure drop in the evaporator for set 7 (adapted from Brendel et al. (2022b)).	184
Figure 103: Modeled charge, experimental charge migration and experimental pressure drop for set 1.	185
Figure 104: Schematic of evaporator coil for fin-tube heat exchanger.	186
Figure 105: Schematically illustrated charge migration.	187
Figure 106: Two-phase flow in straight tube before (image 1) and shortly after compressor start-up (image 2-4) (Brendel et al., 2022a).	189
Figure 107: Time till flooding and elapsed time of liquid flooding for standard evaporator in horizontal and vertical orientation (Beck et al., 2021).	190
Figure 108: Time till 30 kPa for evaporator in horizontal and vertical orientation (Beck et al., 2021).	191
Figure 109: Overlay plot of processed data points for three different quantifiers (Brendel et al., 2022a).	192
Figure 110: Overlay plot of clustered data points for three different quantifiers (Brendel et al., 2022a).	192

Figure 111: Comparison of flow regimes in terrestrial and microgravity (Brendel et al., 2022a).	193
Figure 112: Effect of boiling heat transfer coefficient on heat exchanger capacity.	197
Figure 113: Flow rates at heat exchanger outlet temperatures for secondary loops.	220
Figure 114: MDV and IIR for artificial datasets.....	221

NOMENCLATURE

Acronym	Meaning
<i>CCAA</i>	Common cabin air assembly
<i>CHF</i>	Critical heat flux
<i>COP</i>	Coefficient of performance
<i>DAQ</i>	Data acquisition
<i>EES</i>	Engineering Equation Solver
<i>EOR/F</i>	Enhanced orbiter refrigerator/freezer
<i>ESA</i>	European space agency
<i>FBCE</i>	Flow boiling and condensation experiment
<i>Fl</i>	Fluid
<i>GLACIER</i>	General Laboratory Active Cryogenic ISS Experiment
<i>ISS</i>	International Space Station
<i>LSLE</i>	Life Sciences Laboratory Equipment
<i>MELFI</i>	Minus Eighty Degree Laboratory Freezer for ISS
<i>MERLIN</i>	Microgravity Experiment Research Locker/Incubator
<i>NASA</i>	National Aeronautics and Space Administration
<i>OBS</i>	Open Broadcaster Software
<i>OR/F</i>	Orbiter refrigerator/freezer
<i>RC</i>	Refrigerated centrifuge
<i>SABL</i>	Space Automated Bioproduct Lab
<i>SBIR</i>	Small business innovation research
<i>TRL</i>	Technology Readiness Level
<i>USD</i>	US-Dollar
<i>VCC</i>	Vapor compression cycle

Symbol	Meaning	SI-Unit
A	Surface area	m^2
avg	Average	
a	Fitting coefficient	—
b	Fitting coefficient	—
Bo_k	Bond number (k to distinguish differently defined Bond numbers)	—
c	Fitting coefficient	—
\dot{C}	Capacitance rate	W/K
c_p	Specific heat	$kJ/(kg \cdot K)$
cus	Cumulative sum	
D or D_h	Hydraulic diameter	m
D_F	Geometric parameter	m
dp/dz	Pressure gradient	Pa/m
Eo	Eötvös number	—
exp	Experimental result	
f	Friction factor	—
Fr_k	Froude number (k to distinguish differently defined Froude numbers)	—
$Fr_{k,tr}$	Froude number transition value	—
G	Mass flux	$kg/(m^2 \cdot s)$
g	Gravitational acceleration	m/s^2
g_e	Gravitational acceleration on earth	m/s^2
h	Enthalpy	kJ/kg
h_{eff}	Effective height	m
htc	Heat transfer coefficient	$W/(m^2 K)$
IIR	Inclination impact ratio	%
ini	Initial value	
j_f	Velocity of liquid phase if alone in tube (superficial liquid velocity)	m/s
j_g	Velocity of vapor phase if alone in tube (superficial liquid velocity)	m/s

J_G	Dimensionless gas velocity	—
L	Length	m
L_h	Length of heater	m
L_{char}	Characteristic length	m
\dot{m}_r	Mass flow rate (usually liquid line mass flow rate)	g/s
$\dot{m}_{r,2}$	Suction line mass flow rate	g/s
MDV	Mean deviation	[various]
mmx	Min-max quantifier (maximum minus minimum)	
mod	Modeled result	
m	Charge	g
Δm_{PD}	Charge migration during pump down (i.e. refrigerant charge in evaporator)	g
M_{el}	Equivalent mass due to energy consumption	kg
M_{sys}	Mass of cooling system components (main components, tubing, fittings)	kg
M_{tot}	Total equivalent mass	kg
M_{vol}	Equivalent mass due to occupied pressurized volume	kg
NTU	Number of heat transfer units	—
P	Pressure	N/m^2
\dot{Q}	Heat transfer	W
R_e	Radius of earth	m
Re	Reynolds number	—
r_{Air}	Relative distance in airflow direction	—
r_X	Relative distance in x-direction	—
r_Y	Relative distance in y-direction	—
r_Z	Relative distance in z-direction	—
S	Slip ratio (vapor velocity divided by liquid velocity)	—
T	Temperature	K
$\Delta t_{g=0}$	Time of experienced weightlessness	s
ΔT_{0G}	Time of zero-gravity	s

ΔT_{30kPa}	Time elapsed from compressor start until test section pressure reaches 30 kPa	s
ΔT_{70kPa}	Time elapsed from compressor start until test section pressure reaches 70 kPa	s
$\Delta T_{elapsed}$	Time elapsed with visible flooding	s
ΔT_{start}	Time from compressor start until first flooding	s
u_f	Velocity of liquid phase	m/s
u_g	Velocity of vapor phase	m/s
u_r	Reference flow velocity ($= u_{x0}$)	m/s
u_x	Mean flow velocity at quality x	m/s
u_{x0}	Velocity of saturated liquid	m/s
u_{x1}	Velocity of saturated vapor	m/s
Δu_{ig}	Difference between mean gas velocity and liquid–vapor interfacial velocity	m/s
UA	Conductance	W/K
$UA_{overall}$	Overall conductance (see definition in text)	W/K
v	Specific volume	m ³ /kg
\dot{V}	Volumetric flow rate (usually for air)	m ³ /s
V_{sys}	Total pressurized volume occupied by refrigeration system	m ³
\dot{W}	Power	kW
We_k	Weber number (k to distinguish differently defined Weber numbers)	—
x	1. Quality 2. Distance	— m
\dot{x}	Placeholder for measurement in general equations	
X or X_{Mar}	Martinelli parameter	—
Y	Dimensionless number to relate gravity forces in flow direction and pressure drop	—

Greek symbol	Meaning	SI-Unit
α	Void fraction	
Δ	Differential	—
ϵ	Emissivity	—
η_{fins}	Fin efficiency	—
η_{2nd}	Second law efficiency	—
λ_{el}	Equivalent mass per average electrical power	kg/kW_{el}
λ_v	Equivalent mass per volume	kg/m^3
μ	Viscosity	$kg/(m \cdot s)$
ϕ	Inclination angle of tube	°
ρ	Density	kg/m^3
ρ''	Modified density	kg/m^3
σ	Surface tension	N/m
σ_b	Stefan-Boltzmann constant	$W/(m^2 K^4)$
θ	Inclination angle	°

Subscript	Meaning
a	1. Ambient 2. Air 3. Accelerational (pressure drop component)
ALT	Alternative technology to VCC
avg	Average
c or $cond$	Condenser
dis	Discharge
DS	Deep space
e or $evap$	Evaporator
exp	Experimental
exp, v	expansion valve

<i>f</i>	1. Liquid phase 2. Frame
<i>F</i>	Fanning friction factor
<i>g</i>	1. Vapor phase 2. Gravitational (hydrostatic) pressure drop component
<i>h</i>	High
<i>i</i>	Inner coordinate system
<i>in</i>	Inlet
<i>l</i>	Low
<i>liq</i>	Liquid
<i>mod</i>	Model
<i>out</i>	Outlet
<i>r or ref</i>	Refrigerant
<i>sat</i>	Saturated
<i>src</i>	Source
<i>sub</i>	Subcooling
<i>suc</i>	Suction
<i>sup</i>	Superheat
<i>t</i>	Tuning
<i>tot</i>	Total
<i>tp</i>	Two-phase
<i>VCC</i>	Vapor compression cycle
<i>xz</i>	In xz-plane
<i>z</i>	Gravity acting direction perpendicular to test stand in horizontal orientation (downward)

ABSTRACT

As space exploration continues to accelerate, various cooling applications follow suit. Refrigeration and freezing of biological samples, astronaut food as well as electronics cooling and air-conditioning are necessary and demand increased capacity. In the past, these demands have been met by thermoelectric cooling or cryogenic cycles, which are easily adapted to a microgravity environment but have a relatively low efficiency in the refrigeration and freezing temperature range. A number of studies have investigated the development of higher efficiency vapor compression cycles for spacecraft, which would have the benefit of a smaller mass penalty due to the reduced power consumption. Despite notable research efforts during the 1990s, the number of vapor compression coolers that have operated in microgravity until today is small and their performance was insufficient to provide confidence into the technology for microgravity applications. Related experimental research has decreased since the 2000s.

For this dissertation, all vapor compression cycles (VCC) that have operated in microgravity according to the open literature were reviewed with their applications, compressor types and reported issues. Suggested design tools were summarized with a focus on gravity independence criteria for two-phase flow. For the most effective increase of the technology readiness level, simple but systematic experiments regarding the stability of VCCs against orientation and gravity changes were prioritized in this dissertation. An important goal of the research was the continuous operation and start-up of vapor compression cycles on parabolic flights, experiments that have not been reported in the open literature. Two separate test stands were built and flown on four parabolic flights, totaling 122 parabolas for each experiment.

The parabolic flight experiments were prepared with extensive ground-based testing. Multiple anomalies were encountered during the pursuit of continuous vapor compression cycle operation through a rotation of 360 degrees, including liquid flooding of the compressor. Systematic inclination testing was conducted with two different cycle configurations and a wide range of operating conditions. A strong correlation was found between the relative stability of the heat source heat transfer rate and the refrigerant mass flux for an inclination procedure with angle changes once every 2 minutes.

The parabolic flights exposed the test stand to quickly alternating hyper and microgravity. The evaporation temperature reacted to the different gravity levels with fluctuations that stretched

on average 2.2 K from the maximum to minimum temperature measured during one set of parabolas. Changes of the evaporator inlet flow regime as a function of gravity were observed visually and the low-side pressure and mass flow rate sometimes oscillated in microgravity. The cycle responses induced by ground-based inclination testing were typically stronger than changes caused by the parabolic flight maneuvers for relatively low mass flow rates. Overall, the parabolic flight maneuvers were not detrimental to the cycle operation.

The second test stand was dedicated to liquid flooding observations at cycle start-up. Different flow regimes were observed in microgravity during testing with a transparent evaporator but the absence of gravity did not significantly alter the general time-based flooding quantifiers.

Design recommendations are drawn from the research where possible and summarized at the end of the dissertation. Selected data, code, pictures and videos were released together with this dissertation (Brendel, 2021).

1. INTRODUCTION

1.1 Motivation

Starting from the space race between the United States and the Soviet Union in the 1950s, uncountable spacecraft have been launched into lower earth orbit, among them multiple space stations that orbited for several years. Other spacecraft were sent far beyond lower earth orbit and are still travelling and communicating to earth.

Recent policies and events assure that the exploration of space by mankind will not only continue but accelerate. The global space economy was worth over 300 Billion USD in 2015 (Bockel, 2018; Bryce Space, 2017) and a further increase is expected. Apart from governmentally driven developments, private companies are now offering services, such as microgravity research platforms or carrier flights to the International Space Station (ISS) and nanosatellites so small that a single academic laboratory can acquire enough funding to design and fabricate them.

The need for and realization of cooling in microgravity is a topic mainly discussed by the respective engineers and researchers but rarely of widespread public interest although quite fundamental for many missions. Cooling during space travel has indeed been a need from the 1960s on, when missions included more and more measurement equipment. Ross (2006) explains the evolution of cryogenic cooling which was initially needed for infrared sensors as well as gamma-ray and x-ray detectors. Dewars filled with liquid Hydrogen and Oxygen for fuel cells and breathing are reported as the first cryogenic applications in space in 1968, one year later followed by an open cycle Joule-Thomson cryocooler to enable infrared spectroscopy of Mars.

The increased presence of humans in space led to yet more cooling applications. For example, the collection of biological samples and their preservation for return to earth started the need for cooling at typical refrigerator/freezer temperatures. One example is a 400 page report by Johnston (1977) about the biomedical results of Skylab. The report finishes with seven recommendations, one of which stating “*Some means of refrigeration or freezing for experimental samples should be provided in the return vehicle...*”. Also air-conditioning (cooling and dehumidification) are human-related needs for cooling in space.

Looking at long term manned missions, refrigeration of food is needed and calls for more efficient cooling technologies. Humans on the ISS can rely on storage and regular resupply with

food. During a mission to Mars without frequent resupply, the nutritional value of astronaut food would decay over time if at ambient temperature (Cooper et al., 2017; Smith et al., 2009). The needed volume for appropriate amounts of food is significantly larger than a cabinet to temporarily store biological samples. Larger volumes of refrigerated items inevitably bring higher cooling loads, such that the attention widens from mere reliability to energy efficiency. Considering these aspects, the energy efficiency of a *vapor compression cycle* as compared to other cooling technologies becomes more and more desirable.

On earth, the vapor compression cycle (VCC) is the dominant cooling and heat pumping technology in the temperature range from freezing to moderate heating for its superior efficiency (El Fil et al., 2021). VCCs are utilized in household refrigerators and freezers, building and car air-conditioners, transport refrigeration, industrial cooling and many other fields.

Despite billions of VCCs that operate or have operated on earth, there are less than 10 that have operated in a microgravity environment. The goal of this dissertation is to increase the confidence into vapor compression cycles for extraterrestrial applications through experimental work. Extraterrestrial applications include both microgravity and reduced gravity environments. Microgravity applications impose the greatest uncertainty because fluid phases of different density are not separated by gravity. As mankind pursues extraterrestrial habitats on the surface of the Moon or Mars, the topic of reduced gravity naturally accompanies the topic of microgravity but microgravity applications are prioritized in this dissertation.

1.1.1 Thermal management of spacecraft

Thermal communication with ambient

Spacecraft absorb heat since they are exposed to the sun. Moreover, solar energy is collected and used, ultimately becoming one of the sources of waste heat inside the spacecraft. Because spacecraft fly in a vacuum, they cannot reject heat to their surroundings via convective heat transfer. The only means to reject heat is radiative heat transfer, which must be, over some time period, equal to the total of absorbed thermal and harvested electrical energy as well as any internal heat loads (like humans).

Heat rejection systems for spacecraft can be categorized as passive or active systems. Small satellites in lower earth orbit employ passive systems if the components can tolerate the resulting

bandwidth of temperatures. The cyclical exposure to sunshine and shade leads to a cyclic temperature swing of the satellite. If the satellite temperature does not naturally stay within the temperature bounds, insulation material or material with specific absorptivity or emissivity values can be leveraged. If such purely passive means do not suffice, another option is to turn on electrical components only during certain times or to add electrical heaters to avoid too cold temperatures. Larger spacecraft require more sophisticated active thermal control systems to balance out varying heat loads and protect against overheating. Figure 1 shows the ISS with its solar panels and radiators facing in different directions to enhance energy collection and heat rejection, respectively. Figure 2 shows a close up of the ISS-radiators in front of a solar panel. The radiators have actuators through which the total heat loss can be controlled.

Thermal management inside spacecraft

The internal thermal management system of a manned spacecraft transfers heat from various sources to the external thermal management system, i.e. the radiators. An example configuration similar to the one on the ISS is depicted in Figure 3 from Brendel et al. (2021g). Single phase ammonia circulates through the radiators and rejects heat, generating capacity to pick up heat when flowing through the water-ammonia heat exchanger interfacing with the environment inside the spacecraft. The heat exchanger separates the two thermal systems and avoids the danger of ammonia release inside the space station. The water loop can be used as a heat sink for devices within the spacecraft that need to reject heat.

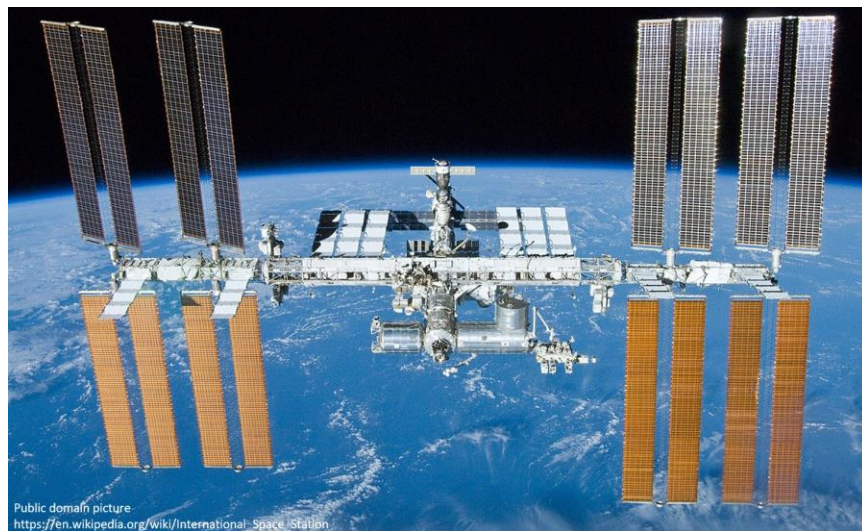


Figure 1: International Space Station with solar panels and radiators.

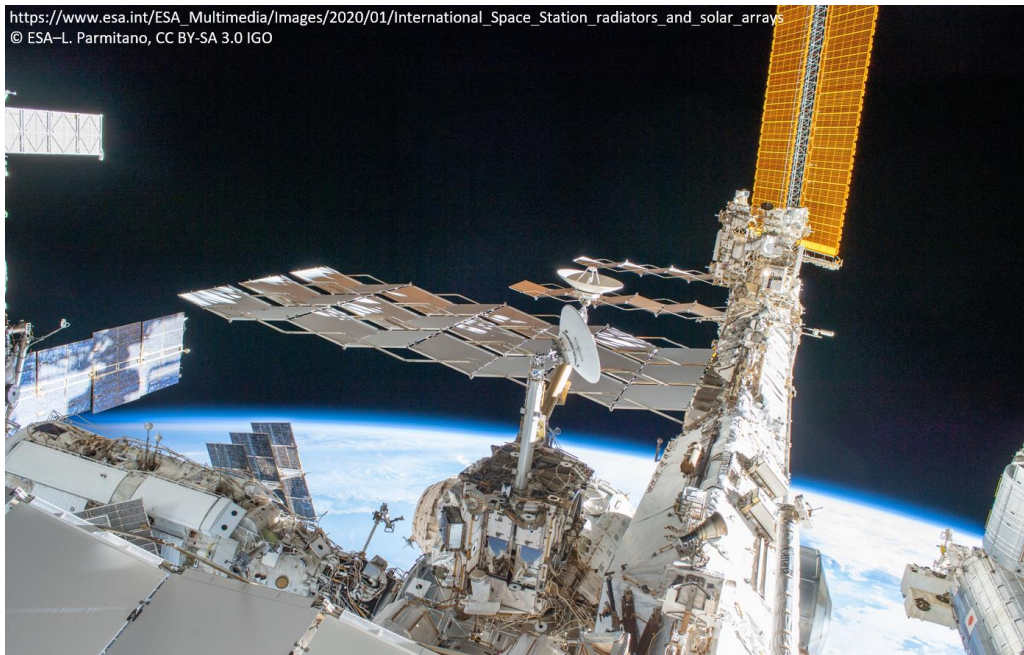


Figure 2: Radiator panels of International Space Station.

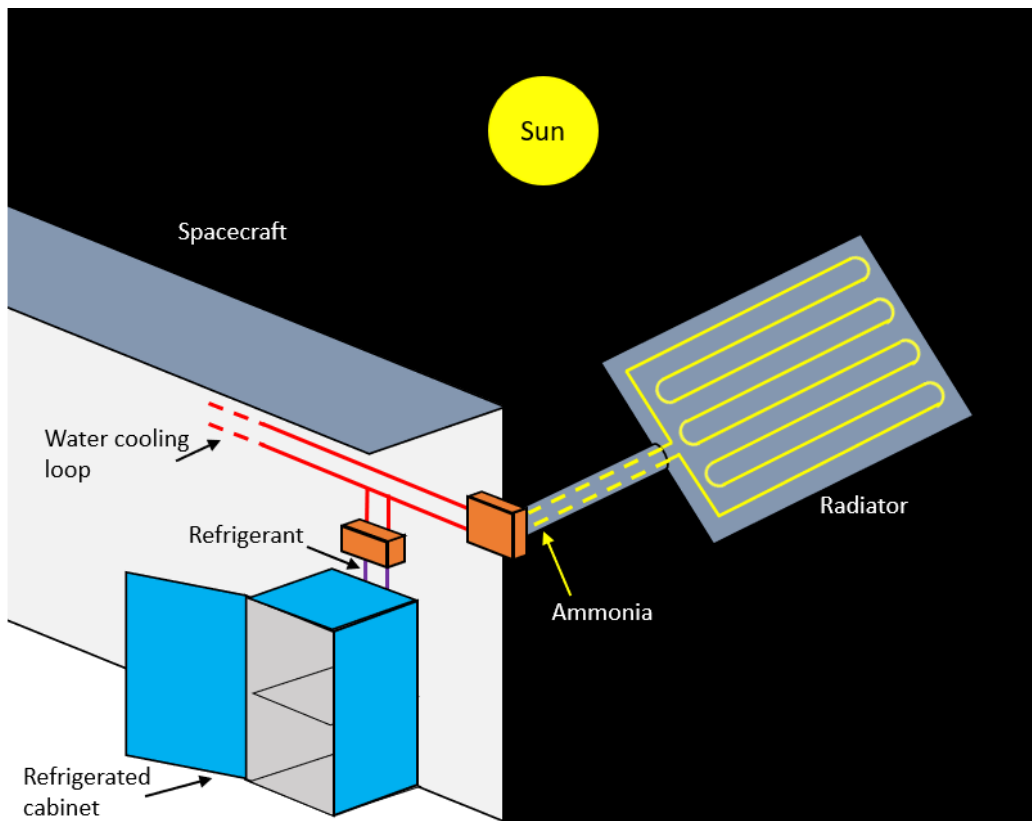


Figure 3: Schematic of thermal management system of the ISS (Brendel et al., 2021g).

1.1.2 Cooling technologies for microgravity applications

A variety of cooling technologies have already been employed in space. The Cryogenic Engineering Group at the University of Oxford provides an overview of coolers used in space on their website (University of Oxford, 2020):

- Radiators
- Cryogen in tanks
- 1-stage Stirling
- 2-stage Stirling
- Pulse tube
- Peltier
- Joule-Thompson
- Sorption
- Reversed Brayton
- Adiabatic demagnetization refrigeration

In particular, thermoelectric cooling, the Stirling cycle and the reversed Brayton cycle have been commonly used in space applications. A few examples with references are listed in Table 1 as published in Brendel et al. (2021g). Most of these devices are inherently single-phase cycles/technologies such that they are mostly gravity independent and could be rapidly developed for space applications. In contrast, the vapor compression cycle is a two-phase cycle, meaning that liquid evaporates and vapor condenses in different parts of the cycle. The two phases undergoing mass transfer coexist in one tube during these processes. The processes are well understood in terrestrial applications, but removing the buoyancy forces makes the performance and behavior in microgravity difficult to predict. The cycle should still be considered because of its favorable energy efficiency.

Table 1: Examples of devices for refrigeration in space with temperature range and technology (Brendel et al., 2021g).

Name	Temp. range	Technology	Reference
Biorack	-17°C to + 8°C	Thermoelectric	(Hartley, 2018; Manieri et al., 1996)
MELFI	-95°C to + 2°C	Reversed Brayton	(Hartley, 2018; Ravex et al., 2005)
MERLIN	-20°C to +48°C	Thermoelectric	(Hartley, 2018; Rouleau, 2019)
Polar	-95°C to + 4°C	Stirling	(Hartley, 2018; Rouleau, 2019)
GLACIER	-160°C to + 4°C	Stirling	(Hartley, 2018; Rouleau, 2019)
SABL	-5°C to +43°C	Thermoelectric	(Niederwieser et al., 2015)

1.1.3 Mass penalty for power draw and occupied volume

The equivalent mass of a cooling technology is the main argument that favors the pursuit of VCCs for spacecraft. When designing spacecraft, excess mass is to be avoided because it would increase the required size and fuel of the launch vehicle. Mass as a core evaluation criterion dictating launch cost has led to equations that also translate power consumption and occupied pressurized volume to mass as illustrated in Figure 4. This is intuitive for the power requirement: Not only does a higher power draw require larger solar panels, but also larger radiators. Hence, every additional kW of power draw increases the total mass of the spacecraft on two ends. An approximation is an additional 83 kg of mass for every additional 1 kW of average power consumption (see Table 3.4 and 3.6 in Anderson et al. (2018)). “Occupied pressurized volume” is a term for the internal areas of a spacecraft that the crew can access without a spacesuit. The larger the volume, the larger and heavier the spacecraft. Approximately 67 kg can be accounted for 1 m³ of occupied pressurized volume. These values should be considered when comparing different refrigeration technologies. Brendel et al. (2021g) suggested an equation to compare the total equivalent mass of cooling technologies, considering their system mass, the average power draw and the occupied pressurized volume:

$$M_{tot} = M_{sys} + M_{el} + M_{vol} = M_{sys} + \dot{W}\lambda_{el} + V_{sys}\lambda_v, \quad (1)$$

where:

M_{tot} : Total equivalent system mass [kg]

M_{sys} : Mass of refrigeration system [kg] (If the refrigeration enclosures are similar for different cooling technologies, the mass cancels out in comparisons)

M_{el} : Mass penalty due to increased power consumption [kg]

M_{vol} : Mass penalty due to need for occupied pressurized volume

\dot{W} : Average electrical power [kW]

V_{sys} : Total pressurized volume occupied by refrigeration system [m³] (if the refrigeration enclosures are similar for different cooling technologies, the associated mass cancels out in comparisons)

λ_{el} : Equivalent mass per average electrical power [kg/kW_{el}]

λ_v : Equivalent mass per volume [kg/m³]

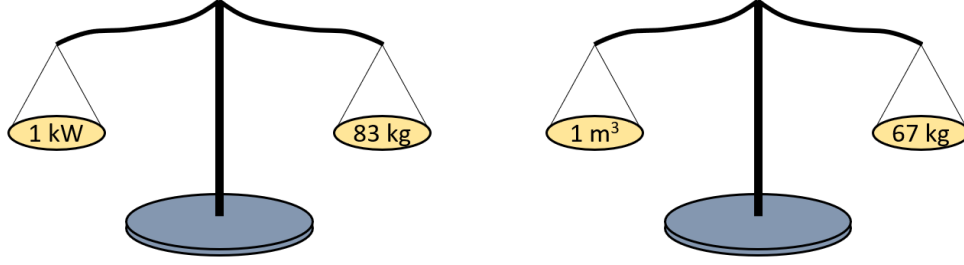


Figure 4: Illustration of mass and volume penalties in spacecraft design (Brendel et al., 2021f).

The formulation for the mass penalty due to power consumption only is hence:

$$M_{el} = \dot{W} \lambda_{el} \quad (2)$$

Equation 2 can be rearranged for a direct comparison of two cooling technologies with comparable M_{sys} and V_{sys} but different second law efficiency η_{2nd} defined as

$$\eta_{2nd} = \frac{\frac{\dot{Q}}{\dot{W}}}{\frac{T_h - T_l}{T_l}}. \quad (3)$$

Using the second law efficiency and substituting \dot{W} in the Equation 2 for the mass penalty due to electrical work, a new expression for M_{el} results:

$$M_{el} = \frac{\lambda_{el} \dot{Q} (T_h - T_l)}{T_l} \cdot \frac{1}{\eta_{2nd}}. \quad (4)$$

The equivalent mass *advantage* of a VCC over an alternative technology (ALT) *due to a higher COP* is then

$$\Delta M_{el} = \frac{\lambda_{el} \dot{Q} (T_h - T_l)}{T_l} \cdot \left(\frac{1}{\eta_{ALT}} - \frac{1}{\eta_{VCC}} \right). \quad (5)$$

For example: A vapor compression cycle with 400 W cooling capacity and a second law efficiency of 0.3 would have a mass advantage of 35 kg over an alternative cooling technology with a second law efficiency of 0.1, when both are operating between a heat source at -20 °C and a heat sink at 20 °C, given a mass penalty factor of $\lambda_{el}=83 \text{ kg/kW}$. Figure 5 shows this graphically for a range of second law efficiencies of the hypothetical alternative technology. The black line holds for $\eta_{VCC} = 0.3$ and intersects the $\eta_{ALT} = 0.1, \Delta M_{el} = 35 \text{ kg}$ point of the example. The line crosses the x-axis for $\eta_{ALT} = 0.3$ because there is no mass benefit at equal second law efficiencies.

The green line is shown for $\eta_{VCC} = 0.2$, which causes a constant offset of 8.8 kg. The blue and red areas show efficiency estimates for thermoelectric coolers and Reversed Brayton cycles. Due to the hyperbolic trend, an uncertainty of η_{VCC} has a relatively smaller impact at generally lower values for η_{ALT} .

Brendel et al. (2021f) provided a mass break down of a real vapor compression cycle to put these results into perspective. The system had a design cooling capacity of 100 W for a heat source temperature of about -20°C and a heat sink temperature of about 20°C . The cooling system had a total weight of approximately 9 kg (3.3 kg for the compressor, 0.5 kg for the evaporator, 1.4 kg for the condenser and the rest for the valve, fan, controller and miscellaneous parts). If system mass scaled linearly with capacity, the weight of a 400 W VCC would then be 36 kg, which is comparable to the mass savings it generates according to the previous example. If the VCC saves its own weight due to a reduced power consumption, then it effectively saves the weight of the alternative technology which is replaced with the VCC.

Across large capacity ranges, the system weight will not scale linearly with the capacity. A dedicated study about the absolute masses for VCCs and alternative technologies at varying capacities would be required. It is also currently unclear what the required capacity will be for future missions and by how many separate cycles it should be provided. These and other information will ultimately determine the mass benefit of VCCs over alternative technologies.

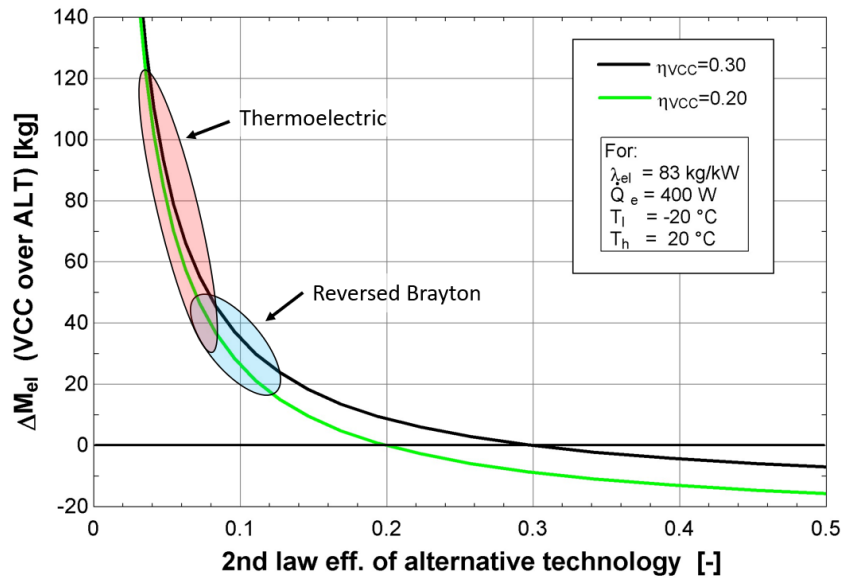


Figure 5: Mass benefit of a VCC due to energy savings as a function of the second law efficiency of an alternative technology (Brendel et al., 2021f).

1.2 Literature review

The previous section described the main benefit of a VCC for spacecraft. The COP could result in lower mass penalties. The benefit is opposed by a lower technology readiness level for vapor compression cycles applied in space as compared to most other cooling technologies. Until today, there have been only very few vapor compression systems in microgravity and despite numerous additional modeling efforts, the confidence into the technology is still low. This section describes vapor compression refrigeration devices with microgravity flight experience. A related review paper exists and should be referred to for more detailed information (Brendel et al., 2021g). Additionally, conceivable problems for VCCs in microgravity are discussed together with microgravity testing opportunities. The concepts of gravity independent two-phase flow and thermal gravitational scaling are briefly reviewed, too.

1.2.1 History of vapor compression cycles on orbit

Ginwala (1961) might be the first serious consideration of VCCs for spacecraft. The project report concludes that “*Conventional evaporators and condensers would become inoperable*” in microgravity and suggests rotating heat exchangers and other sophisticated solutions. Interest in VCCs for space applications has been expressed frequently since Ginwala’s report (Gerner et al., 2015; Hye, 1985; Morton et al., 1998; Williams et al., 1973). However, when searching the literature for testing of VCCs in microgravity, one is surprised. First, a wealth of researchers has advocated for VCC on spacecraft, discussing the merits and modeling approaches but there have been very few systems developed. Second, two-phase flow research has produced experimental microgravity results so numerous that they have been summarized in several review papers. Many of the two-phase *flow* research papers declare in the introduction that the ultimate goal of two-phase flow research is to enable two-phase *systems* in microgravity. Then, there should have been a research branch experimentally investigating VCC in microgravity a long time ago. In contrast, the existing literature on VCC operation in microgravity environments is very scarce. Milestones for VCCs in microgravity are summarized in a timeline in Figure 6 and important information is tabulated in Table 2.

Williams et al. (1973) operated a prototype condensing radiator on parabolic flights in order to prepare it for use in a VCC in spacecraft. However, the researchers did not operate a

complete vapor compression cycle. This was done for the first time almost 10 years later by Lipson (1982), who used an oil-free diaphragm compressor and successfully froze a sample in zero-G and returned it to earth.

The confidence in applications of VCC in zero-G from these earlier studies gave rise to a program that resulted in three additional VCCs that all flew in microgravity during the 1990s, probably the most active decade with respect to this research area. OR/F and EOR/F ((Enhanced) Orbiter Refrigerator/Freezer) are very similar coolers, both driven by an oil-free diaphragm compressor. They flew multiple times from 1991 to 1998. LSLE (Life Sciences Laboratory Equipment Refrigerator/Freezer, see Figure 7) was larger by volume but built for a similar temperature range from -22°C to 10°C . All three were mostly used for cooling of biological samples. In a technology assessment by Gaseor et al. (1996), the authors were critical and noted the need for a solution with “*substantially longer life, higher reliability, less maintenance and no CFCs*”.

It may have been reports like this that diminished interest in further developing VCCs for microgravity. Only one more VCC was launched under a NASA project in the 2000s. The system had been tested on the ground at varying orientations (Grzyll & Cole, 2000). It was supposed to cool a centrifuge, but “*Cooling became unavailable soon after on-orbit operation*” (NASA, 2019). Unfortunately, it remains unclear why the refrigerated centrifuge (RC) failed. A picture of the installed RC is shown in Figure 8. Apparently, the cooling system has been removed from the ISS since and cannot be investigated for the specific failure mode anymore.

The only two vapor compression cycles that are known to currently operate in space are SKV-1 and SKV-2 in the Russian Module Zvezda. The SKV devices use approximately 750g of R218 to provide air-conditioning and dehumidification. Wieland (1998) describes that the compressors are oil-lubricated but the refrigerant is separated from the oil by means of a bellows. The systems were installed around the year 2000 and some maintenance work or refrigerant spills have been reported, but overall the systems seem to be functional.

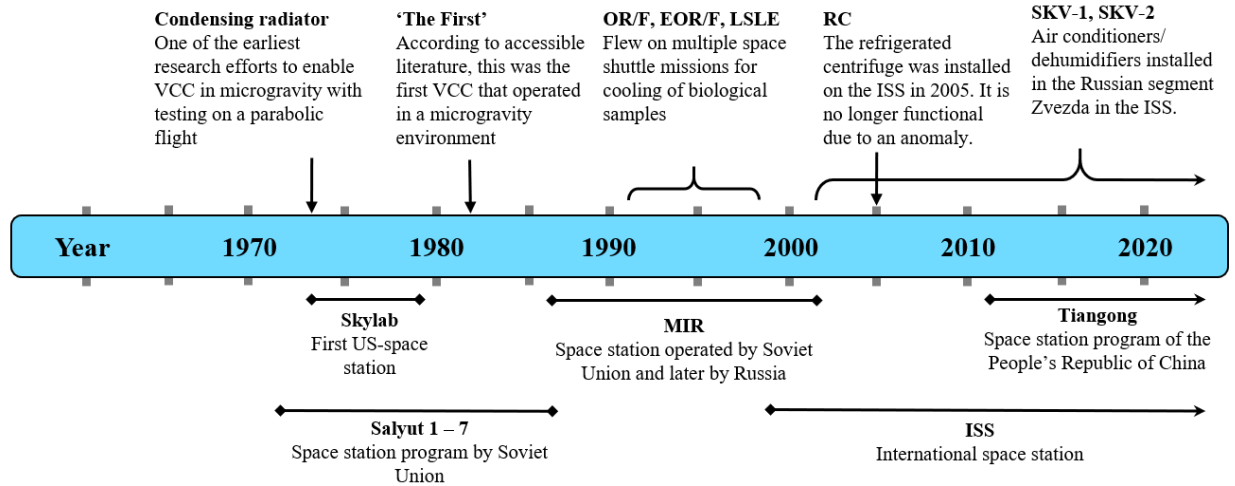


Figure 6: Timeline of important events in the history of VCCs in zero-G (Brendel et al., 2021g).

Table 2: Vapor compression technology that was documented to have operated in microgravity. More detailed table available in Brendel et al. (2021g).

Name	Year	Compressor	Application	Comments
N/A	1982	Oil-free diaphragm compressor (Lipson, 1982)	Life Sciences experiments and future need for food storage (Lipson, 1982)	Successfully froze sample and returned to earth frozen (Lipson, 1982)
OR/F	1991-1998 (NASA, 2018b)	Oil-free diaphragm compressor (Jimenez, 2019)	Biological samples and solutions. (NASA, 2018b)	Released noxious gases during STS-40 (Matney et al., 1993).
EOR/F		Oil-free diaphragm compressor (Cole et al., 2006; Jimenez, 2019), linear compressor flew once (Jimenez, 2019) on IML-2 (Gaseor et al., 1996)	Biological samples and solutions. (NASA, 2018b)	Enhanced version of OR/F (NASA, 2018b).
LSLE	1991 - 1998 (NASA, 2018a)	Unclear: Modified double-headed commercial compressor (NASA, 2018a) or oil-free diaphragm compressor (Jimenez, 2019)	Freeze perishable samples (blood, urine, saliva). (NASA, 2018a)	Internal volume: 71 liter. Two modules were often flown together. (NASA, 2018a).
SKV-1 and SKV-2	~2001 – today	Micro-compressor, oil-lubricated but oil and refrigerant are separated (Wieland, 1998)	Air cooling and dehumidification (Goerig, 2001)	Installed on ISS for many years. Needed occasional maintenance.
RC	2005 (NASA, 2019)	Oil-less hermetic reciprocating compressor. Modification of an existing compressor.	Maintain rotor chamber temperature of centrifuge (NASA, 2019)	“Cooling became unavailable soon after the start of on-orbit operation” (NASA, 2019).



Figure 7: LSLE refrigerators.



Figure 8: Astronaut using Refrigerated Centrifuge (Image from NASA (2019)).

1.2.2 Conceivable problems for vapor compression cycles in reduced and microgravity

The previous section listed six different vapor compression refrigerators that operated in microgravity with differing degrees of success (counting SKV-1 and SKV-2 as one). If all flights had been documented from a refrigeration research point of view, there would undoubtedly be a better understanding of the problems to be expected due to microgravity. The reality is the opposite: None of the VCCs flown in microgravity were documented in detail and the research community has not even agreed on a list of issues and their relevance for VCC in zero-G. Problems highlighted in the literature and issues that can be conceived by thought experiments are discussed in the following sections. All potential problems could be much easier if there was unlimited access to microgravity testing platforms.

Vicious cycle of VCC in zero-G

Bringing a payload into orbit is usually a tremendous investment of time, effort and money. The reliability requirements for the technology are accordingly high. The obstacle for VCCs in space has often been that other cooling technologies were already more mature and fundamentally more robust against changing gravity levels. The availability of such cooling technologies led to limited funding and therefore limited access to zero-G testing for researchers that wanted to push the TRL of VCCs in zero-G higher. The low number of VCCs that have been deployed in space has not proven the requirement for high reliability. This vicious cycle is not found in the literature but interpreted from the overall body of literature and is depicted in Figure 9. In 2017, an SBIR project was started to develop a vapor compression refrigerator for food stowage on spacecraft (Rohleder et al., 2018). This project restarted experimental work on VCCs for microgravity. The initial Phase I was continued with Phase II and Phase II-E which were the projects funding the work of this dissertation.

Technical problems

The following subsections describe technical problems that can arise for VCCs in microgravity applications. Figure 10 shows a vapor compression cycle schematically. Aspects that need to be considered about microgravity are written at the relevant locations around the cycle and

discussed in more detail in the following. These problems for VCCs in microgravity are also discussed in Brendel et al. (2019a; 2021g).

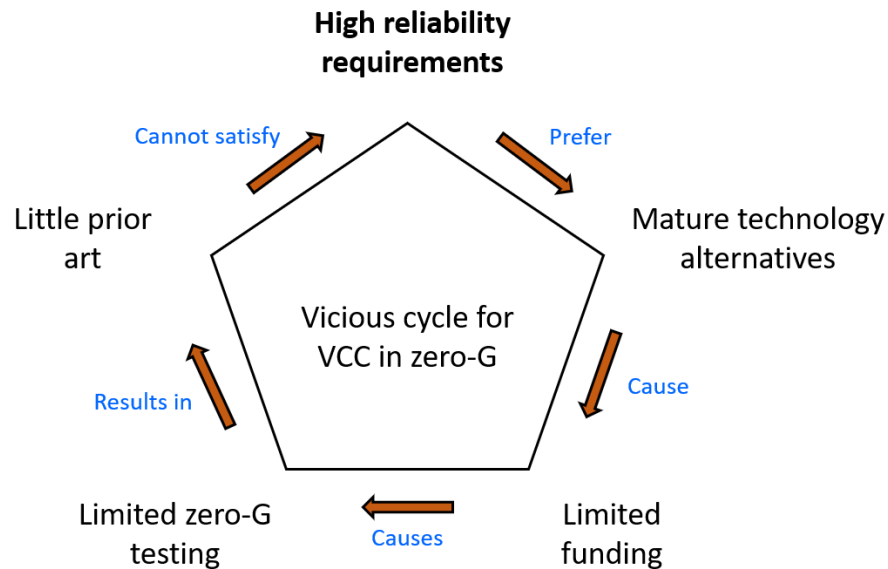


Figure 9: Vicious cycle for VCC in zero-G.

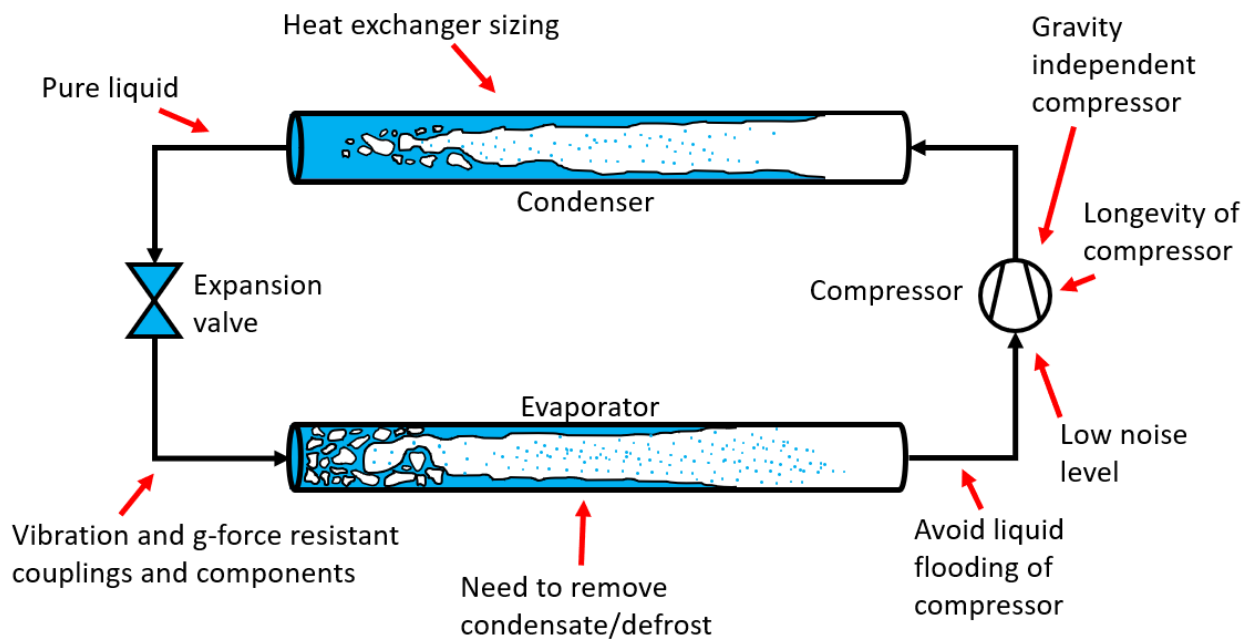


Figure 10: Aspects to consider for a vapor compression cycle operation in microgravity adapted from Brendel et al. (2022e).

Liquid flooding of compressor

For refrigeration and air-conditioning in the lower capacity range, the most common compressors are of type positive displacement. These have a fixed volume ratio that is dictated by the design. Intake of incompressible fluids can therefore lead to damage. The tolerance of compressors to liquid intake varies by type and design, but generally speaking it should be avoided. A service engineer is quoted in Foster (1967): “*A refrigerant reciprocating compressor becomes a liquid pump just before it becomes a wreck.*” Siewert (1972) conveys the same idea saying “*As with poison or drugs in a human, the first time may be the last.*” Other resources state that damage due to liquid flooding is rather rare to occur (Liu & Soedel, 1995; Singh et al., 1986), but in light of a spacecraft on a long mission given limited spare parts and technician capacity, liquid flooding should simply be avoided.

Although liquid flooding has not been experimentally proven to be an issue in microgravity, it can easily be conceived to occur during start-up. In stand-by, the location of the liquid is difficult to predict and there is a chance for migration towards the suction port. It would then quickly enter the compressor upon start-up. While the cycle is in operation, the danger for liquid refrigerant reaching the compressor is minimal, because the expansion valve can control the mass flow rate to ensure superheat regardless of gravity.

Even if the liquid did not migrate into the suction line but is located in the evaporator, liquid slugging can be a concern. Flashing and boiling due to the rapid pressure decrease at start-up can push liquid refrigerant out of the evaporator and into the compressor shell. When liquid refrigerant enters the compressor shell in normal gravity, it usually pools at the bottom of the compressor. Gravity prevents it from reaching the suction valves. If liquid refrigerant entered the compressor shell in microgravity, the location would be impossible to predict. In an unlucky scenario, liquid refrigerant could indeed reach the suction valve and enter the compressor.

Overall, vapor compression cycles for spacecraft have such high reliability requirements, that liquid in the compressor shell should generally be avoided. The low probability of issues is not a valid argument to waive concerns in this case.

Gravity independent compressor

The vast majority of compressors are oil-lubricated and achieve lubrication using an oil-pump. The pump picks up oil from the oil-sump at the bottom of the compressor as shown in Figure 11 (left). This works well on earth, but a gravity-driven oil sump is by definition unreliable in microgravity. In microgravity, given the moving parts and vibrations of the compressor, the location of the oil is difficult to predict. Without vibrations and capillary forces, the oil would most likely hug the shell of the compressor as exemplified in Figure 11 (right). Overall, three solutions appear possible:

1. An oil-free compressor would avoid the concern of oil entirely, trading it off against lower efficiencies and a potentially shorter life-time.
2. The oil-lubrication system could be designed to be gravity independent. The oil could for example be carried as a mist in the suction gas. Oil-return from the cycle should be a smaller problem in microgravity than for terrestrial applications. The gravity independence of a mist-lubricated compressor could be verified easily on an inclinable test stand.
3. The oil-lubrication system could be designed for microgravity. For example, the compressor shell in Figure 11 could be formed such that capillary forces accumulate the oil where the oil-pump can pick it up.

The discussion of compressors and oil in microgravity often forgets SKV-1 and SKV-2. As mentioned in the previous section, those compressors are oil lubricated but oil and refrigerant are separated by means of a bellows.

Longevity of compressor

High quality compressors in terrestrial applications are designed to last very long times without maintenance. For example, residential refrigerators can last 20 years and more without a single maintenance service. Refrigeration compressors have not been extensively tested in microgravity. Even though the oil-lubrication system is the only aspect that is clearly gravity reliant, it is not experimentally verified that no other problems arise from microgravity. Oil-free compressors circumvent the oil-management issues, but are less understood in terms of longevity.

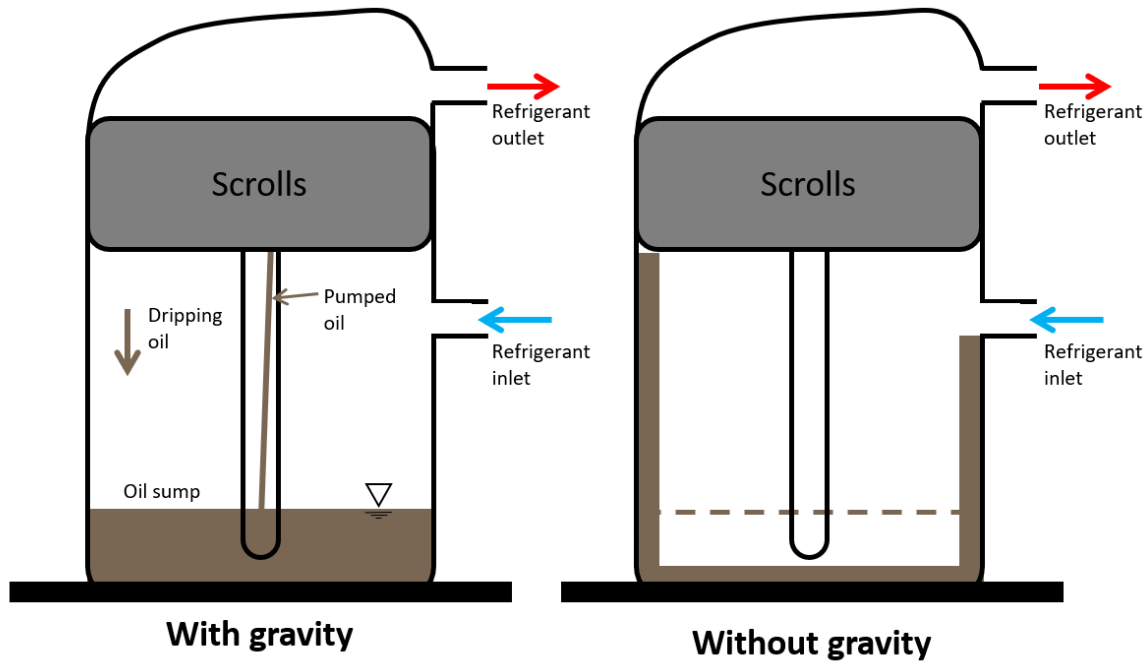


Figure 11: Conventional oil-management with and without gravity.

Low noise level

A spacecraft environment calls for low noise levels. Goodman and Grosveld (2015) wrote a book about “Acoustics and noise control in space crew compartments” and identified the refrigerators OR/F and LSLE as severe sources of noise (page 215). The text does not exactly distinguish between the refrigerators and other sources of noise. Still, the refrigerators are said to contribute to a noise level that interfered with sleep of the astronauts, communication with the ground and caused headaches to most of the crew. Future vapor compression cycles must be able to stay below an acceptable noise threshold.

Unpredictable heat transfer coefficients

A heat transfer coefficient correlation in which gravity has a validated effect is virtually non-existent. The two-phase flow community agrees that flow boiling and flow condensation is not dysfunctional in microgravity, but that the heat transfer coefficients may deviate from those within a gravity environment. Unfortunately, the magnitude of the deviation is not yet cast in reliable correlations. Balasubramaniam (2019) and Mudawar (2017) present extensive reviews of microgravity two-phase flow which are briefly summarized in Brendel et al. (2021g), but they

agree that a dedicated zero-G correlation is not available. This situation may change with the “Flow Boiling and Condensation Experiment” (FBCE), which is a two-phase flow test rig which was inserted into the ISS in August 2021 for accurate long duration measurements of heat transfer coefficients and CHF in microgravity (deFiebre & Guzik, 2019; Pike, 2021).

Subcooled liquid at expansion valve

A typical four component vapor compression cycle operates with approximately 5 Kelvin of subcooling at the expansion valve. In terrestrial applications, the amount of charge dictates the subcooling level and the expansion valve is situated below or level with the condenser outlet such that the pure liquid phase enters the valve. In a microgravity environment, the relative positioning of components cannot be leveraged to maintain subcooling.

Launch loads and vibrations

The vibrational and accelerational loads during a rocket launch are significant. Past launches of VCCs prove that the tubing and couplings can be built to withstand the stress, but the exposure to such loads is still unusual for terrestrial applications and therefore a specific problem for space-bound VCCs.

Removal of condensed water from evaporator coils

A refrigerator or air-conditioner operating below the dew point of the heat source will dehumidify air, causing condensate to build up on the evaporator coil. With gravity, the condensate drains off naturally. In microgravity, the condensate may build up around the evaporator coils as illustrated in Figure 12. This diminishes the overall conductance (UA) of the heat exchanger and even increases the air side pressure drop if the fin spacing is low. A gravity independent condensate removal or dehumidification approach will be needed for air-refrigerant evaporators in microgravity. On the ISS, the Common Cabin Air Assembly (CCAA) has a “condensing heat exchanger” which utilizes a hydrophilic coating to condense water vapor and then feed it to a liquid/air separator (Balistreri et al., 2018; Carter, 2017). Also, the SKV-1 and SKV-2 appear to successfully dehumidify air, but detailed technology documentation could not be found.

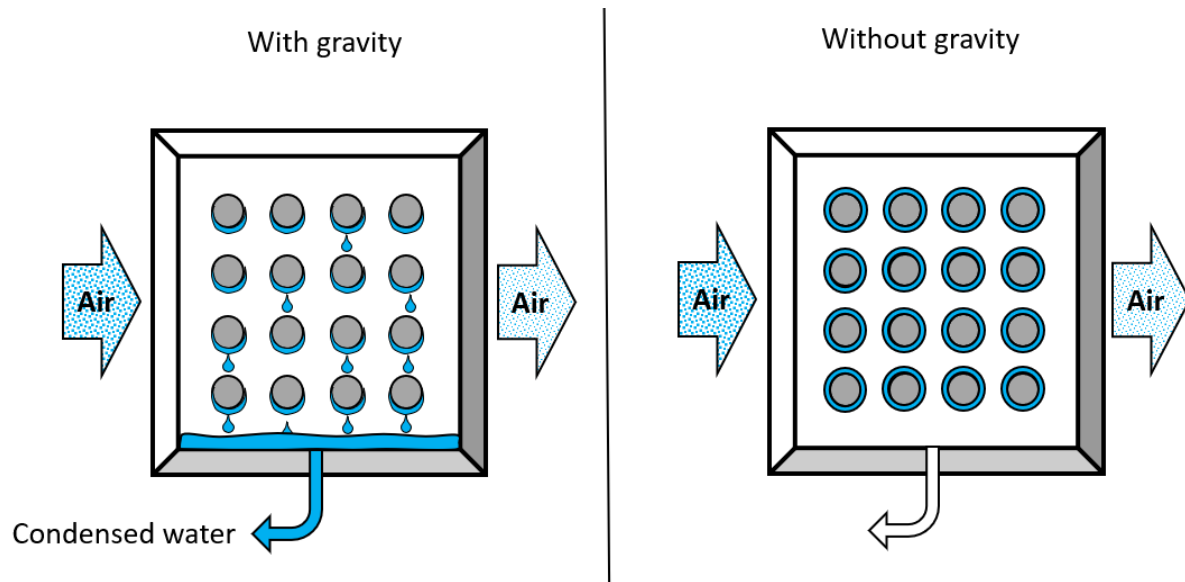


Figure 12: Water drainage of evaporator coil with and without gravity.

Microgravity critical heat flux (CHF)

Vapor bubbles in microgravity do not experience buoyancy forces and are removed from the wall only by forces induced by the flow in which the bubbles grow. This leads to a reduction of the critical heat flux (CHF) and should be carefully considered if the heat source is of constant heat flux type like in electronics cooling or if the temperature differential between the heat source and the saturated refrigerant is extreme. In typical refrigeration of biological samples or food as well as in air-conditioning, the CHF is not problematic. In situations where the CHF is indeed important, heat exchanger designs should pay attention to two-phase flow gravity independence criteria specifically for CHF as for example published in Zhang et al. (2004).

1.2.3 Microgravity testing opportunities

Gravity

Gravity is one of four fundamental forces (together with electromagnetic, weak and strong interactions). Gravity forces have an infinite range and, in contrast to electromagnetic forces, cannot be shielded against. Therefore, no stationary laboratory to perform microgravity testing on earth can exist.

The intensity of gravity diminishes with distance according to the following equation:

$$g = g_e \left(\frac{R_e}{R_e + x} \right)^2 . \quad (6)$$

R_e is the radius of earth, g_e the gravity at the surface and g the gravity at distance x . This equation was used to create the plots in Figure 13. On the left-hand side, the gravity is plotted from the surface of the Earth to a distance similar to the orbit of the ISS. On the right-hand side, the gravitational acceleration is plotted from the surface of the Earth to a distance similar to the distance between the Earth and the Moon. A common misunderstanding is that objects in spacecraft, like the ISS, would experience weightlessness due to their distance from earth. In reality, the ISS is still accelerated towards earth with about 80% of the acceleration humans experience on the surface of earth. Weightlessness results from the constant free fall which orbiting spacecraft experience.

All microgravity testing platforms available for research rely on free-fall to provide a microgravity environment. In order of increasing microgravity duration these are: drop-tower, parabolic flight, sounding rocket and orbiting spacecraft. The characteristics of these testing platforms are important in the design phase of zero-G experiments and are explained in the following subsections. An inclinable test stand is included in the comparison although it will not provide a microgravity environment.

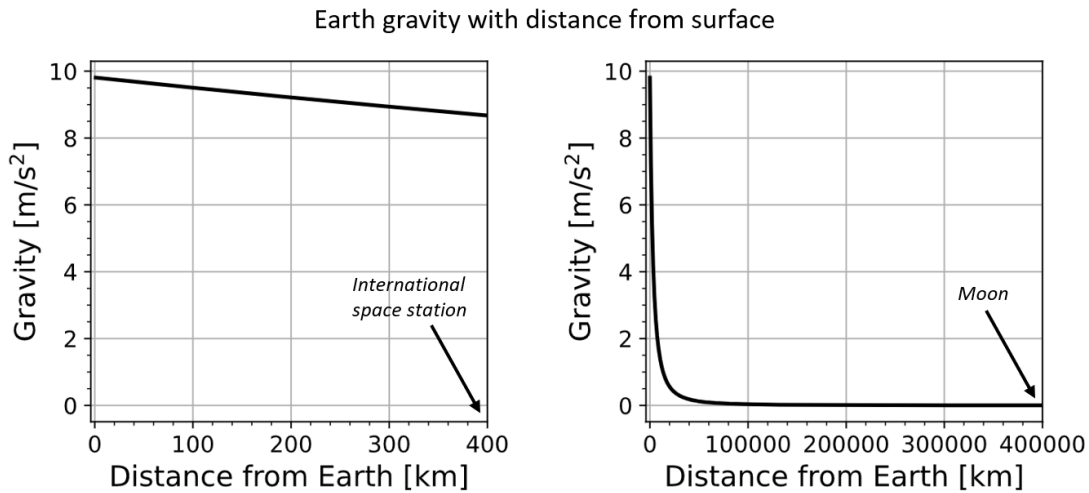


Figure 13: Earth gravity as a function of distance to the ISS (left) and the Moon (right).

Available testing platforms

This section introduces the four microgravity testing platforms along with inclination testing. Albeit inclination testing on earth will not generate a microgravity environment, it is still an important testing vehicle and therefore listed in this comparison. The testing platforms are introduced in more detail in Brendel et al. (2019a) and a thorough overview of microgravity testing opportunities is also given by the European Space Agency (ESA) (2014). The testing platforms are first introduced qualitatively followed by a table with quantitative characteristics.

Inclination testing

A test setup with flexible inclination angle allows studies of the effect that gravity has on an experiment. Moreover, certain angles can be used to purposefully create worst-case scenarios for the test object and develop gravity independence studies. Terrestrial inclination testing has the tremendous benefits of being inexpensive, not restricted by time and offering perfect accessibility for the researcher at all times.

Drop tower

Payloads in a drop tower travel on a vertical trajectory. The payload either simply drops from top to bottom or is catapulted from the bottom and travels up and then down, constantly experiencing free fall. Drop towers are a relatively inexpensive testing facility but researchers can usually not access their experiment during the free-fall and free-fall durations are mostly less than 10 seconds, typically even less than 5 seconds.

Parabolic flight

The free-fall in a parabolic flight is achieved by an airplane that flies on a specific trajectory mirroring free-fall. By changing the trajectory, parabolic flights can also simulate reduced gravity environments. Parabolic flights offer the largest payload size of the four microgravity testing platforms and researchers can manually interact with their experiments at all times. On the downside, the microgravity duration of one parabola is limited to approximately 20 seconds. One parabolic flight provides usually about 30 parabolas which allows researchers to repeat an experiment, change parameters or make minor modifications. Inevitably, the microgravity periods

are interspersed with hyper gravity periods which is beneficial or disadvantageous depending on the specific payload.

Sounding rocket

A sounding rocket can carry multiple experiments, which are typically stored in lockers. A rocket travels to a height of approximately 100 km and then separates from a capsule holding the payload lockers. Due to the very low ambient density at this altitude, the capsule then experiences free-fall for about 3 minutes. While 3 minutes is an appreciable microgravity duration, the payload lockers are both expensive and small and cannot be accessed during the flight. Each locker is provided with digital information about the state of the capsule (for example the start of microgravity) upon which the experiment must be controlled automatically.

Orbital spacecraft

Testing on an orbital spacecraft is the only option for long term zero-gravity testing. However, the accessibility and the required preparation are significant downsides. Orbital spacecraft are a suitable testing platform for more mature experiments that have undergone testing on one or more of the other microgravity testing platforms.

Advantages, disadvantages, cost

All testing platforms have advantages and downsides that are described by Brendel et al. (2019a). Costs and allowable volume or mass of payload vary by the provider of the testing platform and are often difficult to find in the open literature. To give the reader a better understanding, example payloads and their main characteristics for each platform (time of zero-G, allowed volume, allowed mass, cost and accessibility of researcher to the experiment) are presented in Table 3. Since these are examples, the provided values are realistic but still change among flight providers.

Table 4 compares the testing opportunities with their main characteristics using a “good”, “medium” and “poor” scale.

Table 3: Examples of testing platforms. The information in the table provides specific examples and not limits or ranges for the testing platform characteristics. As published in Brendel et al. (2019a).

Platform	$\Delta t_{g=0}$	Volume for payload	Mass for payload	Cost in US\$	Accessibility	Ref
Inclined stand	Not applicable	1.7 m ³	100 kg	\$10000	High	Personal experience
Drop tower	9.3 s	0.34 m ³	162 kg	N/A	Low	(European Space Agency, 2014)
Parabolic flight	20 s	9.3 m ² (+ personnel)	635 kg	~\$44500 for two flights	High	(ZERO-G, 2020; ZERO-G, 2021)
Commercial sounding rocket	3 minutes	0.052 m ³	11.3 kg	~\$115000	Low	(Wagner, 2019)
Orbital spacecraft	Several months	~0.2 m ³	~165 kg	N/A	Low	(deFiebre & Guzik, 2019; Pike, 2021)

Table 4: Comparison of body-force and microgravity testing platforms for VCC on a "good", "medium" and "poor" scale for five aspects.

Aspect	Inclinable Stand	Drop Tower	Parabolic Flight	Sounding Rocket	Orbital Spacecraft
$\Delta t_{g=0}$	●	●	●	●	●
Cost	●	●	●	●	●
Allowed volume/mass	●	●	●	●	●
Accessibility	●	●	●	●	●
Availability	●	●	●	●	●

1.2.4 Direct condensing radiators

Williams et al. (1973) conducted microgravity tests for a direct condensing radiator. “Direct” means that the condensing process takes place inside of the radiators. This is in contrast to most radiators until today which have no fluid flow at all or a single-phase flow as depicted in Figure 3. Williams was not the only researcher that proposed to make the condenser of a refrigeration cycle also the radiator of a spacecraft. The reasoning was simple: If heat transfer due to radiation follows the temperature to the power of 4, a small increase of the condensing temperature would suffice to reject significantly more heat. Hence, from a given design point, the high side pressure would not increase much if the operating conditions of the cycle demanded a higher heat rejection. The reasoning is incorrect if the heat is rejected against a very low

temperature (like the deep space temperature). Table 5 shows the governing heat transfer laws for convective and radiative heat exchange. T is the temperature at which heat is rejected (surface of the heat exchanger). For the parameters in Table 5 and $T = 300\text{ K}$, the heat exchanger relying on convection and the radiator both reject heat at a rate of 200 W. Figure 14 shows the heat rejection rates as a function of increasing T . Clearly, the heat exchange via convection increases with a much steeper slope than the heat rejection rate of the radiator. This means for an incremental temperature change, the convective heat transfer increases more.

This is initially counterintuitive but simple to understand: The driving potential for the convective heat transfer is initially at $300\text{ K} - 295\text{ K} = 5\text{ K}$. Increasing T by 10 K triples this and so does the rate of heat rejection. For the radiator, the driving potential for heat rejection is initially $(300\text{ K})^4 - (0\text{ K})^4 = 8.1\text{e}+9\text{ K}^4$. Increasing T to 310 K changes this to $(310\text{ K})^4 - (0\text{ K})^4 = 9.2\text{e}+9\text{ K}^4$, which is a *relatively* small increase of 14% because the driving potential was increased by a margin which is small *relative* to the initial driving potential.

Table 5: Equations and parameters for example in Figure 14.

Convection		Radiation	
Governing law	$\dot{Q} = Ah_a(T - T_a)$	Governing law	$\dot{Q} = A\epsilon\sigma_b(T^4 - T_{DS}^4)$
Area	$A = 1.74\text{m}^2$	Area	$A = 0.5\text{m}^2$
Heat transfer coefficient	$h_a = 15\text{ W/m}^2\text{K}$	Emissivity	$\epsilon = 0.8$
Ambient temperature	$T_a = 295\text{ K}$	Stefan-Boltzmann constant	$\sigma_b = 5.67 \cdot 10^{-8}\text{ W/m}^2\text{K}^4$
		Deep space temperature	$T_{DS} \approx 0\text{ K}$

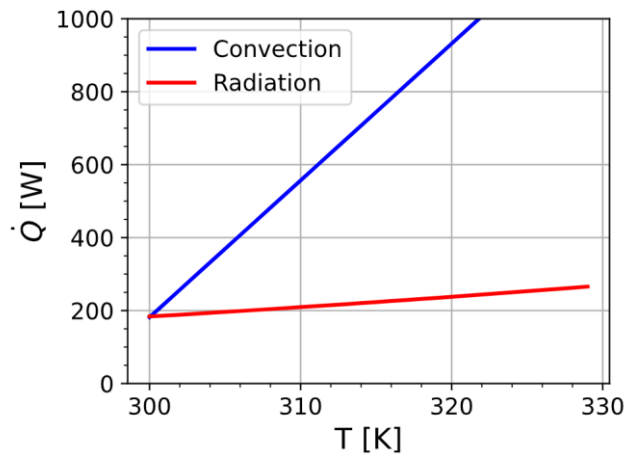


Figure 14: Heat rejection capacity as a function of condensation temperature.

1.2.5 Gravity independence criteria

In the following, two-phase flow is discussed as the flow of one fluid that exists in both the liquid and the vapor phase (as opposed to two different fluids or a solid in a fluid). As such, the two phases have a different density and due to gravity, a stratified flow will be observed for low flow-rates in a horizontal tube. In a stratified flow, the higher density phase flows at the bottom and the lower density phase at the top. When the flow rate increases, there will be a transition to annular flow, seemingly negating the effect of gravity. This observation is fundamental for what is commonly called “gravity independent two-phase flow”. It is a two-phase flow that is not notably influenced by gravity and therefore interesting for the design of two-phase systems for microgravity. If a system is gravity independent, its performance on a spacecraft would be equivalent to its performance on earth, promising a reduction of expensive microgravity testing.

Negation of effects of gravity for two-phase flow

Fundamental concept

O'Neill et al. (2017) presents a plot that illustrates the idea of gravity independent two-phase flow very clearly. A sketch of this plot is shown in Figure 15. The author measured the condensation heat transfer coefficient of two-phase flow for vertical up-flow, vertical downflow and for horizontal flow. He then normalized the heat transfer coefficients by dividing the ones for vertical flow by the measured value for horizontal flow. For a flow velocity of 0.1 m/s (of the saturated liquid), the ratios were very different. The heat transfer coefficient of the vertical downflow was higher than for horizontal flow and the heat transfer coefficient for vertical up-flow was lower than for the horizontal flow. With increasing flow velocity, the two ratios merged and became unity, meaning that the heat transfer coefficients for all flow orientations were equal. Many other studies confirmed the statement “A higher flow velocity makes two-phase flow less gravity dependent” and proposed different criteria for a threshold to achieve gravity independence.

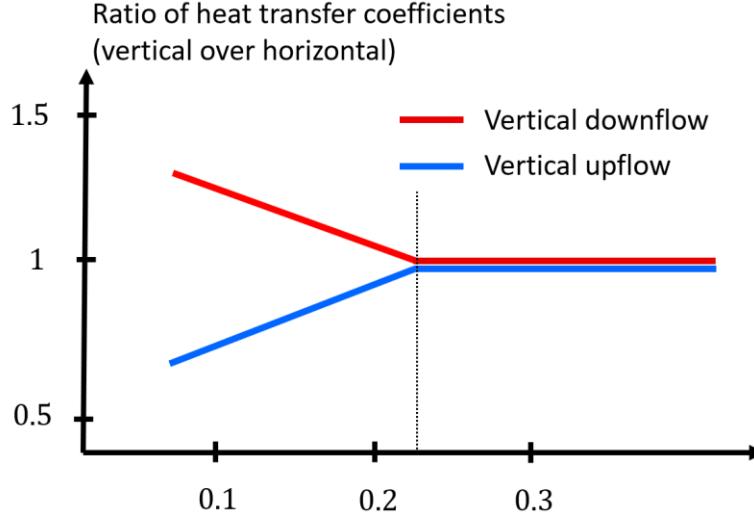


Figure 15: Ratio of heat transfer coefficient for different flow orientation as a function of flow velocity. Adapted from O'Neill et al. (2017).

Normalization of criteria

To facilitate a comparison between different criteria, they must be normalized to some parameter of comparison. Most approaches in the open literature use a flow velocity. Looking at a two-phase flow changing from a saturated liquid to a saturated vapor, there are seven different velocities one could use to compare criteria. These are labeled $(u_{x0}, u_f, j_f, u_x, u_g, j_g, u_{x1})$ and depicted in Figure 16. The velocity of the saturated liquid u_{x0} is chosen as the reference velocity ($u_r = u_{x0}$) and if criteria use other velocities, they will be converted to the reference velocity. A more detailed derivation of the various velocity conversions based on the slip-flow model for two-phase flow can be found in Brendel et al. (2020c). When “the threshold velocity” of a gravity criterion is discussed in the following, this will always refer to the reference velocity if not stated otherwise.

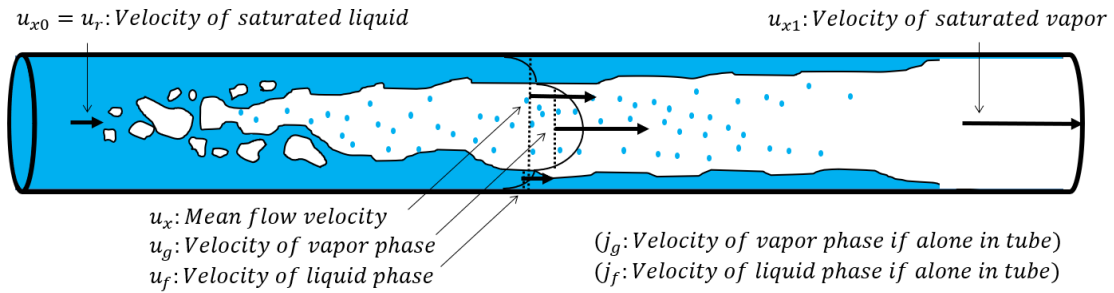


Figure 16: Illustration of seven different flow velocities relevant in the slip-flow model for two-phase flow (Brendel et al., 2021a).

General trends

Before analyzing the different criteria, thought experiments can be telling about the trends that are to be expected. The thought experiments weigh inertia forces, buoyancy forces and surface tension forces against one another. Figure 17 shows the threshold flow velocity as a function of four different parameters in simplified linear plots. Higher gravity levels g are expected to require higher flow velocities u_r if inertia forces are to overcome buoyancy forces. From left to right: Higher saturation temperatures yield smaller density ratios and therefore smaller buoyancy effects, requiring smaller inertia forces and thus a lower flow velocity. A larger diameter D requires a larger threshold flow velocity for a stable two-phase flow because capillary forces are lower and bubbles have more space to move lateral to the flow direction. Finally, a larger quality x requires a lower threshold flow velocity, because the volume of liquid is smaller and stabilizing it against buoyancy forces requires less inertia forces.

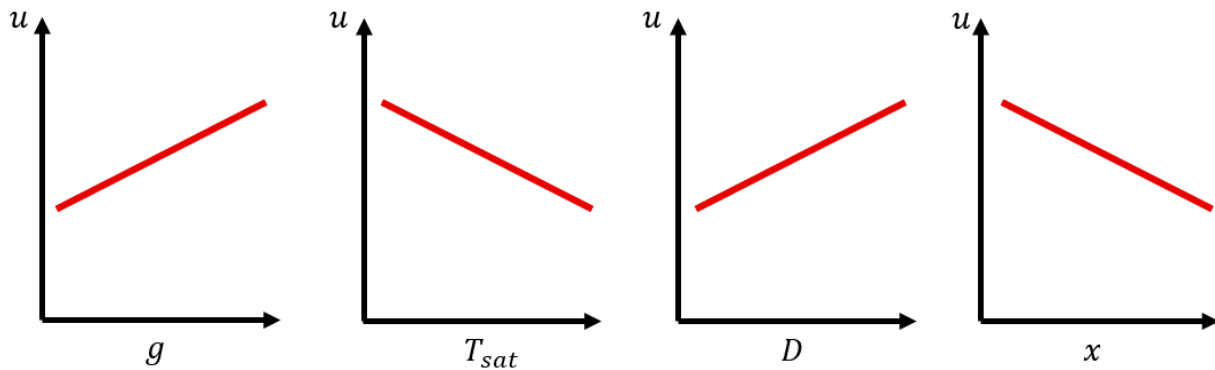


Figure 17: Generally expected trends of threshold flow velocity for gravity-independent two-phase flow with four different parameters.

Types of criteria

The suggested gravity independence criteria in the literature span a spectrum from purely empirical to largely mechanistic ones. The criteria can also be categorized by the *aspect* of two-phase flow that shall be gravity independent (CHF, flow regime, heat transfer). Three criteria are presented as illustrative examples for the derivation of gravity independence criteria. A more detailed explanation of the origin of all gravity independence criteria can be found in Brendel et al. (2020c).

Zhang et al. (2004) built a criterion based on measurements of the critical heat flux (CHF) in a channel at eight different orientations with varying flow rates. In the following, this criterion is referred to as the CHF-criterion. For complete gravity independence, the authors deemed three conditions important: gravity forces in parallel to the flow direction must be negated, gravity forces perpendicular to the flow direction must be negated and the wavelength must be shorter than the length of the heated section. For each condition, a dimensionless measure was derived and a threshold was given to it based on the experimental results obtained from the study. The three conditions are included here for completeness (subscripts are used for any dimensionless numbers that have been defined differently in different studies):

$$\frac{Bo_3}{We_2^2} = \frac{(\rho_f - \rho_g)(\rho_f + \rho_g)^2 \sigma g}{\rho_f^2 \rho_g^2 u_r^4} \leq 0.09, \quad (7)$$

$$\frac{1}{Fr_2} = \frac{(\rho_f - \rho_g)gD_h}{\rho_f u_r^2} \leq 0.13, \quad (8)$$

$$We_2 = \frac{\rho_f \rho_g u_r^2 L_h}{(\rho_f + \rho_g)\sigma} \geq 2\pi. \quad (9)$$

A few years before the CHF-criterion, Ungar (1998) based a gravity independence criterion for horizontal flow on the observation that a stratified flow is clearly gravity dependent. If a flow is not stratified, it may be annular or dispersed/intermittent. Ungar proposed that annular flow is gravity independent but dispersed/intermittent flow is only gravity independent if the size of the bubbles fills the tube, such that their location is determined. Ungar selected the flow map from Taitel and Dukler (1976) and defined the margin for non-stratified flow as 10 times greater than the transition criteria in the flow map. He arrived at the following two conditions:

$$Fr_1 \geq 10 Fr_{1,tr}$$

$$and Bo_1 \leq 1 if X > 1.6.$$

$X > 1.6$ is the condition for dispersed/intermittent flow and $Bo_1 \leq 1$ is the condition for bubbles to fill the cross-sectional area of the tube before growing axially? Figure 18 shows the three relevant areas of the criterion in the flow regime map of Taitel and Dukler (1976) for R134a at $T_{sat} = 0^\circ C$ and $D = 4mm$. The criterion is referred to in the following discussion as the “Flow-regime criterion”.

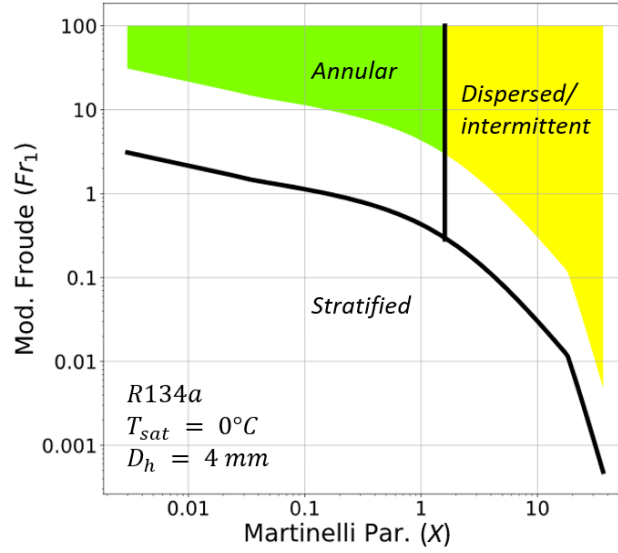


Figure 18: Unconditionally and conditionally gravity independent two-phase flow based on Flow-regime criterion (Ungar, 1998) in Taitel and Dukler flow-map (Taitel & Dukler, 1976). Published in Brendel et al. (2021a)

Zhao et al. (2000) distinguished gravity dominated, surface tension dominated and inertia dominated two-phase flow, of which the two-phase flow categorized as one of the latter two would be gravity independent. He then estimated the transition values for the Bond number (Bo_2) and Froude number (Fr_1). Figure 19 depicts the gravity independent region in green and the transition values with solid lines. Baba et al. (2011) used a similar idea but defined the Froude number differently (Fr_3) and found new transition values. For high qualities (x), $Fr_1 \approx Fr_3$ such that the two criteria can be compared in one plot for high x . In Figure 19, the criterion of Baba et al. (2011) is plotted with dashed lines. The two criteria are labeled Bo-Fr-1 and Bo-Fr-2 in the following.

Usage of criteria

Figure 20 shows a qualitative comparison of the CHF criterion (Zhao et al., 2000) and the Bo-Fr-1 criterion (Zhao et al., 2000). If one was interested in designing a system that operates independent of gravity forces on earth, a value of $g \approx 9.81 \text{ m/s}^2$ is found on the x-axis and a corresponding flow velocity is found on the y-axis for each criterion (here approximately 0.3 m/s and 3 m/s). In the design process, a mass flow rate can be calculated based on a needed capacity and a pipe diameter can then be calculated to achieve the flow velocity required by the criterion.

Figure 20 also shows how the division of criteria into multiple conditions can lead to step changes in the plots. Moreover, sometimes a criterion does not require any flow velocity (usually if a Bond number condition is predominant as in the Bo-Fr-1 criterion in Figure 20 for $g < 3 \text{ m/s}^2$). Since 0 m/s cannot be plotted on a log-scale, a lower bound of 1 mm/s is introduced for all criteria. Flow velocities lower than that are very rare and impractical for vapor compression cycles.

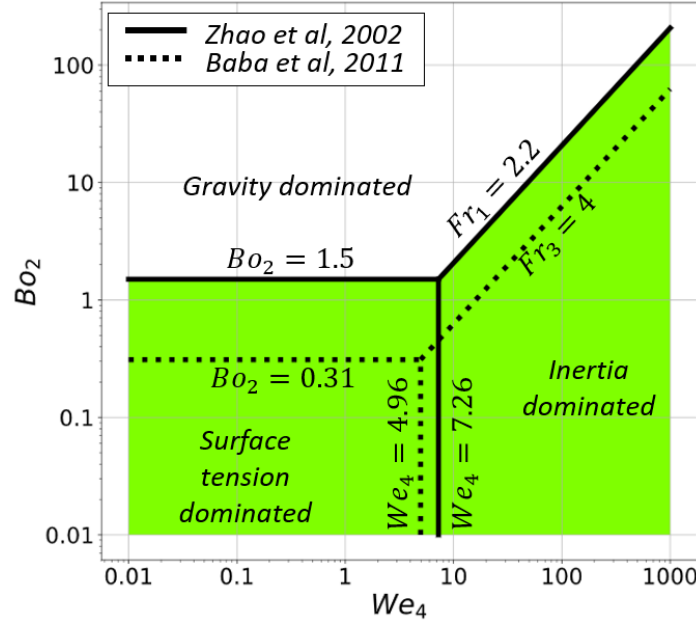


Figure 19: Gravity independent region in Bond-Weber chart according to Bo-Fr-1 and Bo-Fr-2 criterion (Brendel et al., 2021a).

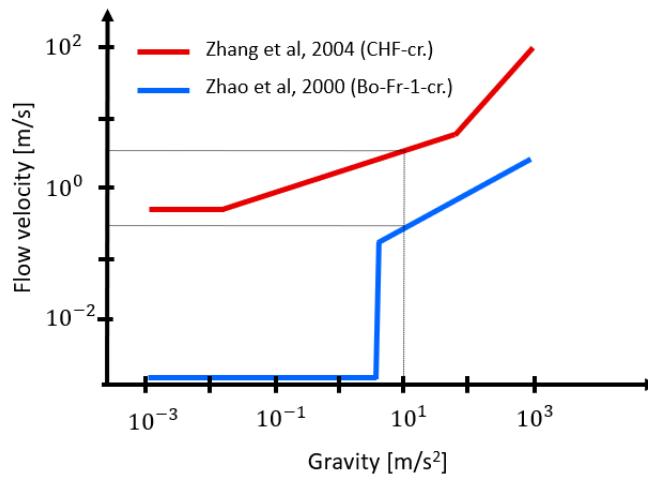


Figure 20: Example threshold flow-velocity for the CHF and Bo-Fr-1 criterion as a function of gravity.

Comparison of published gravity independence criteria

A comparison of the existing gravity independence criteria normalized to the reference velocity u_r is published in Brendel et al. (2020c). Some key findings are summarized here, but the publication offers more depth, in particular a summary of all equations of the different criteria in a consistent nomenclature. A total of 13 criteria were found that describe a threshold for gravity independent two-phase flow. To facilitate the discussion of these, each criterion has been given a name, which is based on the derivation or important dimensionless numbers of the criterion. All references, names and the functional forms of the criteria are shown in Table 6. Comparing the criteria shows that authors used different definitions for dimensionless numbers. To clearly distinguish all of them, each dimensionless number is assigned a subscript. The various definitions of dimensionless numbers are shown in Table 7.

Table 6: Table of all compared gravity independence criteria and their functional form. Each criterion has been given a name for easier referencing (Brendel et al., 2021a).

Reference	Name	Form	Reference	Name	Form
(Hye, 1985)	<i>Reynolds-cr.</i>	$G = f(FL, T_s, D)$	(Sardesai et al., 1981)	<i>JG cr.</i>	$G = f(FL, T_s, D, g, x)$
(Brauner, 1990)	<i>Buoyancy-cr.</i>	$D = f(FL, T_s, g)$	(Baba et al., 2011)	<i>Bo-Fr-2-cr.</i>	$G = f(FL, T_s, D, g, x)$
(Ungar, 1998)	<i>Flow regime-cr.</i>	$j_g = f(FL, T_s, D, g, x)$	(Konishi et al., 2013)	<i>CHF-x-cr.</i>	$u_r = f(FL, T_s, D, g, x, L_h)$
(Zhao et al., 2000)	<i>Bo-Fr-1-cr.</i>	$j_g = f(FL, T_s, D, g, x)$	(Del Col et al., 2014)	<i>Y-cr.</i>	$G_g = f(FL, T_s, D, g, x)$
(Zhao et al., 2002)	<i>We-Ca-cr.</i>	$j_g = f(FL, T_s, D, g, x)$	(O'Neill et al., 2017)	<i>U-char-cr.</i>	$\Delta u_{ig} = f(FL, T_s, D, g, x)$
(Zhang et al., 2004)	<i>CHF-cr.</i>	$u_r = f(FL, T_s, D, g, L_h)$	(Zhang et al., 2018)	<i>We-Eo-cr.</i>	$u_r = f(FL, T_s, D, g, L_h)$
(Bower & Klausner, 2006)	<i>Lift-off-cr.</i>	$u_r = f(FL, T_s, \Delta T_s)$			

Table 7: Overview of dimensionless numbers with different definitions employed by authors of gravity independence criteria (Brendel et al., 2021a).

Reynolds	Bond	Froude	Weber
$Re_1 = \frac{GD_h}{\mu_g}$	$Bo_1 = \frac{g(\rho_f - \rho_g)(D/2)^2}{\sigma}$	$Fr_1 = \sqrt{\frac{\rho_g}{\rho_f - \rho_g}} \cdot \frac{j_g}{\sqrt{Dg \cos(\theta)}}$	$We_1 = \frac{\rho_g j_g^2 D}{\sigma}$
$Re_2 = (1 - x)GD/\mu_f$	$Bo_2 = \frac{(\rho_f - \rho_g)gD^2}{\sigma}$	$Fr_2 = \frac{\rho_f u_r^2}{(\rho_f - \rho_g)gD}$	$We_2 = \frac{\rho_f \rho_g u_r^2 L_h}{(\rho_f + \rho_g)\sigma}$
$Re_3 = xGD/\mu_g$	$Bo_3 = \frac{(\rho_f - \rho_g)gL_h^2}{\sigma}$	$Fr_3 = \frac{G}{\sqrt{\rho_x(\rho_f - \rho_g)gD}}$	$We_3 = \frac{u_r^2 \rho_f h_c}{\sigma}$
$Re_4 = \frac{\rho_f u_r h_c}{\mu_f}$	$Bo_4 = \frac{(\rho_f - \rho_g)g \cos(\theta) L_{char}^2}{\sigma}$	$Fr_4 = \frac{\rho_g \Delta u_{ig}^2}{\rho_f g D_f \sin(\theta)}$	$We_4 = \frac{G^2 D}{\rho_x \sigma}$
$Re_5 = \frac{\rho_g \Delta u_{ig}(D - 2\delta)}{\mu_g}$	-	-	$We_5 = \frac{(\rho_f'' \rho_g'') \Delta u_{ig}^2 L_{char}}{(\rho_f'' + \rho_g'')\sigma}$
-	-	-	$We_6 = \frac{\rho_f \rho_g u_r^2 D}{(\rho_f + \rho_g)\sigma}$

All criteria that include a velocity were compared in four parametric studies. The default values for parameters that were not varied are $T_s = 0^\circ\text{C}$, $D_h = 4\text{mm}$, $g = 9.81\text{ m/s}^2$, $x = 0.2$. These default values are indicated with a vertical dashed line in Figure 21. Necessary assumptions and a more detailed evaluation can be found in Brendel et al. (2020c). The “X” in any plot shows a non-obvious transition of conditions within one criterion. Criteria not sensitive to a parameter were plotted as a horizontal line to facilitate an easy comparison of the magnitude of u_r .

The four parametric studies show that criteria derived from gravity sensitive two-phase flow aspects (CHF, flow regimes transitions, bubble departure) or mechanistic models consistently result in the highest flow velocities and are plotted with dashed lines (Flow-regime, CHF, Lift-off, U-char and We-Eo criterion). On the other end of the spectrum, the Reynolds criterion always has the lowest threshold at the default parameters. This criterion is the oldest but one of the few where the authors are more concerned with systems than with pure two-phase flow. Since the Re criterion only asks for a minimum Reynolds number to be exceeded, its threshold flow velocity decreases with increasing diameter, which is improbable to be correct. Overall consistency in magnitude and trend can be observed among the Bond-Froude criterion 1 and 2, the Weber-Capillary criterion, the JG criterion and the Y-criterion.

Gravity independence criteria for vapor compression cycles

Despite the multitude of gravity independence criteria for two-phase *flow*, similar criteria for two-phase *systems* are missing, with the exception of the Reynolds criteria which was meant to be used for systems from the beginning. Brendel et al. (2019c) showed with simple modelling that the application of a rather stringent two-phase *flow* criterion (the CHF criterion) to a vapor compression cycle leads to excessive pressure drop in the heat exchangers. Generally, gravity independence is only one design approach, but not necessarily the best for space-bound vapor compression cycles. Moreover, gravity independence criteria only discuss the steady-state operation of a cycle and not the start-up processes.

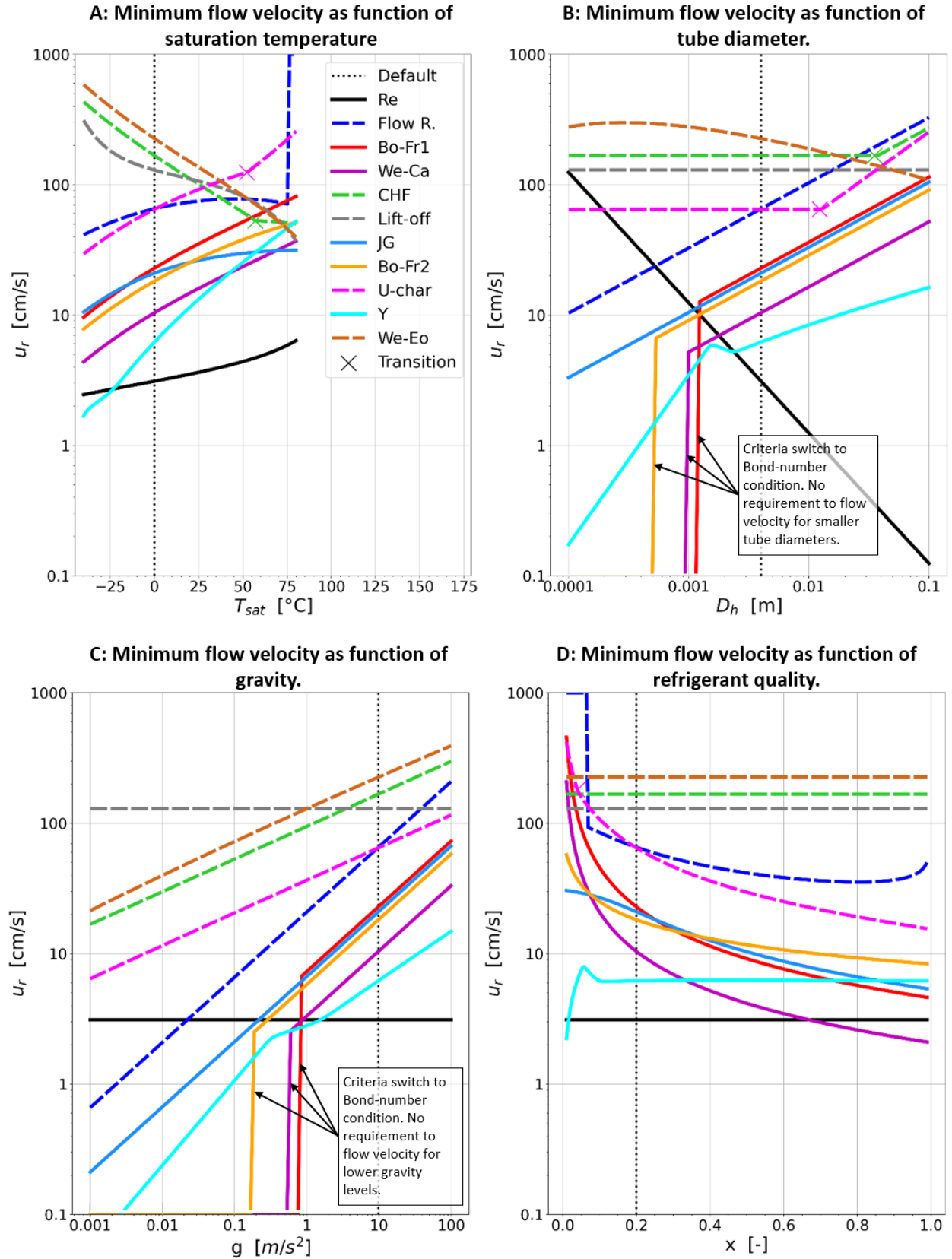


Figure 21: Parametric studies on gravity independence criteria (Brendel et al., 2021a).

1.2.6 Thermal gravitational scaling

“Thermal gravitational scaling” is sometimes also called “theory of similarity”. The goal is to design and test a system on earth (a *physical* model) such that it mirrors a needed prototype for a reduced or microgravity environment. Propositions in the literature usually base this scaling on dimensionless numbers that have to be matched for both environments. Figure 22 illustrates the concept assuming that a Mars air-conditioner is needed for which the refrigerant and evaporation temperature are already determined. Appropriate parameters for the ground-based model (D, T_e , Refrigerant) as well as unspecified parameters of the prototype (D) would then be determined in the process of thermal gravitational scaling. The concept received increased attention in the 1990s and aimed at reducing the need for zero-gravity testing, but research activities faded since the early 2000s.

The main contributors to the field conducted research in the 1990s and early 2000s (Crowley & Izenon, 1989; Crowley & Sam, 1991; Delil, 1989; Delil, 2001; Delil, 1991; Hurlbert, 2000; Hurlbert et al., 2004; Ungar, 1998). However, the research faded at a time where the proposed tools were not useful yet. Until today, there are only ideas, but no practical and verified guidelines regarding the exact application of thermal gravitational scaling. Brendel et al. (2020a) raised the following questions:

- *“What is the gravity level that can be used in dimensionless numbers to approximate zero-gravity? (e.g. if the gravity is in the denominator)*
- *What are real-world examples where thermal gravitational scaling is needed?*
- *Which group of dimensionless numbers are essential for a given system?*
- *How much deviation between dimensionless numbers is tolerable in the scaling process?*
- *What is the appropriate objective function once the set of essential dimensionless numbers is found?*
- *In addition to the Froude number, what other gravity dependent numbers should be added to the list of dimensionless numbers for two-phase flow?*
- *Can inclination testing predict reduced gravity system behavior? “*

Brendel et al. (2020a; 2021d) discuss a possible objective function and the question of the relationship between terrestrial inclination testing and microgravity experiments. Those publications also provide a brief review of Delil's work, who published most actively on the topic during the 1990s.

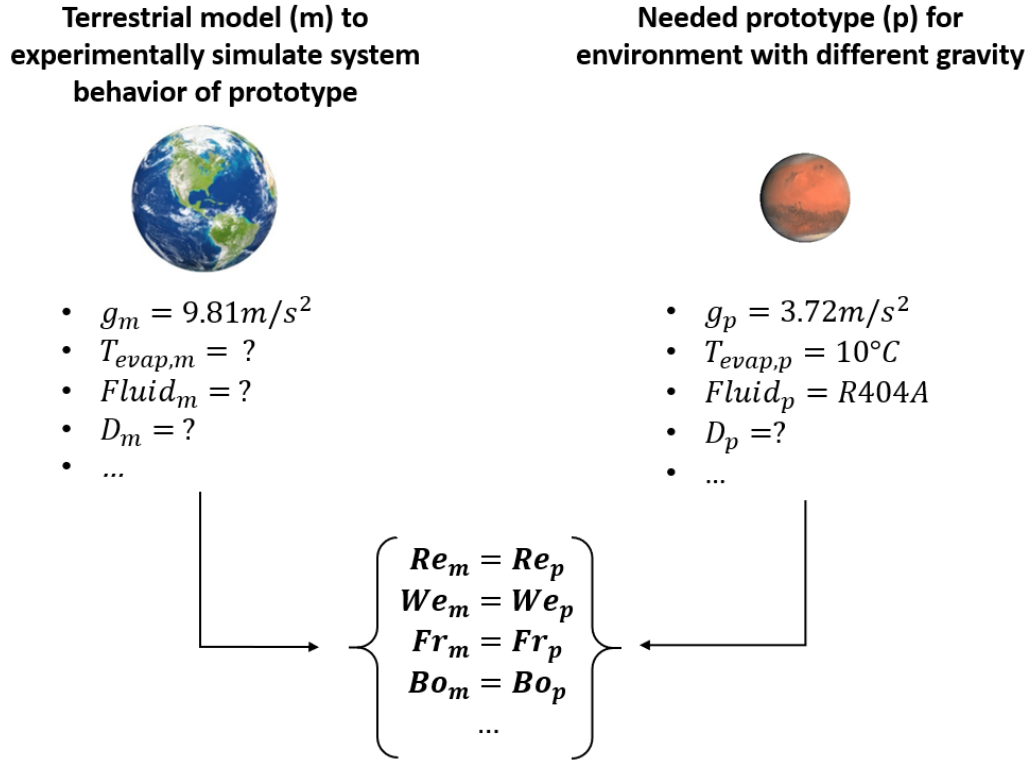


Figure 22: Illustration of the idea of thermal gravitational scaling.

1.3 Summary

1.3.1 Conclusions from literature review

The need for vapor compression cycles in reduced and microgravity environments was motivated by an equivalent mass benefit due to reduced power consumption. Only a few VCCs have operated in microgravity and typically performed poorly with one them failing completely. The confidence in the technology is therefore currently low. Conclusions of this chapter can be summarized as follows:

- 1) *Vapor compression cycles for microgravity were discussed already sixty years ago in Ginwala (1961).*

- 2) *Long duration manned space travel will bring a significantly increased cooling load for food storage (Brendel et al., 2021g).*
- 3) *The value of vapor compression cycles for spacecraft design can be measured by their equivalent mass savings (Brendel et al., 2021g; Brendel et al., 2021f).*
- 4) *One additional kilowatt of average power consumption equates to an equivalent mass of approximately 83 kg in spacecraft design (Brendel et al., 2021g).*
- 5) *When evaluating the equivalent mass benefit of two cooling technologies with different second law efficiency, the mass benefit is typically more sensitive to the lower second law efficiency according to the proposed Equation 5 (Brendel et al., 2021f).*
- 6) *VCCs that are documented to have operated in microgravity are: One without established name in 1982, OR/F, EOR/F and LSLE in the 1990s, RC in the 2005 and SKV1 and SKV2 from approximately 2000 till now (Brendel et al., 2021g). It is unclear how many units were built of OR/F, EOR/F and LSLE.*
- 7) *Most VCCs that operated in microgravity had unusually high maintenance requirements and caused various problems (Brendel et al., 2021g).*
- 8) *Failure modes and maintenance problems were not well documented (Brendel et al., 2021g).*
- 9) *Conceivable problems of vapor compression cycles due to microgravity or the launch environment are (Brendel et al., 2019a; Brendel et al., 2022b):*
 - *Liquid entrainment into the compressor during operation or at start-up.*
 - *Gravity dependence of oil-management/longevity of oil-free compressors.*
 - *Condensate removal from evaporator coil/fins.*
 - *Altered boiling or condensing heat transfer coefficients in microgravity.*
 - *Unexpected mass flow rate oscillations.*
 - *Vibration loads during launch.*
- 10) *A gravity independent lubrication system could be a viable alternative to oil-free compressors in microgravity (Brendel et al., 2021g).*
- 11) *There are four different types of microgravity testing facilities. These have strongly differing characteristics and each offers different opportunities for research (Brendel et al., 2019a).*
- 12) *All VCCs in microgravity were on orbital spacecraft. None has been on less expensive and easier to access testing facilities like parabolic flights or sounding rockets.*
- 13) *Direct condensing radiators for spacecraft can lead to widely varying high-side pressures, because the heat rejection rate is coupled to the condensing temperature*

with a steeper function than for heat exchangers relying on convective heat transfer (Brendel et al., 2019b).

14) Gravity independence criteria for two-phase flow have been proposed. The existing criteria cover a wide range of applications but have usually not been validated by many other publications (Brendel et al., 2021a).

15) Five gravity independence criteria for two-phase flow, three of which are derived differently, predict largely consistent minimum flow velocities (Brendel et al., 2021a).

16) Gravity independence criteria based on gravity sensitive two-phase flow characteristics (CHF, bubble detachment, flow regime) are consistently more stringent than other criteria (Brendel et al., 2021a).

17) Line sizing according to relatively stringent gravity independence criteria for the critical heat flux lead to excessive pressure drop and cannot be applied to vapor compression cycles (Brendel et al., 2019c).

18) Despite the proposition to apply gravity independence criteria for two-phase flow to two-phase systems, it has not been shown, that

- *...a vapor compression cycle can be truly gravity independent (no measurable change of temperatures, pressures or mass flow rate as the gravity vector is changed).*
- *...steady-state gravity independence is needed or beneficial given the potentially large penalties associated with the pressure drop of high flow velocities.*

19) Research on thermal gravitational scaling was most intense in the 1990s but has faded since and never provided design tools of high utility (Brendel et al., 2020a; Brendel et al., 2021d).

1.3.2 Research status and gaps

The research field of microgravity vapor compression cycles can be divided into three groups:

- *Motivation:* Research that motivates or justifies the use of VCCs for space applications. This research is important, but does not increase the technology readiness level.
- *Basic:* Research that enables the technology and increases the level of understanding and experience. Some would argue that this research field is already completed since some vapor compression cycles operated in microgravity in the past. In the opinion of the author, “Basic” research is the group that should receive most attention, since none of the prior art performed compellingly or even just satisfactorily. Moreover, several

discussions with NASA subject matter experts were marked by serious concerns about the operability of VCCs in reduced and microgravity. With the status quo, a VCC would not be adopted for a long duration mission to Mars, given experiences with previous systems: Astronaut complaints about OR/F, EOR/F and LSLE, a never understood failure mode of the refrigerated centrifuge and one apparently functional air-conditioner in the Russian module with barely any accessible documentation. A more systematic understanding of VCCs in microgravity is needed. The Basic class of research is therefore seen as the currently most relevant. Orientation testing, as it often precedes microgravity testing, is part of this group. Similarly, the development of reliable microgravity compressors and a solution for the dehumidification of heat exchanger coils is necessary.

- *Advanced design tools:* Research efforts in this group develop design tools for VCCs in microgravity different from the design tools for terrestrial VCCs:
 - Microgravity specific heat transfer correlations: Reliable correlations are not available yet, but pursued by the two-phase flow community and therefore not a research gap that the VCC *system* researcher must focus on. Last but not least, VCCs can tolerate some uncertainty on the refrigerant side heat transfer coefficient.
 - Gravity independence criteria for systems and thermal gravitational scaling: While these research fields are shiny and tempting, they should not be prioritized over the *Basic* research topics given the current status of the technology. Engineers will only trust advanced design tools for reduced and microgravity if they are supported by a large number of experiments made in a relevant gravitational environment. Until then, it is never wrong to prepare the tools, but proving their reliability loops back to conducting *Basic* research.

Table 8 lists the three research groups with the main examples. The “Comment” column summarizes advances that were made as explained in the sections 1.1 and 1.2.

Overall, sixty years after Ginwala (1961) started to discuss VCCs for space applications and 20 years after several VCCs operated in microgravity, measurements of such systems are still not available to researchers. Not a single vapor compression cycle was investigated on parabolic flights and system-level orientation testing has barely made it out of the starting block.

Table 8: Research fields and their current status regarding vapor compression cycles in microgravity

Research Topic	Comment
<i>Motivation</i>	
Reasoning for VCCs in zero-G	Large number of papers generally supportive. Insufficient number of papers with quantitative and verified reasoning of cost or mass effectiveness.
<i>Basic</i>	
Orientation testing of VCC	Three related literature items. Insufficient depth and documentation to derive general conclusions and confidence.
Microgravity testing of VCC	Multiple VCCs with microgravity flight experience. Some with moderate success, one with failure. No detailed documentation of two-phase flow behavior, cycle performance or failure modes.
Spacecraft suitable compressor	Several compressors utilized in space but never with documentation of efficiency. Some compressors designed and ground-tested. Most approaches oil-free. Development of gravity independent oil-lubricated compressors missing.
Condensed water draining from heat exchanger in zero-G	Successfully done on ISS. Some literature available. Adaption to evaporators operating below 0°C unclear.
<i>Advanced design tools</i>	
Gravity independence criteria for cycles	Many available criteria for two-phase flow, none validated for two-phase systems. Need of gravity independence unclear.
Similarity based design tools	Some tools proposed. No tool verified with experiments.
Heat transfer & pressure drop correlations for zero-G two-phase flow	Correlations with built-in gravity dependence rarely verified for microgravity or varying gravity levels.

1.3.3 Increasing the TRL of vapor compression cycles in microgravity

If the goal is to increase the confidence into space-bound VCCs, *Basic* research fields are in the foreground. Microgravity suitable compressors have been developed in the past and are an active field currently. There is room for improvement but the research is on the way and the products are already useful. Similarly, a heat exchanger with a hydrophilic coating to remove condensed water is on the international space station. For this dissertation, *effects of gravity on vapor compression cycles* was chosen as the core topic, encompassing both gravity acting from different orientations and gravity acting with different magnitudes. The available experimental results in the open literature are minimal and the work is important to increase the confidence into the technology for space applications.

1.4 Research goals

Sections 1.3.2 and 1.3.3 identified a number of research gaps. The following subsections describe three research goals of this dissertation related to these research gaps. In addition, contributions associated with this dissertation that are not addressed in the research goals are listed here for completeness:

- Comparison of gravity independence criteria for two-phase flow (Brendel et al., 2021a)
- Reviewing thermal gravitational scaling and developing an objective function (Brendel et al., 2020a)
- Quantifying the equivalent mass benefit of VCCs in space craft design (Brendel et al., 2021f)
- Matching testing needs to the various zero-G testing opportunities (Brendel et al., 2019a)
- Supporting an industry partner by performance testing for an oil-free scroll compressor prototype (Brendel et al., 2021b; Rohleder et al., 2018).

1.4.1 Goal 1: Quantifying cycle responses due to orientation changes

Only one publication reports successful operation of a vapor compression cycle at angles ranging from 0° to 315° , even though not with continuous operation (Domitrovic et al., 2003). Other attempts resulted in a loss of subcooling (Grzyll & Cole, 2000) or flooding of the suction line (Sunada et al., 2008). The specific goals are therefore:

- Show continuous operation of a VCC through 360 degrees of cycle orientation
- Validate stable subcooling and superheat at any orientation
- Quantify the magnitude of changes due to orientation changes compared to the initial steady-state
- Evaluate the dependence of cycle responses on the mass flux

1.4.2 Goal 2: Quantifying cycle responses from hyper and microgravity

The open literature does not report a vapor compression cycle tested on parabolic flights. Although the microgravity periods themselves are short, the alternating hyper and microgravity

can create a demanding set of robustness tests for a vapor compression cycle. The specific goals are:

- Show that a VCC is not detrimentally affected by hyper or by microgravity, i.e. subcooling and superheat remain stable and the cooling capacity is not significantly decreased
- Quantify maximum responses to alternating gravity levels
- Evaluate the dependence of cycle responses on the mass flux
- Describe recurring effects through all parabolas qualitatively

1.4.3 Goal 3: Assessing the threat of liquid flooding at cycle start-up

The relevance of this goal is controversial, with several reasons for it and others that make it seem superfluous. A debate could look like this:

Critics: There is no need for this research, since a relatively simple pump down approach would avoid flooding.

Supporters: The pump down approach can fail and requires additional hardware (valves) which is to be avoided where possible in spacecraft design.

Critics: Also, if liquid was on the low-pressure side before start-up, it could be in the suction line and not in the evaporator as investigated in this research goal. The research is therefore unrealistic.

Supporters: The liquid will accumulate in the evaporator as the coldest part of the system.

Critics: One could still ramp up the compressor slowly to avoid flooding.

Supporters: It is not understood whether that approach is reliable in microgravity. Besides, if an inverter is available at all, it probably has a minimum starting speed, which may be already above the flooding threshold.

Ultimately, this third research goal was set because the research promised to be insightful regarding microgravity fluid dynamics and systems start-up and the question can be investigated on parabolic flights very effectively. The specific question was: “*Does the risk of flooding increase at microgravity, given a fixed speed compressor start-up with liquid in the evaporator?*”

1.5 Organization of this thesis

The research goals required the development of two independent test stands, the so called “inclinable test stand” and the “start-up test stand”. Both were used extensively on the ground and on parabolic flights. The inclinable test stand was more complex and had a larger set of questions to answer. The experimental results were further supported with a dedicated model which was written as part of this dissertation. After the introduction, the dissertation describes both test stands in chapter 2 and 3. Chapters 4 to 8 are then dedicated to results of and modeling work for the inclinable test stand associated with laboratory and parabolic flight testing. Chapter 9 shows results of the start-up test stand. The last chapter summarizes the research in terms of design considerations and recommends future work.

2. INCLINABLE TEST STAND

2.1 Overview

The inclinable test stand led to the majority of all experimental results of this dissertation. It was built and tested in three configurations on the ground and then installed in the third configuration on the parabolic flights. Additional ground-based testing followed in the months after the parabolic flights. Although the name “inclinable test stand” does not fit, this was also the test stand installed on parabolic flights.

The stand was built over the course of more than a year and reconfigured multiple times. Originally, it was designed for oil-free expander testing. After the project scope changed to orientation testing, an inclination structure was custom fitted to the test rig. It is unprecedented in the open literature to perform both inclination testing and parabolic flight testing with one vapor compression system. Using the same test rig for inclination and parabolic flight testing makes the comparison of the data especially meaningful, since comparisons across two different systems would have been affected by the differences in the hardware to an unknown degree.

2.2 Configurations

The inclinable test stand was always a four-component vapor compression cycle, but the components changed over time. Three different configurations can be distinguished by the employed heat exchangers. The parabolic flight configuration thermodynamically equivalent to the third configuration for best comparability of the results, although visual differences can be seen (polycarbonate panels, additional structural brackets).

2.2.1 Configuration 1 – flat-plate evaporators

⇒ February 2nd, 2020 till September 15th, 2020

- *Two flat-plate evaporators in parallel, but only one used at a time.*
- *Water-glycol on the heat source side*
- Water-cooled tube-in-tube condenser
- Cooling water from building
- Linear or scroll compressor

- Manually operated needle valve
- R134a as refrigerant
- One sight-glass
- Liquid line mass flow meter only

The flat-plate evaporators were the design choice from the originally intended expander test stand. The test stand was used in this configuration for the first inclination shake-down testing. After realizing the great sensitivity of flat-plate evaporators to orientation changes, they were replaced, leading to configuration 2. A system schematic and picture of configuration 1 is shown in Figure 23 and Figure 24.

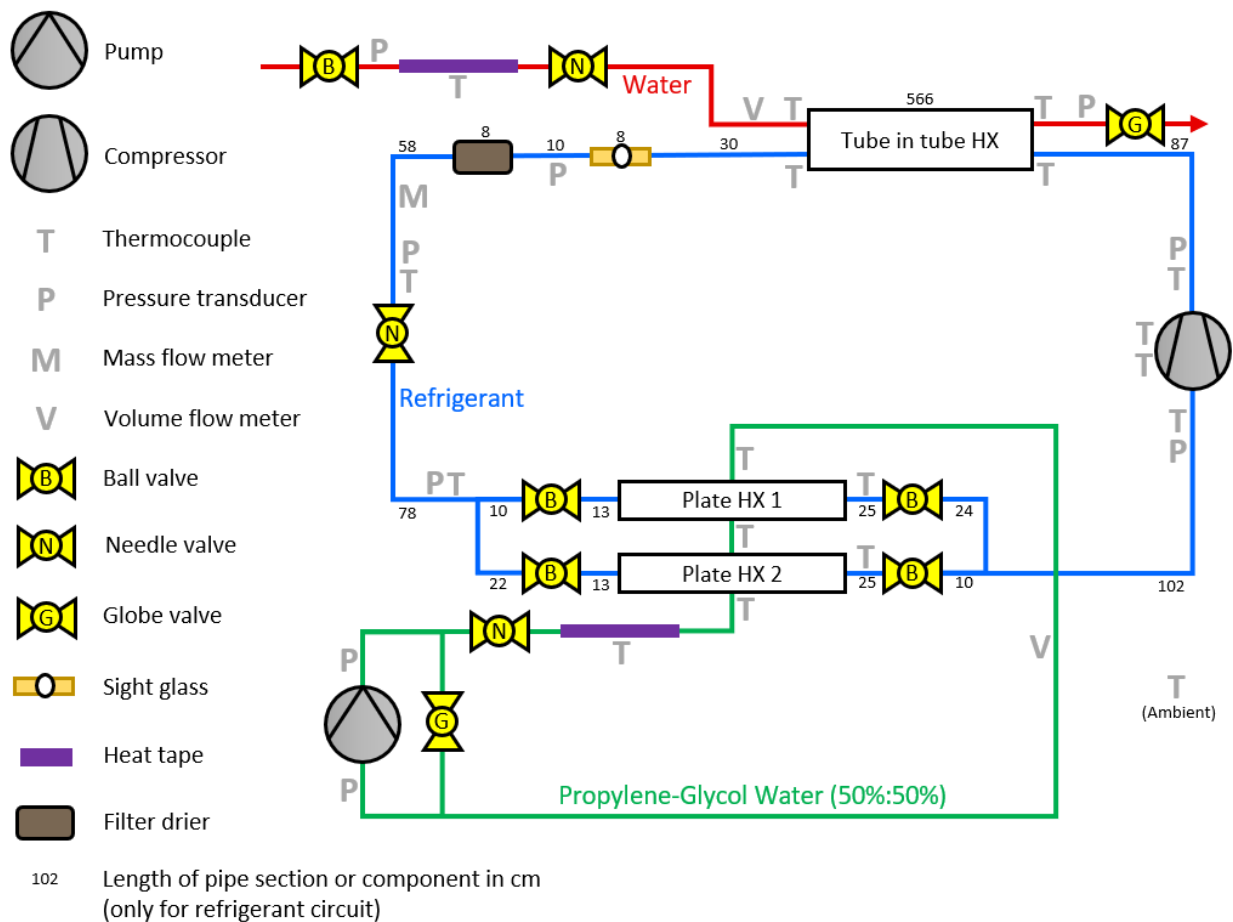


Figure 23: Plumbing and instrumentation diagram of configuration 1.

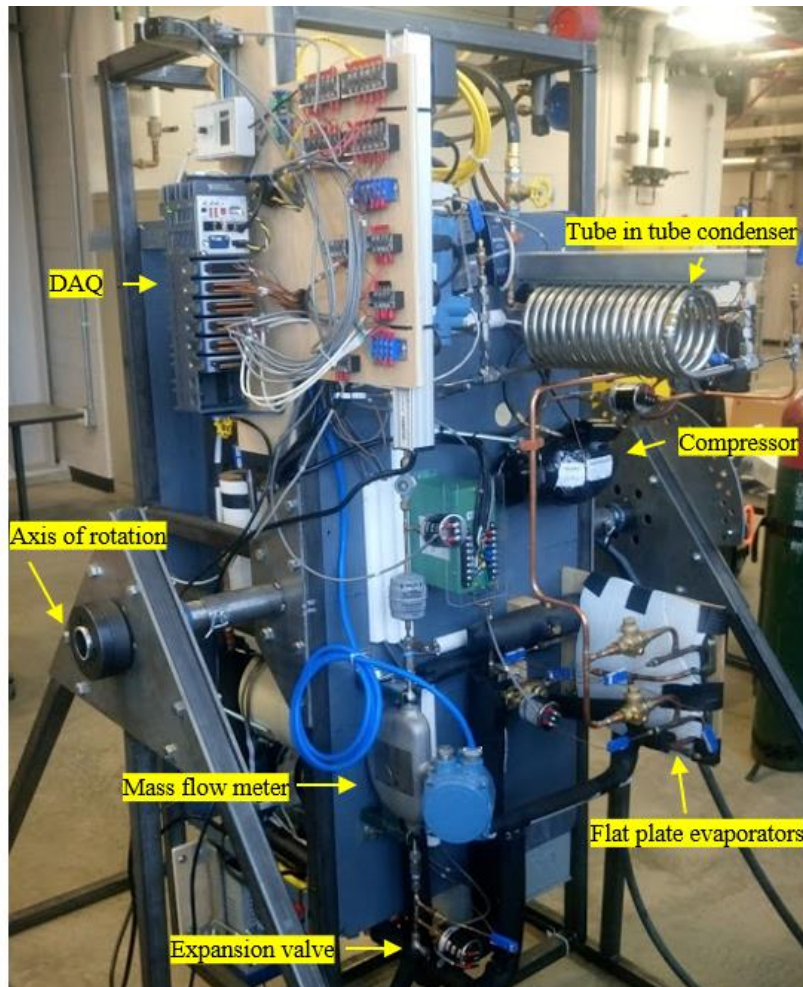


Figure 24: Picture of configuration 1 at an inclination angle of $+90^\circ$.

2.2.2 Configuration 2 – tube-in-tube evaporator

⇒ September 28th, 2020 till November 30th, 2020

- *Water or water-glycol to refrigerant tube-in-tube evaporator*
- Water-cooled tube-in-tube condenser
- Cooling water from building
- Linear or scroll compressor
- Manually operated needle valve
- R134a as refrigerant
- One sight-glass
- *Liquid line and suction line mass flow meter*

Shakedown testing had proven the flat-plate evaporators too orientation sensitive. To further use the installed liquid loop as a heat source, the next evaporator was also chosen to be of liquid-to-refrigerant type, too. A tube-in-tube evaporator was taken from a retired test rig and installed on the inclinable test stand. Refrigerant was in the annulus and water-glycol in the inner tube (unintentionally). Distilled water was used in place of water-glycol after encountered difficulties with the strongly changing viscosity of water-glycol as a function of temperature. Starting from configuration 2, an additional Coriolis-type mass flow meter was installed. A system schematic and picture of configuration 2 is shown in Figure 25 and Figure 26.

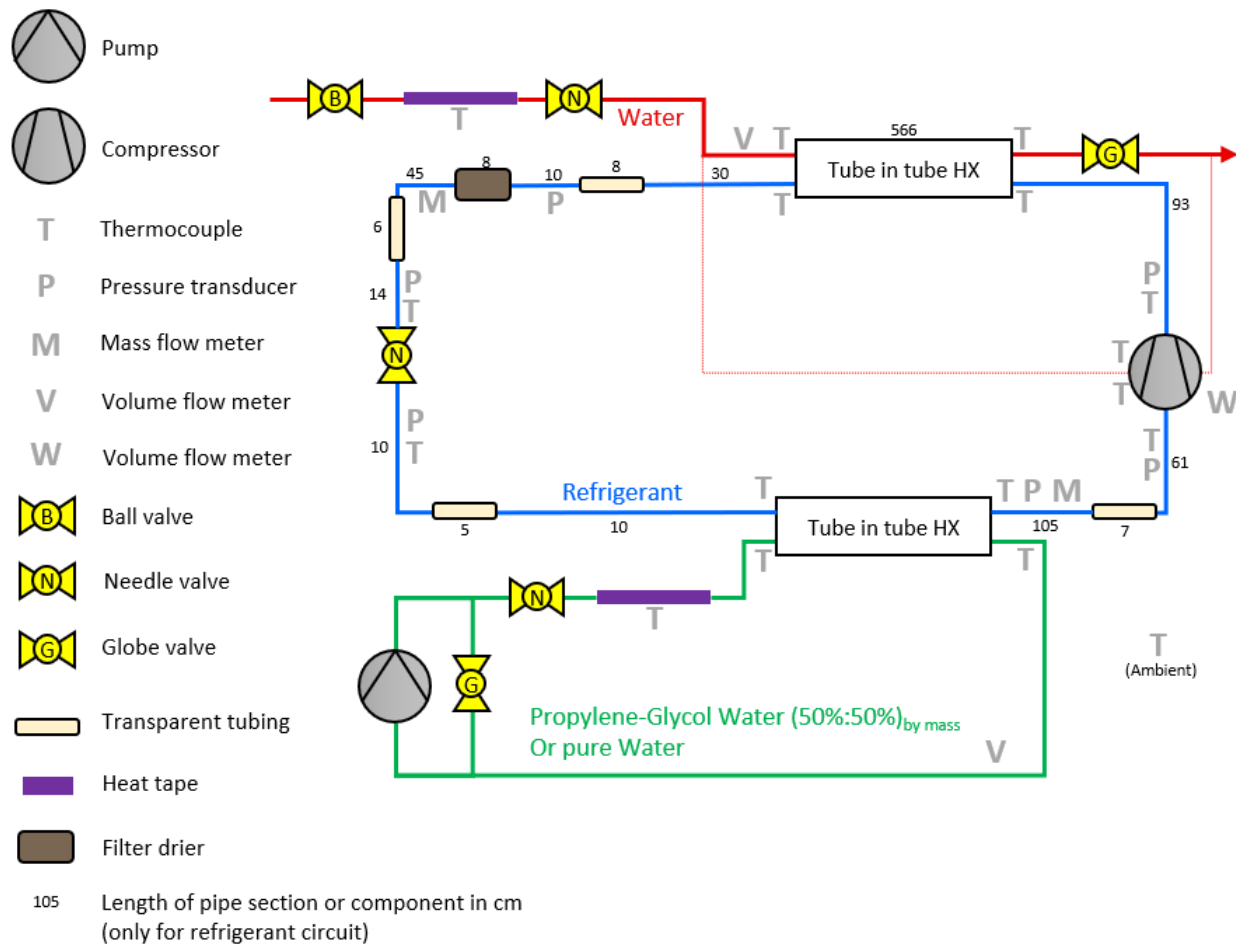


Figure 25: Plumbing and instrumentation diagram of configuration 2.

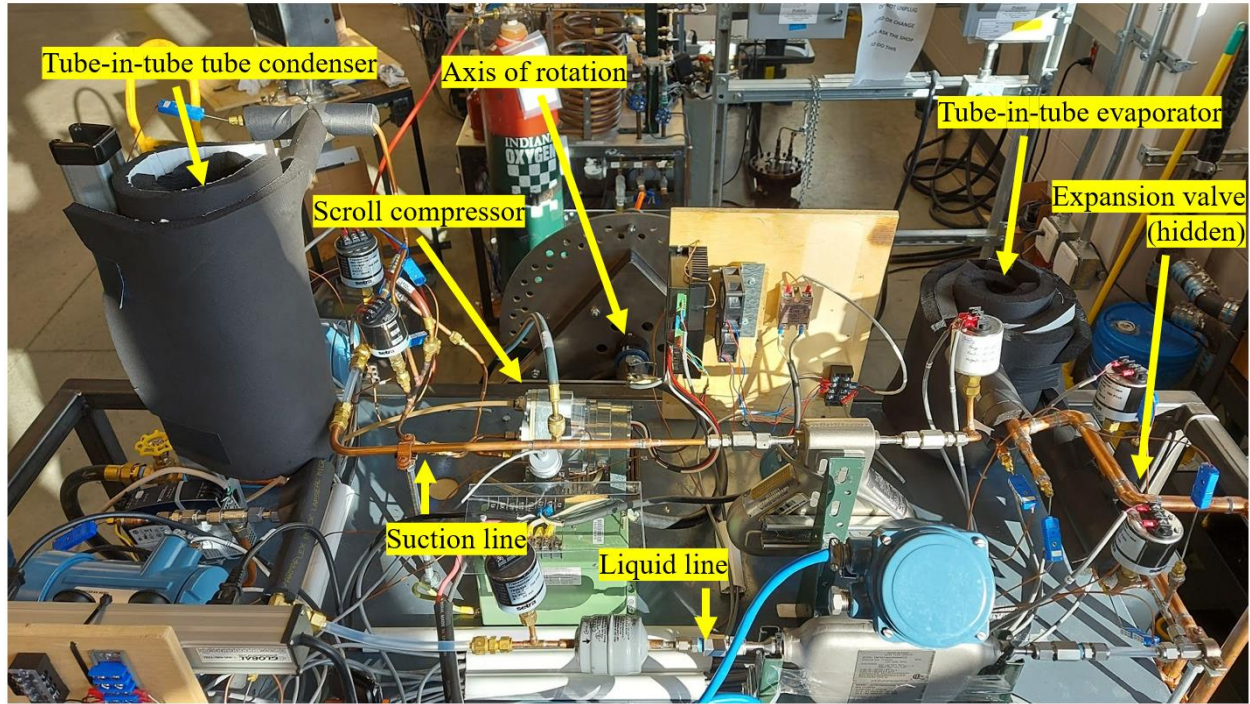


Figure 26: Picture of configuration 2.

2.2.3 Configuration 3 – fin-tube evaporator

- ⇒ November 30th, 2020 till April 9th, 2021
- *Air to refrigerant fin-tube evaporator*
- *Refrigerant to air fin-tube condenser*
- Cooling water for compressor from building
- Linear or scroll compressor
- Manually operated needle valve
- R134a as refrigerant
- *Five transparent tube sections*
- Liquid line and suction line mass flow meter

After extensive research on the test rig with a liquid as the heat source and sink, the system was reconfigured to use air as the heat source and sink. A fin-tube evaporator was installed in a closed air-loop with integrated heater and fans. The fin-tube condenser air loop was open and did not have a heater, such that the air inlet temperature was always the ambient temperature. Configuration 3 was fully commissioned approximately five months prior to the parabolic flights

and was also tested on the ground before installation on the parabolic flights. The sight-glass of configuration 1 and 2 was removed and transparent tubes were installed at several locations in the test stand as shown in Figure 27.

2.2.4 Configuration 3 – parabolic flight setup

- ⇒ April 9th, 2021 till August 1st, 2021
 - Air to refrigerant fin-tube evaporator
 - Refrigerant to air fin-tube condenser
 - *Independent water-cooling loop for compressor*
 - Linear or scroll compressor
 - Manually operated needle valve
 - *R134a or R1234ze(E) as refrigerant*
 - *Five transparent tube sections with three cameras*
 - Liquid line and suction line mass flow meter

The water cooling for the compressor was decoupled from the building cooling water and replaced with a separate closed cooling loop with a water-to-air heat exchanger. Cameras were installed to record the refrigerant flow in transparent tubes. A number of structural brackets and additional framing had to be added to satisfy the safety-requirements for the parabolic flights and polycarbonate panels were added around the upper part of the test stand. However, neither changed the refrigerant or air flow paths such that the configurations from ground-based and parabolic flight testing are directly comparable. The parabolic flights were all flown with R134a as the refrigerant. R1234ze(E) was used as refrigerant for additional inclination testing in July 2021. A system schematic and picture of configuration 3 is shown in Figure 27 and Figure 28.

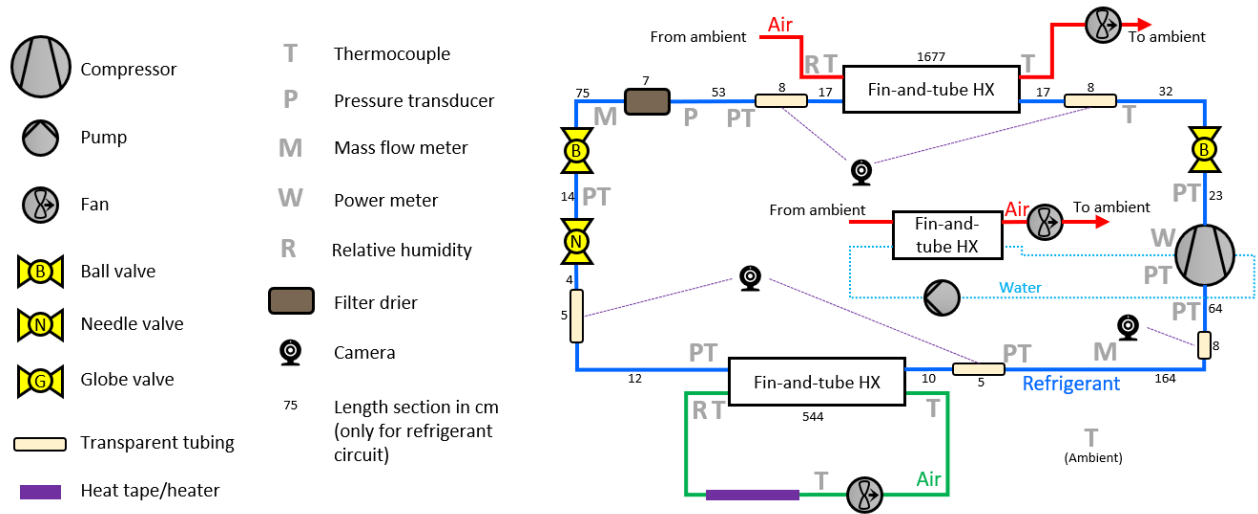


Figure 27: Plumbing and instrumentation diagram of configuration 3.

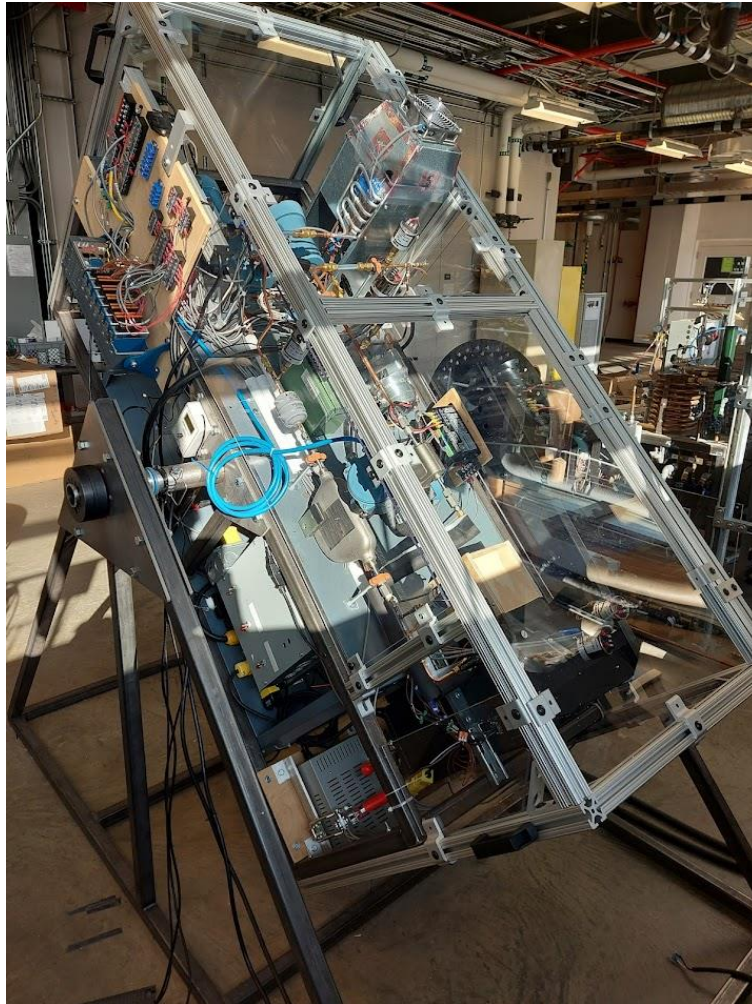


Figure 28: Test stand shortly before parabolic flight testing.

2.3 Components

2.3.1 Heat exchangers

Six heat exchangers were used on the inclinable test stand through the different configurations:

- Two flat-plate heat exchangers
- One tube-in-tube evaporator
- One tube-in-tube condenser
- One fin-tube evaporator
- One fin-tube condenser

Detailed geometry information for the flat plate evaporators and the tube-in-tube condenser is not available. The other heat exchangers are described in the following.

Tube-in-tube evaporator

The tube-in-tube evaporator was recycled from a previous test rig and the connections for the annulus and inner tube were unclear. Unfortunately, the refrigerant was connected to the annulus. This is unusual for an evaporator and worsened the energy balance. The annulus had heat transfer enhancements, the impact of which on the stability on the two-phase flow is uncertain. Figure 29 shows a picture of the evaporator. Figure 30 shows the inner tube and annulus after cutting the heat exchanger.

The diameter of the coil was 13.75 cm. The total length of approximately 5.75 revolutions was 248 cm. The cross-sectional flow area for the refrigerant was difficult to estimate due to the irregular shape of the tubes. The area was approximated to be 1.32 cm^2 . A different person with a different measurement technique found 1.28 cm^2 . A cross-sectional area of 1.32 cm^2 is used throughout this thesis to calculate the mass flux from a measured mass flow rate.



Figure 29: Picture of tube-in-tube evaporator.



Figure 30: Inner tube and annulus of tube-in-tube evaporator with heat transfer enhancements (Brendel et al., 2022c).

Fin-tube evaporator

The fin-tube evaporator was a single-circuit, coated, aluminum heat exchanger. The refrigerant entered at the top and flowed through 8 tubes in serpentine to the bottom of the heat exchanger. The refrigerant flowed up in a second column of 8 tubes and exited next to the location of the inlet. Figure 31 shows a picture of the evaporator with the direction of air-flow.

The inner tube diameter was 6.9 mm and the total length was approximately 5.5 m. The 63 fins were rectangular and of 15 cm height and 6 cm width.

The evaporator was installed in an aluminum box to facilitate a closed air loop. An electric resistive heater acted as the heat source for the air loop and small fans were used to generate air-flow. During shake-down testing, only 2 fans were used. Starting from February 15th, 2021, 4 fans were used to increase the air flow rate. Figure 32 shows a schematic of the air-loop with the evaporator. The box was closed and mostly insulated, but had some air leakages and a non-negligible heat transfer with the ambient air.

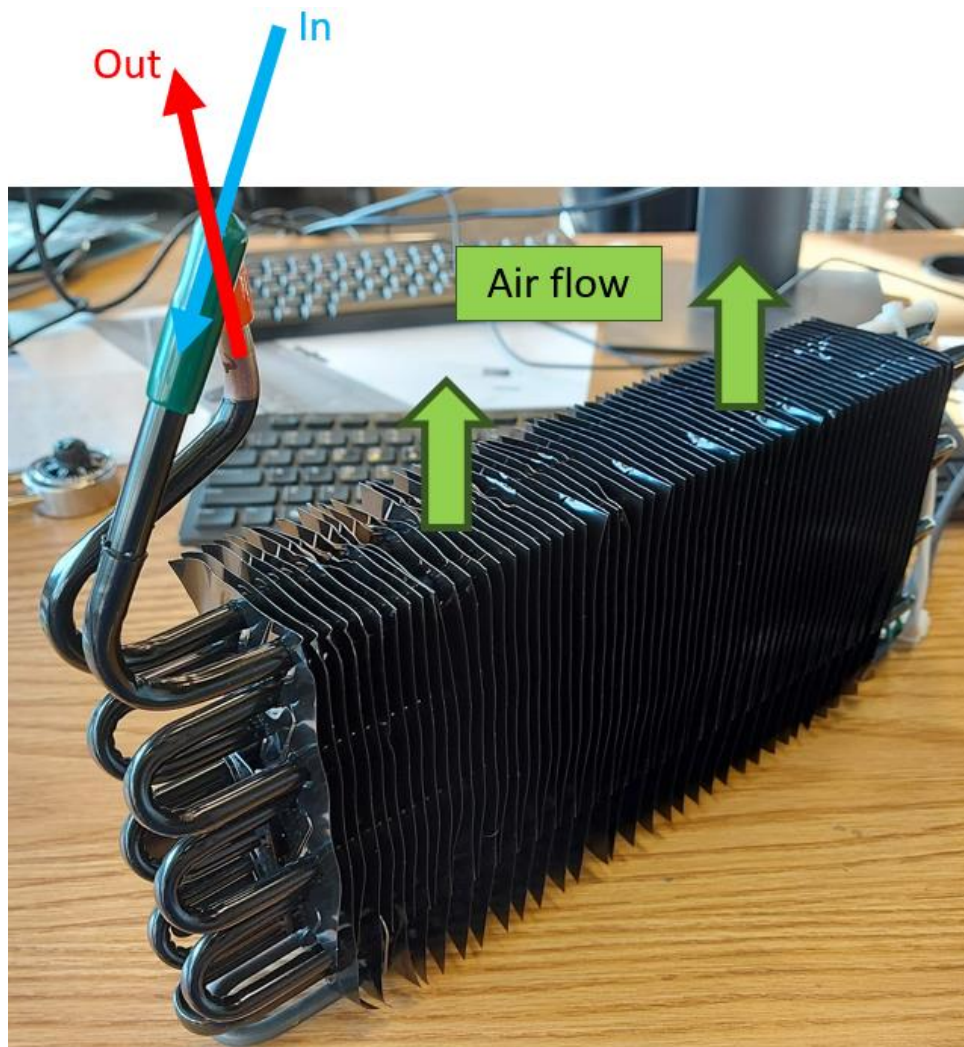


Figure 31: Fin-tube evaporator with inlet, outlet and air-flow direction.

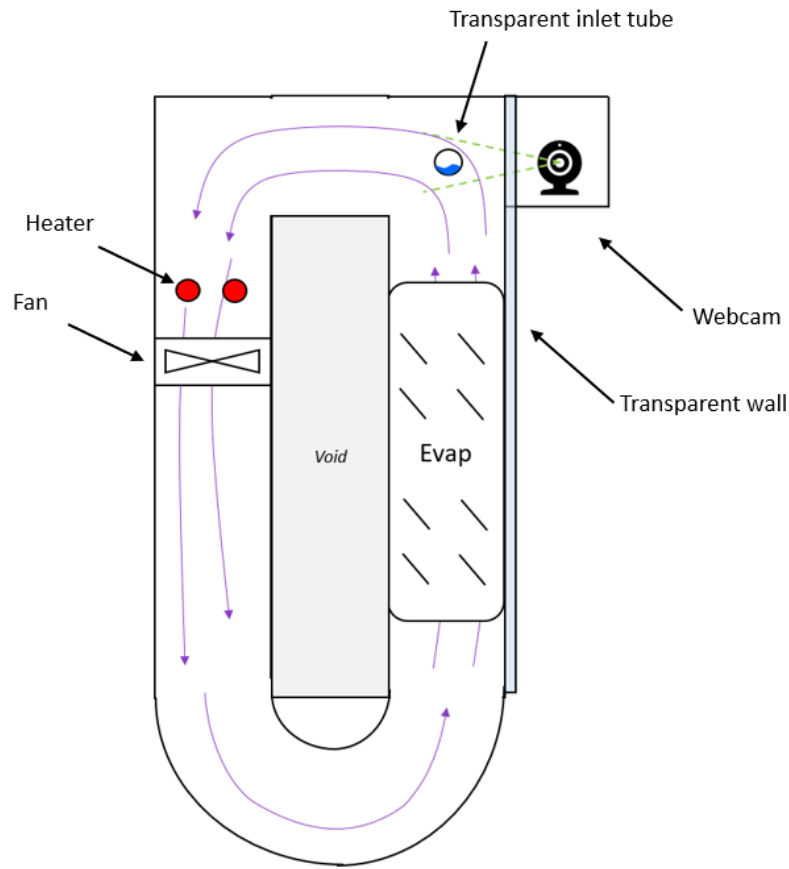


Figure 32: Installation of fin-tube evaporator in closed air-loop (side-view).

Fin-tube condenser

The condenser was a single circuit, aluminum heat exchanger with 66 tubes. Figure 33 shows a picture of the condenser with the inlet, outlet and air-flow direction. The heat exchanger was enclosed in a sheet metal housing with one fan at the top drawing air through the heat exchanger.

The inner diameter of the tubes was 6.2 mm and the total coil length was estimated to be 16.8 m. The 70 fins had side lengths of approximately 20 cm and 15 cm.

The air-loop was open, meaning that the inlet air was always at ambient conditions. This was steady for laboratory experiments. However, during the parabolic flights, the ambient air temperature decreased gradually over time and sometimes fluctuated strongly, which was always reflected in the air inlet temperature for the condenser.

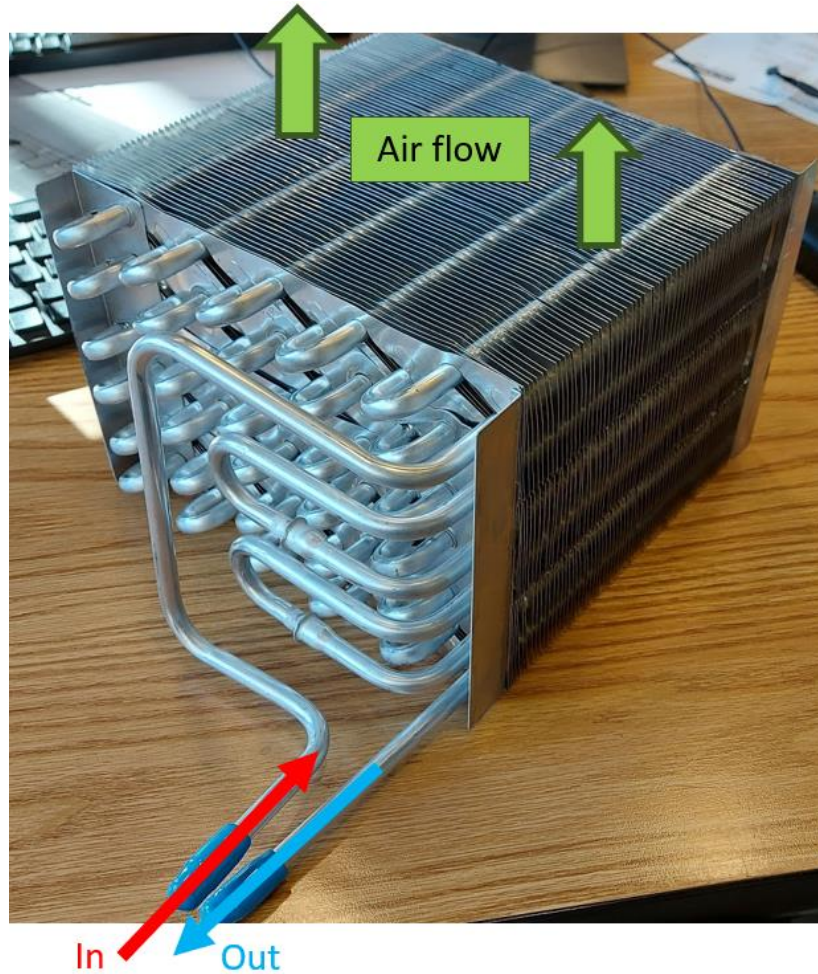


Figure 33: Fin-tube condenser with inlet, outlet and air-flow direction.

Fin-tube heat exchanger capacities

Gravity effects of vapor compression cycles may be altered by oversized or undersized heat exchangers. Since the operating conditions of the inclinable test stand covered cooling capacities from <100 W to >400 W, the heat exchangers must have been over- or undersized for at least some of the operating conditions. The heat exchanger capacities are reported both as a function of the logarithmic mean temperature difference (LMTD) and the temperature driving potential defined as the difference between saturation and air inlet temperature. Steady-state data from ground-based testing in a horizontal orientation was used for this analysis.

Capacity as function of driving potential

Figure 44 shows the heat transfer rates of both heat exchangers as a function of the temperature difference between the air inlet and saturated refrigerant temperatures (driving potential). For the evaporator, the achievable cooling capacity is sensitive to the superheat level. Therefore, only data with superheat levels ≤ 10 K were used. Figure 44 (left) shows that the evaporator heat transfer rate was approximately 100 W at 8 K temperature difference or 400 W at 30 K temperature difference. An overall UA value of 12 W/K was estimated. The overall UA value is here defined as:

$$UA_{overall} = \frac{\dot{Q}}{\Delta T_{drive}} \quad (10)$$

It should not be confused with the UA value commonly used for NTU, effectiveness or LMTD computations (see next subsection).

For the condenser, only datapoints that had no refrigerant inlet superheat had to be removed (because the heat transfer rate could then not be determined). Figure 44 (right) shows that the condenser heat transfer rate is in the range 100 to 520 W for driving potentials of 3 to 14 K. $UA_{overall}$ for the condenser was estimated as 38 W/K.

Both $UA_{overall}$ values are only valid for the provided airflows. Those were never measured but estimated to be 5 l/s for the evaporator and 15 l/s for the condenser. Frost build-up in the evaporator may have decreased the air flow rate.

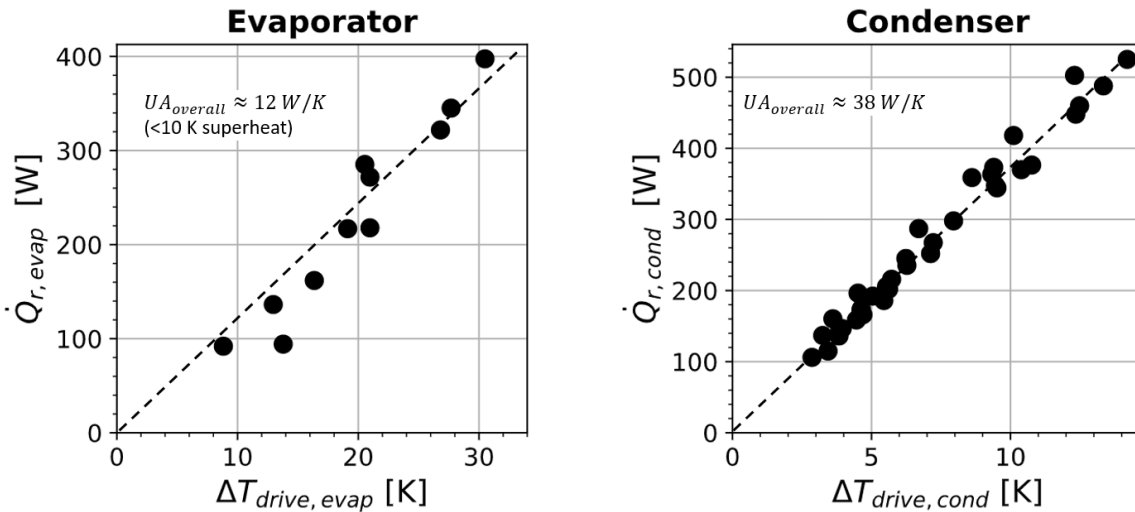


Figure 34: Fin-tube heat exchanger capacities as a function of temperature driving potential for evaporator and condenser.

Capacity as a function of LMTD

Heat exchanger capacities are frequently described as a function of the LMTD defined as

$$LMTD = \frac{\Delta T_A - \Delta T_B}{\ln\left(\frac{\Delta T_A}{\Delta T_B}\right)}, \quad (11)$$

ΔT_A and ΔT_B are the temperature differences on the warm and cold side of the heat exchanger and here defined as:

$$\Delta T_{A,evap} = T_{a,e,in} - T_{r,e,out}, \quad (12)$$

$$\Delta T_{B,evap} = T_{a,e,out} - T_{r,e,in}, \quad (13)$$

$$\Delta T_{A,cond} = T_{cond} - T_{a,c,out}, \quad (14)$$

$$\Delta T_{B,cond} = T_{r,c,out} - T_{a,c,in}. \quad (15)$$

T_{cond} is the only temperature that is not measured directly but calculated as the saturation temperature of the discharge pressure. The LMTD is derived for processes during which the capacitance rates are constant, which is not the case for a process featuring both two-phase and single phase heat transfer (like condensation and subcooling or evaporation and superheating). However, the method may still be applied and can be of interest to readers more familiar with the LMTD than with the previously introduced driving potential. Figure 35 shows the heat transfer rates for both fin-tube heat exchangers as a function of the LMTD. The UA values are now calculated as

$$UA = \frac{\dot{Q}}{LMTD}. \quad (16)$$

The plots show more scatter than the ones in Figure 34, probably a result of the varying specific heats in the considered processes which are assumed constant in the derivation of the LMTD.

2.3.2 Compressors

Three different compressors were used on the inclinable test stand, all of which were oil-free. Initially, only a linear compressor designed for R600a was available and used with R134a for shake down testing. The efficiency was very poor and starting from August 2020, it was replaced with a linear compressor designed for R134a. Both linear compressors were commercial products and of variable capacity. To adjust the capacity, the operator tuned the desired power draw of the

compressor which was translated into a larger or smaller piston stroke by the controller. The power draw was limited to the range 20 W to 120 W.

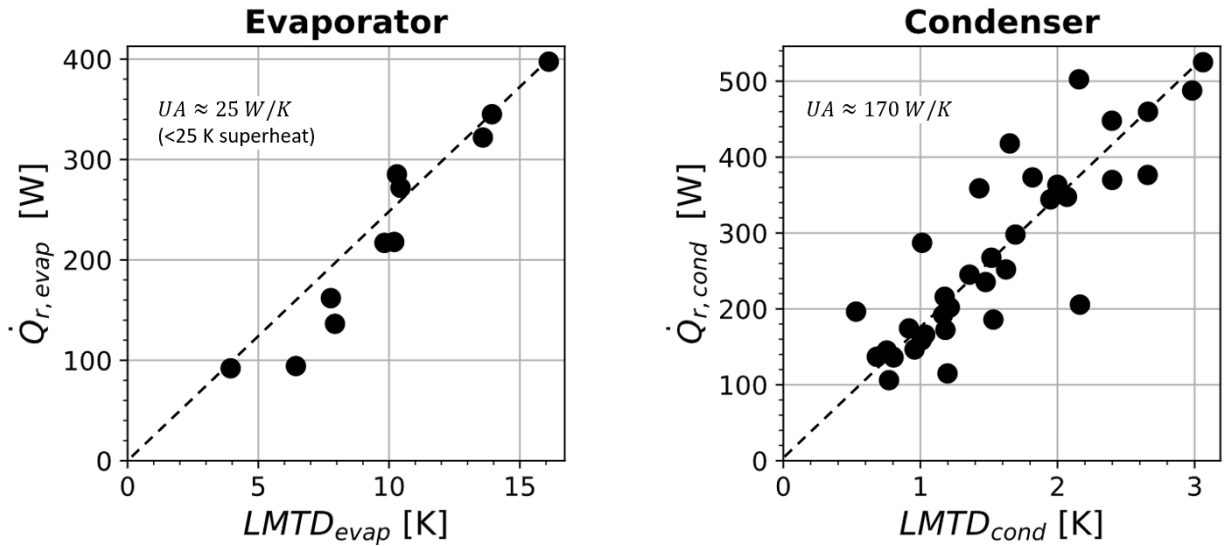


Figure 35: Fin-tube heat exchanger capacities as a function of LMTD for evaporator and condenser.

Starting from late August 2020, an oil-free prototype scroll compressor was installed on the inclinable test stand and used alternatingly with the R134a linear compressor until the end of July 2021. The scroll compressor had a suction volume of 15.2 cm^3 and could be operated at varying frequency for capacity modulation in the range 600 to 4000 RPM (the upper limit was dependent on the operating conditions).

Both compressors were able to provide mass flow rates in the range of 0.5 g/s to 2.2 g/s, depending on the control parameters and evaporation temperature. Throughout all experimental results, the compressor type did not appear to have an impact on the gravity dependence measurements for the two-phase cycle.

2.3.3 Expansion valve

The expansion valve was the SS-SS4-VH model from Swagelok with flow coefficients as shown in Figure 36. The opening was documented as the number of turns. The scale on the handle of the valve for one rotation ranged from 0 to 25. This was translated to decimal values for the documentation. Hence, a value on the handle of 5 translated to 0.2 for the decimal values of the valve opening as shown in Figure 37. Since the opening was changed and documented manually,

it may be affected by human error. However, the expansion valve opening was not used in any of the reported data or modeling.

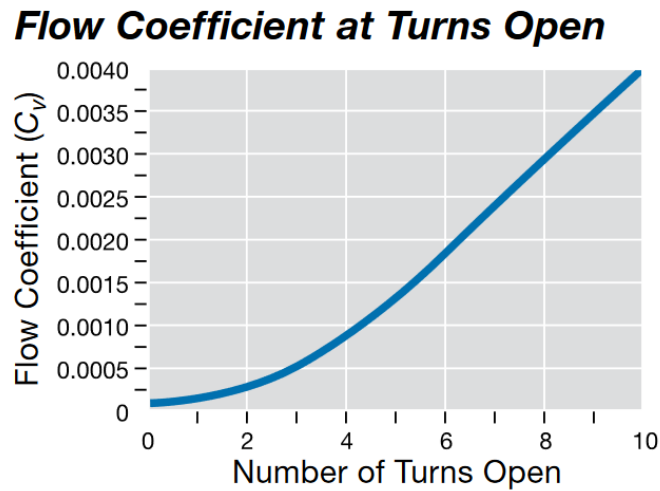


Figure 36: Flow coefficient of needle valve (Swagelok, 2007).



Figure 37: Needle valve 5.2 turns open.

2.4 Inclination capability

2.4.1 Design and development

The idea of an inclinable test stand for this research was developed in early 2019 and is conceptualized in Figure 38. Inclination testing is frequently applied in two-phase *flow* research but the merits of an inclinable two-phase *system* were not immediately clear, such that several months passed until the decision was made to build a test setup to facilitate inclination testing on a vapor compression cycle in June 2019. Three papers in the literature describe results of

inclination testing, but the documentation was insufficient to help in the design of a new test stand (Domitrovic et al., 2003; Grzyll & Cole, 2000; Sunada et al., 2008). The three publications are discussed in more detail in the introduction of (Brendel et al., 2021c).

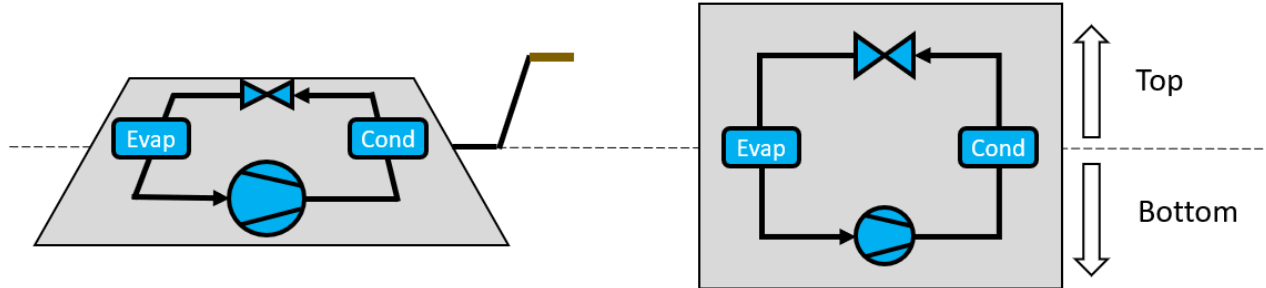


Figure 38: First schematic of inclinable VCC.

A first sketch of the early thoughts for the realization of an inclinable test stand is shown in Figure 39. The sketch displays the idea that all data acquisition should be facilitated on the test stand such that as few cables as possible are coupled to the stationary environment. This simplifies the free rotation of the test stand.

The final design was a test stand consisting of three parts: “Structure”, “Frame” and “Table” as illustrated in Figure 40. The *structure* is composed of two vertical triangles connected at the bottom and holding the axis of rotation. The *frame* in the current setup is a reinforcement of the *table*. The table holds the complete refrigeration circuit and its secondary loops.

The test stand is not motorized and can be inclined around one axis only. It was commissioned in January 2020. A lesson learned regarding the liquid heat source loop is described in Appendix A as a source of information to other researchers building similar test stands.

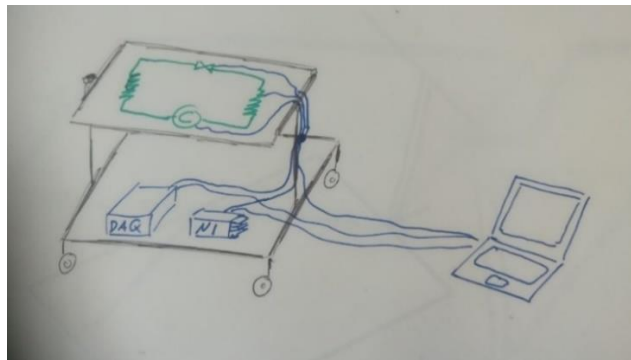


Figure 39: Sketch of strategy to organize wires on an inclinable test stand.

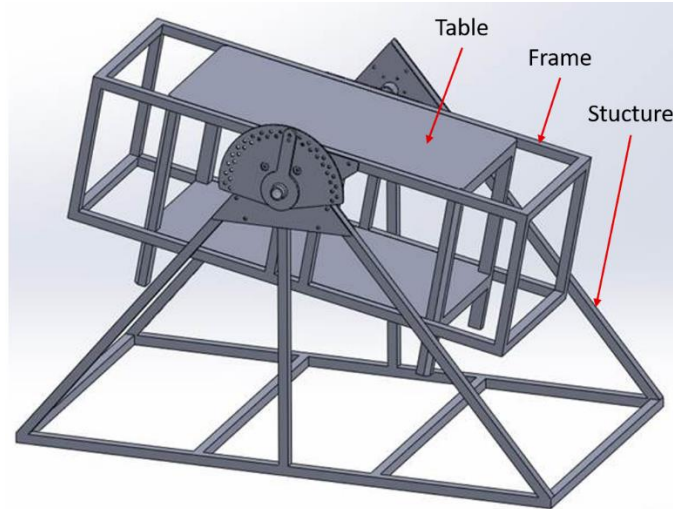


Figure 40: Modular fabrication of inclinable test setup.

2.4.2 Component arrangement, angle convention and example inclination patterns

The interpretation of results from an inclinable test stand is always dependent on the relative component positioning. Figure 41 shows the approximate circuiting and relative positioning of components for all three configurations. For configuration 3: Starting from the compressor discharge port, the refrigerant flowed up and entered the fin-tube condenser from the top. The condenser outlet led into a long horizontal liquid line to the expansion valve. After the expansion valve, the two-phase refrigerant flowed into the evaporator from the top and exited at the top. From the evaporator outlet it flowed down to the compressor suction port. For configuration 1 and 2, the evaporator inlet was at the bottom. The two flat-plate evaporators in configuration 1 were connected in parallel but only one at a time was used when testing. The other evaporator was closed off with ball valves.

When the test stand was inclined, a component arrangement supporting or counteracting the normal cycle operation resulted: Figure 41 shows how an inclination of -30° elevates the expansion valve relative to the condenser outlet. This could result in backflow of liquid. At the same time, the compressor is lowered with respect to the evaporator, which could lead to liquid slugging into the compressor. Based on this, a simple convention for the angle has been adopted for this test stand:

- Positive angles support the normal cycle operation (positive \rightarrow good)
- Negative angles counteract normal cycle operation (negative \rightarrow bad)

Later experiments showed that liquid slugging could also result from positive angles, but the convention was maintained through all results presented and is also used in all publications associated with this dissertation.

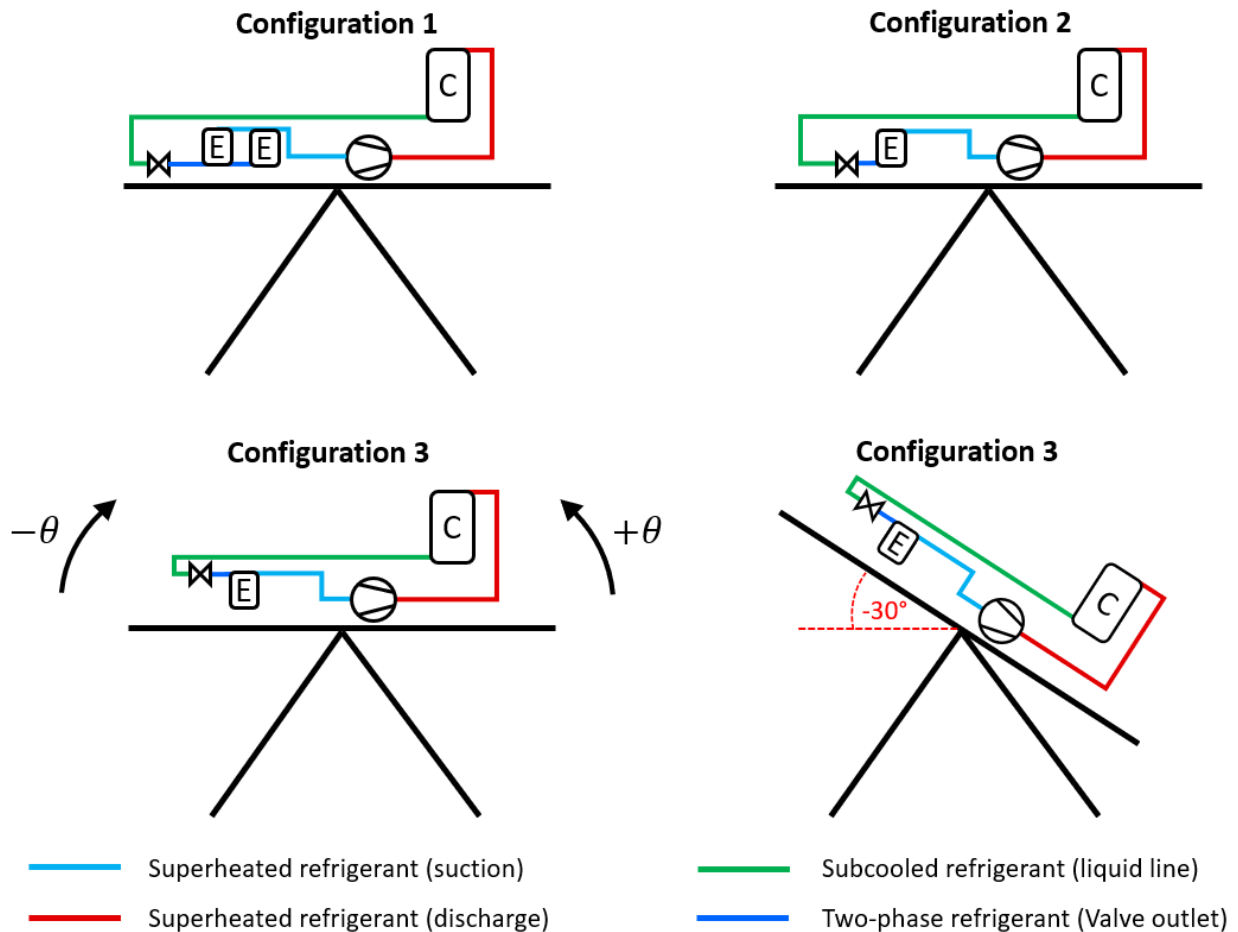


Figure 41: Approximate relative component positioning and refrigerant circuiting.

The range of inclination is only limited by cables or hoses connected to the test stand. Currently their length facilitates an inclination range of $\pm 180^\circ$.

Figure 42 shows example inclination patterns that can be leveraged for testing (measured using an inclinometer). The operator can lock the stand at angles in 5° increments using a safety bolt, if static testing is desired. Without the safety bolt, a continuously swinging motion of the table is possible to represent a dynamic application.

The inclination angle is given the symbol θ .

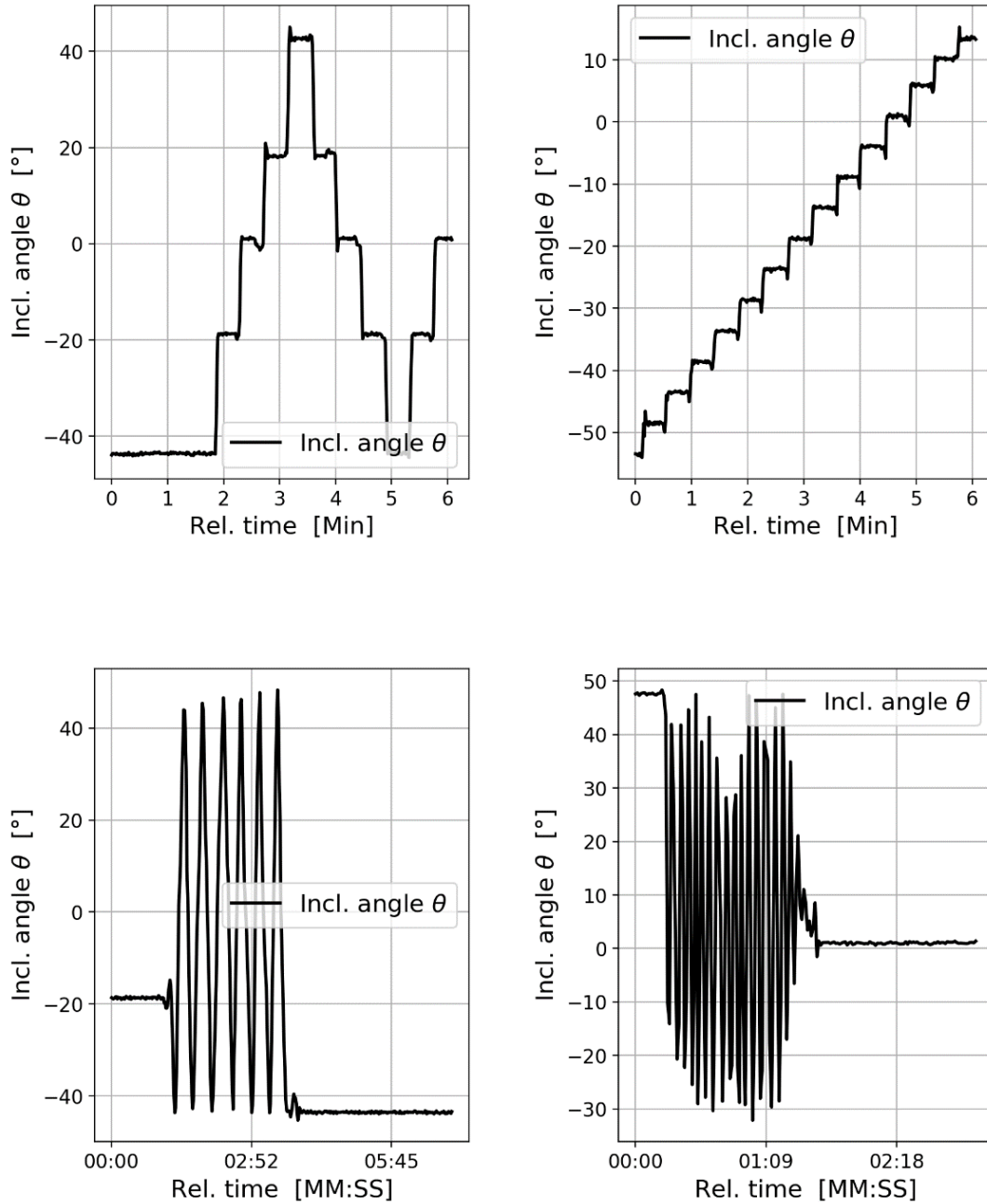


Figure 42: Example inclination patterns possible on an inclinable test stand.

2.5 Instrumentation

The exact numbers and locations of sensors varied through the 3 configurations. Overall, both heat exchangers and the compressor had dedicated inlet and outlet temperature and pressure measurements. Starting from configuration 2, two Coriolis-type mass flow meters were used, one in the suction line and one in the liquid line. The secondary loops in configuration 1 and 2 (liquid

loops) had volume flow meters. Air flow meters were not installed but the relative humidity of the air at the evaporator outlet and the condenser inlet were measured. Sensor types and uncertainties are listed in Table 12. Locations of sensors are indicated in Figure 23, Figure 25 and Figure 27.

Table 9: Types of sensors and associated uncertainties.

Property	Sensor type	Range	Uncertainty
Temperature	T-type thermocouple	-250-350 [°C]	1 Kelvin
Pressure	Absolute and gauge	Various	0.13% of full scale
Mass flow rate	Coriolis	0.5-5 [g/s]	0.1 % of reading
Liquid volume flow rate (heat source)	Axial paddle wheel	0.1 to 2 [l/min]	1 % of reading
Liquid volume flow rate (heat sink)	Pelton wheel	0.1 to 1 [l/min]	1% of full scale
Power (linear compressor)	AC Watt transducer	0-500 [W]	0.2% of reading + 0.04% of full scale
Power (scroll compressor)	AC Watt transducer	0-1250 [W]	1% of full scale
Power (air heater)	AC Watt transducer (after SCR)	0-500 [W]	1% of full scale
Humidity	Relative humidity	15 – 95 [%]	5% absolute uncertainty
Angle	1 axis- inclination sensor	-180 to 180 [°]	0.25°
Accelerometer	3-axis accelerometer	$\pm 6g_e$ for each axis	Unclear

Air side heat transfer rate

It should be noted that the air flow rate in the heat exchangers of configuration 3 was not measured. The air flow rate is assumed constant at a particular operating condition, because orientation or gravity changes do not affect single-phase flow. The air flow rate was estimated by equalizing the air-side and refrigerant side heat transfer rate for $t=0$ seconds of a dataset for a particular operating condition. When analyzing air-side heat transfer results, changes are therefore due solely to temperature and humidity changes. Although this method does not allow an energy balance of the heat exchanger, it accurately shows *changes* of the heat transfer rate (given that the flow rate is indeed constant).

2.6 Cameras

Cameras were installed to record flow regimes in transparent tubes. A Logitech C525 webcam was suitable for close-up flow visualizations. One camera was installed to record the inlet and outlet of the evaporator. Another camera recorded the inlet and outlet of the condenser. One more camera recorded the suction line between the mass flow meter and the compressor. Hence, the operator could use the cameras to check for evaporator outlet or suction line flooding. Moreover, the verification of available condenser outlet subcooling and compressor discharge superheat was enabled. Last but not least, the flow regime at the evaporator inlet could be determined.

OBS Studio was used to generate screen recordings from Labview with footage from two cameras. This method avoided creating several video files which would have to be aligned in post-processing. It was limited by recording footage from at most two cameras at a time.

2.7 Instability quantifiers

A prime goal was to let a vapor compression cycle operate through any orientation (laboratory testing) and over a range of gravity levels (parabolic flight testing). A related goal was to answer the question: Is the instability of the cycle that occurs at different orientations or gravity levels correlated to the mass flux or any other operating conditions? Hence, “instability” had to be quantified, but the open literature does not provide suggestions. Several quantifiers were developed and empirically tested for correlations with certain operating conditions.

2.7.1 mmx and 80% – quantifier

Figure 43 shows example data from the inclinable test stand during the parabolic flights. The black line shows the evaporation temperature on the left-hand side y-axis. Gravity is plotted in purple using the right-hand side y-axis. The evaporation temperature clearly fluctuates due to gravity. A simple approach to quantify the instability is to look for the maximum and minimum temperature and calculate the difference. The difference is then a temperature band within the measurements fluctuated. This is called the “*min-max*” or “*mmx*” quantifier and can be applied to pressures, flow rates, heat transfer rates, etc.

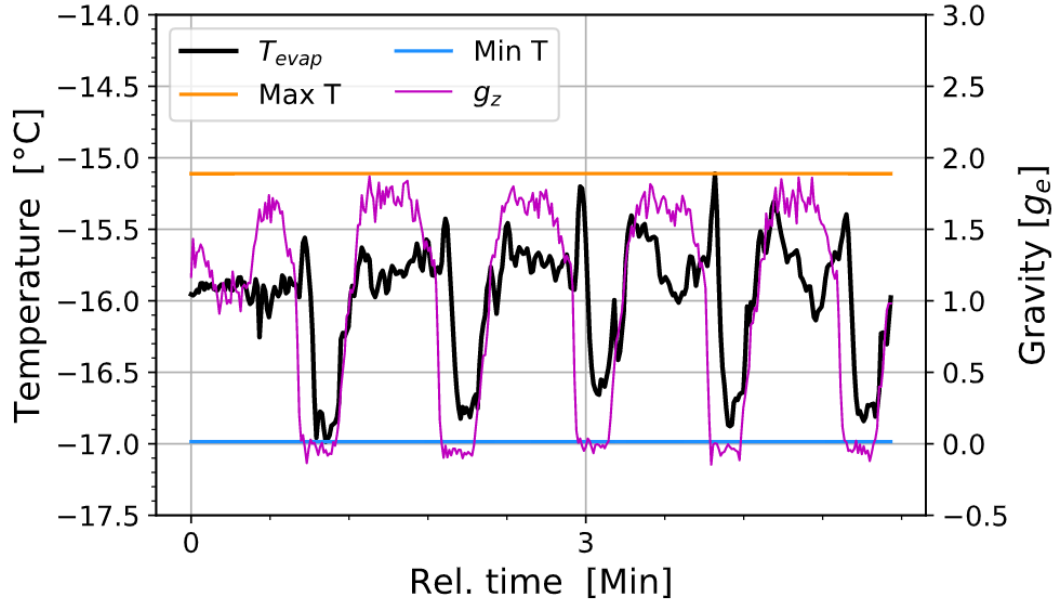


Figure 43: Evaporation temperature through set of parabolas with maximum and minimum measured temperature (Brendel et al., 2022e).

Even short spikes will immediately widen the *mmx*-band. Hence, the quantifier is enlarged even if a gravity perturbation does not lead to a change in the long run but only to a short spike. For example, the maximum temperature in Figure 43 (orange line) is set by a spike that is not representative of the trend of the data. This may be desired or not desired, depending on the research question. A second quantifier based on the *mmx* is the “80%” quantifier which neglects brief spikes of data. From all data points, 80% were selected such that the *mmx* of the remaining data was the smallest. Short spikes do not impact this quantifier as long as they do not make up more than 20% of all datapoints. 80% of the datapoints is here equivalent to 80% of the time of data collection, because data was collected at a constant sampling rate.

It may be relevant to measure the band between minimum and maximum value relative to the measured value itself. For this purpose, the *mmx* quantifier can be divided by the average value (*avg*) of the data or by the value at the beginning of the considered data (*ini*). Typically, these are approximately the same:

$$\left(\frac{mmx}{avg}\right)_x \approx \left(\frac{mmx}{ini}\right)_x, \quad (17)$$

where x is the measurement for which the instability is evaluated. The resulting ratio is often small and easier to work with after a conversion to a percentage by multiplication with 100%. If x is a

temperature reading, it must be converted from Celsius to Kelvin. However, only non-temperature measurements were evaluated relative to their initial value in this dissertation.

2.7.2 MDV and IIR quantifier

The *MDV* and *IIR* are additional quantifiers, essentially the mean deviation and relative mean deviation of a measurement from its initial value due to gravity perturbations. Figure 44 shows the heat source heat transfer rate in blue plotted as a function of time. In the first two minutes, the cycle is at steady-state and the heat transfer rate is 452 W. The inclination changes indicated in gray and plotted against the right-hand side y-axis lead to strong changes of the heat transfer rate. To quantify the deviation of the heat transfer rate from its initial value (green dashed line), the absolute difference is integrated. This is called *MDV* (mean deviation). To compare datasets collected over different durations, it is convenient to divide the integrated difference by the total time, essentially resulting in a mean deviation. The formulation for this quantifier is then:

$$MDV_{\dot{x}} = \frac{\int_{t_{start}}^{t_{end}} |\dot{x}(t) - \dot{x}(0)| dt}{(t_{end} - t_{start})}. \quad (18)$$

The *MDV* was previously called *IAI*, a label which may still be used in databases that were not updated. *IAI* was the acronym for “integrated absolute deviation of initial value”, but *MDV* was preferred as a more intuitive name and acronym. The *MDV* can be converted to a relative quantifier by dividing the *MDV* by the initial value of the dataset and is then called the inclination impact ratio (*IIR*):

$$IIR_{\dot{x}} = \frac{MDV}{\dot{x}(0)} = \frac{\int_{t_{start}}^{t_{end}} |\dot{x}(t) - \dot{x}(0)| dt}{\dot{x}(0)(t_{end} - t_{start})} \cdot 100\%. \quad (19)$$

The *MDV* and *IIR* are intuitive for flow rates and heat transfer rates. However, the equation can also be applied to pressures. The result is then a weighted average deviation (absolute or relative). As a reference, the data in Figure 44 resulted in a relatively low inclination impact ratio of $IIR \approx 7\%$. Appendix B shows the *MDV* and *IIR* for artificial data sets to gain intuition about its behavior.

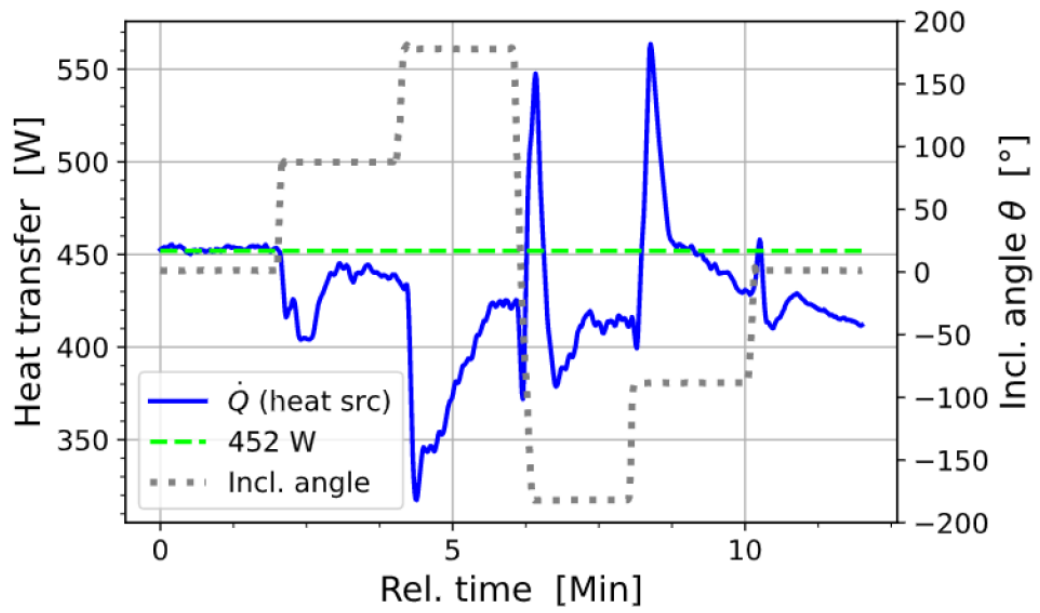


Figure 44: Heat transfer rate as a function of time through 6-angle testing procedure compared to a constant heat transfer rate of 452 W (Brendel et al., 2022c).

3. START-UP TEST STAND

3.1 Overview

The start-up test stand was designed to address one particular question: “*Does the likelihood for liquid flooding from the evaporator into the compressor upon system start-up increase at the absence of gravity?*” The compressor is the only component in the VCC with moving parts and most vulnerable to failure. The literature for ground-based compressor operation is not clear about the amount of liquid in a positive displacement compressor that can cause harm. However, there is consensus that liquid flooding is undesirable and poses an unnecessary risk.

Increased flooding at the absence of gravity seemed likely to multiple subject matter experts that were confronted with the above question prior to the research. If the liquid is not pulled to the bottom, moving vapor could push it out of the heat exchanger easier, was a common reasoning. As a result, a dedicated test stand was designed with the sole purpose of investigating the influence of gravity on liquid flooding during start-up given liquid in the evaporator. The test stand was designed to fulfill a set of requirements:

- Be quickly executable multiple times to collect a large number of tests; due to a large anticipated uncertainty of the results, repetition of tests was important
- Produce repeatable and reproducible data
- Allow the test execution with a known amount of liquid in the evaporator
- Allow visualization of the two-phase flow regimes during start-up
- Be robust against the occurrence of liquid flooding (since searching for a threshold of flooding will necessarily also lead to flooding)

The resulting test setup was similar to a vapor compression cycle, but a liquid tank was used instead of a condenser and a ball valve instead of an expansion device (for fast charging and complete closure during a test run). The compressor was a commercial recovery pump built to tolerate even large amounts of liquid. Figure 45 shows a schematic of the test setup and Figure 46 shows the start-up test stand as it was also installed on the parabolic flights.

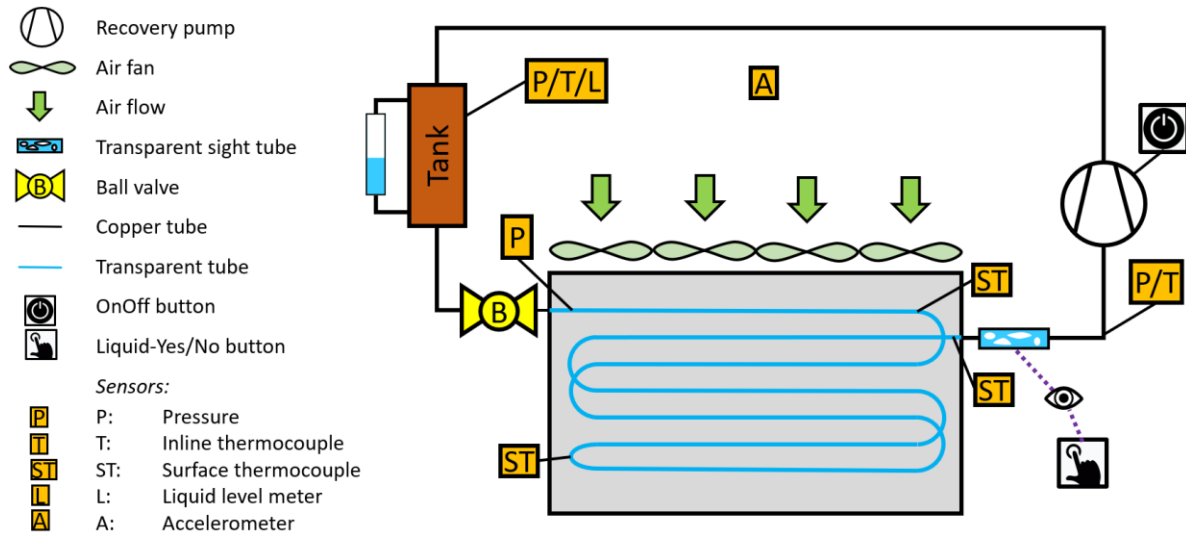


Figure 45: Schematic of start-up test stand (Brendel et al., 2022a).



Figure 46: Completed assembly of start-up test rig (Brendel et al., 2022a).

3.1.1 Test execution

Before starting a test, liquid refrigerant was in the tank, visible for the operator through the transparent tube connected in parallel. The evaporator was at a low pressure < 70 kPa and thus only filled with residual refrigerant vapor but no liquid refrigerant. The compressor was turned off. To initiate an experiment, the operator opened the ball valve while observing the liquid level tube next to the tank. Refrigerant was driven into the evaporator due to the pressure differential and the operator monitored the charging process through the sight glass. The operator closed the ball valve to stop the charging process. Next, the fixed speed compressor was turned on and started to suck refrigerant out of the evaporator, thereby reducing the pressure and causing boiling and flashing in the liquid-phase. If only a small amount of liquid was in the evaporator at compressor start-up, flashing and boiling actions could not push liquid up through the serpentine coil and out of the test section. If a large amount of liquid had been charged, the flashing and boiling threw liquid out of the evaporator after several seconds. The operator hit a push button for the entire duration of a visible liquid-phase at the outlet of the evaporator. This signal was recorded just like the on-signal for the compressor and allowed to find the time of liquid flooding and other parameters in post-processing. Most quantifiers for the intensity of liquid flooding were time-based because a measurement of the mass of liquid refrigerant that had flooded was not possible. The quantifiers are explained in detail in section 3.4. The operator let the compressor run until the pressure was below a set threshold (initially 30 kPa, later 70 kPa). After turning the compressor off, it sealed against back-flow such that the pressure in the test section remained low and was ready for repeated charging and execution.

3.2 Components

3.2.1 Evaporators

Two different evaporators were tested both on the ground and on the parabolic flights. They are called “standard” and “transparent” evaporator. The standard evaporator was the same evaporator model that is also installed on the inclinable test stand. It is shown in Figure 47 (left) in a metal cage for easier mounting. A transparent tube has been attached at the outlet to visually detect liquid flooding. The geometry of the evaporator is explained in section 2.3.1. The

transparent evaporator was built to observe flow regimes during start-up. Its geometry was chosen to be as similar to the other evaporator as possible, even though an exact match was not possible.

The transparent evaporator is made of polycarbonate tubes of 6.35 mm inner diameter and 1.59 mm tube thickness. The copper u-bends have an inner diameter of 4.06 mm and a wall thickness of 0.76 mm. All fittings are 3/8 (polycarbonate) to 1/4 (copper) compression fitting adapters. Figure 47 (right) shows a picture of the transparent evaporator. The evaporator had eight horizontal tubes in one column going down and nine tubes in an adjacent column going up. The ninth tube was added to resemble the added transparent tube of the standard evaporator.

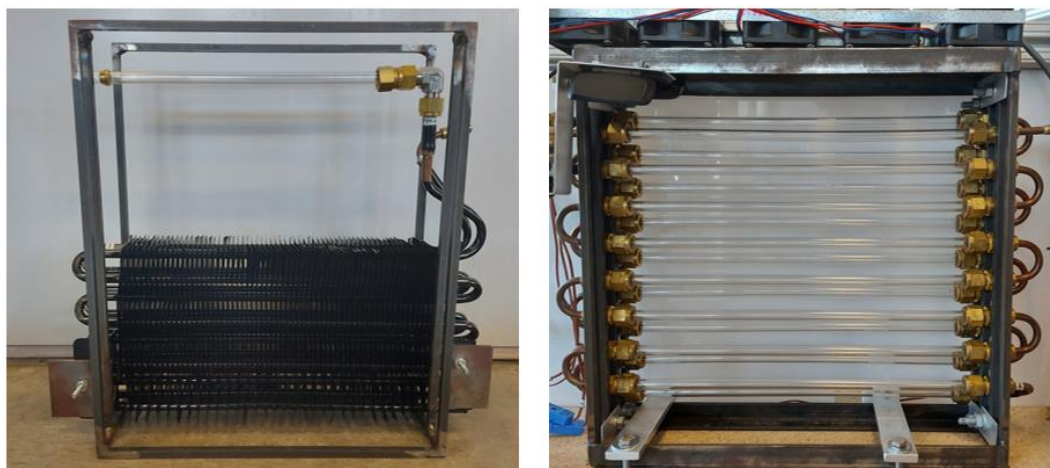


Figure 47: Test sections (Brendel et al., 2022a).

3.2.2 Compressor

A commercial recovery pump was used to resemble the compressor. The pump could tolerate even large amounts of liquid ingestion. Since the testing goal was to find the threshold for liquid flooding, liquid flooding occurred very often and a normal compressor could not have been used. Compressor and recovery pump are used synonymously when discussing this experiment.

3.2.3 Liquid tank

The refrigerant tank was custom built from a large diameter copper tube. The transparent tube in parallel showed the liquid level which was calibrated to determine the mass of refrigerant in the tank before and after charging which is equivalent to the charge mass of refrigerant. A liquid level probe was also used to determine the charged mass exactly in post-processing. Additionally,

the tank functioned as the condenser and therefore warmed up over time. The temperature typically leveled out between 30 °C and 50 °C depending on the frequency of testing.

3.2.4 Hoses and valves

Standard refrigerant charging hoses were used as flexible connections between the evaporator, compressor and tank. This was useful to facilitate evaporators of different height and width. All valves in the test stand were ball valves. A needle valve at the evaporator inlet would have made the charging process too slow.

3.2.5 Fans

A 5x1 array of fans was installed on top of the evaporators. Those supported the air to refrigerant heat transfer and warmed up the evaporator after an executed test for repeatable initial conditions. The fans were turned on also between tests when the compressor was off to continuously warm the evaporator up close to the ambient temperature.

3.3 Instrumentation and data acquisition

Three pressure transducers were installed to track the pressure in the tank and at the evaporator inlet and outlet. Thermocouples were immersed in the tank and at the outlet of the evaporator. Three surface thermocouples were installed on the evaporators. An accelerometer measured the gravity force and a liquid level meter measured the amount of liquid in the tank. Additionally, the status of the compressor (on or off) was recorded and the time for which the operator pressed the so-called “LiquidYesNo” button. Data was collected using an Arduino with a sampling rate of approximately 1.2 Hz. The scripts that were used are open-source and can be downloaded from a Github repository (Ore, 2021)

The pressure transducers were calibrated against a reference pressure transducer. The thermocouples were not calibrated since their readings are not directly relevant for the executed experiments. It was noticed that plugging in a light source changed the values of the thermocouples by approximately 2 Kelvin. The thermocouple accuracy is therefore no more than 2 Kelvin, potentially worse. This was acceptable since the temperature readings are not used in the presented evaluation.

3.4 Flooding quantifiers

A sensor to measure the amount of liquid flooding (e.g. mass) was not available. Instead, time-based quantifiers were developed to describe the liquid-flooding behavior. The different quantifiers were based on certain “events” that occurred during a test execution. All relevant events and quantifiers are listed in Table 10 and shown in Figure 48. Figure 48 (top) shows the evaporator pressures on the left-hand side y-axis and the gravity during the parabolic flights on the second right-hand side y-axis. The Boolean signal for the status of the compressor and the occurrence of flooding are plotted against the first right-hand side y-axis. The events “Zero-G starts” and “Zero-G ends” were determined by the measured gravity level. These did not exist for ground-based testing. During the parabolic flights, the operator started a test (“Pump on”) always directly after the event “Zero-G starts”. The next two events were “Flooding starts” and “Flooding ends”, determined by visual inspection of the transparent outlet tube. These events were not detected automatically and the signal therefore impacted by human error. If no flooding occurred, the two events did not exist. Finally, the time of the pressure falling below 70 kPa was determined in post-processing and the “Pump off” signal was recorded automatically when the operator pressed the relevant button.

Time differences between the described events were used as liquid-flooding quantifiers. All quantifiers are also illustrated in Figure 48. The three most used ones are:

- ΔT_{start} : The time from starting the pump until the first occurrence of liquid in the transparent outlet tube. This measure shows how quickly flooding starts.
- $\Delta T_{elapsed}$: The total elapsed time for which liquid was visible in the outlet tube. This measure is most indicative of how much liquid flooded, even though it cannot be converted to a mass of liquid.
- $\Delta T_{70\text{ kPa}}$: The time from starting the pump until the pressure reached 0 kPa. This is a measure of how effectively the compressor empties the test section.

Table 10: Events and quantifiers during a typical test run.

Events	Quantifiers
Zero-G starts	ΔT_{start}
Pump on	$\Delta T_{flooding\ ends}$
Flooding starts	$\Delta T_{elapsed}$
Flooding ends	ΔT_{0G}
Zero-G ends	$\Delta T_{70\ kPa}$
$P_{out} = 70\ kPa$	
Pump off	

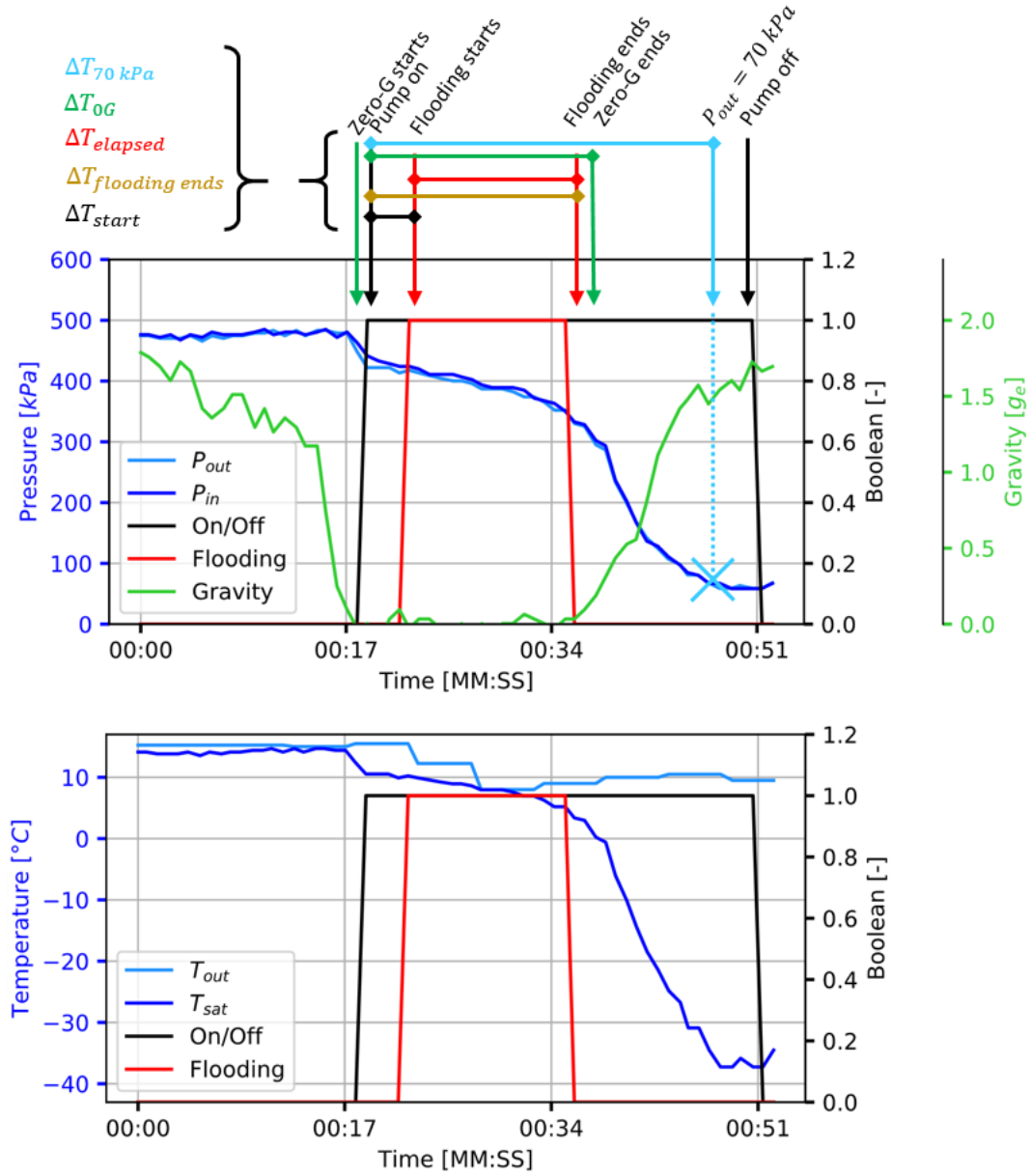


Figure 48: Typical transient data for one test run (Brendel et al., 2022a).

4. CYCLE OPERATION THROUGH 360°

4.1 Motivation

The initial motivation for inclination testing was to increase the confidence into vapor compression cycles for space applications. Even though well aware that inclination testing does not create weightlessness, several NASA scientists had agreed that continuous operation through 360° would indeed prove robustness against gravity changes and thereby raise the confidence in application of the technology in the absence of gravity. The inclinable test stand also helped preparing parabolic flight testing which involve alternating hyper and microgravity flight maneuvers. Inclination testing was the best playing field to identify and practice particular experiments and operating conditions for the parabolic flights. For example, the response time of the cycle to gravity changes was evaluated and reaching new steady-states in less than 4 minutes (typical parabolic flight cruising time) were practiced in the laboratory with the inclinable test stand.

In addition to the focus on TRL improvements and preparing for parabolic flight testing, the inclination was meant to test for liquid flooding of the compressor or a loss of subcooling at the expansion valve as observed by previous studies (see introduction in Brendel et al. (2021c)).

4.2 Anomalies during inclination testing

4.2.1 Dependence on charge distribution

Test stand configuration 1 (flat-plate evaporator, tube-in-tube condenser), linear compressor, R134a.

The test stand was operated at steady-state. Figure 49 shows that the subcooling measured both at the condenser outlet as well as at the expansion valve inlet was steady for an initial inclination angle of 0°. Although both subcooling levels were steady, there was a 4 K difference between the two locations. A sight glass near the condenser outlet showed two-phase flow. The condenser outlet and expansion valve inlet were connected with a liquid line of approximately 1 m in length containing a mass flow meter and a filter/drier. From the steady-state in the horizontal orientation, the test stand was inclined to -20°, back to 0°, and then again to -20° over the course of approximately 7 minutes. The subcooling at the expansion valve fell from 4.5 to 1.8 K with the

first angle change to -20° . In contrast, it was not impacted at all when the test rig was inclined from 0° to -20° a second time shortly thereafter. At this time, the sight glass that had shown two-phase flow earlier was filled with liquid. Due to the inclination changes, the condenser outlet subcooling started to increase, indicating a charge migration into the condenser or an increased condensing temperature. Overall, Figure 49 shows that the response of the test rig to inclination changes is not merely dependent on the operating condition but also on the charge distribution which had changed after the first inclination changes to and away from -20° . It is therefore valuable to have multiple transparent tube sections and several pairs of temperature and pressure sensors when conducting inclination testing with two-phase flow systems. Later experiments confirmed the observation that the cycle could be in an unstable or stable steady-state. This experiment was also described in Brendel et al. (2020b).

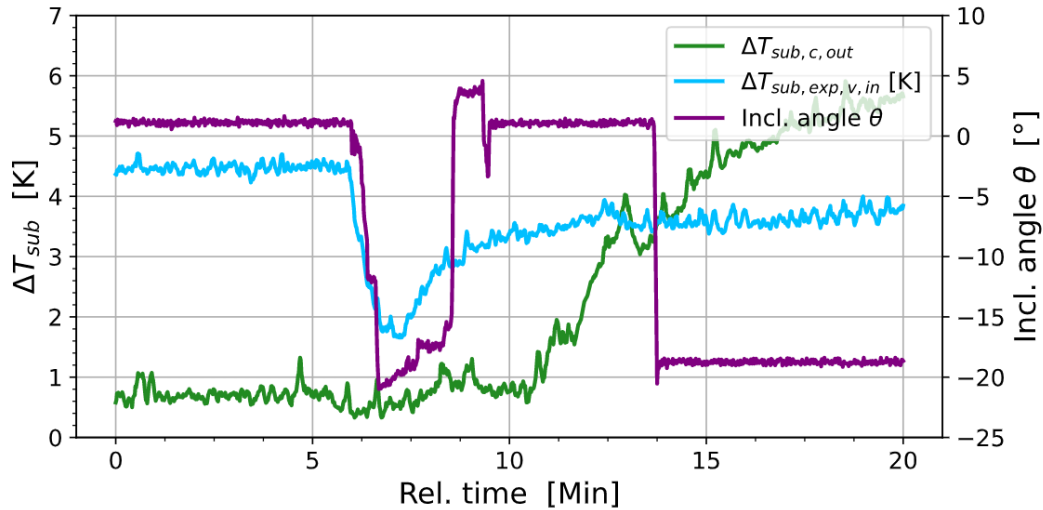


Figure 49: Subcooling at the condenser outlet and the expansion valve inlet as a function of time (adapted from Brendel et al. (2020b)).

4.2.2 Flat-plate evaporator flooding

Test stand configuration 1 (flat-plate evaporator, tube-in-tube condenser), linear compressor, R134a.

The test stand was operated at steady-state and initially inclined to -60° . At this inclination angle, the flat plate evaporator was tilted but still pointed upwards and the compressor was situated lower than the evaporator. A cooling capacity of approximately 200 W was measured, cooling the water-glycol brine from 13°C to -10°C and giving the refrigerant 15 K superheat. This is shown

throughout the first 12 minutes in Figure 50. The inclination angle was then changed from -60° to -90° , laying the flat-plate evaporator on its side. Instantaneously, the refrigerant lost all superheat and the water-glycol outlet temperature approached the inlet temperature, meaning the cooling capacity approached 0 W. At -90° , the liquid phase entering the evaporator was no longer distributed over the width of the plates. Instead, the liquid flowed along the bottom of the heat exchangers, having poor thermal contact with the water-glycol solution. This was indicated by the loss of subcooling and quickly became more evident through frost accumulation along the bottom edge of the evaporator. The frost at the edge of the plates and along the suction line is shown in Figure 51, where the test stand had been inclined already to -120° . Even the compressor shell built up frost around the suction line port, showing that the liquid phase of the refrigerant travelled through the complete suction line into the compressor. This experiment was also described in Brendel et al. (2021c).

Note that the measurements changed before the inclination angle because the angle was recorded with a 20-second delay. This problem in the data acquisition was resolved later.

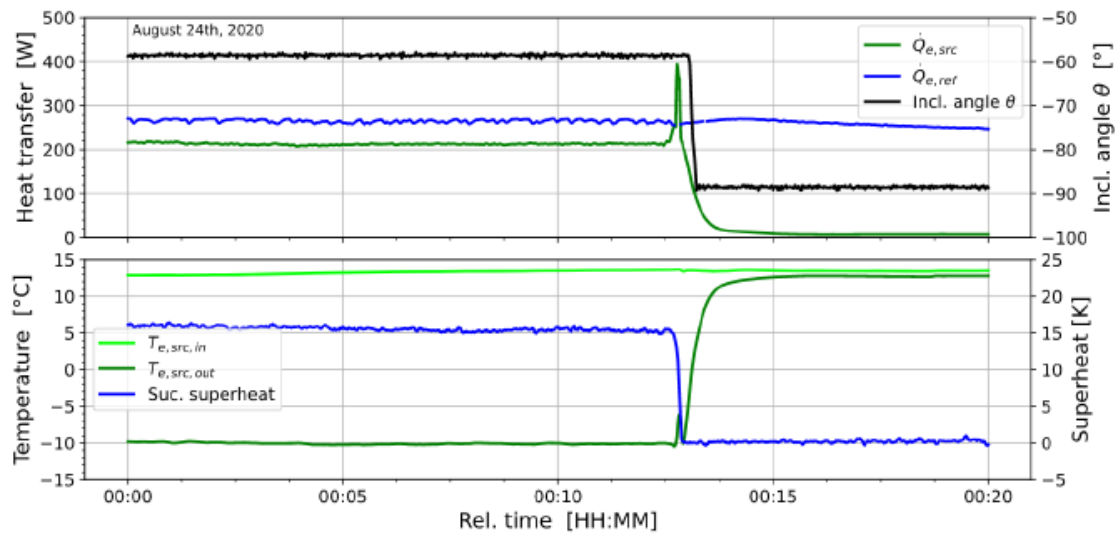


Figure 50: Loss of cooling capacity due to inclination of flat-plate evaporators (Brendel et al., 2021c).

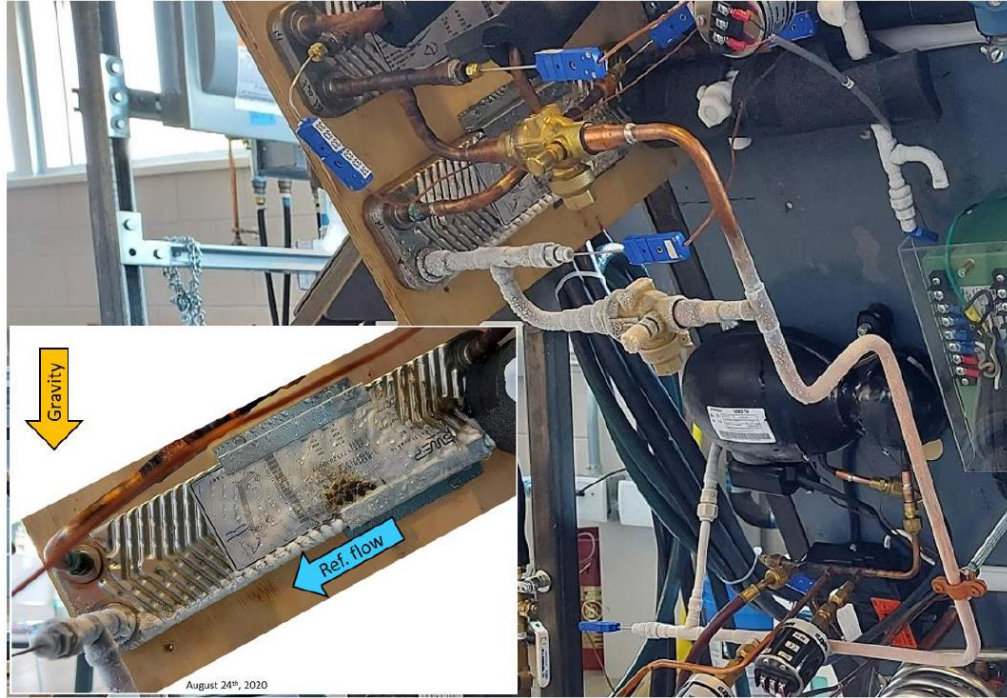


Figure 51: Incomplete boil-off in flat-plate heat exchanger with spatially separated frost accumulation along flow direction (Brendel et al., 2021c).

4.2.3 Flooding against gravity

Test stand configuration 2 (tube-in-tube evaporator, tube-in-tube condenser), scroll compressor, R134a.

The inclinable test rig was initially in the horizontal orientation and operated at steady-state. The mass flow rate of 2.25 g/s was relatively high, the suction temperature was 10 °C, approximately 20 K higher than the saturation temperature corresponding to the suction pressure (20 K superheat). This situation is shown in the first 1.5 minutes of Figure 52. From this situation, the test rig was inclined to +25°. This change lowered the evaporator relative to the compressor, such that the refrigerant had to flow upwards through the more than 1.5-meter-long suction line. Figure 52 shows that the suction superheat collapsed upon the inclination change and that the suction line mass flow rate rose quickly to more than 2.75 g/s and oscillated. The liquid line mass flow rate also increased but much slower. After 30 seconds, the inclination angle was set back to 0°, which led to a recovery of the superheat and a decrease of the mass flow rates to the previous values.

What about the 25° change in inclination angle caused liquid to exit the evaporator and travel “uphill” for more than 1.5 meter of tubing and through a Coriolis-type mass flow meter? The answer is unclear. Potentially the tilting of the helical coil evaporator created pockets of vapor trapped by liquid. These could splatter a liquid front into the suction line from where the liquid would be carried further by the vapor phase.

The phenomenon was repeatable immediately afterwards. However, at other operating conditions, the same inclination change did not always cause liquid flooding of the compressor. Different system charge levels may have also determined whether the flooding occurred or not, which is discussed more thoroughly in section 5.4.4. Not enough data was collected to understand and reliably predict whether liquid flooding would occur. Flow visualizations of the boiling process in the evaporator would probably help in understanding the measurements but are particularly difficult to realize for helical coil tube-in-tube heat exchangers. This experiment was also described in Brendel et al. (2021c).

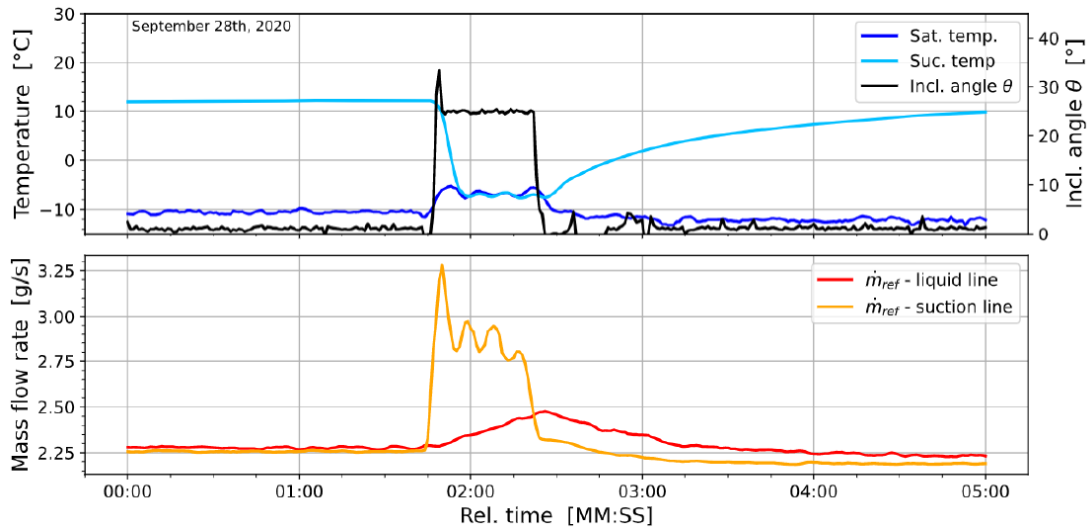


Figure 52: Liquid flooding of the suction line upon lowering the evaporator relative to the compressor (Brendel et al., 2021c).

4.2.4 Impossible start-up at $\theta = -30^\circ$

Test stand configuration 1 (flat-plate evaporator, tube-in-tube condenser), linear compressor, R134a.

At negative inclination angles, the expansion valve was located higher than the condenser outlet. Thus, when the system was turned off, liquid refrigerant that was at the expansion valve during operation travelled away from the valve into the condenser. Experiments were performed to evaluate the start-up behavior of this situation and to compare it to the opposite case, where the expansion valve is located lower than the condenser outlet and therefore has a standing liquid column at its inlet during start-up. The latter scenario allowed a cycle start-up without problems, which was experimentally demonstrated as shown in Figure 53 on the left-hand side. As the compressor power draw went up (compressor start), both a mass flow rate of 0.4 g/s and 2 K of subcooling were established quickly and maintained until the compressor was turned off. In contrast, when starting the cycle at a negative inclination, the mass flow rate fluctuated between 0 and a high value but did not become steady even after five minutes of constant compressor operation. For this case, the refrigerant state measured at the expansion valve inlet was saturated, but it is unclear whether it was a saturated vapor or a two-phase mixture. This experiment shows that for terrestrial applications, the orientation of the cycle may cause start-up problems.

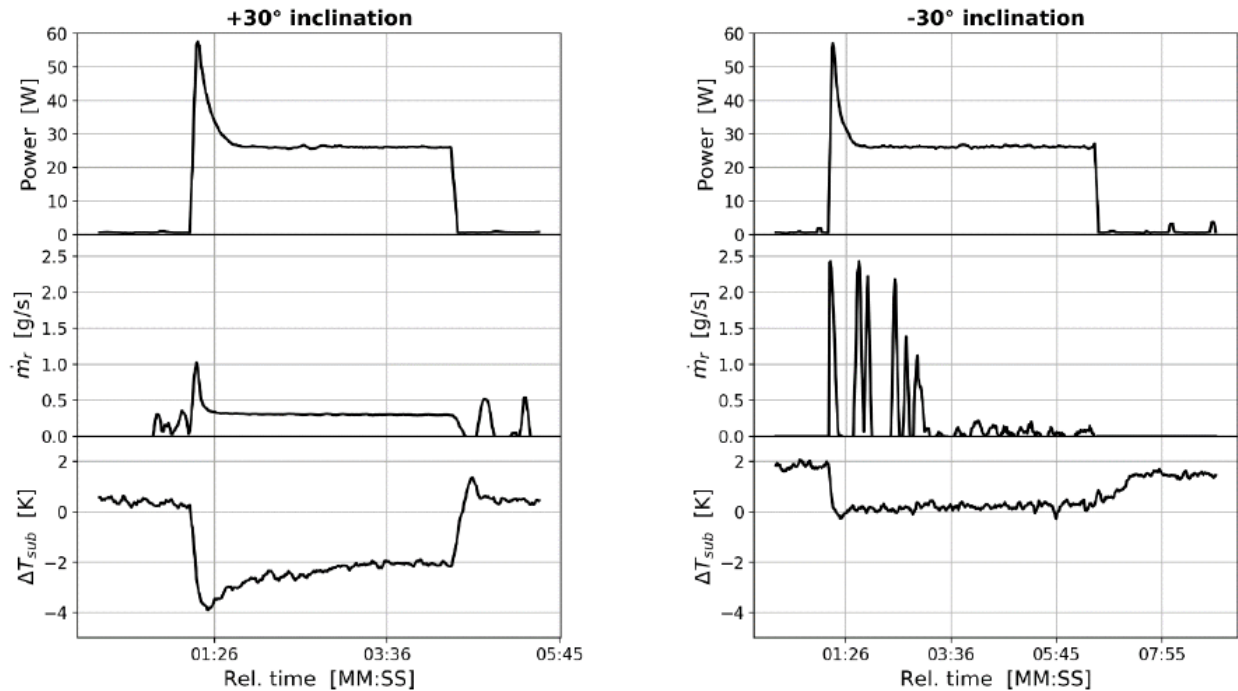


Figure 53: Successful and unsuccessful start-up at an inclination angle of +30° and -30°, respectively.

4.3 First completed loop

Test stand configuration 2 (tube-in-tube evaporator, tube-in-tube condenser), linear compressor, R134a.

Although the first completed loop did not result in an anomaly, it is listed here because the result was an important stepping stone in the evolution of the test stand and test practices. It was also a surprising (positively) result at the time. Dozens of completed loops followed in successive testing.

With flat-plate evaporators, a complete loop had never been possible because superheat was always lost at some angle. With the second configuration, loss of superheat was still a potential issue but did not always occur. Eventually, mostly through trial and error, operating conditions and system charge level were found such that superheat and subcooling remained above 10 K and 5 K, respectively. This was an important day in the course of this project, because a continuous and seamless operation of the test rig through 360° was shown for the first time. For the first systematic study, the test rig was initially set to 180°. The inclination angle was then changed in -10° increments until -210° and each angle was locked for one minute, regardless of the steadiness of the measurements after one minute. For each angle, from second 45 to 55, data was averaged in post-processing to obtain a sample of the operating conditions. Figure 54 shows the transient mass flow rate data (left) and the samples of the evaporation, condensation, suction, discharge and expansion valve inlet temperature (right). The right-hand side plot is chronologically read from right to left, since the angle was changed from +180° to -210°.

The mass flow rate in the left-hand side plot of Figure 54 started out at approximately 1.4 g/s. It fell after the first incremental change of the inclination angle but came up slowly again as the test rig approached the horizontal orientation. At the horizontal orientation, the mass flow rate increased to 1.5 g/s and then gradually fell to 1.4 g/s before it sharply fell to 1.25 g/s at approximately -90°. The mass flow rate was then mostly steady except for a slight fall towards the very last tested inclination angles. All the orientation changes affected the evaporation temperature samples (dark blue scatter plot, chronologically from right to left). Higher and lower evaporation temperatures resulted in a change of the evaporation pressure. This affected the suction density and therefore the mass flow rate of the cycle. The other temperatures were mostly steady throughout the 390°. This experiment was also described in Brendel et al. (2021c). Achieving the first complete loop initiated systematic testing of 360° loops shortly thereafter.

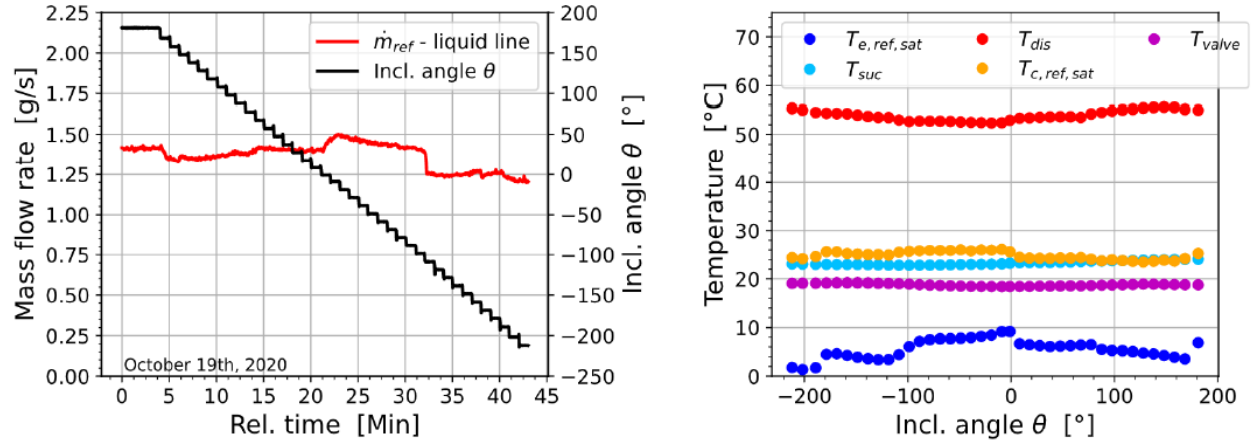


Figure 54: Stable operation of cycle through 390° (Brendel et al., 2021c).

4.4 Unstable steady-state conditions

Test stand configuration 2 (tube-in-tube evaporator, tube-in-tube condenser), scroll compressor, R134a.

The following phenomenon was observed multiple times and sometimes negatively impacted some of the systematic testing results. The test stand was initially at a steady-state condition and in the horizontal orientation. The inclination angle was then adjusted to several different angles but eventually set to the horizontal position again. The expectation was that the test stand would then settle to the initial steady-state, because no control parameters had been changed. With the same compressor frequency, expansion valve opening and heating rate of the heat source, the operating conditions of the cycle should be well defined. In contrast, measurements sometimes led to a new steady-state condition that was markedly different from the initial steady-state.

An example of this is shown in Figure 55. The top plot shows the liquid and suction line mass flow rate, which both started out at 1.82 g/s. The inclination changed from minute 2 to minute 10 as shown by the gray line and led to perturbations in the two mass flow rates. From minute 10, the test rig was in the horizontal position again and the inclination angle was no longer changed. The mass flow rates settled to 1.6 g/s, which was 11% less than initially. Even though it cannot be finally proven, the best explanation for this anomaly seems to be a charge migration. When integrating the difference of the mass flow rate in Figure 55 (top), the green line in the second row plot results ($\Delta\dot{m}_r$ (cus)). It shows the cumulative charge migration and is positive if the evaporator

gained charge and negative if the evaporator lost charge relative to the initial charge level. The charge migration leveled out at -10 g. Given that the test stand does not have many pockets for refrigerant to accumulate, 10 g of refrigerant must have been transferred from the evaporator to the condenser and resulted in a different steady-state. This experiment was also described in Brendel et al. (2021c). The third row in Figure 55 shows the cooling capacity (based on the liquid line flow meter ($\dot{Q}_{r,evap}$) and the suction line flow meter ($\dot{Q}_{r,evap,2nd}$). The plot below shows the power draw of the compressor throughout all angle changes. Row 5 shows the relative COP changes of the cycle. This was plotted for the results using the suction line flow meter, because the suction line flow rate is more indicative of the cooling capacity and compressor power draw. The COP increased briefly by up to 25% and leveled out at 85% of the initial COP. However, the operating conditions of the cycle also change with the inclination change, e.g. high and low side pressures and saturation temperatures, which affects the Carnot efficiency. Therefore, the last row of Figure 55 shows the second law efficiency ($\eta_{2nd} = COP/COP_{carnot}$). The second law efficiency remains within a tight band of 92% to 100%. For 75% of the transient data collected, the cycle operates mostly within an even tighter band of 98% and 100%. Hence, the changes in COP are largely determined by the change of operating conditions as opposed to a change of the heat exchanger effectiveness or compressor efficiency.

To summarize, a steady-state condition at the beginning of the experiment turned out to be “unstable” when imposing orientation changes. In other instances, the operating conditions would indeed return to the initial steady-state which will be referred to as a “stable” steady-state. Testing showed that a steady-state at any operating condition was more likely to be stable if the test rig had been rotated back and forth a few times quickly. This often led to a new steady-state close to the initial steady-state which was then more stable. Repeated rotation still affected the measurements, but upon return to the horizontal orientation, the test rig settled to the initial steady-state. This concept is illustrated in Figure 56. Ball A is an unstable steady-state. A change of the inclination angle can change its location (its steady-state). In contrast, B is a stable steady-state, which can still change its location when inclined, but it will return to its initial steady-state when in the initial orientation.

If the charge distribution is indeed the reason, it is unclear why the charge can be distributed differently at all for a given set of control values. It would then also be interesting to understand

this for vapor compression units in the field which never experience inclination changes similar to those tested in the laboratory. Is their charge distribution not well defined either?

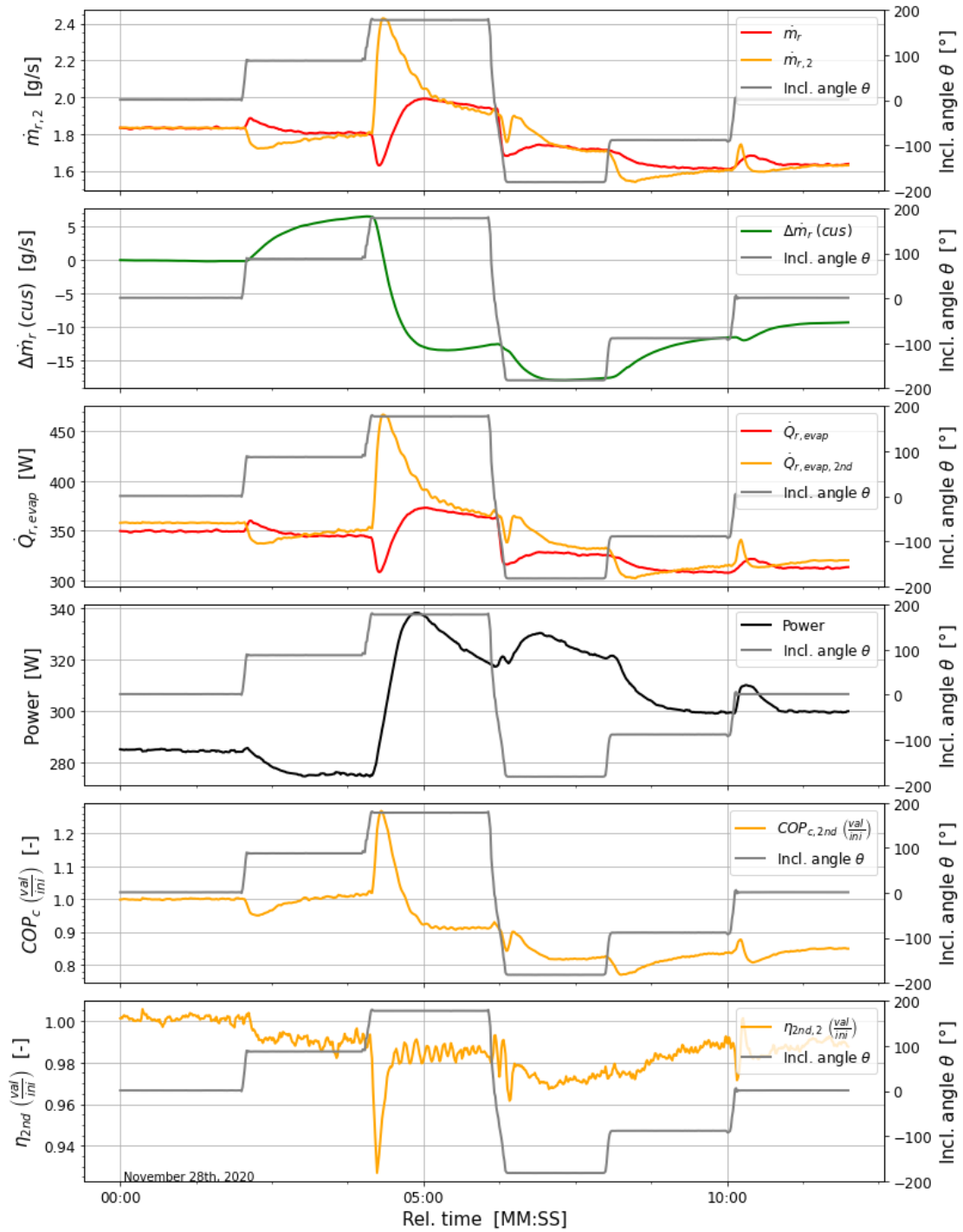


Figure 55: Marked shift in operating conditions after returning to a horizontal orientation (Brendel et al., 2021c).

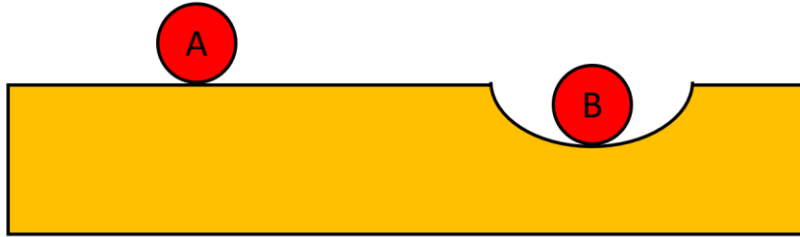


Figure 56: Illustration of unstable and stable condition.

4.5 Summary

Concerns about vapor compression cycles at varying orientations are warranted. Inclinations may lead to start-up difficulties or sudden compressor flooding during operation, even against gravity. The cycle response is strongly dependent on the type of heat exchangers. However, it was indeed possible to continuously operate a vapor compression cycle through 360° without problems, after appropriate components and a suitable charge level was found. It was observed multiple times, though, that a cycle did not return to its initial steady-state after an inclination procedure had been completed, although all control parameters remained unchanged. Conclusions of this chapter can be summarized as follows:

- 1) *Only one publication in the open literature reports the successful operation of a vapor compression cycle at angles from 0 to 315 degrees of orientation, albeit not continuously (Domitrovic et al., 2003).*
- 2) *The effects of inclination on a vapor compression cycle are not merely dependent on the angle and operating conditions but also sensitive to the total refrigerant charge and the charge distribution (Brendel et al., 2020b).*
- 3) *A flat-plate evaporator lost its entire cooling capacity due to a change in the inclination angle from 60° to 90° (Brendel et al., 2021c).*
- 4) *Liquid flooding of the suction line may occur from orientation changes that lower the evaporator relative to the compressor and despite ample superheat before the inclination (Brendel et al., 2021c).*
- 5) *The proper start-up of a VCC may be inhibited due to the inclination angle (section 4.2.4).*
- 6) *A vapor compression cycle can operate continuously through 360° with only small changes in the operating conditions (Brendel et al., 2021c).*
- 7) *A vapor compression cycle at steady-state may operate in a different steady-state in the same orientation after some pattern of inclination changes has occurred (Brendel et al., 2021c).*

5. QUANTITATIVE IMPACT OF ORIENTATION CHANGES

5.1 Motivation

After the inclinable test stand reached configuration 2, repeated operation through 360° was possible. Following this first step, a quantitative description of cycle responses became relevant. Two-phase flow research had proven that stability increases for higher mass fluxes. Whether this theory would hold for vapor compression cycles on a system level was a guiding question. Gravity independence had been reported in the two-phase flow literature and was a goal for system level inclination testing. Lastly, thermal gravitational scaling had been proposed as a method that leverages terrestrial testing of different fluids to predict reduced gravity system behavior. This led to the testing of different fluids subjected to the same inclination changes.

5.2 Classification of collected data

A systematic investigation of inclined vapor compression cycles is not available in the open literature. Hence, there were no previous experiences that could have guided the research and indeed it progressed partially by trial and error. In hindsight, the testing sets are best distinguished by their frequency of inclination angle changes. The lowest frequency testing was “steady-state” testing, where each inclination angle was locked until a steady-state was established. Therefore, an inclination change occurred only every 10 to 20 minutes. Repeatable datasets resulted that can be analyzed with steady-state models. The highest frequency testing was the opposite. Approximately three inclination changes were executed per minute, resulting in much more chaotic data, because the cycle never settled to a steady-state. Steady-state models are useless for an analysis of this data but generalized quantifiers can still show trends. A testing procedure of intermediate frequency is “6-angle testing”, which was chronologically the first systematic testing series conducted. 6 different angles were locked for 2 minutes each. 2 minutes were typically enough to see a clear trend of the measurements that started to level out but did not reach steady-state before the next inclination change was imposed.

5.3 Low frequency orientation changes – steady-state testing

Test stand configuration 3 (fin-tube evaporator, fin-tube condenser), scroll and linear compressor, R134a and R1234ze(E). Frequency of inclination changes: 1 every 10 to 20 minutes.

For steady-state testing, any inclination angle is locked until the system has reached a new steady-state, which makes it a slow type of testing. Testing was conducted in July 2021 and concluded the experimental work for this dissertation. From an educational point of view, this testing would have been better suited in the early stages of the project. Therefore, it is described in this dissertation as the first systematic testing.

R134a and R1234ze(E) were both tested at three different mass fluxes each ($G \approx \{14, 29, 55\} \text{ kg}/(\text{m}^2 \cdot \text{s})$) to have a low, medium and high mass flux dataset. One test run repeated R134a at $G = 29 \text{ kg}/(\text{m}^2 \cdot \text{s})$ for a repeatability check. This makes a total of 7 datasets. One set is defined as inclination changes that start from a steady-state at the horizontal orientation, stepping in constant increments through 360° and settling to a last steady-state at the horizontal orientation again. Increments were typically 45 degrees, except for set 4 and 5 where the increments were 15° and 90° , respectively.

lists all the collected datasets with the number of steady-state points and other information.

Table 11: Collected data sets for steady-state investigation (from Brendel et al. (2022b)).

Set	#SS	Time [h]	Refrigerant	Compressor	\dot{m}_r [g/s]	G [kg/(m ² ·s)]	T_e [°C]
1	10	3.5	R1234ze(E)	Scroll	2.11	55.7	-5.3
2	11	2	R134a	Linear	2.04	53.8	0.3
3	10	1.75	R134a	Linear	0.55	14.6	-11.4
4	26	3	R134a	Linear	1.14	30.1	-19.2
5	5	1	R134a	Linear	1.11	29.4	-20.0
6	10	2.25	R1234ze(E)	Linear	0.53	14.1	-14.1
7	10	2	R1234ze(E)	Linear	1.08	28.6	-16.4

Steady-states were defined by a maximum band of the evaporation and discharge temperature changes of 0.5 K for at least five minutes. The suction and liquid line mass flow rate had to stay within a band of 0.05 g/s for the same time window. For both evaluations, a five second rolling mean was applied to reduce the impact of measurement noise. Post-processing showed that set 3 violated the steady-state criterion but the evaporation and discharge temperature were still in a band of 1 K and the mass flow rates within a band of 0.13 g/s. When the test stand reached a

steady-state, data was collected and averaged over approximately 15 seconds to generate one sample data point.

The inclination angle of the test stand is limited to $\theta = \pm 180^\circ$ (measured from horizontal). Hence, a continuous 360° rotation starting from the horizontal orientation is not possible. Therefore, after incremental changes from 0° to 180° , the test rig was rotated in one sweep to -180° and the incremental stepping continued from there till 0° . Typically, a steady-state was collected both at $+180^\circ$ and -180° . Both data points agreed well in all trends, such that the intermediate sweep is expected to not affect the overall measurements. 360° was added to each of angles $< 0^\circ$ to generate an x-axis which lists the angles chronologically from left to right in scatter plots.

To minimize the chance of starting at an unstable steady-state, the test stand was rotated back and forth by more than $\pm 90^\circ$ two times with a waiting period for settling in between before starting a set (compare with section 4.4).

Results from this section are also documented in Brendel et al. (2022b).

5.3.1 Experimental results

Plotting the collected steady-state samples of one set as a function of the inclination angle showed sinusoidal trends for almost all measurements and throughout all datasets. Set 7 is selected as a representative example and shown in Figure 57. All measurements have a sinusoidal trend, except the evaporator outlet superheat has an inversed sinusoidal trend (like a $-\sin(\theta)$ function). The bottom right plot in Figure 57 shows a fitted boiling heat transfer tuning factor which will be discussed more thoroughly in chapter 8. Most steady-states were stable, meaning that the measurements at 360° were very close to the measurements at 0° .

Another observation can only be seen in transient plots. Figure 58 shows the liquid and suction line mass flow rate for the three datasets collected with R1234ze(E). These are best to compare because all had 45° angle changes. Three observations are apparent from Figure 58:

- Oscillations in the suction line decreased with increasing mass flux (left to right).
- Oscillations were likely to occur between 90° and 270° and were the strongest at 225° .
- The maximum deviation of the mass flow rate from its initial steady-state increased with an increasing mass flux (note that all y-axes span 0.5 g/s).

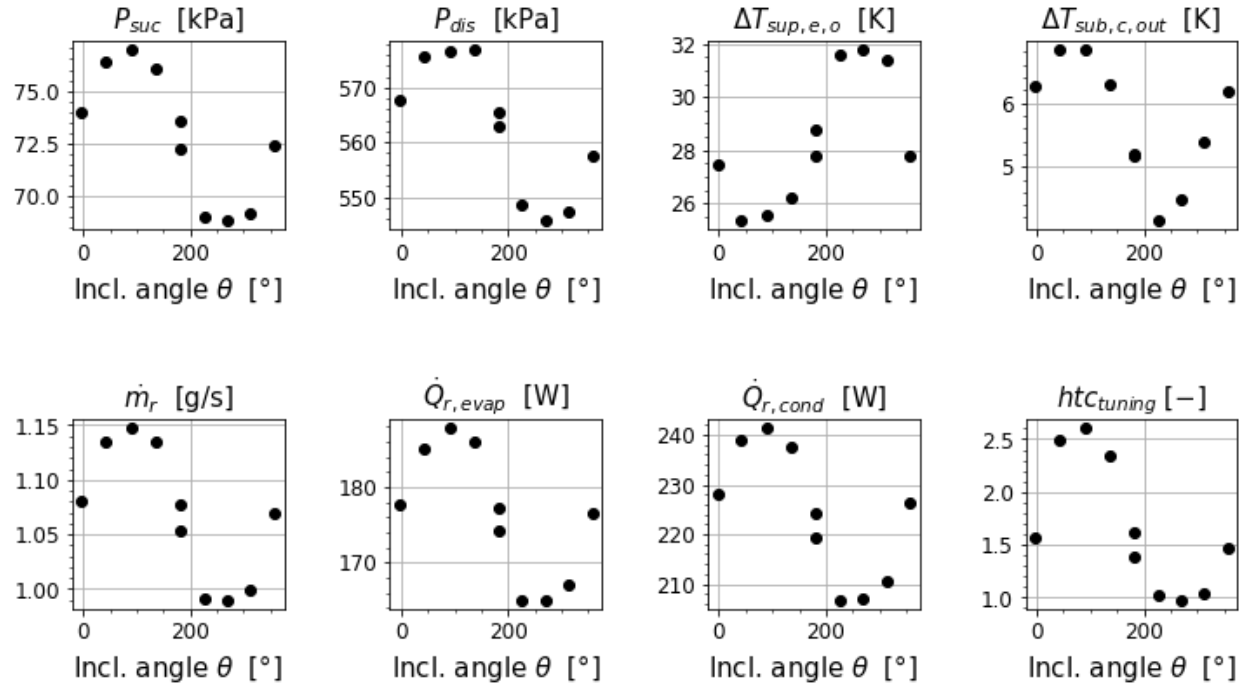


Figure 57: Various measurements from set 7 of the steady-state testing series.

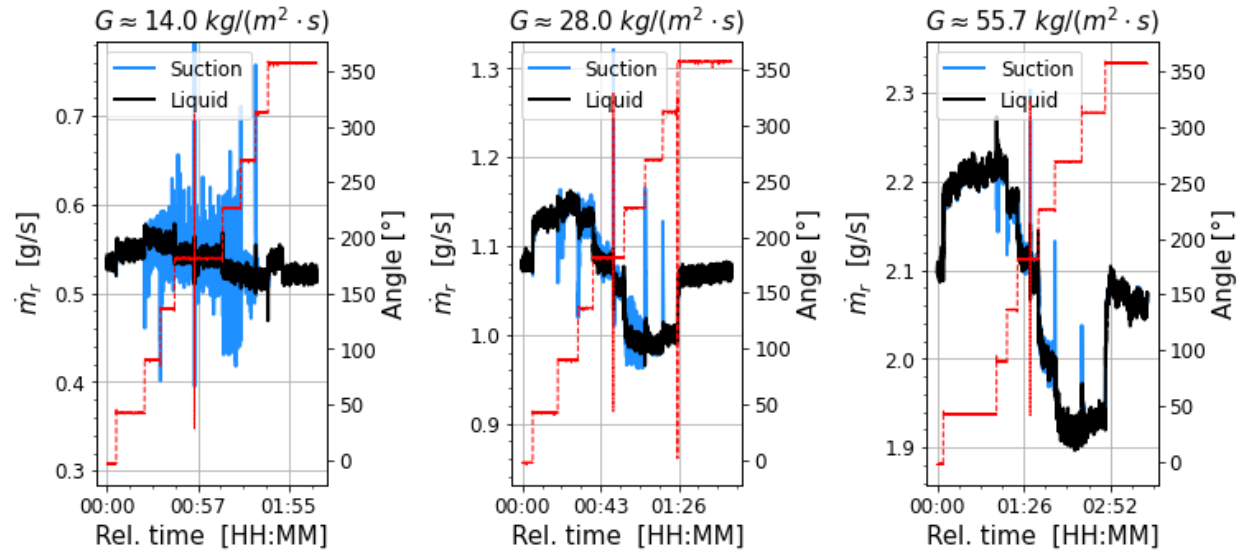


Figure 58: Liquid and suction line mass flow rate during three sets of steady-state testing (Brendel et al., 2022b).

Finally, it was desired to quantify the deviations of the mass flow rate from its initial value for all sets (the amplitude of the sinusoidal trend). For this purpose, the MDV and the IIR (see section 2.7.2 for definitions) were plotted as a function of the mass flux for all 7 sets in Figure 59. A linear and constant trend resulted for the MDV and IIR, respectively. The very clear trends indicate that R134a and R1234ze(E) as similar refrigerants also respond similarly to inclination changes. Even the oscillations for the low mass flux case started and ended at the same angles. It should be noted that all 7 sets were collected over different periods of time as shown in Table 11 but fit into one consistent trend.

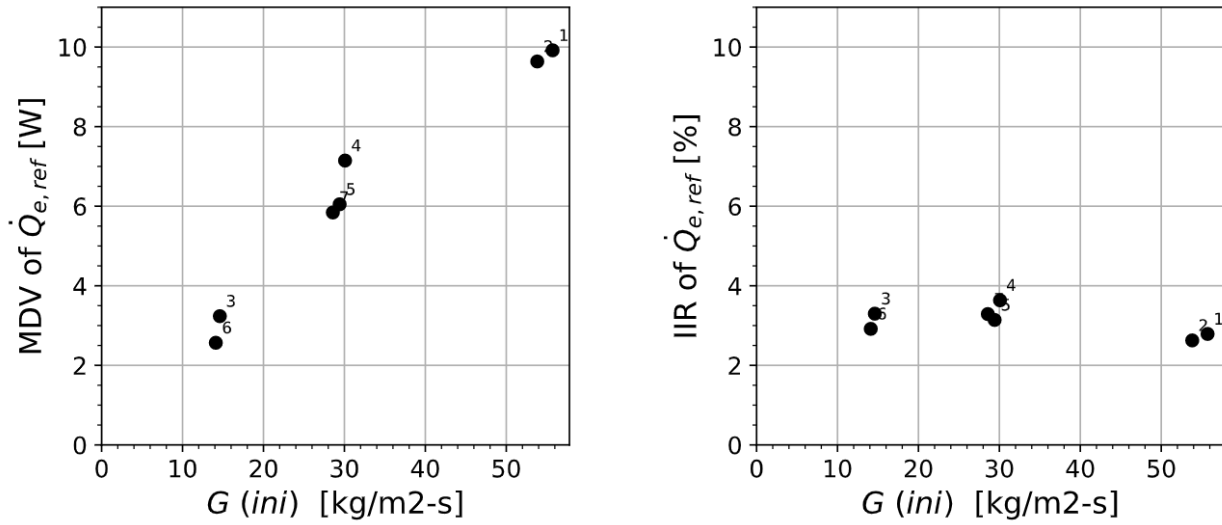


Figure 59: MDV and IIR for steady-state testing (from Brendel et al. (2022b)).

5.4 Medium frequency orientation changes – 6-angle testing

Test stand configuration 2 and 3 (tube-in-tube or fin-tube evaporator, tube-in-tube or fin-tube condenser), scroll and linear compressor, R134a. Frequency of inclination changes: 1 every 2 minutes.

5.4.1 Overview

Chronologically, 6-angle testing started soon after the first successful loop on the test stand in the liquid-to-liquid configuration. It was the first systematic testing and the main motivation was to evaluate the stability of the cycle against inclination changes as a function of different operating conditions (mainly the mass flow rate, evaporation temperature and charge). Initially, an

inclination pattern had to be defined to be repeated at varying operating conditions. Requirements for the inclination procedure were:

- To cover 360° , such that potential orientations for liquid flooding can be found
- To be relatively short so that the procedure can be repeated at many different operating conditions
- To lock any angle long enough for the cycle to respond meaningfully

The result was an inclination pattern where the angles 0° , 90° , 180° , -180° , -90° and 0° were locked for two minutes each starting with the cycle at steady-state. Figure 60 shows data from the inclination angle of one execution of the 6-angle testing. 2 minutes did not allow the test rig to reach a new steady-state, but the trend of a response can be identified. Compared to steady-state testing, the 2-minute time windows were much shorter, but compared to the timescale of parabolic flights, 6-angle testing is still slow. Hence, it is a testing procedure of intermediate timescale.

Table 12 provides an overview of the collected data. The 6-angle testing was conducted for R134a in configuration 2 (tube-in-tube heat exchangers) and with R134a and R1234ze(E) in configuration 1 (air-to-air heat exchangers). 10 loops had to be discarded from the configuration 2 data due to unclear data acquisition or operating conditions. This is explained in detail in Brendel et al. (2022c).

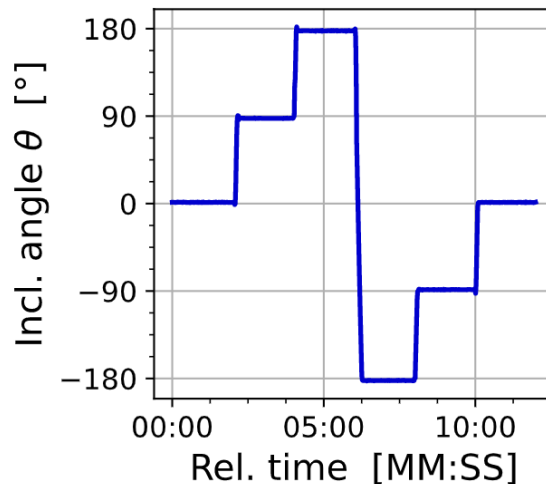


Figure 60: Inclination pattern for six-angle testing.

Table 12: Collected dataset according to the 6-angle inclination procedure.

Information	Liquid-to-liquid	Air-to-air
Number of datasets	32 (all R134a)	42 (31x R134a, 11x R1234ze(E))
Number of clean datasets	22	42
Time of data collection	October – December 2020	February – July 2021

5.4.2 Instability results

The motivation of the 6-angle testing series was to search for a correlation of the cycle instability due to inclination changes in terms mass flow rate or mass flux. Several quantifiers were tested in a trial and error approach until it was found that the *IIR of the heat source heat transfer rate* correlated well with the mass flow rate for data from configuration 2. This is shown in Figure 61 (left). The IIR reached 25% for very low mass flow rates and leveled out between 5 and 8% for mass flow rates greater than 1.5 g/s. It took several months until system configuration 3 was completed and the same experiments were repeated. The instability values were much lower for configuration 3, approximately one third of the instabilities of configuration 2 at equivalent mass flow rates. However, the trend for both configurations was very similar (Figure 61 (right) for R134a).

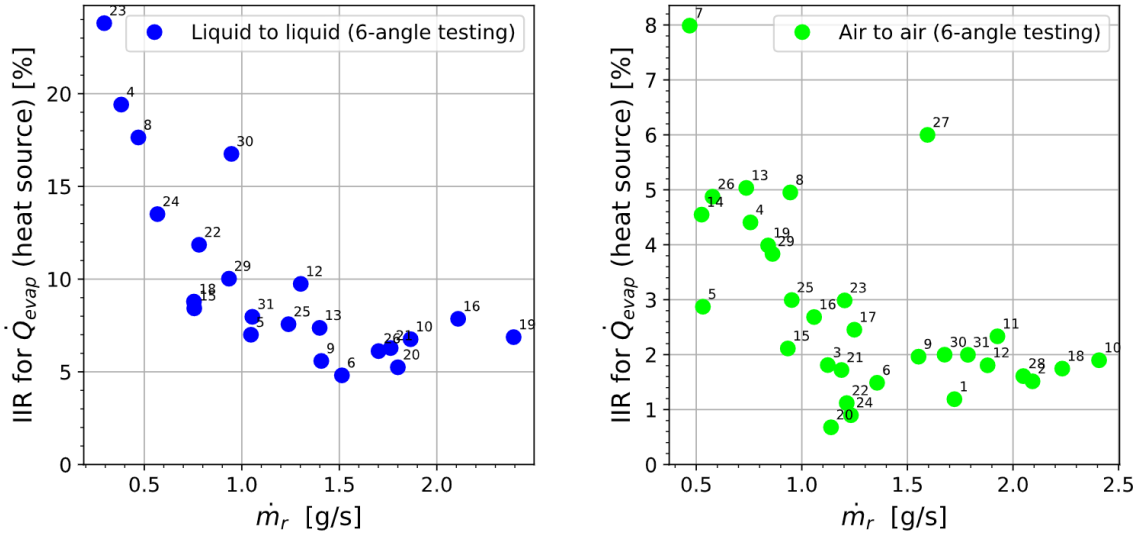


Figure 61: IIR of the heat source heat transfer rate as a function of the mass flow rate for configuration 2 (left) and configuration 3 (right). Adapted from Brendel et al. (2021e).

A different picture arose when the data from both configurations was plotted as a function of the evaporator mass flux in one chart. The internal hydraulic tube diameter of the tube-in-tube evaporator was 12.9 mm in contrast to 6.9 mm for the fin-tube evaporator. Therefore, for a given mass flow rate, the tube-in-tube evaporator has a much lower mass flux. The data was shifted such that the highest mass flux values of the tube-in-tube evaporator lined up with the lowest mass flux values of the fin-tube evaporator, producing a very consistent trend over a wide range of mass flux values as shown in Figure 62. Data from R1234ze(E) has been overlaid here, too, and is consistent with data from R134a even though generally slightly higher.

Given the potential sources of error throughout the procedure of obtaining the IIR for both test stands, the trend of the instability data in Figure 62 for R134a was remarkably clear. For curve-fitting the data, a power law function of the form $IIR = a \cdot G^b$ produced much better results (with $a = 48$, $b = -0.8$) than an exponential function of the form $IIR = a + b \cdot \exp(c \cdot G)$.

These results are also described in Brendel et al. (2022c) and Brendel et al. (2021e).

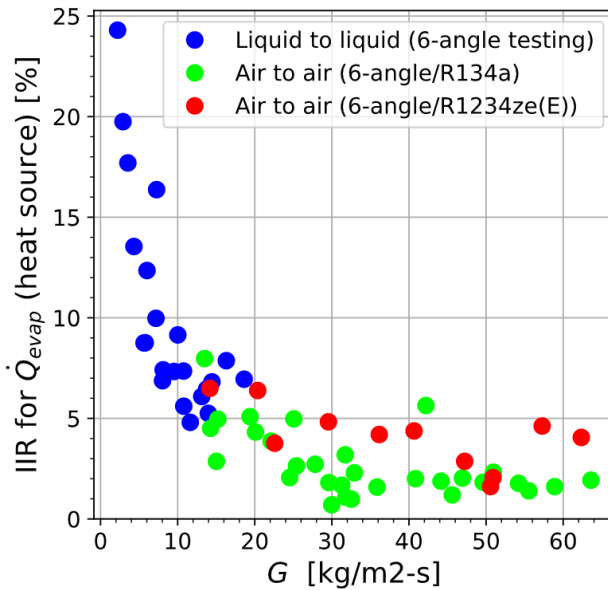


Figure 62: IIR for heat source heat transfer rate for both test stand configurations as a function of the mass flux.

Due to the lack of theoretical support for the experimental results, the confidence in the universality of the findings is limited. For example, the following important questions cannot be answered with the given data:

- Would testing with a third evaporator fit into the trend?
- Would testing of a large-scale system produce instabilities of the same magnitude?
- Would a different inclination pattern produce consistent results, too?
- Could the larger instabilities of configuration 2 be caused by the different heat exchanger type and not by the larger tube diameter?

Finally, the fact that the initially sought result was actually found is always a red flag for confirmation bias and researchers continuing this work should be aware of that. For example, the trend shown in Figure 62 is not as clear for many other measurements. Figure 63 shows this for the IIR applied to the suction and liquid line mass flow rate, the refrigerant side evaporator and condenser heat transfer rate and the expansion valve outlet and discharge pressure (for the chart of the condenser heat transfer rate, 9 liquid-to-liquid loops without compressor discharge superheat were unselected because the condenser inlet enthalpy is unknown if the state point is not superheated, see Brendel et al. (2022c). For the same reason, 7 air-to-air loops with R134a had to be discarded). In addition, the mmx quantifier was applied to the evaporation and condensation temperature in Figure 63. The following observations can be made:

- For the closely coupled evaporation pressure, suction line mass flow rate and refrigerant side evaporator heat transfer rate, the IIR correlates well with the mass flux.
- The discharge pressure IIR for configuration 3 is much more stable than for configuration 2.
- Similarly, the mmx of the condensation temperature is much smaller for configuration 3 than for configuration 2.

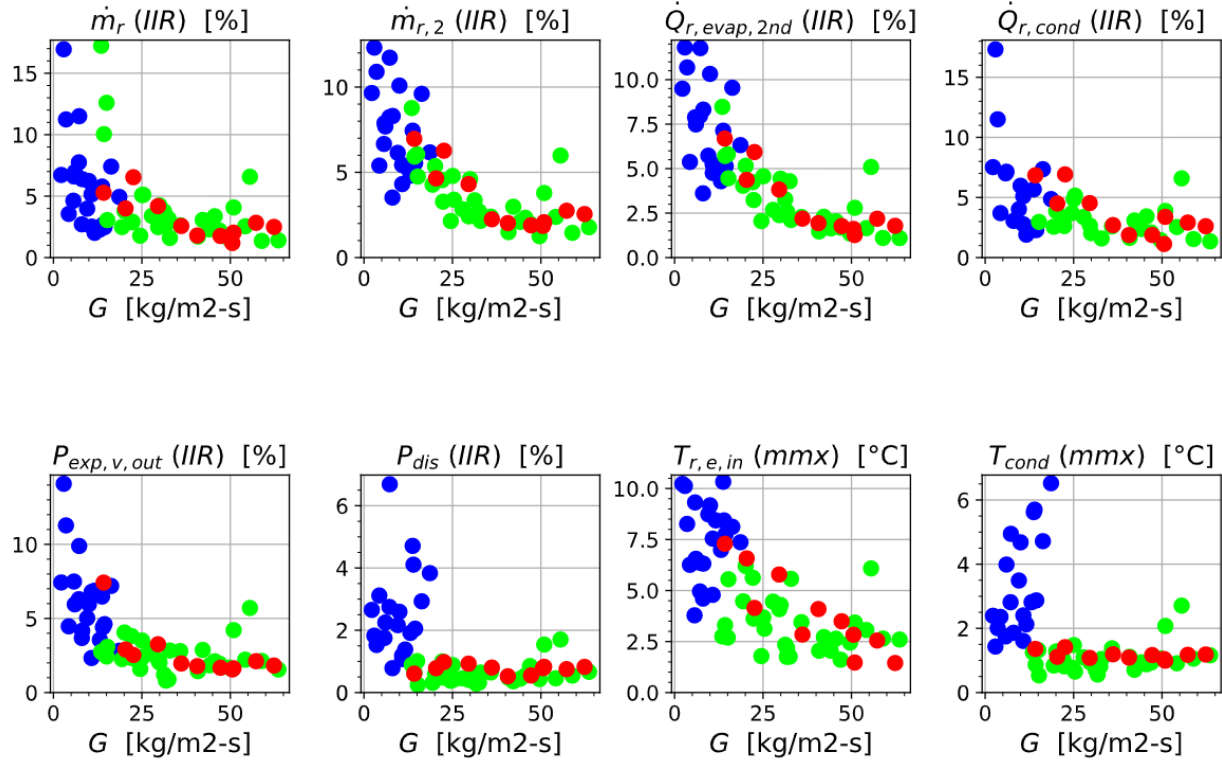


Figure 63: IIR and mmx applied to various measurements and plotted as a function of the mass flux (compare with Figure 62 for the legend).

5.4.3 Heat exchanger geometries

Figure 62 showed a smooth trend of the IIR for the heat source heat transfer rate as a function of the mass flux. In this trend, the IIR for data from configuration 2 showed stronger instabilities than data from configuration 3. It is possible that the trend was solely determined by the higher mass flux of configuration 3. Another valid explanation is that the different stability levels are due to the use of different heat exchanger geometries.

Figure 64 shows the fundamental schematics of both heat exchanger geometries. The tube-in-tube heat exchanger has an inlet at the bottom followed by a continuous up-flow of the refrigerant. The fin-tube heat exchanger has the inlet and outlet at the top with a down and up-flow in between. This is also shown in a simplified height-length graph in Figure 65. The fundamental difference is best realized with a thought experiment:

“Fill 50% of the evaporator with water and close the inlet but keep the outlet open. Turn it up-side down. How much water is left?”

More water will be left in the fin-tube heat exchanger. Gravity cannot act towards the outlet for all liquid in the heat exchanger, which is not the case when the tube-in-tube heat exchanger is up-side down. The contribution of this geometry difference to the instabilities in Figure 64 is unclear, but its potential to affect instability data should be kept in mind.

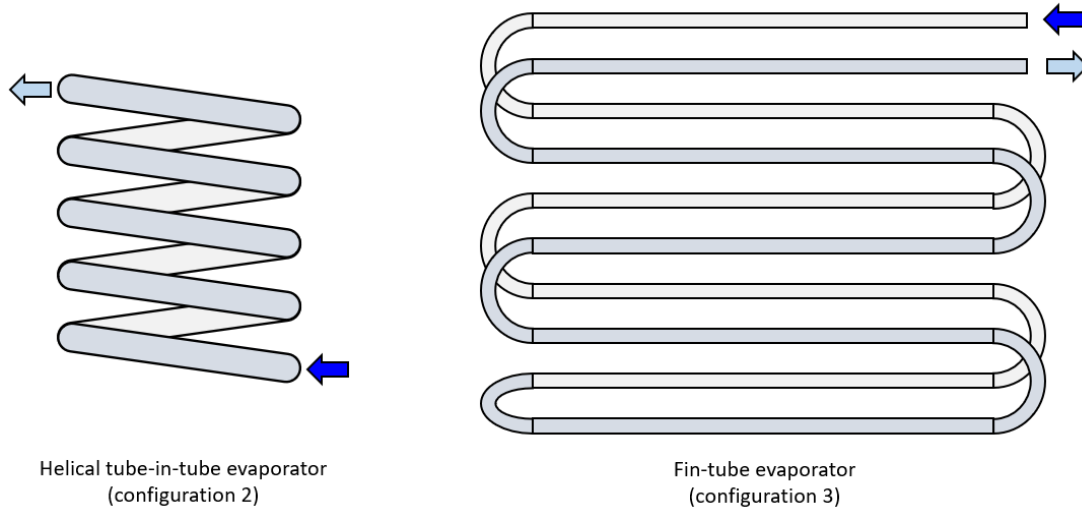


Figure 64: Schematic of coil routing for tube-in-tube and fin-tube heat exchanger (Brendel et al., 2021e).

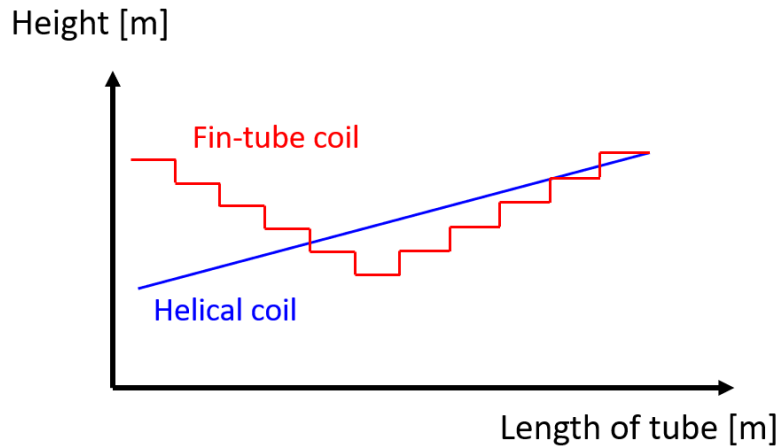


Figure 65: Height as a function of tube length for tube-in-tube and fin-tube evaporator.

5.4.4 Compressor flooding during 6-angle testing

During the first 28 sets of 6-angle testing using configuration 2, liquid flooding of the suction line occurred in set 7, 11, 17, 27 and 28 for no apparent reason, similar to the behavior described in section 4.2.3. The mentioned sets did share relatively high mass flow rates, but it was

unlikely the reason for flooding because other sets at similar mass flow rates did not show flooding. Moreover, high mass flow rates were assumed to stabilize the cycle.

It was found that set 7, 17, 27 and 28 did have unusually high charge levels. This led to the hypothesis of the charge level dictating the flooding behavior and was investigated with a dedicated series of loops (sets 29 to 35). 6-angle loops were conducted at constant operating conditions (1.1 g/s mass flow rate, ≈ 10 °C evaporation temperature) but with increasing charge levels (290 g, 310 g, 350 g, 375 g, 400 g, 430 g). Flooding was quantified by the time in seconds that the compressor suction thermocouple and pressure transducers showed a superheat of less than 1 K. An increase of liquid flooding was found starting from 375 g as shown in Figure 66 (left). At a charge level of 375 g, flooding occurred for 21 seconds. At a charge of 400 g, flooding occurred for 4 minutes and 4 seconds. The last dataset could not be completed because the compressor stalled from liquid flooding. The time of 293 seconds was measured from start of flooding till compressor stall and would have been much higher with a liquid tolerant compressor. It is therefore plotted with a different color.

Figure 66 (right) showed the associated levels of subcooling for each charge level. The subcooling increased non-monotonically between point 32 and 33. At point 32, there was a small amount of liquid flooding at the evaporator outlet which did not reach the compressor suction. It is possible that part of this charge went into an attached refrigerant hose in the up-side-down orientation, thereby decreasing the effective charge level and subcooling level. This hose was removed for testing in configuration 3.

All subcooling levels are clearly above typical subcooling levels. The result is therefore less important for its practical implications but more for the understanding that the system charge can impact the likelihood of flooding at varying orientations. For systems of different scale, the charge threshold for flooding could be different and may also fall in a region of normal subcooling levels.

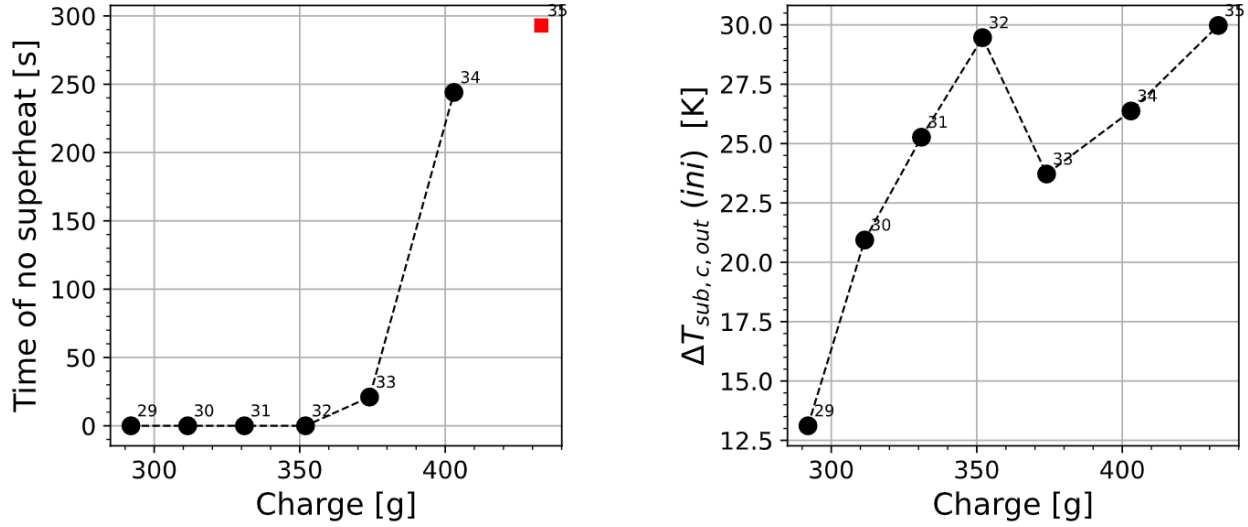


Figure 66: Time of no superheat (left (Brendel et al., 2022c)) and subcooling (right) as a function of the system charge (configuration 2).

The same test series was repeated with the test stand in configuration 3 (1.1 g/s mass flow rate, approximately 10°C evaporation temperature, charge levels 300 g, 350 g, 400 g, 504 g and 600 g). Even at 600 g, no flooding was observed. The charge levels with associated subcooling levels are plotted in Figure 67. It is possible that the geometry difference pointed out in section 5.4.3, apart from making the cycle more stable, also inhibited flooding. However, short durations of flooding were observed in configuration 3 for datasets 10, 24 and 25. These had medium to high mass flow rates, but all three were among the 4 loops with the smallest initial superheat. It appears that the small superheat made flooding more likely but did not necessarily lead to it. Low mass flow rates were clearly not the reason for flooding. Figure 68 shows the transient data for the evaporator outlet superheat for the four sets with smallest initial superheat (10 K, 24 K, 25 K, 35 K). If the superheat was lost, it happened shortly after the rotation from -180° to +180°. Superheat recovered generally much quicker than when the superheat was lost during the charge study with the liquid-to-liquid configuration.

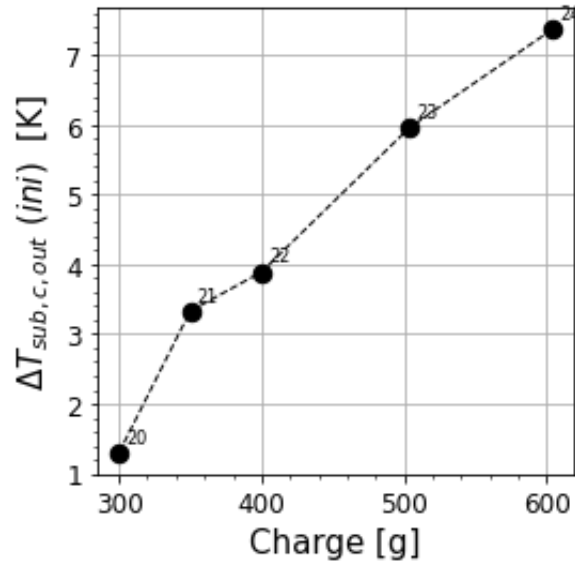


Figure 67: Charge and subcooling levels for flooding test series (configuration 3).

5.4.5 Vapor bubbles in liquid line

During some 6-angle tests, the liquid line mass flow rate signal showed strong oscillations at an inclination angle of -90° . At this inclination, visual inspection of the sight tubes showed vapor bubbles leaving the condenser and travelling upwards in the vertical liquid line where the mass flow meter is located, which explains the measured oscillations. This happened exclusively but not necessarily at low mass flow rates. For example, loop 26 had a very low mass flow rate of 0.6 g/s, too, but a clean liquid line mass flow rate signal. From the loops with the four lowest initial mass flow rates, three showed oscillations but one did not. Figure 69 shows the transient data of the datasets where oscillations occurred. The oscillations are clearly visible at an inclination angle of -90° .

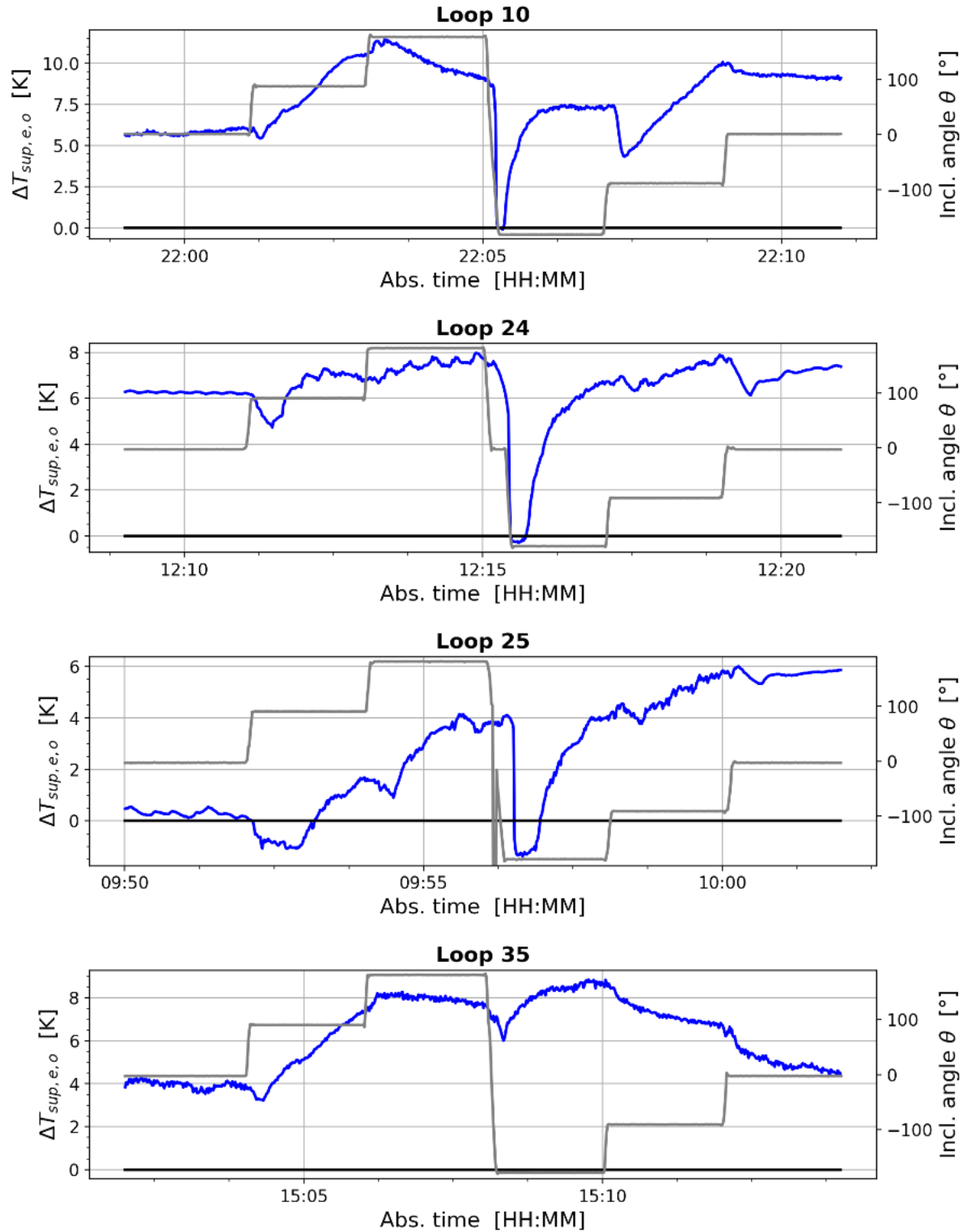


Figure 68: Evaporator outlet superheat for 6-angle testing in air-to-air configuration.

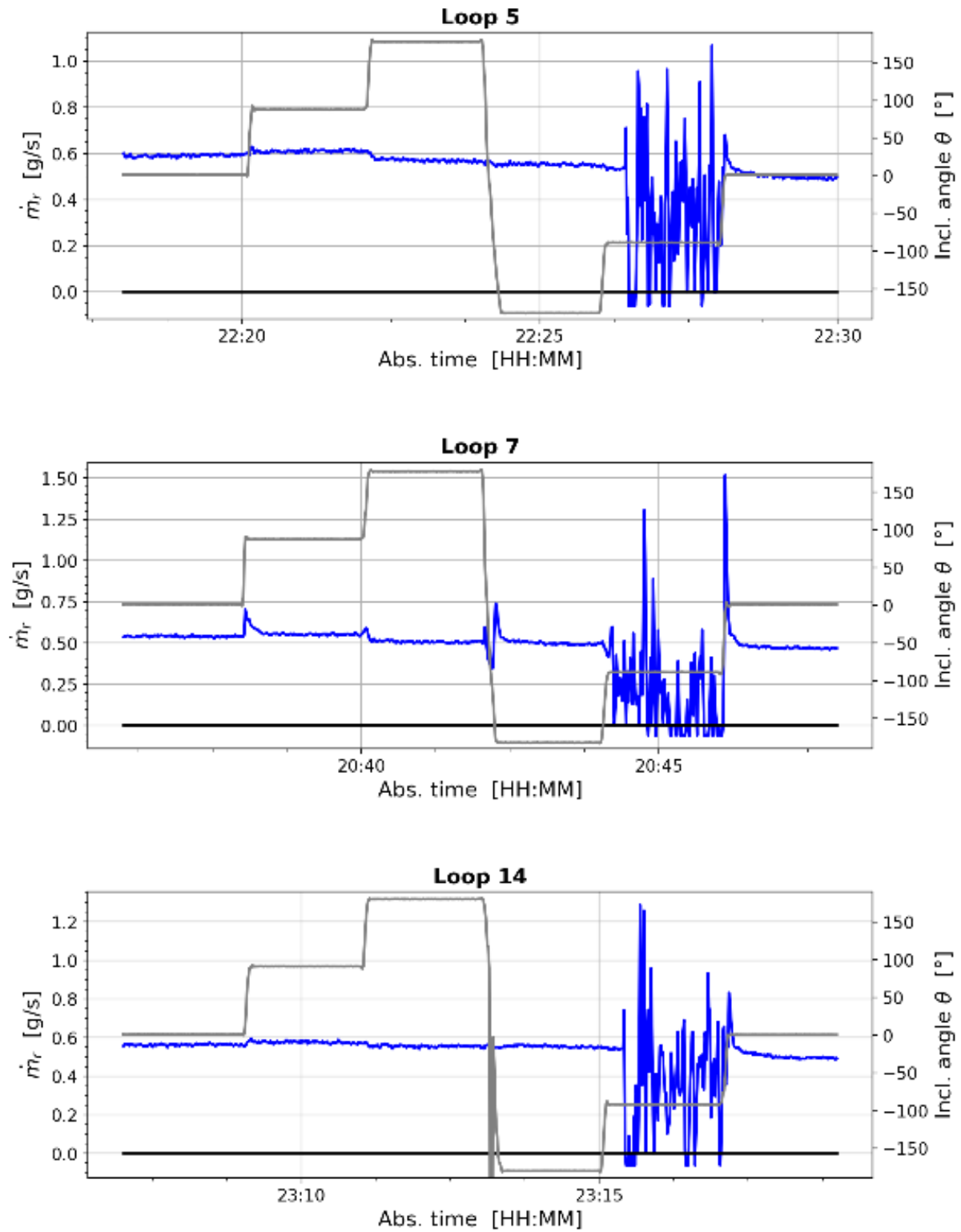


Figure 69: Liquid line mass flow rate with oscillations due to vapor bubbles travelling upwards.

5.5 High frequency orientation changes – parabolic flight simulations

Test stand configuration 3 (fin-tube evaporator, fin-tube condenser), scroll and linear compressor, R134a and R1234ze(E). Frequency of inclination changes: Approximately 3 per minute.

Overview

The idea of thermal gravitational scaling for two-phase system design was relatively popular during the 1990s but the research faded in the 2000s and even more in the 2010s. Still, the concept triggered questions, given inclinable test stand and parabolic flight testing opportunities: Can the response of a vapor compression cycle during parabolic flights be simulated in ground-based inclination testing? Can inclination testing outline a worst-case response of the cycle to the absence of gravity? These questions cannot be answered without experiments. Therefore, a search for an appropriate inclination procedure began. The timing of the inclination pattern should resemble the timing of microgravity and hyper gravity during parabolic flights. The question is then, what inclination angles should simulate normal, hyper and microgravity? Guiding ideas were:

- Normal gravity during the flights (cruise) would be best simulated with the test rig in the horizontal position, since the gravity vector is then equivalent for both situations.
- The inclination pattern is more useful if it provides an upper bound on the results from the parabolic flights. Therefore, inclination changes should be significant.
- Hyper and microgravity should be simulated by angles with a 180° offset.

Based on this reasoning, cruise flight was approximated with 0°, hyper gravity with +90° and microgravity with -90°. To reduce the testing time, the flight simulation was limited to 3 parabolas, resulting in the following timing:

- 20s at +90° (“hyper gravity”)
- 20s at -90° (“microgravity”)
- 40s at +90° (“hyper gravity”)
- 20s at -90° (“microgravity”)

- 40s at +90° (“hyper gravity”)
- 20s at -90° (“microgravity”)
- 20s at +90° (“hyper gravity”)

Figure 70 shows an overlay plot of measured gravity and angle for a set of parabolas (green) and one set of parabola simulations (blue). For a perfect match, the +90° times should have been slightly longer.

Testing was conducted at varying operating conditions with R134a (12 samples) and R1234ze(E) (13 samples). The results are also described in Brendel et al. (2021d).

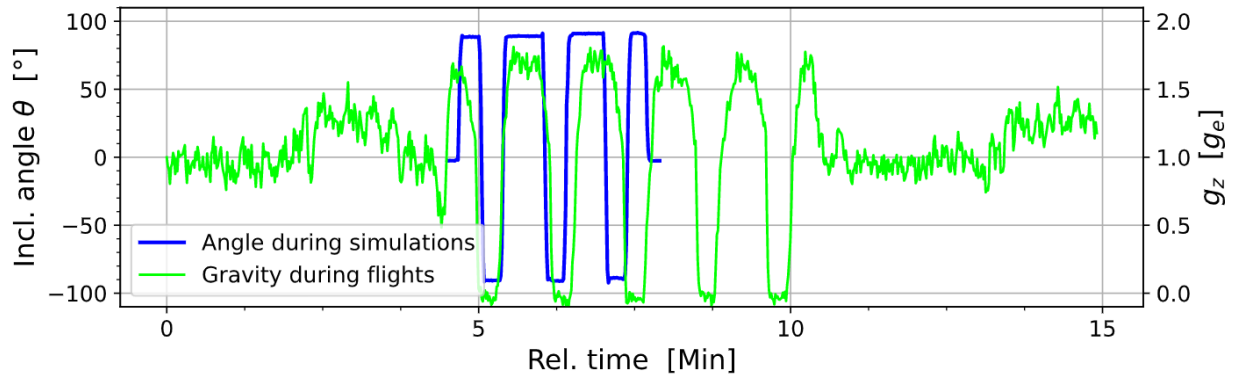


Figure 70: Gravity changes during parabolic flight and angle changes for parabolic flight simulation.

Results

The final goal was to compare the data from simulations against data from parabolic flights. However, the data was first analyzed for trends and similarities between the two refrigerants. During the analysis, a two-phase Weber number was found to correlate the instability results better than the mass flux. The particular Weber number (We_4 according to Brendel et al. (2021a)) is defined as

$$We_4 = \frac{G^2 D}{\rho_x \sigma}. \quad (20)$$

Brendel et al. (2021d) explains in more detail why the Weber number was superior over the mass flux for plotting of the results. The core reason is the inclusion of information about the mass flux but also about the refrigerant quality at the evaporator inlet into the measure. Figure 71 (left) shows the mmx/avg quantifier for the suction line mass flow rate calculated for all test runs and plotted as a function of We_4 . The instabilities of R134a and R1234ze(E) fell on one clearly

defined trend for the mass flow rate. However, when plotting the mmx quantifier for the evaporation temperature Figure 71 (middle), R1234ze(E) reached higher values for low Weber numbers. The evaporation temperature fluctuated in a band of up to 6.5 K for R1234ze(E), while R134a fluctuated within a band of at most 4 K. Figure 71 (right) shows the same quantifier applied to the condensation temperature. The decreasing trends did not apply for the condensation temperature. Instead, the mmx quantifier was almost constant over the complete range of Weber numbers.

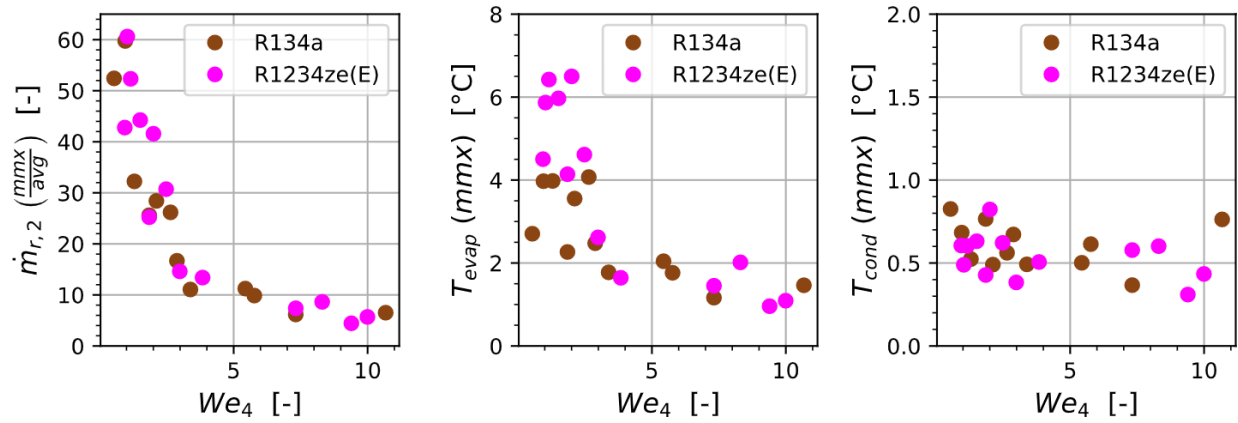


Figure 71: mmx/avg and mmx for flight simulations with R134a and R1234ze(E). Adapted from Brendel et al. (2021d).

5.6 Summary

Steady-state testing showed mass flow rate oscillations at certain angles and mass fluxes. Additionally, a linearly increasing MDV of the mass flow rate was found for increasing mass fluxes while the IIR was approximately constant. This was distinctly different for both intermediate and high frequency inclination testing, where several instability quantifiers showed decreasing trends of the IIR for increasing mass fluxes. However, this observation was not applicable to all measurements. For example, variations of the condensation temperature were independent of the mass flux. 6-angle testing was the only procedure tested across two different system configurations. A notable trend was found for the IIR of the heat source heat transfer rate as a function of the mass flux. The impact of the coil geometry of the different heat exchangers could not be singled out. Conclusions of this chapter can be summarized as follows:

Steady-state testing

- 1) When a vapor compression cycle has time to settle to steady-state in various orientations with constant control parameters, most measurements show sinusoidal responses as a function of the inclination angle (Brendel et al., 2022b).*
- 2) Suction line mass flow rate oscillations occur at certain angles as a function of the operating conditions (Brendel et al., 2022b). These oscillations do not propagate into the liquid line mass flow rate.*
- 3) The absolute deviations of the steady-state mass flow rates for any non-horizontal orientation from the mass flow rate in the horizontal position increase for larger mass flow rates but the relative deviations are constant (Brendel et al., 2022b).*

6-angle testing

- 4) The inclination impact ratio of the heat transfer rate (heat source side) decreased continuously for higher mass flow rates across two cycle configurations by approximately one order of magnitude (Brendel et al., 2021e). The IIR leveled out for mass fluxes $>40\text{kg}/(\text{m}^2\cdot\text{s})$.*
- 5) The inclination impact ratio correlates less clearly for other measurements.*
- 6) The inclination impact ratio is significantly higher for 6-angle procedures that either started with two-phase refrigerant in the liquid line or lost superheat during the procedure (Brendel et al., 2022c).*
- 7) The duration of compressor flooding during a 6-angle procedure increased with the system charge level at otherwise constant operating conditions for the cycle in the liquid-to-liquid configuration (Brendel et al., 2022c).*
- 8) The air-to-air configuration led to liquid flooding in the case of low initial superheat but not for high charge levels (section 5.4.4).*
- 9) Vapor was able to escape the condenser and enter the liquid line at an inclination of -90° in the air-to-air configuration.*

Flight simulations

- 10) An inclination procedure was proposed to mimic gravity perturbations of parabolic flights.*
- 11) The mass flow rate instabilities quantified by the mmx/avg measure correlated with the mass flux in trend and magnitude for both R134a and R1234ze(E) (Brendel et al., 2021d).*
- 12) The evaporation temperature instabilities of R134a correlated with the mass flux like the instabilities of R1234ze(E) in trend but not in magnitude (Brendel et al., 2021d).*

- 13) Instabilities measured during ground-based testing correlated more clearly with a two-phase Weber number evaluated at the evaporator inlet than with the mass flux. The Weber number was superior because it combines information not only about the mass flux but also the flow quality (Brendel et al., 2021d).*
- 14) The condensation temperature instability was constant throughout a range of mass fluxes or Weber numbers (Brendel et al., 2021d).*

6. IMPACT OF HYPER AND MICROGRAVITY

Test stand configuration 3 (fin-tube evaporator, fin-tube condenser), scroll compressor, R134a.

6.1 Motivation

While inclination testing was said to increase the confidence into space-bound vapor compression cycles, it did not count as “testing in a relevant environment”, according to definitions for TRL by NASA (2021). Opportunities for testing in a relevant environment are drop towers, parabolic flights, suborbital and orbital flights. In this project, parabolic flights were chosen for microgravity testing. Drop towers were quickly eliminated for the reason of too short testing times. Experiments on an orbital spacecraft were thought to have an unacceptable lead time.

The decision for parabolic flights instead of suborbital flights took a long time. Several meetings took place with the industry partner and NASA. A frequently used slide in this time (Spring 2020) is shown in Figure 72. Despite being old, the slide is mostly correct and worthwhile to discuss yet another time:

- Parabolic flights provide only ≈ 20 seconds of microgravity. The effects of microgravity to a large thermal system cannot be fully understood in this short time. Parabolic flight testing was therefore classified as a “robustness test” more than a true microgravity test, especially because many parabolas are flown consecutively. If the cycle operated seamlessly through alternating gravity (and varying orientations on the ground), it would most likely also operate seamlessly in microgravity. Moreover, costs were estimated to be \$30,000 per flight (more likely to be \$40,000), which is much less than commercial options for suborbital flights.
- Suborbital flights typically provide about 3 minutes of microgravity. For a small system, this could be enough to start-up the system and make meaningful observations. On the downside, the system must fit into a relatively small box and no operator is allowed to manually intervene in the operation. Especially considering heat sources and sinks, the space constraints are severe. Lastly, costs are well above \$140,000 (depending on the size of the box) for a one-shot experiment.


The cost of \$80k and \$65-\$90k for the payloads indicated in Figure 72 were estimated including the cost for a one-year graduate student research assistantship and should have been higher given the needed equipment and technician labor hours for a completely new test rig.

Overall, the parabolic flights were clearly favored for the following reasons:

- Multiple experiments can be flown
- Operators can be on board
- Lower costs for more testing time
- Hyper and reduced gravity testing as side effects from microgravity testing
- “Start-simple”

➤


Summary μg testing opportunities




- **Parabolic flight**
 - **Robustness test**
 - Evaluate gravity independence criteria at different flow rates
 - Can test start-up and operation of complete refrigerated cabinet
 - 20s not a true zero-G
 - Two flight campaigns
- **Suborbital flight**
 - **Zero-G start-up demonstration**
 - About 3 minutes of zero-G
 - Location of liquid after launch difficult to determine
 - Very tight volume and power constraints
 - One shot experiment

Costs are rough approximations!

Tot. ≈\$140,000




≈\$60k
(two flights)




≈\$80k
(reduced scale)

Tot. ≈\$260,000



≈\$170k
(double locker,
-50k for single locker)



≈\$65 – 90k
(bread-board)

Costs are rough approximations!

Figure 72: Discussion slide about the best microgravity testing opportunity from May 2020.

6.2 Flight preparations

The opportunity for parabolic flights was confirmed in July 2020. Over the fall of 2020, it was decided to use the inclinable test rig as one experiment on the parabolic flights, because it seemed valuable to have inclination and parabolic flight data from the same test rig. The test rig was flown in configuration 3 (fin-tube heat exchangers) without modifications to the refrigeration

133

cycle as compared to the ground-based testing with configuration 3. The only modification was that the water cooling for the compressor, which was previously supplied by building water, was changed to be a closed loop with a fin-tube heat exchanger cooling the water against the ambient air. This raised the compressor cooling water temperature from approximately 15 °C using the building water loop to 25 °C using the closed water loop. After the parabolic flights, all ground-based testing using the scroll compressor was performed with the closed water loop.

As per the ZERO-G requirements, several components had to be attached more rigidly. A polycarbonate enclosure was added to the refrigeration cycle and a metal enclosure to the water loop. Padding was added to the edges of the outer frame. Preparations of the test stand for the flights lasted into April 2021 and the parabolic flight tests were conducted from May 4th till 7th 2021. Figure 73 shows the inclinable test stand bolted to the fuselage of the airplane.

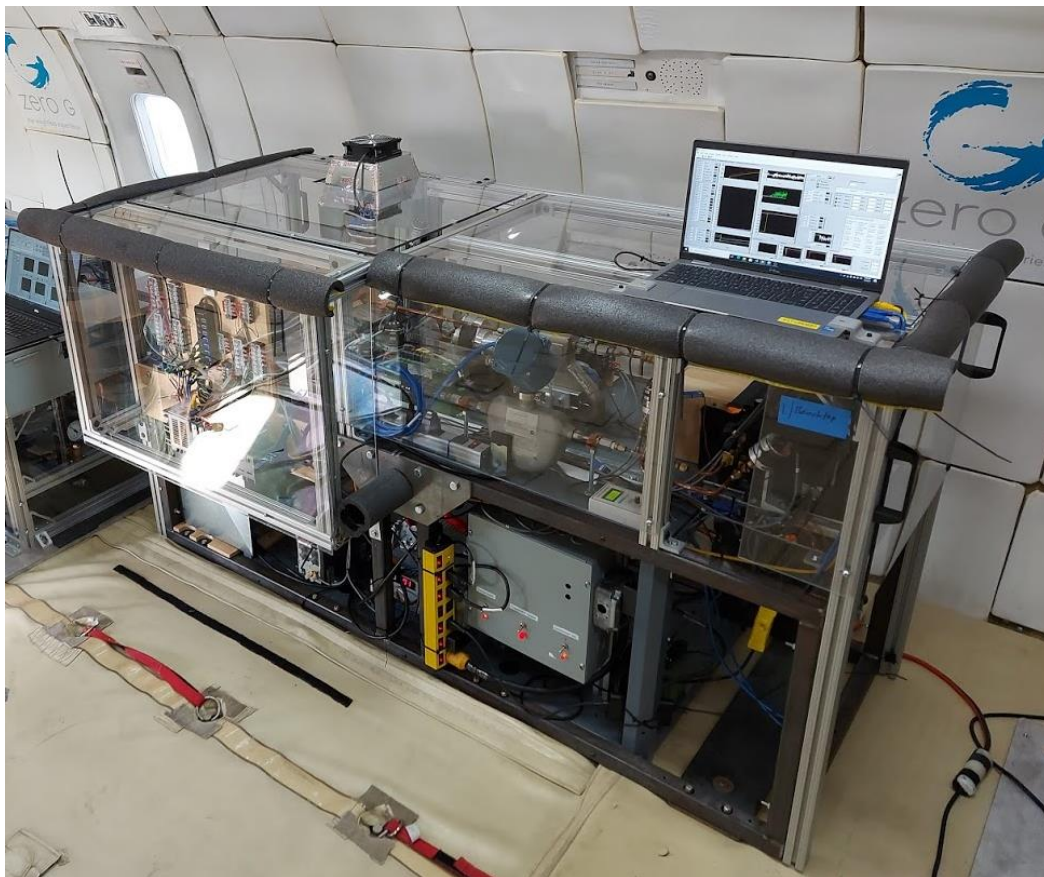


Figure 73: Inclinable test stand installed on the parabolic flight aircraft (Brendel et al., 2022e).

6.3 Quantity and quality of data

122 parabolas were flown over four days. 114 were microgravity parabolas, four each were Lunar and Martian parabolas. Parabolas were flown in sets of 5 or 6 consecutive parabolas and 6 sets were flown per day. The test stand operated throughout all 122 parabolas, but several difficulties were experienced rendering some sets of parabolas not useful for analysis. The most important problems were as follows:

- For parabola sets 1, 3, 4, 5 and 6, the data acquisition system malfunctioned and recorded all voltage and current signals with a strongly increased sampling time of 5 to 15 seconds. Temperature readings were still saved once every second.
- Data from an ambient pressure transducer was not saved. The ambient pressure transducer should have been used to correct readings from gauge type pressure transducers. This was still possible using an ambient pressure estimate of 85 kPa during the flights based on the comparison of absolute and gauge type in-line refrigerant pressure transducers.
- The operator accidentally turned off the compressor during set 17 by hitting one of the red switches visible in Figure 73. Data from set 17 cannot be used but stable operation was reached again by the start of set 18.
- During set 14 and 21, the operator decided to change control parameters during a set of parabolas in order to reach a steady-state by the time of the next set of parabolas. These sets are therefore not only affected by the parabolas but also by the new control parameters.
- Post-processing showed a dependence of the electric heater in the closed evaporator air loop on the gravity level. Figure 74 shows how the power changed by more than 10 W with the gravity level. A possible explanation is an unsteady voltage supply by the airplane which throttles and accelerates the engines as it performs flight maneuvers. It is unlikely that the changes in the heater power propagated strongly into the refrigeration side measurements.

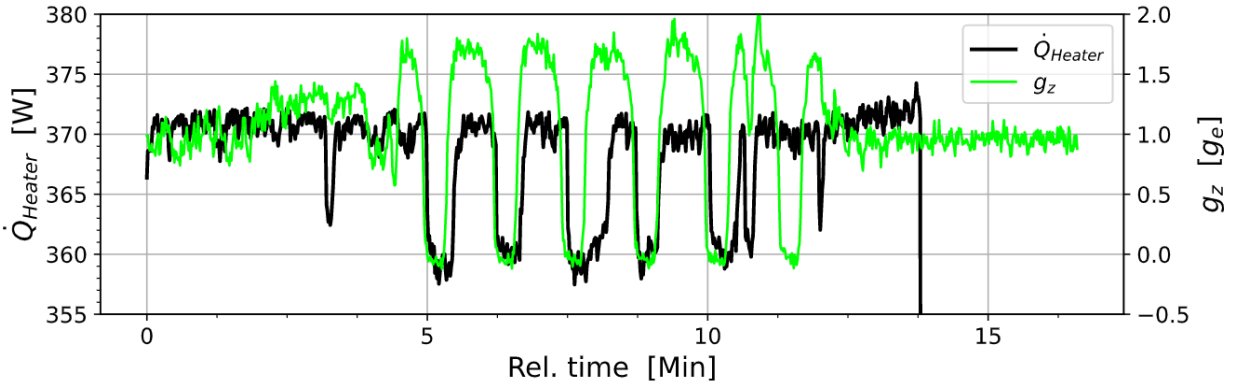


Figure 74: Measurement of heater power and gravity level during set 18.

Table 13 provides an overview of all sets of parabolas. The “Code” column shows a sequence of letters and numbers describing each set of parabolas:

- Codes starting with “Z” indicate that all parabolas were flown as microgravity parabolas. “M” stands for mixed type of parabolas. The two “M” sets consisted of 2 Martian, 2 Lunar and 1 Zero-G parabola.
- A 1 was assigned as the first number if the DAQ functioned properly, no control parameters were changed during the set of parabolas and the compressor was not accidentally turned off.
- A 1 was assigned as the second number if the evaporator outlet superheat was >1 K throughout the set of parabolas.
- The last number is set to 1 if the vapor compression cycle was evaluated to have operated at steady-state. Due to the quick testing and unstable environment the criterion was not strict: A steady-state was defined by the mean evaporation temperature of 12 seconds before the first parabolas and 12 seconds after the last parabola being within 2 Kelvin.

Table 13: Overview of parabolas flown with inclinable test stand.

Day/Date	Set	# of Par.	Code	Comment
Day 1, May 4 th , 2021	1	5	Z0-0-1	Mild DAQ problem
	2	5	Z1-1-1	
	3	5	Z0-1-1	Severe DAQ problem
	4	5	Z0-1-0	Severe DAQ problem; unusually long time between 3 rd and 4 th parabola
	5	5	Z0-1-1	Severe DAQ problem
	6	5	Z0-1-1	Severe DAQ problem
Day 2, May 5 th , 2021	7	5	Z1-1-0	
	8	5	Z1-1-1	
	9	5	Z1-1-1	
	10	5	Z1-1-1	
	11	5	Z1-1-1	
	12	5	Z1-1-1	
Day 3, May 6 th , 2021	13	5	M1-1-1	
	14	5	Z0-1-0	Changed control inputs during parabolas
	15	6	Z1-1-1	
	16	5	Z1-1-1	
	17	5	Z0-0-0	Compressor turned off during parabolas
	18	6	Z1-1-1	
Day 4, May 7 th , 2021	19	5	M1-0-1	
	20	5	Z1-1-1	
	21	5	Z0-0-0	Changed control inputs during parabolas
	22	5	Z1-1-1	
	23	5	Z1-1-1	
	24	5	Z1-1-1	

6.4 Repeatability of parabolas

Many experiments typically conducted on parabolic flights are of short duration. The operators wait until weightlessness begins and then execute their experiment within the 15 to 20 seconds of microgravity. In contrast, the inclinable test stand ran continuously through hyper and microgravity flight maneuvers as well as during cruise in between sets of parabolas. For a fair comparison between sets of parabolas, it is therefore important that the parabolic flight maneuvers are flown in a repeatable manner regarding the gravity levels and timing. Figure 75 overlays gravity measurements for four sets of parabolas, which are aligned by the first measurement of $g_z < 0.1 g_e$. Very good agreement is observed for the first two parabolas. For parabolas three, four and five the misalignment increases. The disagreement is deemed acceptable for a comparison

of cycle responses among different sets of parabolas. Observed differences between sets of the measurements were never particular to the last 2 or 3 parabolas of a set.

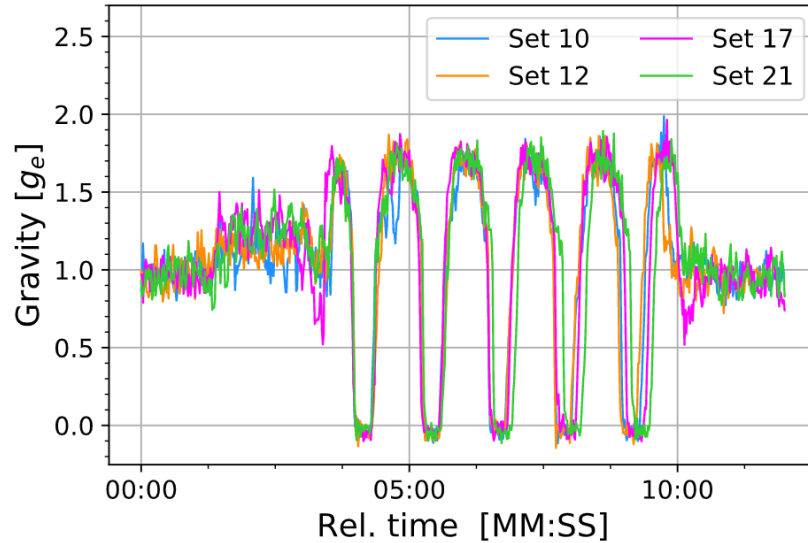


Figure 75: Gravity measurements through four sets of parabolic flights (Brendel et al., 2022d).

6.5 Transient data

The open literature does not provide transient data of a vapor compression cycle operating in hyper or microgravity or entering either of the two from normal gravity. Figure 76 and Figure 77 show such data for set 10 as a low mass flow rate sample and set 18 as a high mass flow rate sample. Plotted variables are:

- evaporation temperature measured and condensation temperature calculated from discharge pressure
- evaporator inlet and compressor discharge pressure
- liquid and suction line mass flow rate
- superheat and subcooling (measured at the heat exchanger outlets)

A low and high mass flow rate sample are compared because the cycle response to parabolas was expected to be mostly dependent on the mass flow rate. This was not clearly observed in post-processing. Still, the data is shown here to give the readers an example of reaction times and responses of the cycle. The y-scales for a particular variable use the same range for the

low and high mass flow rate sets for an easier comparison. The following observations can be made when looking at the data in Figure 76 and Figure 77:

- Temperatures and pressures responded very quickly to microgravity
- Microgravity perturbed measurements more than hyper gravity
- Temperatures varied by 1 to 2 K and pressures by 10 to 20 kPa due to the parabolic flight maneuvers
- The suction line mass flow rate ($\dot{m}_{r,2}$) was perturbed more than the liquid line mass flow rate (\dot{m}_r) due to parabolic flight maneuvers
- The suction line mass flow rate in set 10 responded to the parabolas with quick oscillations but the suction line mass flow rate in set 18 responded with a short spike followed by a large drop.

6.6 Thermodynamic stability

The previous section showed transient responses of the cycle to parabolic flight maneuvers for sets 10 and 18. Through data processing, the results of multiple sets of parabolas were generalized. A focal point was the stability of the cycle through sets of parabolas. The mmx, 80%, mmx/avg or 80%/avg measures are simple instability quantifiers and can be calculated for any transient dataset as explained in section 2.7.1. These quantifiers were calculated for all sets that had clean data acquisition, contained only zero-G parabolas and were at steady-state (sets 2,8-12,15,16,18,20,22-24). If the cycle is not approximately at steady-state, the mmx may be more determined by the transient change than by the responses of the cycle to hyper and microgravity, therefore, transient data was not included in this study. Figure 78 shows the average and spread of the instability quantifier for the

- evaporation temperature (mmx and 80% in K, left-hand side y-axis)
- evaporation outlet superheat (mmx and 80% in K, left-hand side y-axis)
- evaporation pressure (mmx/avg and 80%/avg in %, right-hand side y-axis)
- suction line mass flow rate (mmx/avg and 80%/avg in %, right-hand side y-axis)
- refrigerant side cooling capacity (mmx/avg and 80%/avg in %, right-hand side y-axis)

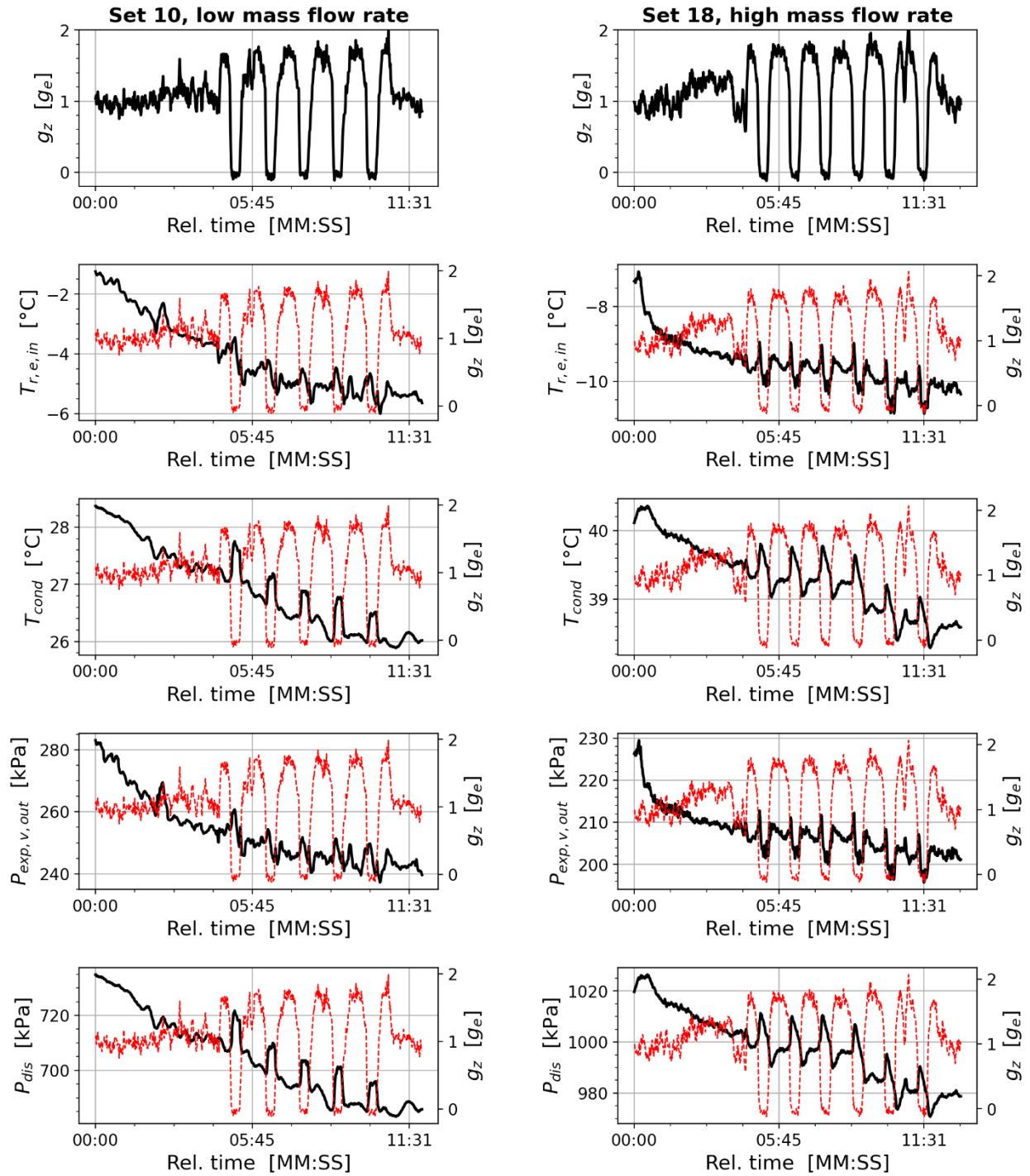


Figure 76: Transient temperature and pressure measurements from parabolic flights (sets 10 and 18).

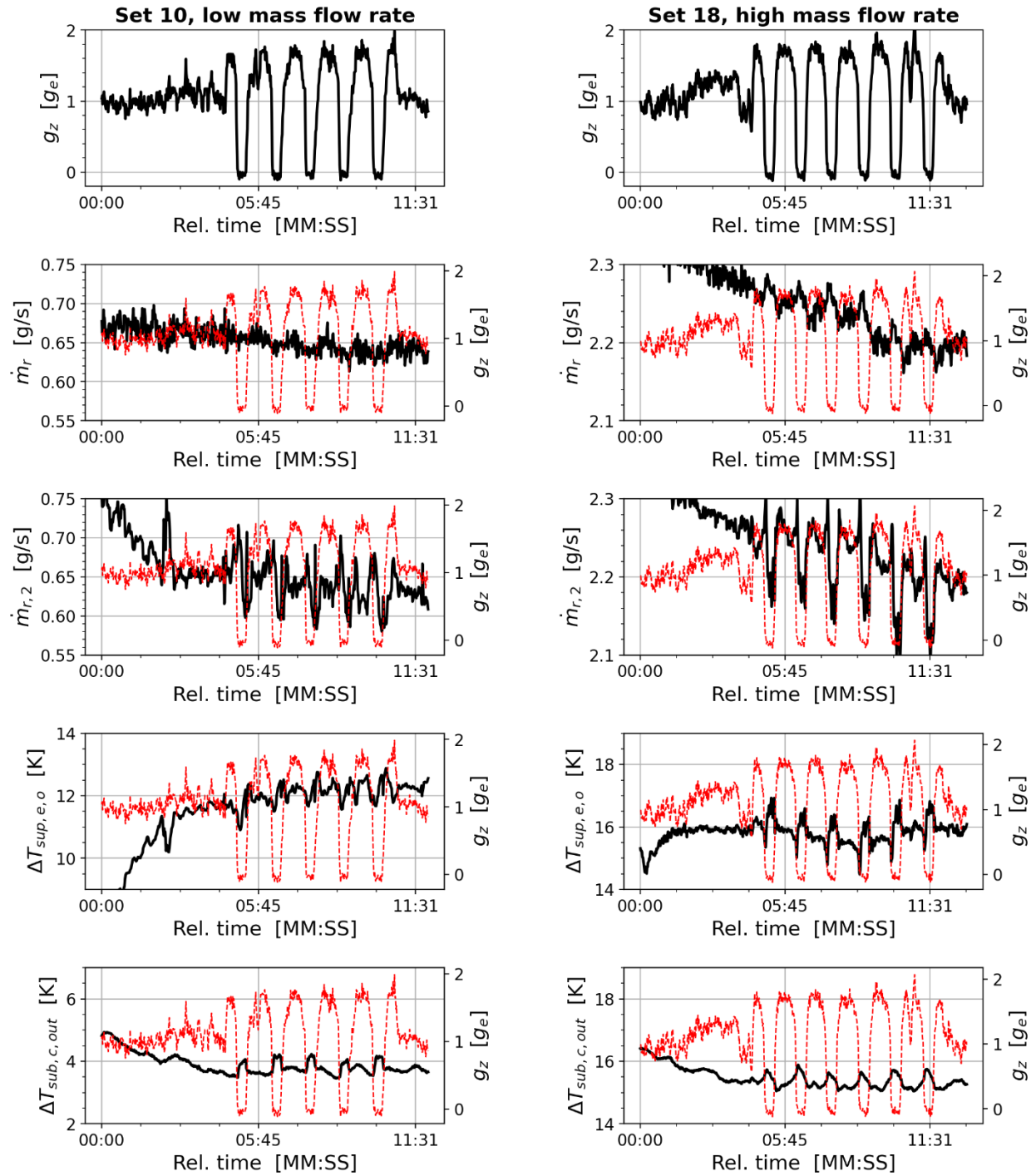


Figure 77: Transient mass flow rate, superheat and subcooling data from parabolic flights (sets 10 and 18).

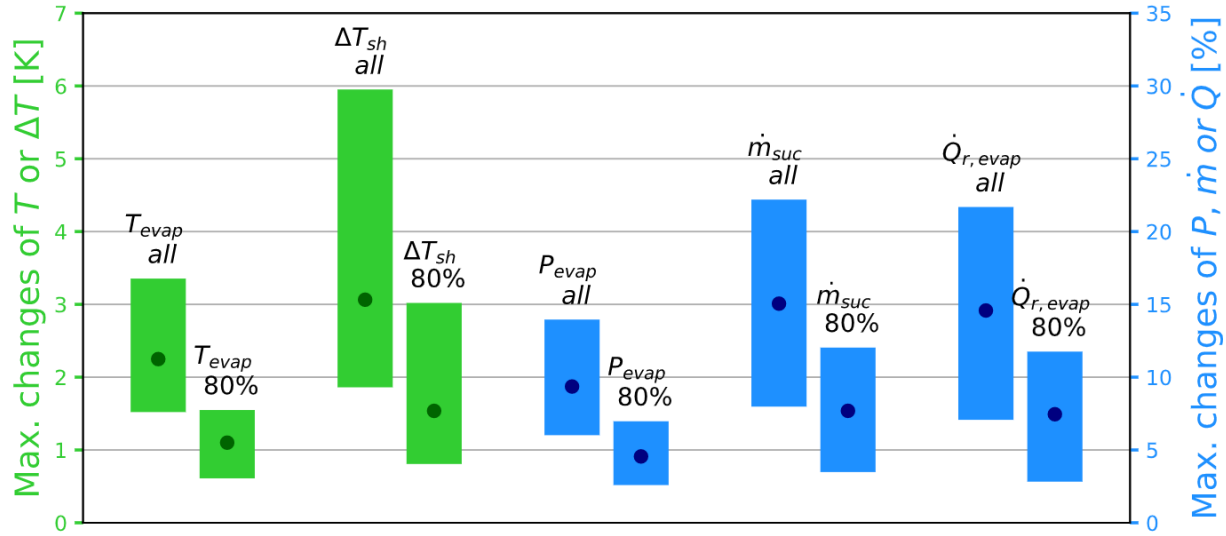


Figure 78: Maximum, minimum and average mmx or mmx/avg value for sets 2, 8-12, 15, 16, 18, 20, 22-24 for all or only the tightest 80% of the data. Adapted from Brendel et al. (2022e).

Figure 78 can be interpreted as follows: “Throughout all considered sets, the evaporation temperature never fluctuated more than within a band of 3.4 K (top of bar). The smallest band of fluctuations was 1.5 K (bottom of bar). The average bandwidth of fluctuations throughout the considered sets was 2.2 K (dark dot). When considering only the 80% of the transient data which give the smallest band of fluctuations, those values decrease to 1.5 K maximum fluctuation bandwidth, 0.6 K minimum fluctuation bandwidth and 1.1 on average.” Green bars are in units of Kelvin (mmx and 80%) and blue bars are in units of % (mmx/avg and 80%/avg). The high-pressure side counterparts are not shown here because they always had a lower instability such that the low-pressure side information represents an upper bound.

6.7 Evaporator outlet superheat

A major concern for vapor compression cycles in microgravity applications is compressor flooding with liquid refrigerant. This is important because the compressor is the only moving part in the system and depending on the compressor type, even small amounts of liquid pose a risk of damage to the compressor.

The code in Table 13 shows for each set of parabolas whether the superheat was above 1 K at all times. The only sets for which this was not the case were 1, 17, 19 and 21. In set 17, the

compressor was turned off which caused the superheat to diminish to 0 K. In set 19, there was no superheat before the parabolas, so the superheat was not lost as a result of gravity perturbations. In set 21, control parameters were changed which caused the superheat to reach 0.9 K for a short time, but again not due to gravity perturbations. Set 1 is therefore the only set in which parabolas were the cause for a loss of superheat. Transient data of the superheat for this set is shown in Figure 79 (left). The superheat started at 1.4 K, rose to 3 K but fell again to 1.5 K shortly before the beginning of the first hyper gravity condition. The superheat then fell to 0 K as the gravity fell to 0 g_e . The superheat recovered in the next hyper gravity period but vanished again in microgravity. From there on, the superheat increased continuously and reached more than 4 K at the end of the parabola set.

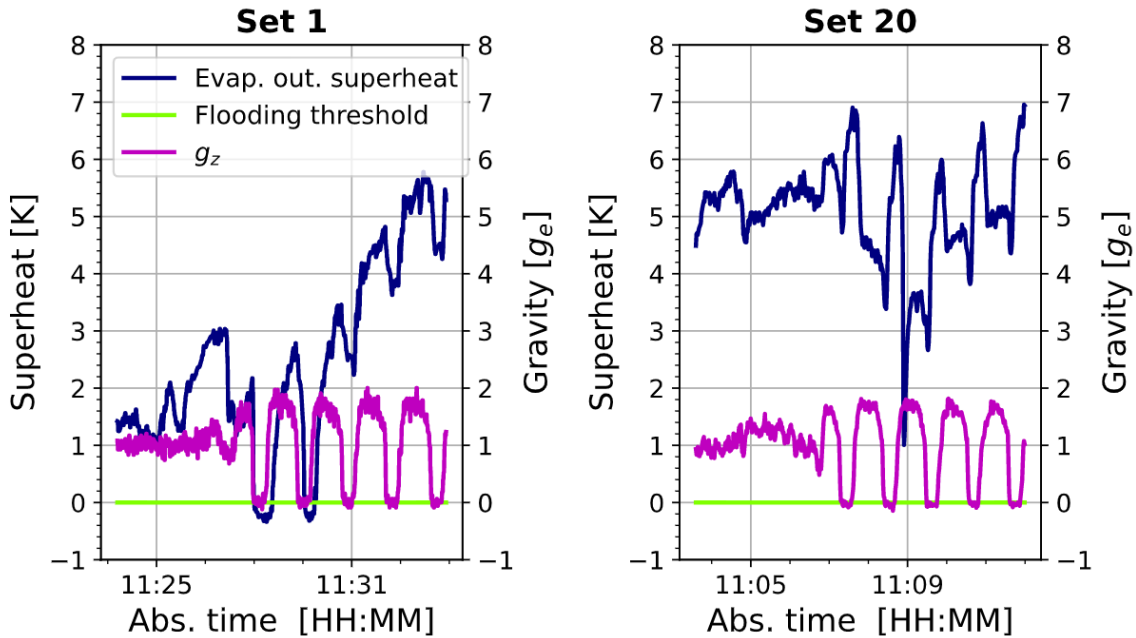


Figure 79: Superheat at the evaporator outlet in set 1 and set 20. Set 1 as shown in Brendel et al. (2022e).

A low superheat of 1 K means that the transition from a two-phase to single-phase flow occurs close to the evaporator outlet. Due to the proximity to the outlet, any gravity perturbation has a high chance to cause a measurable liquid flooding. However, this is not necessarily a large liquid slug but could also be a slight mist of liquid droplets in the refrigerant vapor. The video camera installed at the evaporator outlet could not capture the flow regime for this set of parabolas

so the flow regime is unknown. The quick recovery of superheat starting after the second parabola makes it unlikely that the liquid phase during flooding was significant.

With respect to superheat, set 20 is noteworthy, too. Figure 79 shows how the superheat was around 5 K until after parabola 2, where the superheat suddenly dropped to 1 K. The reason for this significant drop is unclear. Since the superheat rose to 3 K immediately afterwards, it may even be measurement noise. This set also caused the high upper limit of 5.95 K in Figure 78 for $\Delta T_{sh,all}$. Except for sets 1 and 20, the superheat changes were not concerning and typically closely related to the changes in the evaporation temperature.

6.8 Flow visualizations

The refrigerant circuit was built with five approximately 10 cm long transparent tube sections, which were observed with three cameras. One transparent tube section was installed between the expansion valve and the evaporator inlet. It was installed inside the evaporator box with a light source and a sheet of paper acting as a light diffuser on one side. A camera provided recordings from the outside of the box through a transparent part of the box. Recording was challenging because the sight tube easily accumulated condensate or ice. A few clear videos were still obtained and allow a comparison of normal gravity and microgravity flow patterns at the inlet to the evaporator.

Two operating conditions were selected for comparison, one with a high mass flow rate, the other with a low mass flow rate. The evaporation temperatures were 7 °C for the low mass flow rate and -10 °C for the high mass flow rate sample. The inlet qualities were calculated to be 0.11 and 0.22, respectively, assuming an isenthalpic expansion process. A slip flow model for two-phase flow was used to estimate the void fraction using a correlation for the slip ratio (Zivi, 1964) as follows:

$$\alpha = \frac{1}{1 + S \frac{\rho_g}{\rho_f} \frac{1-x}{x}} \quad \text{with } S = \left(\frac{\rho_f}{\rho_g} \right)^{\frac{1}{3}}. \quad (21)$$

Figure 80 shows images from video footage for both samples as well as simplified sketches. The images were obtained with screenshots from the video and simple post-processing in MS Word. Three screenshots are shown next to each other from different timestamps to represent the

different observations at one flow condition. Row A shows two-phase flow with a low mass flow rate during cruise and row B shows the flow shortly after the onset of microgravity. A calm, stratified flow transitioned to slug flow due to the absence of gravity. The vapor slugs in microgravity did not hug the top of the tube but were mostly centered. A slight buoyancy was possible from residual gravity forces. Tiny vapor bubbles were observed in the liquid phase and some small liquid droplets were observed in the vapor slugs. Rows C and D show these observations in simple schematics.

Rows E and F show images from video footage from the higher flow rate condition. During cruise, a stratified flow regime was observed with a wavy surface, indicating a higher ratio of vapor to liquid velocity than in row A. This flow regime transitioned to an annular flow in the absence of gravity, still with a wavy surface. Rows G and H show this again in a simplified schematic.

The transitions of flow regimes were distinct and typically completed in less than 3 second. Microgravity imposed a flow regime change that would not have been possible at any inclination angle on the inclinable test stand. The observation is solely qualitative, though, and cannot answer the quantitative impact of the flow regime change on the heat exchanger or cycle performance.

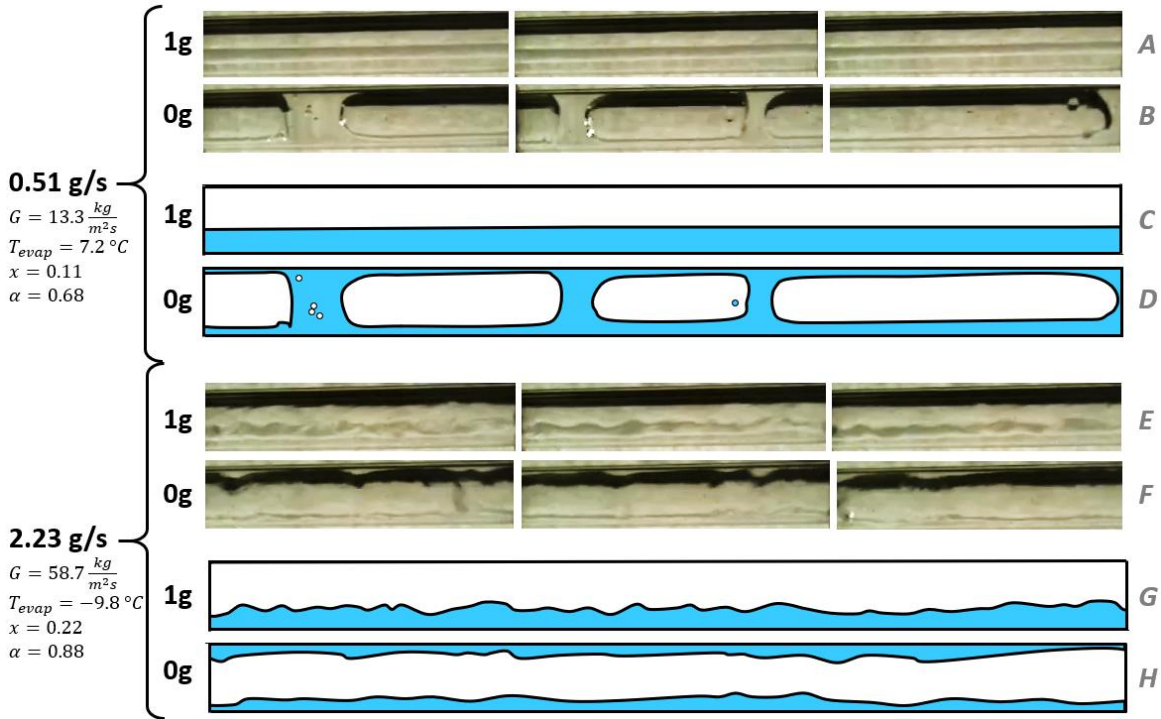


Figure 80: Flow visualizations from the parabolic flights during cruise and in microgravity (Brendel et al., 2022d).

6.9 Flow oscillations

Pressure drop or charge oscillations can occur in two-phase flow for different reasons. Some collected datasets showed flow oscillations to start due to microgravity. Flow oscillations can be mistaken for increased measurement noise if they have a high frequency. However, flow oscillations during the parabolic flights were measured independently by multiple sensors:

- A thermocouple at the evaporator inlet
- A pressure transducer at the evaporator inlet
- A mass flow meter
- A density calculated by a pressure transducer and thermocouple at the compressor suction (≈ 7 m downstream of the evaporator inlet measurements).

Figure 81 shows all these measurements and the gravity level in one overlay plot. In the first minute shown, the measurements were mostly steady with the exception of noise. All measurements fell and recovered during the first hyper gravity section. At the onset of microgravity, pressure, temperature, density and mass flow rate spiked and then fell far below the initial value. The measurements started to oscillate until the airplane entered the next hyper gravity period which caused the oscillations to stop immediately.

The oscillations were in the range of ± 0.5 K for the saturation temperature or ± 4 kPa for the pressure. The mass flow rate oscillations were approximately ± 0.04 g/s. Since variations in this range would not negatively impact the operation of a vapor compression cycle, they can be classified as mild oscillations and are tolerable. However, it is unknown whether the oscillations would remain, increase or decrease in sustained microgravity. Similarly, the data does not allow prediction of the occurrence or magnitude of oscillation in a system of different size.

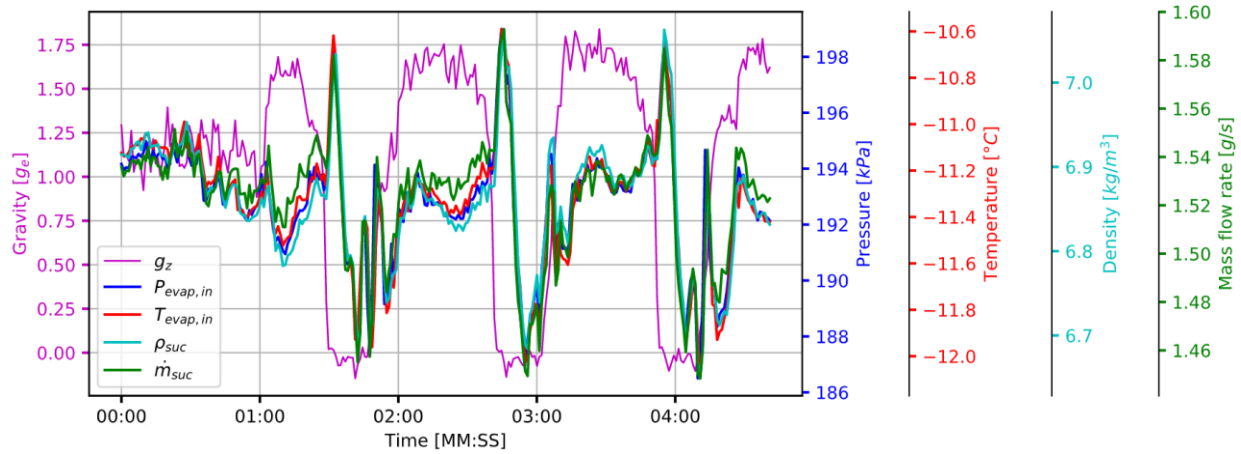


Figure 81: Oscillations in microgravity measured during set 8 (Brendel et al., 2022d).

6.10 Clustering cycle responses to microgravity

During post-processing, the cycle responses to microgravity for different sets of parabolas were compared. Figure 77 showed already that the suction line mass flow rate responded differently to microgravity in set 10 than in set 18. This was also observed for the refrigerant side cooling capacity, which is dictated by the suction line mass flow rate. Through a comparison of all data sets, four different response patterns were identified. These are shown with one example each in Figure 82 and can be described as follows:

- A. The cooling capacity fluctuates with short spikes. The capacity is a little bit higher in microgravity than in hyper gravity.
- B. The cooling capacity spikes and then falls below the initial value, sometimes with oscillations.
- C. The cooling capacity spikes but does not fall significantly below the initial value.
- D. The cooling capacity does not spike but falls below the initial value.

It was possible to assign the data sets 2, 7-16, 18, 20-24 (all except 3-6 due problems with the DAQ, 1 and 19 due to a lack of superheat and 17 because of the compressor shut down) to one of the four groups based on their responses to microgravity. Table 14 shows the assignment of parabola sets into the groups.

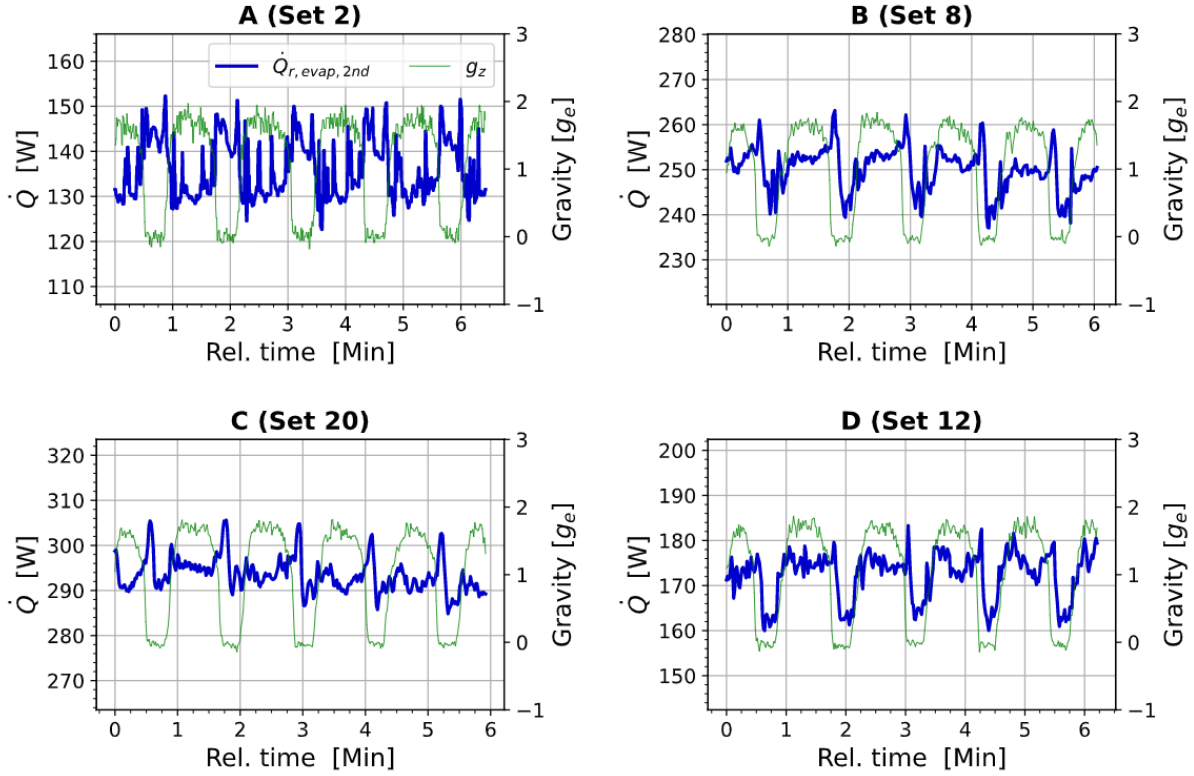


Figure 82: Patterns of cooling capacity response to microgravity (Brendel et al., 2022d).

A mechanistic explanation for the different responses would be desirable, but is not readily available. A correlation is offered through the use of Figure 83, though. The sets are plotted by their average mass flow rate and superheat. In this figure, the four groups cover different areas of the chart. Group A occurs for low mass flow rates and may be a cause of low inertia forces and dominant gravity or surface tension forces. For higher mass flow rates and a low superheat level, group C is more likely while at higher superheat levels, groups B and D occur. The superheat may well be decisive because it strongly influences the fraction of the heat exchanger that is used for two-phase heat transfer compared to the fraction used for single-phase heat transfer. Since only the two-phase fraction can be gravity sensitive, the superheat level may indeed play into the general response of the evaporator to varying gravity levels. However, an exact reasoning is missing.

There is an additional argument for the superheat to be influential regarding the cycle response. Unfortunately, it is again entirely empirical and also difficult to quantify. For completeness, the results are still presented here to emphasize the *possibility* that the superheat level plays a key role in the response of the cycle to gravity perturbations.

Table 14: Assignment of sets into groups (Brendel et al., 2022d).

Group	Sets	Confidence (0 or 1)
A	2	1
	10	1
	11	1
	14	1
	24	1
B	8	1
	9	1
	18	1
C	7	1
	20	1
	21	1
	22	0
	23	1
D	12	1
	15	1
	16	0

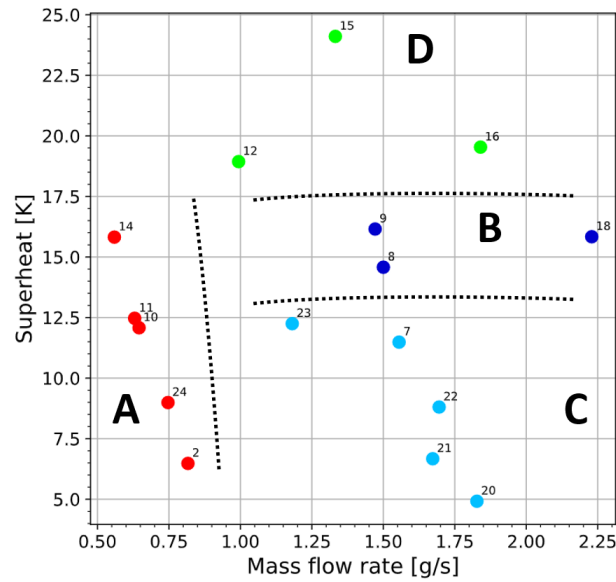


Figure 83: Plotting of operating conditions by superheat and mass flow rate (Brendel et al., 2022d).

When comparing the evaporation temperature at the onset of microgravity with the temperature measured at the end of the microgravity maneuver, one can find increases, decreases or equal temperatures. Observing only the two temperatures (just before start and at end of

microgravity), disregards any spikes occurring during microgravity. Figure 84 shows an example plot of measured evaporation temperatures and gravity levels. The change of the evaporation temperature $\Delta T_{r,e,in}$ during microgravity is indicated with a green arrow. It can be observed that in set 2, the evaporation temperature typically increased during zero-G. It slightly decreased in set 23 and strongly decreased in set 12.

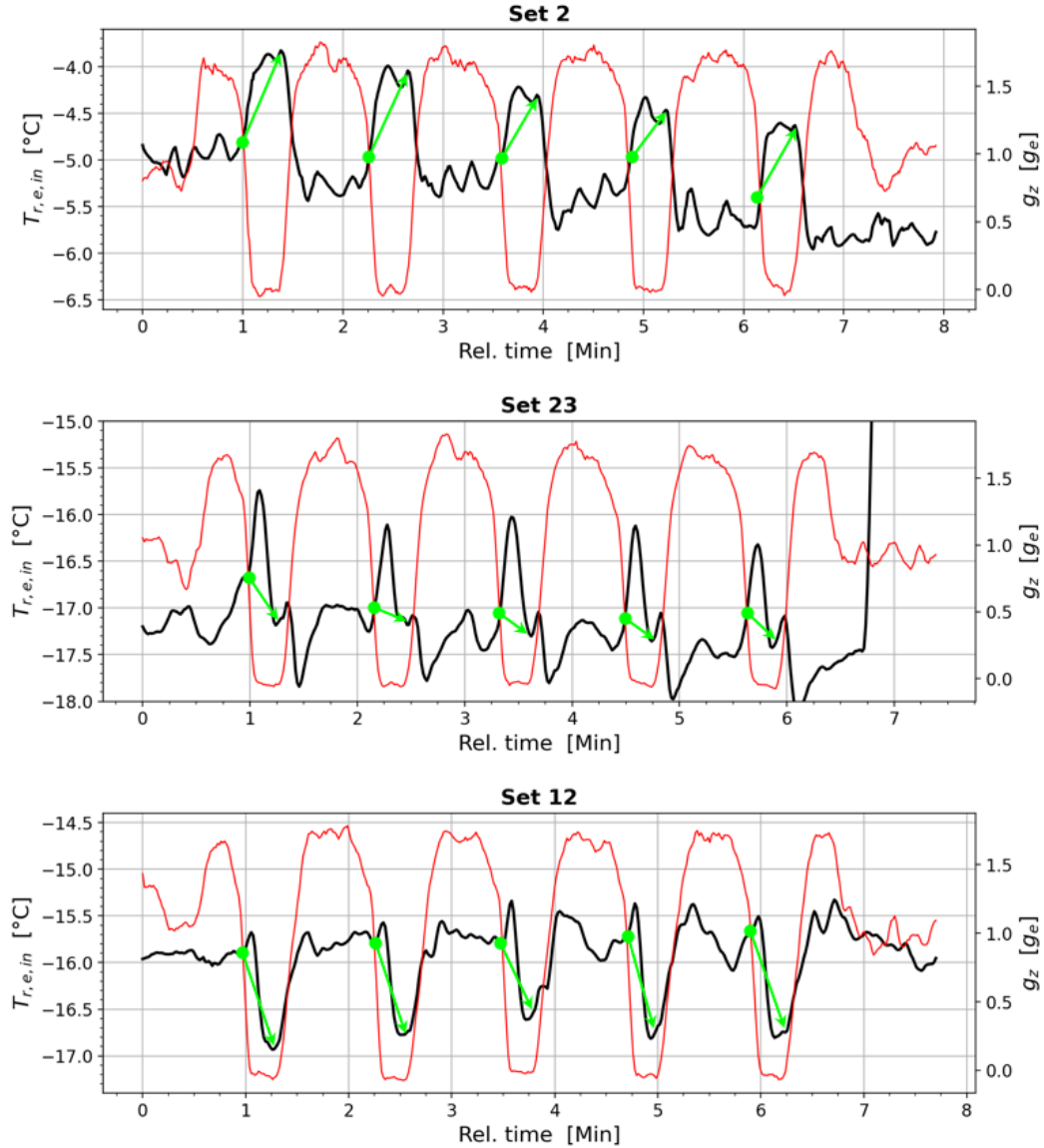


Figure 84: Evaporation temperature changes due to microgravity.

In a next step, the changes over the parabolas are summarized in one number. This is prone to human error because the change cannot be precisely measured. For the three sets in Figure 84, it was determined by visual inspection that the evaporation temperature changed on average by

+0.75 K for set 2, by -0.25 K for set 23 and by -1.25 K for set 12. A finer resolution than 0.25 K was not attempted. Analyzing all sets led to the results in Table 15. Sets that have a comment instead of a value were removed from this analysis.

Finally, the manually estimated changes in the evaporation temperature were plotted as a function of the average evaporator outlet superheat (averaged from 10 seconds before till 10 seconds after the last microgravity section). The results are shown in Figure 85. A linear trend from positive to negative changes of the evaporation temperature is visible from low to high superheat values. This is another indication that the superheat influences cycle responses. Changes in the evaporation temperature are an especially important parameter to predict, because those are coupled to the evaporation pressure, suction line mass flow rate and therefore cooling capacity.

Table 15: Evaporation temperature changes during microgravity.

Set	$\Delta T_{r,e,in}$ in K or comment	Set	$\Delta T_{r,e,in}$ in K or comment
1	1.25	13	Set with reduced gravity parabolas
2	0.75	14	Change of control parameters during set
3	1	15	-1.5
4	0.25	16	-1
5	-0.5	17	Compressor accidentally turned off
6	-0.5	18	-0.5
7	-0.25	19	Set with reduced gravity parabolas
8	-0.25	20	0
9	-0.25	21	Positive and negative changes, one large temperature drop.
10	-0.5	22	-0.25
11	-0.5	23	-0.25
12	-1.25	24	0.75

6.11 Increase of condensation pressure at the onset of microgravity

The previous section showed that the evaporation pressure (and the cooling capacity) would sometimes decrease, sometimes oscillate and other times stay almost the same. However, the condensation pressure showed a consistent increase at the onset of microgravity throughout all sets of parabolas. This was found for all datasets that had clean data acquisition and that resulted from flights experiencing microgravity (all except 3-6, 13, 17, 19). Changes in condensing pressure were difficult to compare because the changes were small and the initial pressures differed between sets. It is therefore helpful to normalize the discharge pressure. For each data set, the pressure at the time when $g = 0.5 g_e$ in a set of parabolas is used as the reference pressure of the set. Then

all datasets have a normalized pressure of 1 [-] directly before the onset of microgravity. This is shown in Figure 86 for 17 datasets. For each dataset, only the first parabola is shown. The gravity measurement from set 24 is overlaid as a reference. The pressures increased sharply with the onset of microgravity by 1-3%. The pressure remained high until hyper gravity in some cases and slowly decreased in other cases. The onset of hyper gravity showed a much smaller effect on the condensation pressure than the onset of microgravity.

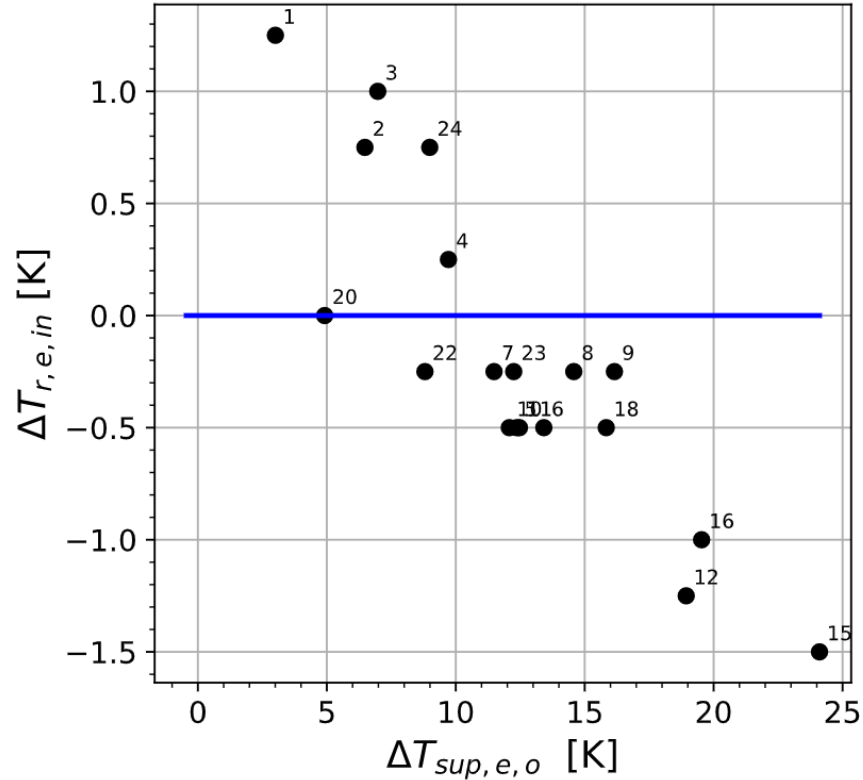


Figure 85: Change of the evaporation temperature due to microgravity as a function of the average superheat through the set of parabolas.

The probable explanation is a worsened heat transfer in the condenser in microgravity. Azzolin et al. (2018) found a decreased condensation heat transfer coefficient in microgravity and argued that the lack of gravity allows a liquid layer to build up on the tube wall and reduce the convective heat transfer. While condensed liquid is pulled to the bottom of the tube in normal gravity, this effect is missing in microgravity and may lower the heat transfer rate. It is likely that the same explanation holds also for the observations in Figure 86.

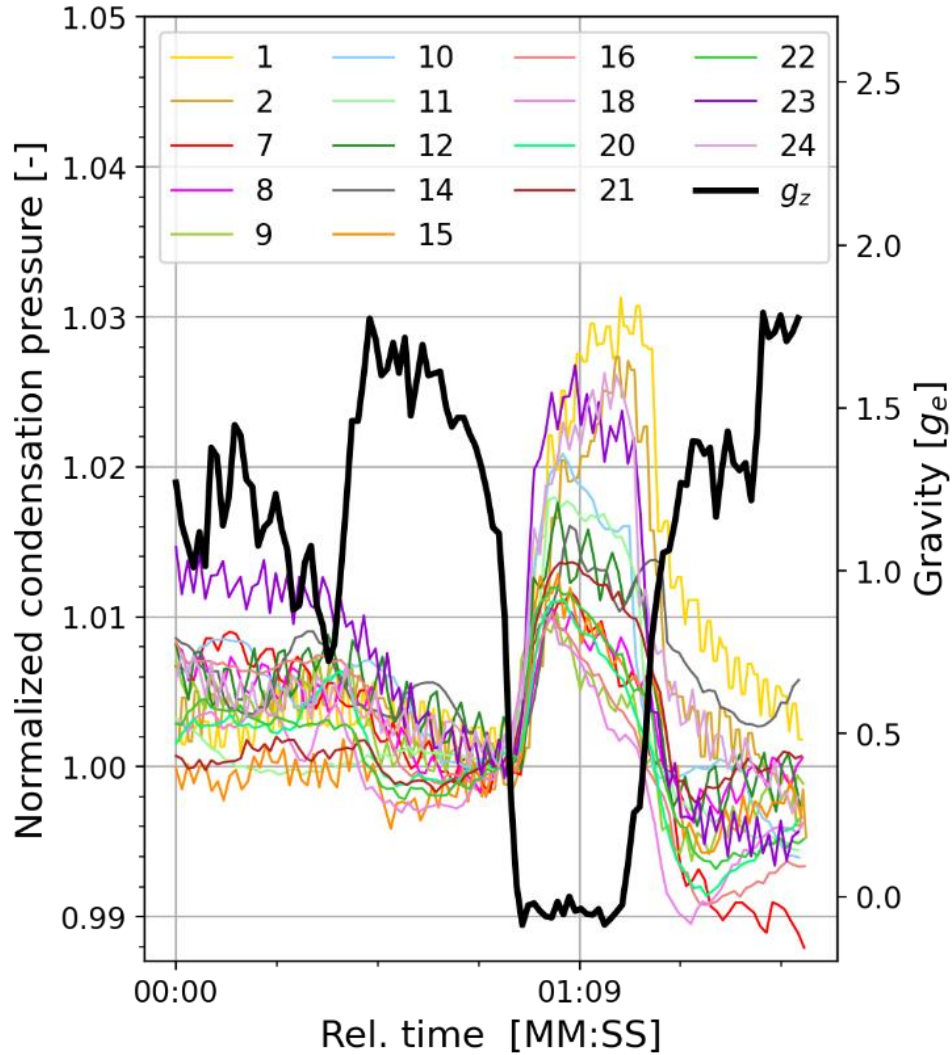


Figure 86: Overlay plot of normalized condensation pressures (Brendel et al., 2022d).

6.12 Comparison of ground-based and parabolic flight data

“Thermal gravitational scaling” is a research field that promises to be useful for design of systems for non-terrestrial gravity environments based on terrestrial experiments. In the open literature, several dimensionless numbers have been highlighted that could theoretically be used to predict performance of a system in different gravity environments. In the available literature on thermal gravitational scaling, inclination testing has not been proposed for the design of microgravity systems.

For example, the question of whether ground-based inclination experiments can be used in the design process for extraterrestrial two-phase *systems* has not been discussed. This may be

because nobody has had a database available that comprised results from both inclination testing and microgravity testing. This database is now available and it may be beneficial that the microgravity testing involved alternatingly changing between hyper and microgravity. The effects of varying gravity levels are probably easier to mimic with some inclination pattern rather than a constant reduced gravity level with one particular orientation of the test stand. For the purpose of comparing ground-based and parabolic flight test results, the high frequency testing approach introduced in section 5.5 was conducted and is here directly compared to parabolic flight data.

6.12.1 Parabolic flights and high frequency inclination testing

Figure 87 shows data from parabolic flight testing on the left-hand side and from parabolic flight simulations (high frequency testing, see section 5.5) on the right-hand side. The top part of the plots shows the gravity level or inclination angle. The second row of plots shows the mass flow rate measured in the liquid and suction line with a y-axis span of 0.5 g/s for both plots. The parabolic flight maneuvers clearly affected the *suction* line mass flow rate. During microgravity, the mass flow rate was approximately 0.05 to 0.09 g/s less than during the initial steady state. The mass flow rate returned to its initial steady-state value in hyper gravity. Significant changes of the *liquid* line mass flow rate cannot be observed. Inclining the same system from $+90^\circ$ to -90° perturbs the mass flow rate much more. The suction line mass flow rate spikes by up to 0.2 g/s and is different from the initial steady state for both $+90^\circ$ and -90° . The liquid line mass flow rate was clearly affected by the inclination changes, too.

The third and fourth row of Figure 87 show the cooling COP and second law efficiency. Similar to the mass flow rate, the COP varies more strongly for inclination changes than for parabolic flights. The second law efficiency varies generally a little bit less relative to the initial value than the COP. This shows that some changes are attributed to the change in high and low side pressure and saturation temperature, which was already observed in Figure 55.

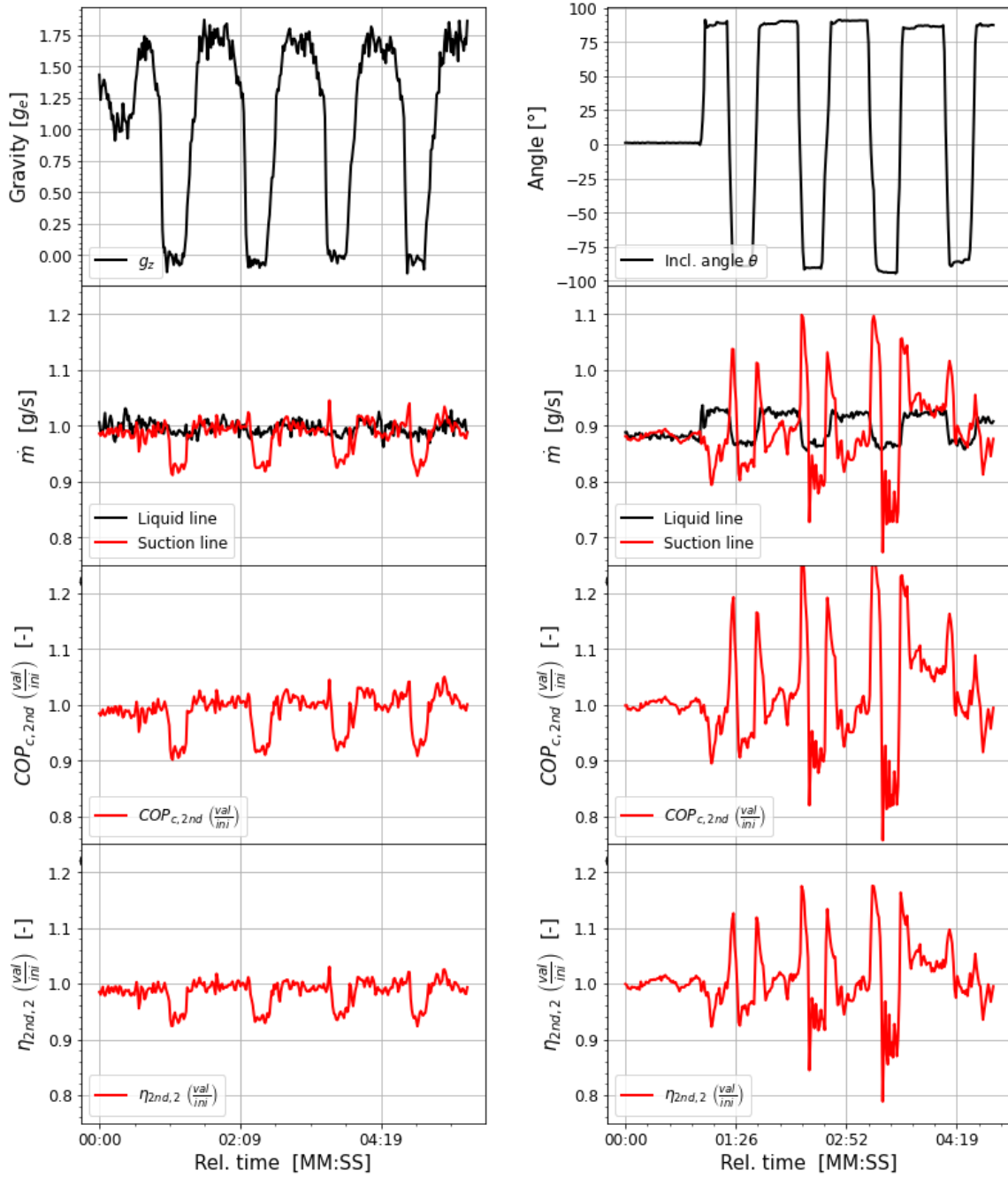


Figure 87: Mass flow rate measurements, relative COP and relative η_{2nd} changes during parabolic flights and ground based flight simulations (Brendel et al., 2022e).

When comparing more test runs at varying operating conditions, inclination testing proved to be harsher for the system at low mass flow rates. For higher mass flow rates, the variations of the suction line mass flow rate were similar for parabolic flights and inclination testing. This trend

is shown in Figure 88 (left). The mmx/avg quantifier is applied to the suction line and shows high values for Weber numbers smaller than 2. For Weber numbers from 2 to 12, the parabolic flight maneuvers caused slightly larger variations but the differences were small compared to the range $We < 2$.

The suction line mass flow rate is one of the most telling measurements for the system stability. The suction line flow rate is usually reflected in the suction pressure and evaporation temperature and will propagate through the entire cycle, affecting other measurements, too. Can inclination testing always approximate the stability of a vapor compression cycle on parabolic flights? Data from one test rig is certainly insufficient to answer this question. However, the data is promising for identifying a relationship between parabolic flight and inclination testing.

Applying the mmx quantifier to the condensation temperature shows a different result. Figure 88 (right) shows the maximum band of condensation temperature variations for parabolic flights in orange and high frequency inclination testing in blue. No trend is visible with the Weber number (closely linked to the mass flux) and the parabolic flight maneuvers caused stronger variations than the inclination testing. The variations in the condensation temperature are explained by greater variations in condensation heat transfer. In microgravity, condensed refrigerant can build up better on the walls and form a liquid layer. This worsens the heat transfer and therefore increases the condensation temperature and pressure. For inclination testing, 90% of the heat exchanger coil is always horizontal such that the heat transfer in those tubes is barely affected by the inclination angle.

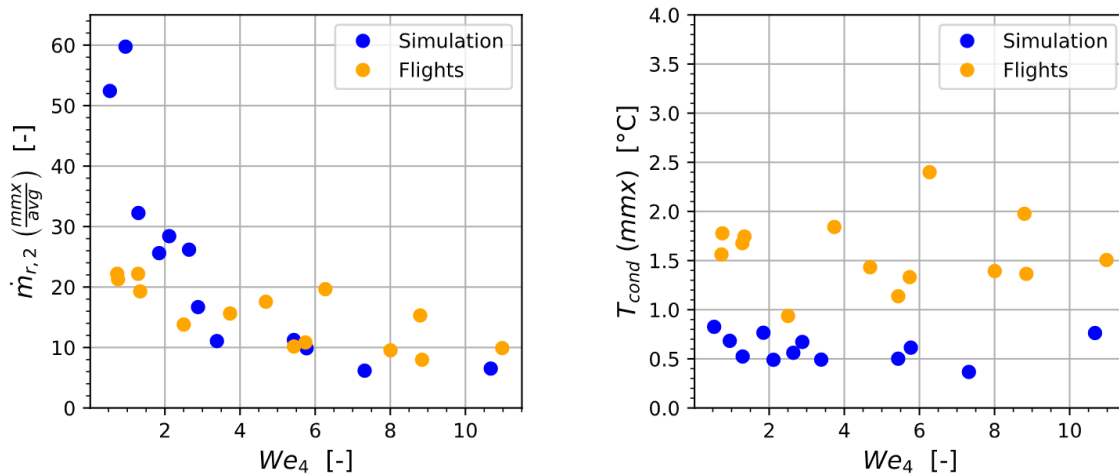


Figure 88: mmx/avg and mmx indicator plotted as a function of We_4 for ground-based flight simulations and parabolic flights.

6.12.2 All testing series

The high frequency inclination testing was specifically developed to resemble parabolic flights and the comparison was shown in the previous section. In addition, comprehensively comparing data from all types of testing is insightful. Seven collected datasets can be differentiated in order of increasing frequency (or chronologically for sets with the same frequency):

- Steady-state testing (air-to-air configuration, R134a and R1234ze(E) treated as one dataset due to small number of datapoints)
- 6-angle testing (liquid-to-liquid configuration with R134a)
- 6-angle testing (air-to-air configuration with R134a)
- 6-angle testing (air-to-air configuration with R1234ze(E))
- Parabolic flight simulations (air-to-air configuration with R134a)
- Parabolic flight simulations (air-to-air configuration with R1234ze(E))
- Parabolic flights (air-to-air configuration with R134a)

For a comparison of all datasets, the MDV or IIR are not recommended. The comparison would not be fair because of the different frequencies of gravity and inclination changes. The mmx and mmx/avg quantifiers are independent of time and therefore more suitable. However, the mmx and mmx/avg quantifiers are very sensitive to singular spikes in the data. For example, if the evaporator loses superheat even for only a short time, the calculated heat transfer rate can change dramatically in an artificial manner since the outlet state is not defined. This would make the mmx quantifier very large although the remainder of the collected data could have been relatively stable. A few datapoints were therefore removed for this study as outlined in detail in the following section.

Sub-selection of data

6-angle testing in liquid-to-liquid configuration

- During loop 18, the DC power supply for all pressure transducers was briefly turned off. Therefore, the mmx quantifiers for the calculated condensation temperature and for all heat transfer rates were removed for set 18.
- Dataset 31 showed an unusually large change in the high side pressure measurements. It may be related to a lack of discharge superheat at the initial steady-state of this loop.

The mmx quantifiers for the condensation temperature and heat transfer rate were therefore removed.

6-angle testing in air-to-air configuration

- During loop 24 and 25, the evaporator briefly lost superheat. Therefore, the mmx quantifiers for the evaporator heat transfer rate on the refrigerant side were removed for set 24 and 25 (compare with section 5.4.4).
- During loop 5, 7 and 14, vapor bubbles escaped the condenser and entered the liquid line mass flow meter, interrupting the clean measurement of the mass flow rate. Therefore, the mmx quantifiers of the refrigerant side heat transfer rate in the condenser were removed for these datasets (compare with section 5.4.5).

Comparisons

Figure 89 shows the mmx quantifier applied to the evaporation and condensation temperature data for all test series. The evaporation temperature is labeled as $T_{r,e,in}$ to distinguish it as measured by a thermocouple from T_{cond} which was calculated based on the discharge pressure.

The *evaporation* temperature had a decreasing trend across all datasets for high mass fluxes. Variations were mostly >5 K for the liquid-to-liquid testing and mostly <6 K for all air-to-air test series (Figure 89, top left). Good agreement was found for the parabolic flight testing and flight simulations using R134a. Only very few datasets showed a bandwidth of changes <2 K. Most of these observations were contrasted by the mmx quantifier for the *condensation* temperature, which was generally lower (Figure 89, top right). Moreover, liquid-to-liquid data did not form a trend with the rest of the data. Almost all air-to-air datasets showed variations of the condensation temperature that were constrained by a band of 2 Kelvin and therefore much more stable than the evaporation temperature. The parabolic flight data showed slightly larger changes in the condensation temperature than most other air-to-air inclination testing datasets explained with the worsened heat transfer in microgravity (see section 6.12.1).

Figure 89 also shows the mmx/avg quantifier for the *refrigerant side* heat transfer rate computed using the suction line mass flow rate (bottom left). A decreasing trend from up to 100%

to approximately 10% was observed as a function of the mass flux. For a mass flux of $G > 40$ $\text{kg}/(\text{m}^2 \cdot \text{s}^1)$, the variations were within a band of less than 20% of the measured heat transfer rate.

For the heat transfer rate on the *heat source side* (lower left plot, $\dot{Q}_{src, evap}$), almost all air-to-air data had an mmx/avg quantifier of less than 20%. Air side measurements typically react slower than measurements for a liquid heat source, which could contribute to the strong discrepancy between the liquid-to-liquid and air-to-air configuration.

Generally, it should be noted, that the variations during the parabolic flights were not significantly stronger than for any other ground-based inclination testing.

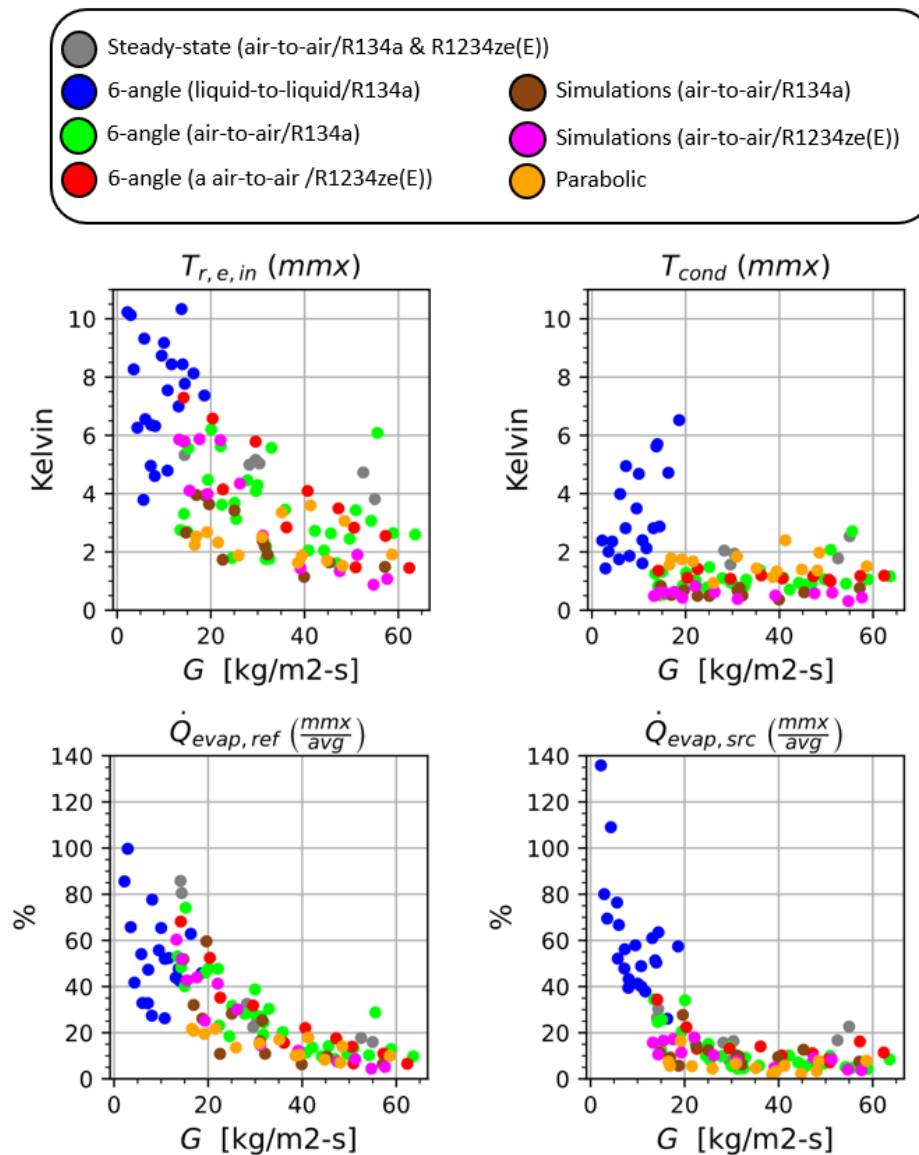


Figure 89: mmx and mmx/avg quantifier for all testing series.

For any measurement and quantifier, each testing series shown in Figure 89 has a maximum, a minimum and an average value. These are shown for the same measurements as in Figure 89 in a bar chart in Figure 90 which emphasizes the generally small impacts of the flight maneuvers on the cycle operation: For $T_{r,e,in}$, $\dot{Q}_{r,evap,2nd}$ and \dot{Q}_{evap} , the parabolic flight maneuvers resulted in the smallest average and the smallest maximum bandwidth of changes. Only for T_{cond} was the mmx quantifier slightly higher for the parabolic flights than for the rest of the air-to-air data.

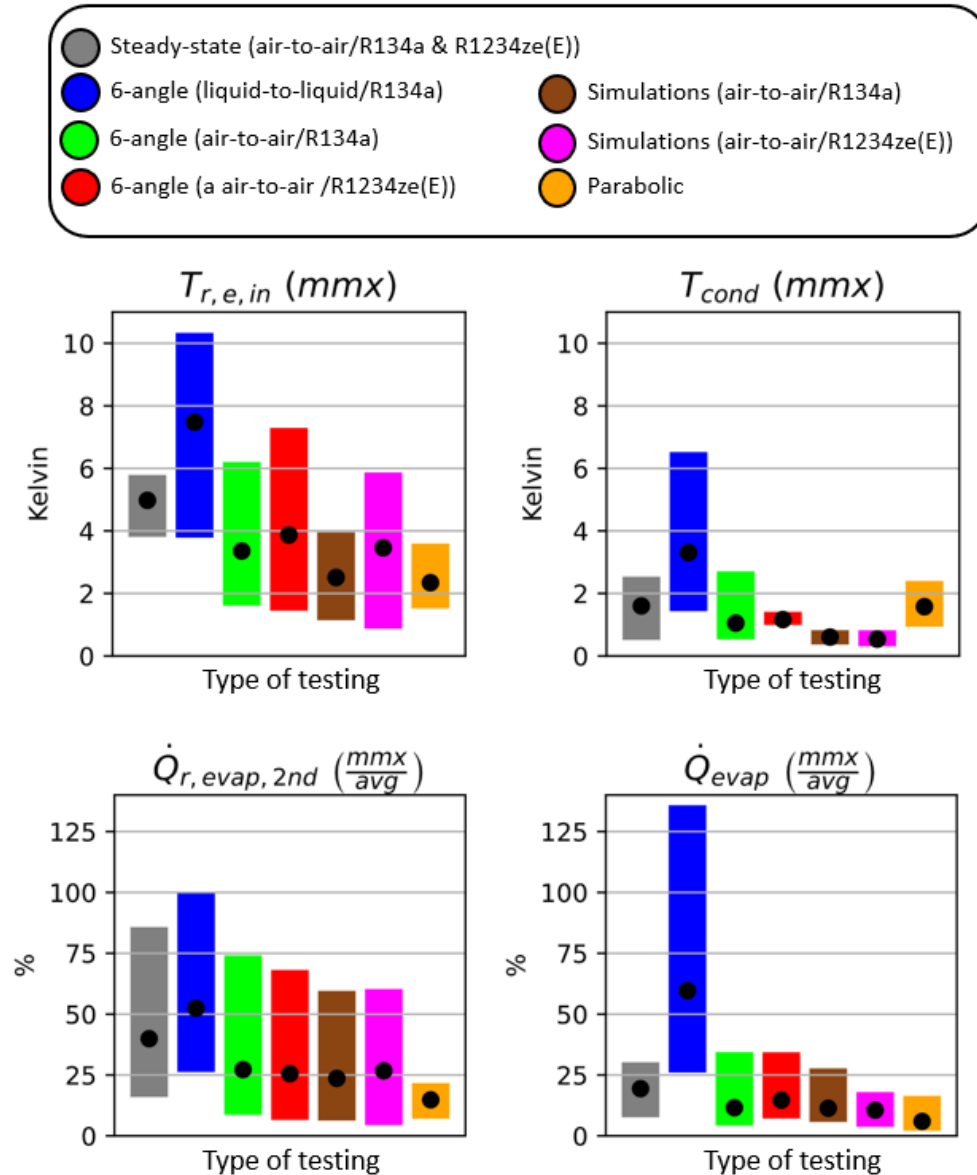


Figure 90: Maximum, minimum and average mmx and mmx/avg quantifier for all testing series.

6.13 Summary

Flow visualizations showed immediate flow regime changes at microgravity and effects of the parabolas were measured at every location in the cycle. However, changes were relatively small. On average, the evaporation temperature remained within a band of ± 1 K and the mass flow rate within a band of $\pm 7.5\%$ through a set of parabolas. A loss of subcooling was not observed and a loss of superheat due to microgravity only occurred for one unusual operating condition. Also, the observed flow oscillations were mild and probably not detrimental to the cycle even if they were sustained in prolonged microgravity. Conclusions of this chapter can be summarized as follows:

- 1) Transient measurements through sets of parabolas show generally mild responses of the cycle (Brendel et al., 2022e).*
- 2) The evaporation temperature remained within a band of 3.5 K as the test rig experienced hyper and microgravity alternatingly. 80% of this data was within a band of only 1.6 K (Brendel et al., 2022e).*
- 3) Superheat and subcooling were always maintained throughout sets of parabolas with only one exception. The one exception occurred when the set of parabolas was started with a particularly low level of superheat which was lost during the first two parabolas but recovered and increased through the last three parabolas without changes in the control parameters (Brendel et al., 2022e).*
- 4) Flow visualizations through normal, hyper and microgravity showed stratified flow in normal gravity which transitioned quickly to a slug and annular flow for low and high mass flow rates, respectively (Brendel et al., 2022d).*
- 5) The discharge pressure consistently increased at the onset of microgravity. It is hypothesized that this is due to a reduction in the two-phase heat transfer coefficient in microgravity (Brendel et al., 2022d).*
- 6) Oscillations were observed during microgravity at some operating conditions. The oscillations quickly stopped in hyper gravity (Brendel et al., 2022d).*
- 7) The cycle response to hyper and microgravity varied with operating conditions. Four different typical responses were found for the refrigerant side heat transfer rate. The clusters seem to be differentiated by different superheat and mass flow rate levels (Brendel et al., 2022d).*
- 8) Whether the evaporation temperature increased or decreased in microgravity showed a strong correlation to the superheat (section 6.10).*
- 9) At low mass flow rates, the instabilities caused by a ground-based parabolic flight simulations were greater than the ones caused by parabolic flights (Brendel et al., 2022e).*

- 10) Ground-based parabolic flight simulations on the inclinable test stand were found to conservatively predict the instabilities of the suction line mass flow rate due to gravity changes on parabolic flights (Brendel et al., 2021d).*
- 11) The same method did not predict variations in the condensation temperature well.*
- 12) The mmx values for the evaporation temperature during the parabolic flights fit into an overall decreasing trend for higher mass fluxes when comparing all testing types. So do the mmx/avg quantifier for both the refrigerant side and heat source side heat transfer rate.*
- 13) The average mmx of the evaporation temperature as well as the mmx/avg of the refrigerant side and heat source side heat transfer rate was smaller for the parabolic flights than for any of the inclination testing series.*

7. ORIENTATION DEPENDENT HEAT EXCHANGER MODEL

7.1 Introduction

7.1.1 Motivation

The development of an orientation dependent heat exchanger model from scratch was motivated by two reasons which explain some of its characteristics. Firstly, experimental results from the inclinable test stand showed cycle responses that were not intuitively explainable (e.g., unstable steady-states, section 4.4). Having a largely mechanistic model promised further insights into the observations. Secondly, heat exchanger models employed in available VCC simulation tools (e.g., ACHP) do not include the effects of orientation on pressure drop or heat transfer. Typically, effects of orientation can be neglected and so there is no widely used approach/nomenclature/tool for modeling a vapor compression cycle that is rotated. A modification of existing models was thought to be more challenging than developing a new model. Overall, the model is novel in the formulation of orientation dependence but otherwise simple and easy to extend.

7.1.2 General notes about the model

The model was developed for fin-tube heat exchangers. In this thesis, the model was tuned by using measured input data and comparing model predictions with the experimental results. Once appropriately tuned, the model can provide detailed information about the frictional, acceleration and gravitational (hydrostatic) pressure drop as well as the charge, all of which are not measurable.

The model is discretized and semi-mechanistic and tracks the heat transfer, pressure drop and charge for each tube segment. It uses empirical correlations only for a few submodels as for example the friction factor, slip ratio and heat transfer coefficients.

In this model, the air outlet temperature is an input instead of an output like in most other heat exchanger models.

7.1.3 Model inputs

Most heat exchanger models use the air flow rate as one of several inputs and predict the air outlet temperature as one model output. For the inclinable test stand, air flow rate measurements were not available. Therefore, the measured air outlet temperature was used as a model input to impose a temperature gradient on the various tube segments. The air flow rate was estimated from an energy balance (disregarding thermal communication with the ambient) and then used as a model input in the computation of the air side heat transfer coefficient and the heat exchanger effectiveness. The flow rate was not calculated for every test run but one time using the average of several datapoints. The air flow rate was assumed constant for all considered datapoints because the flow paths and fan arrangements did not change.

The complete list of model inputs is as follows (some terms will be explained in the subsequent sections):

- Inclination angle of heat exchanger
- Refrigerant
- General heat exchanger geometry information
 - Total length
 - Total fin surface area
 - Total tube surface area
 - Outer tube diameter
 - Inner tube diameter
 - Cross sectional area of air duct
 - Number of rows
 - Transverse pitch
 - Longitudinal pitch
- Heat exchanger information for each segment:
 - Length
 - Internal inclination θ_i
 - Internal rotation angle ϕ_i
- Estimated volumetric air flow rate (based on energy balances)
- Refrigerant mass flow rate
- Refrigerant pressure upstream of expansion valve

- Refrigerant temperature upstream of expansion valve
- Refrigerant temperature at evaporator inlet or pressure at condenser inlet
- Air inlet temperature (averaged from thermocouple grid)
- Air outlet temperature (averaged from thermocouple grid)
- Relative humidity of air at outlet (evaporator) or inlet (condenser)
- Tuning factor for two-phase frictional pressure drop
- Tuning factor refrigerant side heat transfer coefficient
- Tuning factor air side heat transfer coefficient
- Ratio of air outlet temperatures (evaporator only)
- For model validation:
 - Refrigerant outlet pressure
 - Refrigerant outlet temperature

7.1.4 Disclaimer

The novelty of this model lies in tracking the orientation of any tube segment as the overall heat exchanger is rotated. This allows determination of gravitational pressure gradients and their dependence on the inclination angle. A few capabilities that may be assumed solely based on the label “orientation dependent” have *not* been implemented:

- The coefficients for convective two-phase flow heat transfer and friction are not modeled as orientation dependent. The model uses standard correlations without implementing gravity dependence for these coefficients. A few orientation dependent correlations exist, but the experience with those is too small to rely on them in a general model. Such correlations could be easily implemented in the future because the tracking of tube segments and their angles is provided in the model.
- Orientation dependence is enabled for rotation around one axis. A second and third axis could theoretically be implemented, but were not needed for the research conducted.
- The model was built for single-circuit heat exchangers. For multi-circuit heat exchangers, the fundamental proposal for describing the coil may still be useful, but modifications would be needed to the heat exchanger template for the geometry description and in several parts of the code.

- This is a low fidelity model in most aspects. Only the minimum level of detail needed to consider the use case of the present work has been implemented. The model structure allows for straightforward implementation of additional details.

7.2 Orientation dependence

7.2.1 Coil description

The model should be able to predict the gravitational pressure drop for varying orientations of the heat exchanger. It is therefore essential to clearly describe the orientations of all segments such that they can be tracked when the inclination of the heat exchanger is changed. Facilitating this description mathematically is the main contribution of this model. The model is universal enough to describe any geometry of a *single-circuit fin-tube* heat exchanger.

It is proposed to work with two coordinate systems. The *inner* coordinate system is fixed to the heat exchanger. From the perspective of the inner coordinate system, angles of tubes do not change when the heat exchanger is rotated. Additionally, there is a global inclination angle θ , which describes the inclination of the inner coordinate system relative to the gravity vector (in the outer coordinate system). Additional angles could be introduced to describe rotation of the inner coordinate system around other axes.

Inner coordinate system

To describe the heat exchanger coil in the inner coordinate system, it is divided into straight segments. Each segment can then be described in the inner coordinate system with three parameters in polar coordinates:

- θ_i ($[0^\circ, 180^\circ]$)
- ϕ_i ($[0^\circ, 359^\circ]$)
- L ($[0 \text{ m}, \infty]$)

The subscript “i” will be used for angles that refer to the inner coordinate system. The three parameters are shown in Figure 91 where the solid brown line is an example segment of a coil. The inner and outer coordinate systems are by definition aligned as follows for all presented trigonometric relationships to be correct:

- y_i is in parallel to the axis of rotation

- z_i points against the gravity vector when the test rig is in its “normal” or “horizontal” orientation
- Angles of the heat exchanger θ in the range $0^\circ < \theta < 180^\circ$ cause the positive x_i axis to point down (in the direction of gravity). θ in the range $180^\circ < \theta < 360^\circ$ causes the positive x_i axis to point up (against the direction of gravity). Note that θ and θ_i are different angles!

Figure 92 shows how the inner coordinate system was aligned with the test rig (the heat exchangers themselves are in enclosures and cannot be seen). The positive x-axis points from the condenser to the evaporator, the z-axis points up (against gravity) and the y-axis follows the axis of rotation.

Tracking the effective height

The effective height is the change in height of a tube segment. The model computes this effective height based on the orientation within the inner coordinate system and changes in the angle θ (rotation around the y_i -axis). Rotation around the x- and z-axis is not included in this model.

Because θ describes a rotation around the y-axis, it is convenient to firstly project a given tube segment into the xz-plane as shown in Figure 91. It is then described with an angle θ_{xz} ($[0^\circ, 359^\circ]$) and a length in the xz-plane called L_{xz} . Once θ_{xz} and L_{xz} are known, the angle θ can be added to θ_{xz} to obtain θ_{tot} and the effective height is calculated from $h_{eff} = L_{xz} \cos(\theta_{tot})$. Section 7.2.2 shows the equations step by step.

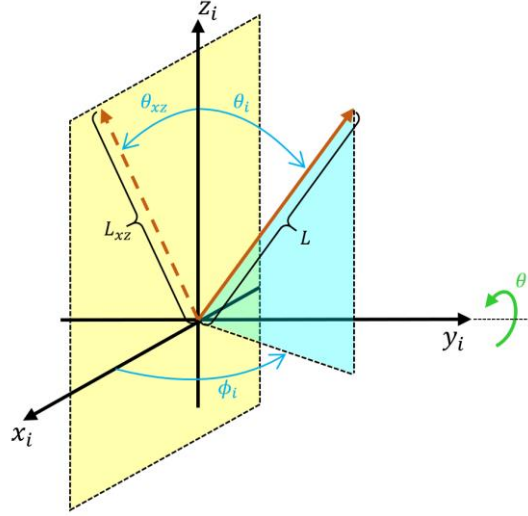


Figure 91: Nomenclature for orientation dependent heat exchanger modeling.

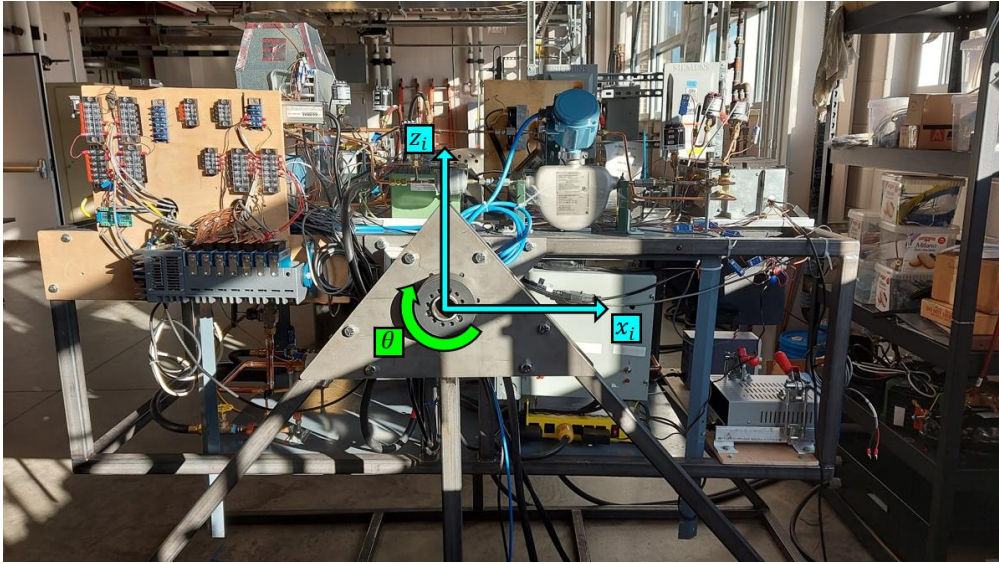


Figure 92: Picture of inclined test rig with x- and z-axis of inner coordinate system. The y-axis goes through the test stand and is the axis of rotation.

Example of coil description

Based on the previous discussion, a coil made from three segments is described here as a simple example. The coil consists of a straight segment, a u-bend pointing down and another straight segment pointing in the opposite direction of the first straight segment. This is visualized in Figure 93. The inner coordinate system was aligned such that the y-axis is in parallel to the straight segments for this example. The u-bend points in the negative z direction. Furthermore, the

u-bend was approximated as a straight tube. If a higher fidelity was needed, the u-bend could be approximated with 2 or 3 straight segments and also the long straight segments could be divided into more segments.

The flow in the first segment follows the positive y-axis. As per the definitions in Figure 91, this is described with $\theta_i = 90^\circ$ and $\phi_i = 90^\circ$. Segment 2 points straight down, which is described with $\theta_i = 180^\circ$. Since the tube is in the xz-plane, ϕ_i should be set to 0° . The third segment is like the first one, but the flow direction has changed. Therefore, $\theta_i = 90^\circ$ and $\phi_i = 270^\circ$.

This method seems tedious at first for large coils. However, the use of a spreadsheet program and thoughtful use of the copy-paste function allow a quick description of a complete single circuit coil. An example of a filled spreadsheet for the evaporator is provided later (Figure 98 and Figure 99). The model has not been built for multi-circuit heat exchangers but could be modified accordingly.

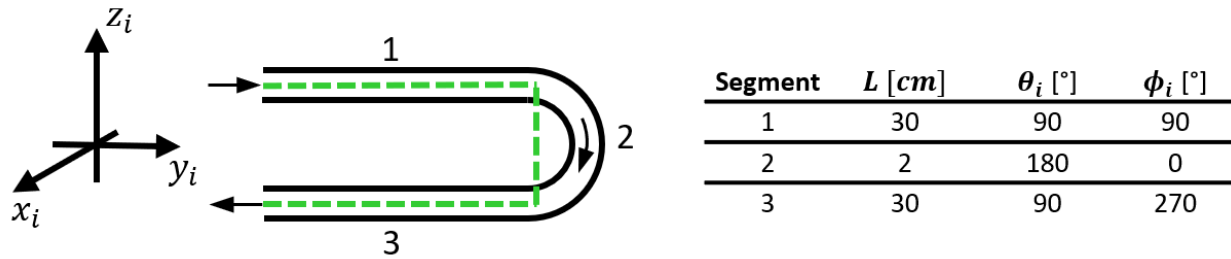


Figure 93: Example of coil description with Length, θ_i and ϕ_i .

Position of segments

The description of the orientation and length of each segment has an additional advantage. It is relatively simple to track the x-y-z coordinates of the inlet or outlets of the tubes. Hence, it is defined whether a segment is close to the air inlet or outlet, close to a wall or approximately in the middle of the heat exchanger. With this information, it is also possible to impose varying air temperatures on the segments as a function of their position within the heat exchanger.

7.2.2 Equations for effective height

All equations needed to obtain the effective height and effective tube angle are listed in the following. It is assumed that θ, θ_i, ϕ_i and L are known for all segments. The length of a tube segment projected into the xz-plane is calculated as:

$$L_{xz} = L\sqrt{\cos(\theta_i)^2 + (\sin(\theta_i) \cos(\phi_i))^2}. \quad (22)$$

The segment angle projected in the xz-plane can be found with:

$$\theta'_{xz} = \tan^{-1} \left(\frac{\sin(\theta_i) \cos(\phi_i)}{|\cos(\theta_i)|} \right). \quad (23)$$

The previous equation results in values ranging only from $+90^\circ$ to -90° . An if-statement translates this to the range 0° to 270° depending on θ_i :

$$\theta''_{xz} = \begin{cases} \theta'_{xz} & \text{for } \theta_i \leq 90^\circ \\ 180^\circ - \theta'_{xz} & \text{for } \theta_i > 90^\circ \end{cases} \quad (24)$$

Moreover, values of θ''_{xz} between -90 and 0 are translated to be between 270° and 360° :

$$\theta_{xz} = \begin{cases} 360^\circ + \theta''_{xz} & \text{for } \theta''_{xz} < 0^\circ \\ \theta''_{xz} & \text{for } \theta''_{xz} \geq 0^\circ \end{cases} \quad (25)$$

After the modifications of θ'_{xz} and θ''_{xz} , θ_{xz} is confined to the range 0° to 360° . The total tube angle, also considering the inclination of the inner coordinate system is:

$$\theta_{tot} = \theta_{xz} + \theta. \quad (26)$$

Then the effective height of the tube is:

$$h_{eff} = L_{xz} \cos(\theta_{tot}). \quad (27)$$

If computational speed is important, the calculations to obtain L_{xz} and θ_{xz} could be executed a priori and the values could be stored in a lookup table. Only θ would then be a variable for repeated model executions.

7.3 Heat transfer, pressure drop and charge modeling

A few modelling methods are highlighted here. The model was implemented in EES (Klein & Alvarado, 2002) and the source code should be referenced for a detailed listing of all equations, both in raw and in formatted form.

- The experimental heat transfer rate on the refrigerant side was calculated assuming an isenthalpic expansion process for the evaporator. For the condenser, both the inlet and

outlet enthalpy were calculated from the respective temperature and pressure measurements at the superheated and subcooled inlet and outlet of the condenser.

$$\dot{Q}_{c,exp} = \dot{m}_r(h_{r,c,out} - h_{r,c,in}) \quad (28)$$

$$\dot{Q}_{e,exp} = \dot{m}_{r,2}(h_{r,e,out} - h_{r,e,in}) \quad (29)$$

$$h_{r,e,in} = f(T_{r,exp,v,in}, P_{r,exp,v,in}) \quad (30)$$

- The air inlet and outlet temperatures were calculated as the average of all thermocouples in the respective grids.
- Condensation of water from the air in the evaporator has not been considered. The relative humidity was only measured at the outlet of the evaporator and at the inlet to the condenser. An experimental model verification would not have been possible. Therefore, the measure relative humidity was assigned to each segment of air in the model.
- The heat exchanger effectiveness for in-tube refrigerant flow with air cross flow was calculated from an NTU which was itself calculated from a UA value for each segment.
 - For segments with two-phase refrigerant:

$$\epsilon = 1 - \exp(-NTU) \quad (31)$$

$$NTU = \frac{UA}{\dot{m}_{a,share} c_{p,a}} \quad (32)$$

- For segments with single phase refrigerant:

- For $\dot{C}_a < \dot{C}_r$:

$$\epsilon = \frac{1}{C^*} \cdot (1 - \exp(-C^*(1 - \exp(-NTU)))) \quad (33)$$

$$C^* = \frac{\dot{C}_a}{\dot{C}_r} \quad (34)$$

$$NTU = \frac{UA}{\dot{m}_{a,share} c_{p,a}} \quad (35)$$

- For $\dot{C}_r < \dot{C}_a$:

$$\epsilon = 1 - \exp\left(-\frac{1}{C^*}(1 - \exp(-C^* \cdot NTU))\right) \quad (36)$$

$$C^* = \frac{\dot{C}_r}{\dot{C}_a} \quad (37)$$

$$NTU = \frac{UA}{\dot{m}_r c_{p,r}} \quad (38)$$

- With the UA value (neglecting tube wall resistance):

$$UA = \frac{1}{\frac{1}{A_r h t c_r} + \frac{1}{A_a h t c_a}} \quad (39)$$

- ϵ is the heat exchanger effectiveness (for a segment), $\dot{m}_{a,share}$ is the share of the air mass flow rate that is in thermal communication with the tube segment, \dot{C} is the product of mass flow rate and specific heat for either air or refrigerant depending on the subscript. A_r is the available area for heat transfer on the refrigerant side. A_a is the surface area for air side heat exchange, containing both the tube area and the fin area multiplied with a fin efficiency assumed to be 80% ($A_a = A_{a,tube} + \eta_{fins} A_{a,fins}$)
- Shah (1982) was used for the boiling heat transfer coefficient (EES built-in procedure). The orientation was always set to horizontal. The heat flux as an input to the correlation was obtained by dividing the total heat transfer by the total inner tube area instead of a discretized heat flux varying by segment. This simplification allowed to solve the heat exchanger model procedure without the need for iterations.
- Shah (2016) was used for the condensation heat transfer coefficient (EES built-in procedure). The orientation was always set to horizontal.
- The EES built-in correlation for internal single phase flow in pipes was used for the refrigerant side single phase heat transfer coefficient.
- The EES built-in correlation for external flow over a staggered bank was used for the air-side heat transfer coefficient.
- The heat transfer resistance of the tube wall was neglected.
- The single phase friction factor was calculated from the Churchill correlation (Churchill, 1977).

- The homogeneous two-phase flow model was assumed for the pressure drop calculations in the two-phase region. Frictional, accelerational and gravitational components were considered.

$$\left(\frac{dp}{dz}\right)_f = -\frac{2}{D} f_{tp,F} v_f G^2 \left(1 + \frac{x v_{fg}}{v_f}\right) \quad (40)$$

$$\left(\frac{dp}{dz}\right)_a = -G^2 v_{fg} \frac{dx}{dz} \quad (41)$$

$$\left(\frac{dp}{dz}\right)_g = -\frac{g}{v_f + x v_{fg}} \cos(\theta_{tot}) \quad (42)$$

- The two-phase friction coefficient was based on the Churchill correlation (Churchill, 1977) with a Reynolds number computed using a mixture viscosity based on the flow quality. The relative roughness was set to 0.0002.

$$f_{tp,F} = \frac{f_{Darcy}}{4} \quad (43)$$

$$f_{Darcy} = f(Re_{tp}, RelRough) \quad (44)$$

$$Re_{tp} = \frac{4\dot{m}}{\pi \mu_{tp} D} \quad (45)$$

$$\mu_{tp} = x \mu_g + (1 - x) \mu_f \quad (46)$$

- The void fraction was calculated using the slip-flow model with the slip ratio calculated according to (Zivi, 1964).

$$\alpha = \frac{1}{1 + S \frac{\rho_g}{\rho_f} \frac{1-x}{x}} \quad (47)$$

$$S = \left(\frac{\rho_f}{\rho_g}\right)^{\frac{1}{3}} \quad (48)$$

- The refrigerant density in segments with two-phase flow is calculated as

$$\rho = \alpha \rho_g + (1 - \alpha) \rho_f. \quad (49)$$

- The charge of the heat exchanger is the sum of the refrigerant charges of the segments which are calculated as

$$m = L \frac{D_i^2}{4} \pi \rho. \quad (50)$$

- Any accelerational pressure drop in the single phase region from thermal expansion was neglected.

7.4 Ratio of air outlet temperatures

Tracking the position of tubes allows the imposition of varying temperatures on the tube segments. Using the air outlet temperature as an input to the model, the air temperature was assumed to decrease linearly from the measured inlet to the measured outlet temperature in the basic model.

The testing phase of the model showed strange results for the evaporator, which resulted in a model refinement. The issue was in the coil routing, which is shown schematically in Figure 94 (left). The refrigerant enters at the top and flows to the bottom of the heat exchanger in one column before it flows up in a second column in parallel to the first row. Hence, there is generally high heat transfer during the downflow but less in the up flow (higher refrigerant temperature and lower heat transfer coefficient). In some test runs, the refrigerant was superheated in the bottom third of the evaporator to a temperature higher than the measured *average* air outlet temperature. The model thus cooled the refrigerant back down as it reached the top section of the evaporator. In reality, the air was probably not well mixed and cooled down more in the part of the coil that had two-phase heat transfer than in the part of the coil with superheated refrigerant as illustrated in the right hand side of Figure 94 (the measurements cannot confirm or disproof this because the thermocouple “grid” was only a 1x3 array). Therefore, the air was described with two outlet temperatures $T_{a,out,1}$ and $T_{a,out,2}$, one for each column in the heat exchanger. The air was modelled to decrease linearly to the two heat exchanger outlet temperatures, the average of which was constrained to be the measured outlet temperature. The ratio of the slopes was defined empirically to be $ratio = 5$. The equation subsystem to be solved is then:

$$T_{a,out} = \frac{T_{a,out,1} + T_{a,out,2}}{2}, \quad (51)$$

$$ratio = \frac{T_{in} - T_{a,out,1}}{T_{in} - T_{a,out,2}} = 5. \quad (52)$$

$T_{a,in}$ and $T_{a,out}$ are the measured average air temperatures and $T_{a,out,1}$ and $T_{a,out,2}$ are the modelled air outlet temperatures.

The condenser had a different coil routing and did not need the model refinement. It was modeled with one linear temperature gradient from air inlet to air outlet.

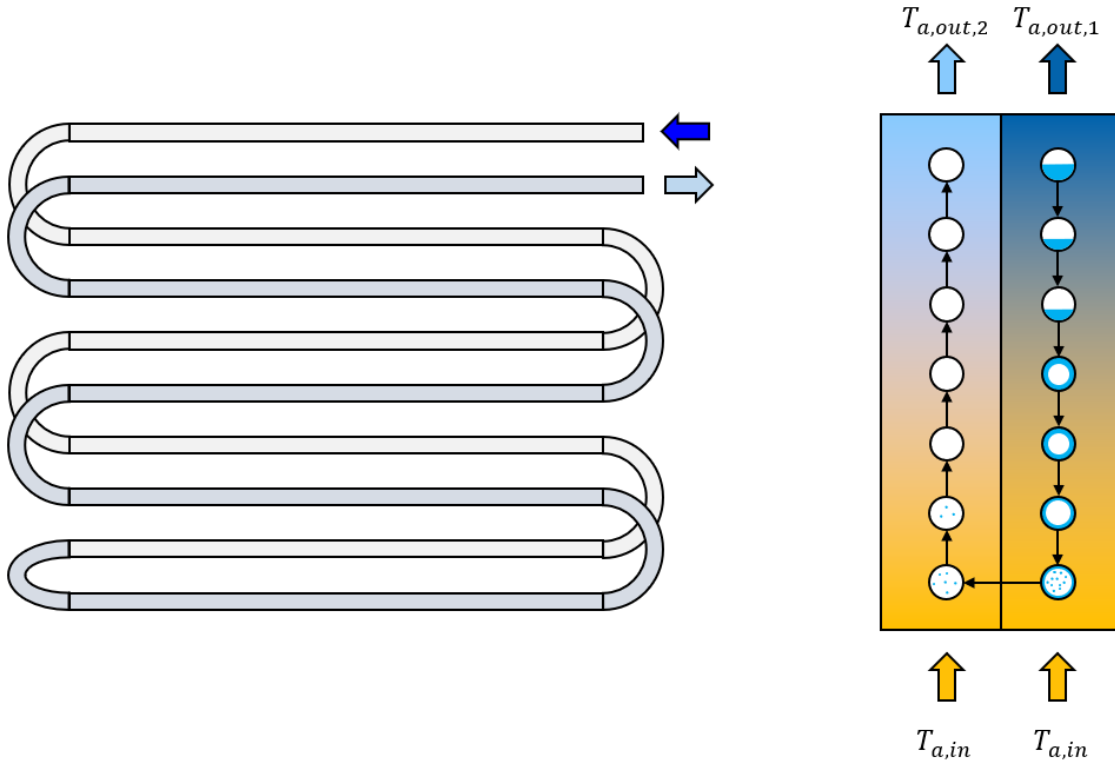


Figure 94: Evaporator geometry from a front and side view.

7.5 Model tuning factors and validation

7.5.1 Heat transfer and pressure drop

Seven steady-state data points at $\theta = 0^\circ$ were used for model validation and tuning. The refrigerant, the mass flow rate, the saturation temperature and the assumed volumetric air flow rate for these data sets are listed in

Table 16 for the evaporator and in

Table 18 for the condenser. For both heat exchangers, tuning factors for the air-side ($htc_{a,t}$) and refrigerant-side ($htc_{r,t}$) heat transfer coefficient as well as for the two-phase friction factor ($f_{TP,t}$) were fitted manually. These are shown with experimental and modelled results for the heat transfer rate and pressure drop in

Table 17 and

Table 19 for the evaporator and condenser, respectively. The errors are calculated as

$$ErrX = \frac{X_{exp} - X_{mod}}{X_{exp}} \cdot 100 [\%]. \quad (53)$$

X represents the heat transfer or pressure drop and *exp* and *mod* stand for experimental and modelled results, respectively.

For the evaporator, it was necessary to choose a different air side tuning factor for set 1 and 2 than for the other datasets to reach a good agreement between the experimental and modelled results. It appears reasonable that set 1 and 2 have higher tuning factors for the air side heat transfer. These two sets had relatively high evaporation temperatures and therefore less frosting, which was often significant at lower evaporation temperatures. The modelled refrigerant side pressure drops agreed well with the experimental data for a two-phase frictional tuning factor of $f_{TP,t} = 2.5$ for all test runs.

For the condenser (

Table 19), constant tuning factors for all sets resulted in good agreement for the heat transfer. The pressure drop could not be fitted with a single tuning factor. Since the deviations were unsystematic, the tuning factor for the friction coefficient was maintained at 1.

Table 16: Evaporator data sets for validation.

Set	Refrigerant	\dot{m}_r [g/s]	$T_{r,e}$ [°C]	\dot{V}_e [l/s]
1	R1234ZE(E)	2.11	-5.3	5
2	R134A	2.04	0.3	5
3	R134A	0.55	-11.4	5
4	R134A	1.14	-19.2	5
5	R134A	1.11	-20.0	5
6	R1234ZE(E)	0.53	-14.1	5
7	R1234ZE(E)	1.08	-16.4	5

Table 17: Experimental and modelled results for evaporator with tuning factors.

Set	$htc_{a,t}$	$htc_{r,t}$	$f_{TP,t}$	$\dot{Q}_{e,exp}$	$\dot{Q}_{e,mod}$	$Err\dot{Q}_e$ [%]	$\Delta P_{e,exp}$	$\Delta P_{e,mod}$	$Err\Delta P_e$ [%]
1	2.8	1.5	2.5	356.5	362.8	-1.8	7.6	6.0	21.9
2	2.8	1.5	2.5	366.7	354.5	3.3	4.3	3.8	12.7
3	1	1.5	2.5	98.0	97.1	0.9	0.5	0.9	-89.2
4	1	1.5	2.5	197.2	183.9	6.7	3.7	3.8	-1.0
5	1	1.5	2.5	192.8	192.3	0.3	3.5	3.5	1.1
6	1	1.5	2.5	87.7	88.4	-0.8	1.1	1.0	5.7
7	1	1.5	2.5	177.6	176.3	0.7	4.0	3.5	10.8

Table 18: Condenser data sets for validation.

Set	Refrigerant	\dot{m}_r [g/s]	$T_{r,c}$ [°C]	\dot{V}_e [l/s]
1	R1234ZE(E)	2.11	35.9	15
2	R134A	2.04	34.3	15
3	R134A	0.55	25.4	15
4	R134A	1.14	29.9	15
5	R134A	1.11	29.8	15
6	R1234ZE(E)	0.53	25.8	15
7	R1234ZE(E)	1.08	29.4	15

Table 19: Experimental and modelled results for condenser with tuning factors.

Set	$htc_{a,t}$	$htc_{r,t}$	$f_{TP,t}$	$\dot{Q}_{e,exp}$	$\dot{Q}_{e,mod}$	$Err\dot{Q}_e$ [%]	$\Delta P_{e,exp}$	$\Delta P_{e,mod}$	$Err\Delta P_e$ [%]
1	2	1.5	1	-447.6	-443.2	1.0	-0.2	3.4	1818.7
2	2	1.5	1	-424.5	-417.8	1.6	-1.2	3.0	363.1
3	2	1.5	1	-107.7	-108.8	-1.0	-1.0	0.5	150.3
4	2	1.5	1	-255.4	-257.1	-0.7	4.4	1.2	72.7
5	2	1.5	1	-251.9	-252.0	0.0	5.3	1.2	77.6
6	2	1.5	1	-97.5	-98.1	-0.6	0.8	0.4	45.1
7	2	1.5	1	-228.6	-229.4	-0.3	5.2	1.3	75.6

7.5.2 Charge

The heat exchanger models were not implemented into a complete cycle model and therefore the predicted charge could not be validated against a system charge. A small additional series of experiments was conducted to validate the evaporator charge prediction.

The test stand was operated at 6 different steady-states. For each steady-state, the ball valve before the expansion valve was closed, resulting in the liquid line mass flow rate dropping to 0 g/s nearly instantaneously. The suction line mass flow rate decreased much slower. The integrated difference of the two mass flow rates is then the experimentally evaluated evaporator charge.

Figure 95 shows the pressures, mass flow rate and the cumulative charge migration of such a pump down. The suction pressure decreased because refrigerant was pumped out of the low-pressure side and not replenished due to the closed ball valve at the expansion valve. The discharge pressure decreased because the mass flow rates and therefore heat transfer rates decreased. The cumulative charge migration during the pump down changed from 0.2 g to -6.2, indicating that the experimentally evaluated evaporator charge at the given operating conditions was 6.4 g.

Figure 96 shows the results of all six pump down tests. Δm_{PD} is the experimentally evaluated evaporator charge as explained with Figure 95. The steady-state conditions at the time of starting the pump-down were fed to the evaporator model which predicted the modeled charge in the evaporator $Charge_{evap} (mod)$. The trend is linear with an offset. Point 1 is a strong outlier and could be explained with an unusual charge distribution, strongly differing from the assumed slip flow as per the model. Based on points 2-6, the model underpredicts the charge by approximately 3 g (intersection of linear trend with y-axis). This is probably due to the tube segment between the ball valve and the expansion valve which is filled with liquid at the start of the pump-down and not accounted for in the model. Alternatively or additionally, Zivi (1964) may not predict the slip ratio accurately for the existing flow regime and operating conditions.

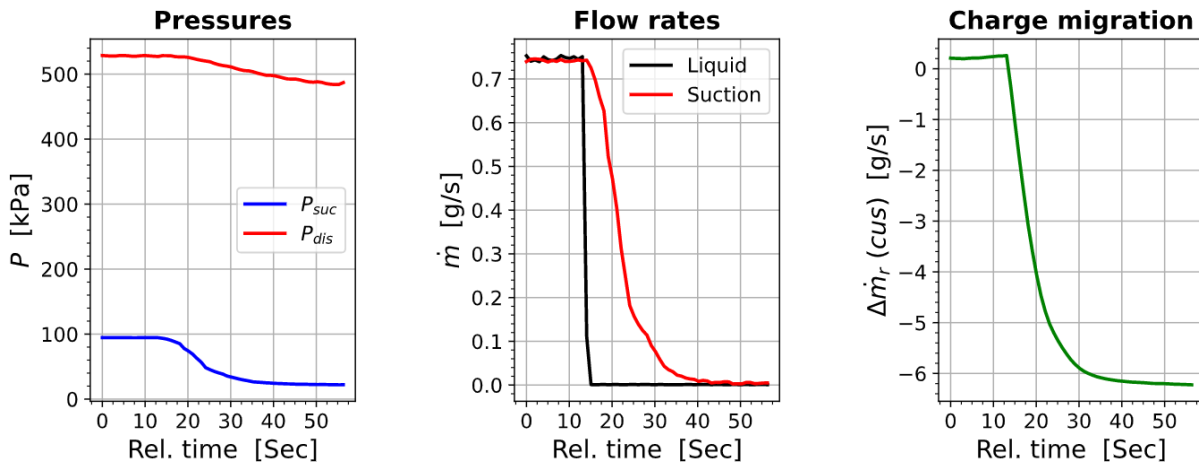


Figure 95: Transient measurement of pump down test number 5.

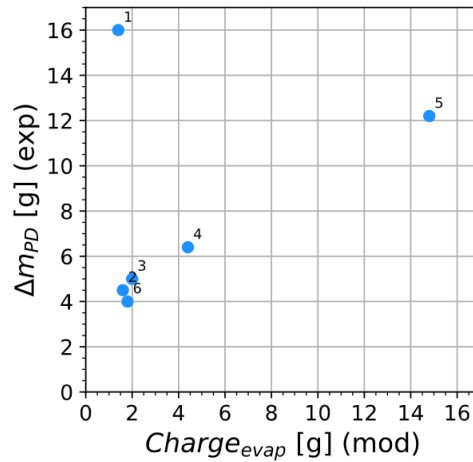


Figure 96: Experimentally evaluated evaporator charge plotted as a function of modelled evaporator charge.

7.6 Heat exchanger tables

Both the evaporator and condenser had to be separated into segments and each segment needed a length, and values for θ_i and ϕ_i . Additionally, certain overall parameters were needed as for example the inner and outer tube diameters and the fin area. All information was prepared in one Excel spreadsheet per heat exchanger and copy pasted into one EES lookup table for the computations. A picture of the evaporator is shown in Figure 97, also indicating the inner coordinate system. The inlet and outlet tubes as well as all u-bends are approximated as vertical. The heat exchanger has two columns of tubes, one leading the refrigerant to the bottom of the heat exchanger and the other one leading up.

Figure 98 and Figure 99 show screenshots of the Excel spreadsheet describing the heat exchanger. The yellow and orange columns are mandatory inputs. All gray columns are calculated. The first three columns show how far a certain segment travels in all three directions. The second three columns show the cartesian coordinates of the outlet of the segment. rX , rY and rZ translate the cartesian coordinates into relative positions within the heat exchanger between 0 and 1. All gray columns are not used in the heat exchanger model and are only supplemental information to show the capability of location tracking using the three input parameters for each tube. The blue columns are used in the model. $rAir$ is the relative location of the air in air flow direction in the heat exchanger. It is used to impose a temperature profile on the air in flow direction. The last blue column describes with what ratio of the total air flow a segment is in thermal communication. This is approximated using the length and diameter of the tube and its orientation.

Figure 100 shows a picture and the inner coordinate system of the condenser. The tables for the condenser are much longer (140 rows) and therefore not shown as screenshots.

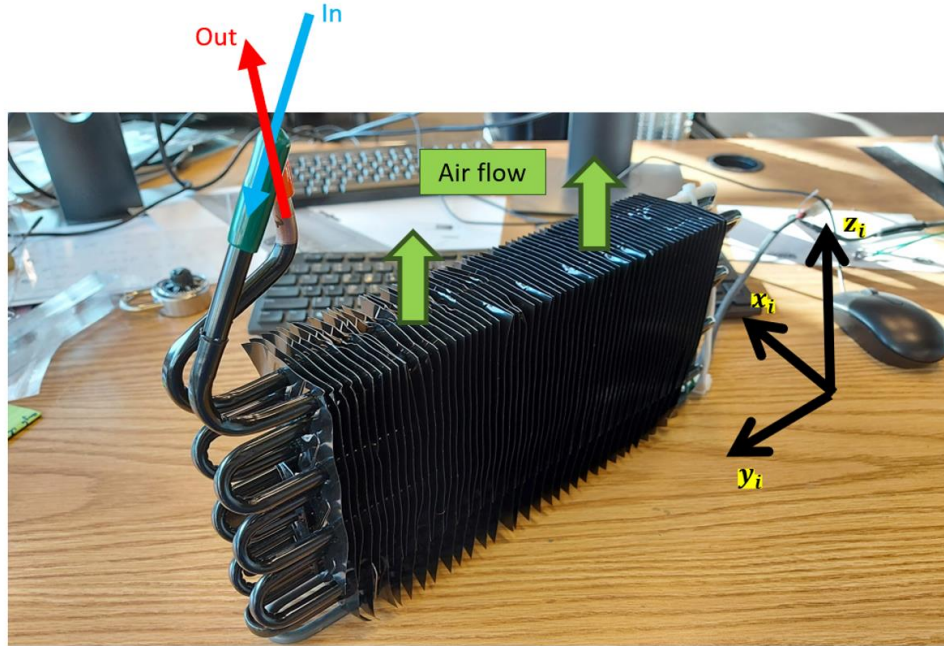


Figure 97: Picture of evaporator with inlet and outlet and orientation of inner coordinate system as installed on the inclinable test stand.

Properties describing the complete HX		Segment number	Length of segment	angle theta of segment	angle phi of segment	travel in x direction of segment	travel in y direction of segment	travel in z direction of segment	x- coordinate	y- coordinate
Property (unit)	Value	Segment	Length cm	theta_i degree	phi_i degree	DeltaX cm	DeltaY cm	DeltaZ cm	X cm	Y cm
TotalLength (m)	6.20192	1	3	180	0	0.0	0	-3.0	0.0	0.0
TotalFinArea (m2)	0.56700	2	35.0	90	-90	0.0	-35	0.0	0.0	-35.0
TotalTubeArea (m2)	0.15470	3	3.6	180	0	0.0	0	-3.6	0.0	-35.0
OuterTubeDiameter (m)	0.00794	4	35.0	90	90	0.0	35	0.0	0.0	0.0
InnerTubeDiameter (m)	0.00694	5	3.6	180	0	0.0	0	-3.6	0.0	0.0
AirCrossArea (m2)	0.02040	6	35.0	90	-90	0.0	-35	0.0	0.0	-35.0
NumberOfRows	8.00000	7	3.6	180	0	0.0	0	-3.6	0.0	-35.0
Transverse_Pitch (m)	0.02000	8	35.0	90	90	0.0	35	0.0	0.0	0.0
Longitudinal_Pitch (m)	0.02000	9	3.6	180	0	0.0	0	-3.6	0.0	0.0
		10	35.0	90	-90	0.0	-35	0.0	0.0	-35.0
		11	3.6	180	0	0.0	0	-3.6	0.0	-35.0
		12	35.0	90	90	0.0	35	0.0	0.0	0.0
		13	3.6	180	0	0.0	0	-3.6	0.0	0.0
		14	35.0	90	-90	0.0	-35	0.0	0.0	-35.0
		15	3.6	180	0	0.0	0	-3.6	0.0	-35.0
		16	35.0	90	90	0.0	35	0.0	0.0	0.0
		17	3.6	90	0	3.6	0	0.0	3.6	0.0
		18	35.0	90	-90	0.0	-35	0.0	3.6	-35.0
		19	3.6	0	0	0.0	0	3.6	3.6	-35.0
		20	35.0	90	90	0.0	35	0.0	3.6	0.0
		21	3.6	0	0	0.0	0	3.6	3.6	0.0
		22	35.0	90	-90	0.0	-35	0.0	3.6	-35.0
		23	3.6	0	0	0.0	0	3.6	3.6	-35.0
		24	35.0	90	90	0.0	35	0.0	3.6	0.0
		25	3.6	0	0	0.0	0	3.6	3.6	0.0
		26	35.0	90	-90	0.0	-35	0.0	3.6	-35.0
		27	3.6	0	0	0.0	0	3.6	3.6	-35.0
		28	35.0	90	90	0.0	35	0.0	3.6	0.0
		29	3.6	0	0	0.0	0	3.6	3.6	0.0
		30	35.0	90	-90	0.0	-35	0.0	3.6	-35.0
		31	3.6	0	0	0.0	0	3.6	3.6	-35.0
		32	35.0	90	90	0.0	35	0.0	3.6	0.0
		33	3.0	0	0	0.0	0	3.0	3.6	0.0

Figure 98: Tabular description of evaporator (part 1).

z- coordinate	Relative location in x	Relative location in y	Relative location in z	Relative location in air flow direction	Relative crosssection of air flow that tube and fin are in contact with	Comment
Z	rX	rY	rZ	rAir	rAir_area	
cm	-	-	-	-	-	
-3.0	0.0	1.0	0.9	0.9	0.09	vertical inlet
-3.0	0.0	0.0	0.9	0.9	0.38	first horizontal tube
-6.6	0.0	0.0	0.8	0.8	0.06	
-6.6	0.0	1.0	0.8	0.8	0.38	
-10.2	0.0	1.0	0.6	0.6	0.06	
-10.2	0.0	0.0	0.6	0.6	0.38	
-13.8	0.0	0.0	0.5	0.5	0.06	
-13.8	0.0	1.0	0.5	0.5	0.38	
-17.5	0.0	1.0	0.4	0.4	0.06	
-17.5	0.0	0.0	0.4	0.4	0.38	
-21.1	0.0	0.0	0.3	0.3	0.06	
-21.1	0.0	1.0	0.3	0.3	0.38	
-24.7	0.0	1.0	0.1	0.1	0.06	
-24.7	0.0	0.0	0.1	0.1	0.38	
-28.3	0.0	0.0	0.0	0.0	0.06	
-28.3	0.0	1.0	0.0	0.0	0.38	last horizontal tube in inlet column
-28.3	1.0	1.0	0.0	0.0	0.06	switching from inlet to outlet column
-28.3	1.0	0.0	0.0	0.0	0.38	first horizontal tube in outlet column
-24.7	1.0	0.0	0.1	0.1	0.06	
-24.7	1.0	1.0	0.1	0.1	0.38	
-21.1	1.0	1.0	0.3	0.3	0.06	
-21.1	1.0	0.0	0.3	0.3	0.38	
-17.5	1.0	0.0	0.4	0.4	0.06	
-17.5	1.0	1.0	0.4	0.4	0.38	
-13.8	1.0	1.0	0.5	0.5	0.06	
-13.8	1.0	0.0	0.5	0.5	0.38	
-10.2	1.0	0.0	0.6	0.6	0.06	
-10.2	1.0	1.0	0.6	0.6	0.38	
-6.6	1.0	1.0	0.8	0.8	0.06	
-6.6	1.0	0.0	0.8	0.8	0.38	
-3.0	1.0	0.0	0.9	0.9	0.06	
-3.0	1.0	1.0	0.9	0.9	0.38	last horizontal tube
0.0	1.0	1.0	1.0	1.0	0.09	vertical outlet

Figure 99: Tabular description of evaporator (part 2).

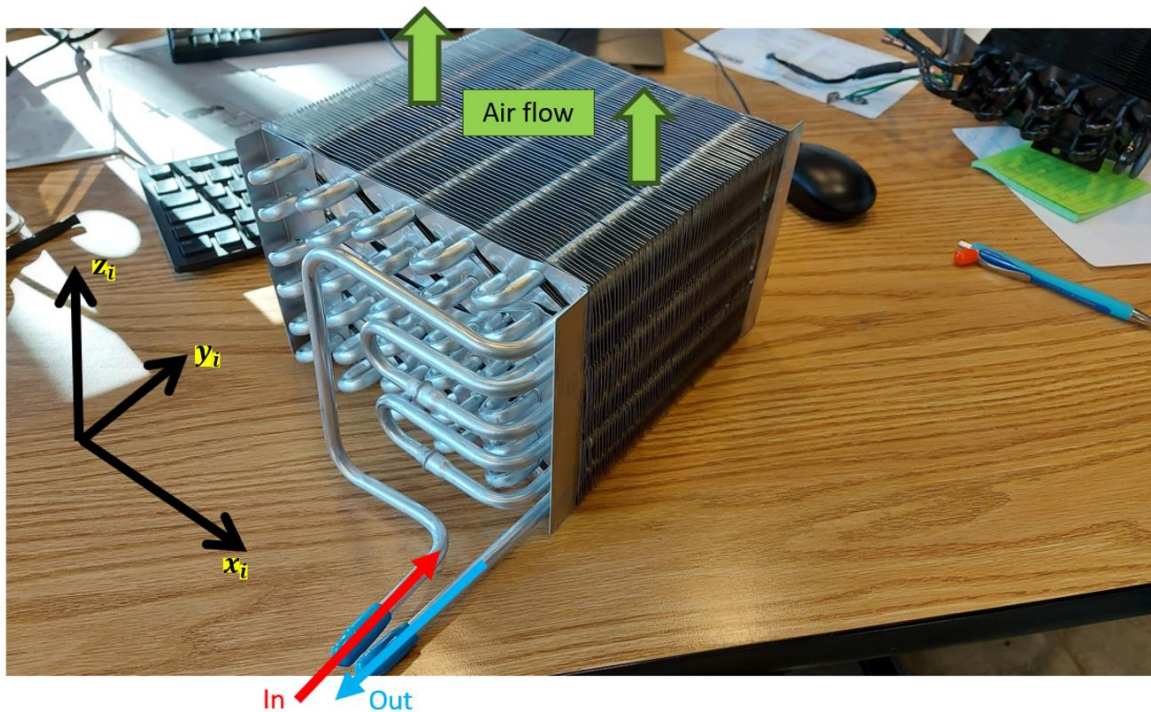


Figure 100: Picture of condenser with inlet and outlet and orientation of inner coordinate system as installed on the inclinable test stand.

8. INSIGHTS FROM MODEL APPLICATION

This chapter applies the orientation dependent heat exchanger model to understand the sinusoidal changes shown in section 5.3. A hypothesis is built by looking at the heat transfer coefficients, the pressure drop and the charge migration.

8.1 Heat transfer coefficient

Figure 57 showed a sinusoidal trend for the heat transfer coefficient when fitted to the datapoints of steady-state sets. The results were obtained by supplying experimentally measured data as inputs to the evaporator model. Then, the tuning factor for the boiling heat transfer coefficient was optimized with the objective of minimizing the difference between the measured and modelled refrigerant side heat transfer rate. This optimization was conducted for each steady-state point throughout all sets. Furthermore, all fitted tuning factors of one set were divided by the tuning factor of the initial steady-state to see a relative change of the tuning factors. These results are displayed in Figure 101 for all three R1234ze(E) datasets. The trends for R134a are similar with the exception of set 4 which showed outliers between 45° and 90° with extremely large tuning factors, probably due to non-convergence of the optimization procedure.

Without exception, all trends are sinusoidal and the lowest absolute and relative changes of the tuning factors were found for the lowest mass flux. However, the largest changes were found for the medium mass flux dataset, breaking the trend of larger absolute changes with higher mass fluxes observed in Figure 58. The normalized heat transfer coefficients in Figure 101 (right) show that the optimization procedure found heat transfer coefficient variations between -40% and +65% for the medium mass flux case. For the low mass flow rate, the range was only -10% to 20%.

It remains to understand cause and effect. A change of the heat transfer coefficient due to the inclination could have altered the evaporation temperature, which would then change the low side pressure, suction density, mass flow rate, evaporator heat transfer rate, condenser heat transfer rate, condensation temperature, subcooling, etc. An inclination dependent heat transfer coefficient for two-phase flow has indeed been observed in the literature and sometimes even been included in correlations. However, in this case it is unlikely that the inclination directly affected the heat transfer coefficient, because 90% of the evaporator coil is horizontal even if the test rig is inclined.

This is because the evaporator is installed with the tubes in parallel to the axis of rotation. Therefore, only the angles of the u-bends change with the inclination of the test rig, but those make up only 10% of the entire length of the evaporator coil. It is more likely that the inclination led to another change which then affected the heat transfer coefficients in the evaporator.

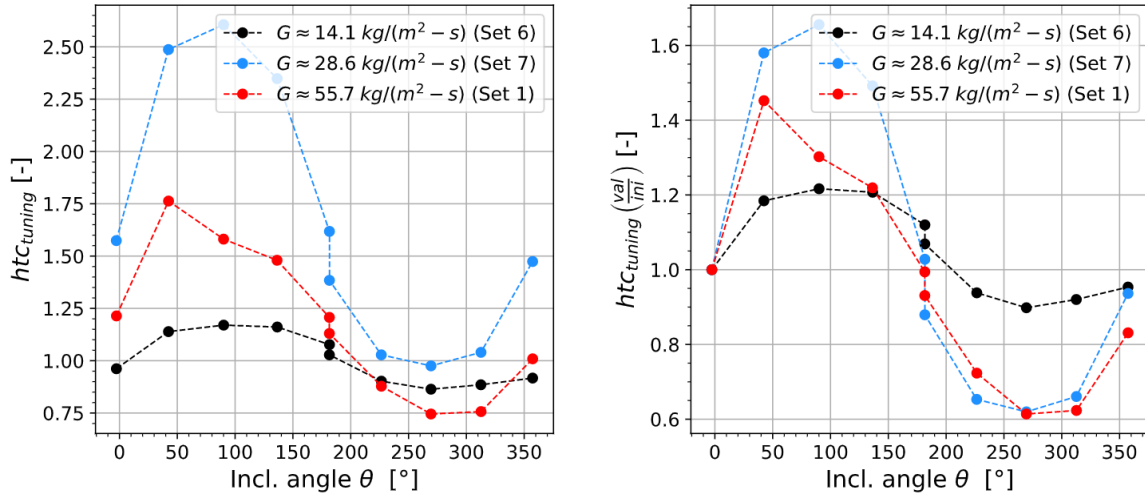


Figure 101: Two-phase heat transfer tuning coefficients for steady-state testing (adapted from Brendel et al. (2022b)).

8.2 Pressure drop

Another explanation for the sinusoidal trends, including the altered heat transfer, could be a charge accumulation in the evaporator. This is indicated by a mismatch of the modelled and measured variation of the pressure drop in the evaporator. Figure 102 shows this in two sets of data:

- The black dots show the measured pressure drop from pressure transducers installed directly at the inlet and outlet of the evaporator. The pressure drop changes from 4 kPa to 5.2 which is a 1.2 kPa difference comparing the horizontal and up-side down position.
- The blue dots show the modeled pressure drop including frictional, gravitational and accelerational effects. It does not show the measured change in total pressure drop of 1.2 kPa, but a change of only up to 0.25 kPa.
- The red dots show the modelled gravitational pressure drop (right hand side y-axis). It is lowest in the horizontal position of the test rig, because in this orientation two-phase refrigerant enters from the top and has completely evaporated approximately at the bottom of the evaporator. After the completion of phase change, only superheated

vapor travels upwards. The liquid phase in the first row of the evaporator causes a negative pressure drop (pressure increase) towards the bottom which the superheated vapor in the second row travelling up cannot exceed. The overall gravitational pressure drop is therefore negative. This is reversed when the evaporator is up-side down. The total change of 0.05 kPa (-0.025 kPa versus 0.25 kPa) is very small, though, because the inlet void fraction is typically around 90%. Hence, there is not much liquid to cause an appreciable pressure drop. Therefore, the trend of the gravitational pressure drop (red dots) does not show up in the total modelled pressure drop (blue dots) which is dictated by the frictional pressure drop and therefore the mass flow rate.

Overall, the experimental data shows a pressure drop of 1.2 kPa more in the up side down orientation compared to the horizontal position. At mostly steady operating conditions, this can only be caused by the gravitational pressure drop component. However, the model predicts only a change of 0.05 kPa for the gravitational pressure drop component. A possible explanation is that liquid accumulated in the evaporator when the inlet was at the bottom and the coil wound upwards. This could significantly decrease the void fraction and increase the pressure drop in the upside down orientation.

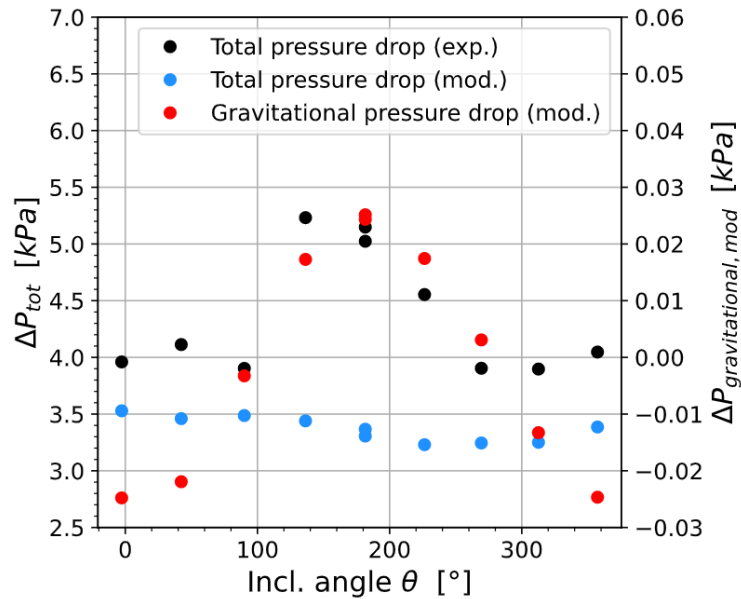


Figure 102: Total experimental and modelled gravitational pressure drop in the evaporator for set 7 (adapted from Brendel et al. (2022b)).

8.3 Modelled and experimental charge migration

For each datapoint, the model provides a charge estimate. Figure 103 (left) shows the modeled charge for all steady-state points of set 1. According to the model, the initial charge was 14 g and varied between 15.2 g and 11.6 g as a function of the inclination angle. The maximum charge migration that occurred during set 1 was 3.6 g and the maximum charge increase compared to the initial state was only 1.2 g.

The charge migration can also be *measured* by integrating the difference of the two mass flow meters over the entire transient data of one set (*cus* will be used as an abbreviation for the cumulative sum in the axis label). The difference is written as

$$\Delta \dot{m}_r = \dot{m}_{liq} - \dot{m}_{suc}, \quad (54)$$

such that a positive value indicates a charge migration from the high-pressure side to the low-pressure side (“filling up the evaporator”). Figure 103 (middle) shows this measured charge migration for set 1 for all steady-state points (all other sets show similar trends). It indicates that approximately 30 g of refrigerant migrated into the evaporator by the angle 135°. After the complete rotation, the charge migration was still at +20 g.

The modeled charge migration was up to +1.2 g for the evaporator but the experimental charge migration was up to +30 g, showing a large discrepancy. These results support an earlier hypothesis that more charge migrated into the evaporator than what the model predicts.

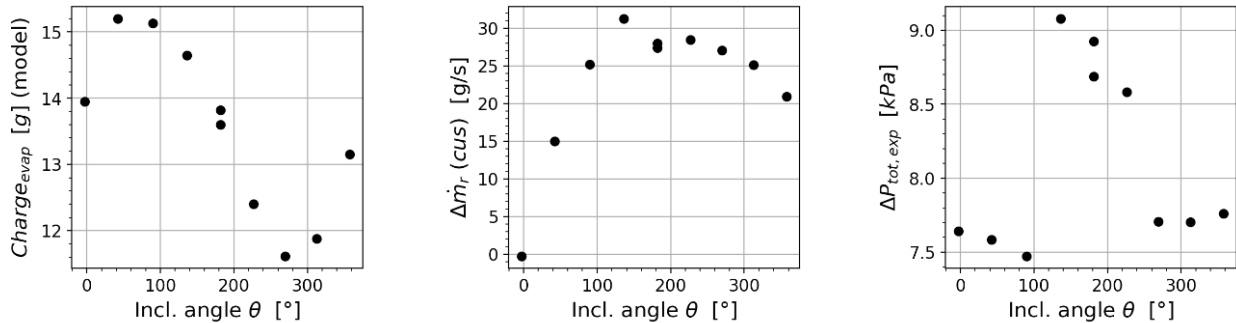


Figure 103: Modeled charge, experimental charge migration and experimental pressure drop for set 1.

Table 20 shows charge migration results based on data and model predictions for all sets. The experimental charge migration was always significantly larger than the theoretical charge migration.

Table 20: Experimental and modelled maximum charge migration.

Set	1	2	3	4	5	6	7
Exp. charge migration [g]	31.8	23.4	15.3	21.5	13.6	17.5	16.9
Mod. charge migration [g]	3.6	5.2	1.7	2.8	1.9	1.1	1.1

A hypothesis for the observed charge migration begins with the use of Figure 104, which shows the coil geometry in the horizontal orientation. Both the inlet and outlet are at the top. The coil winds down, switches columns and then winds up again. Figure 105 shows the cross-section of the evaporator with the tubes cut open. In the left schematic, the flow regimes of a hypothetical initial steady state are shown. Refrigerant enters as a stratified flow and transitions into an annular and mist flow before it leaves the evaporator as superheated refrigerant. Figure 105 (middle) shows the evaporator up-side-down. Charge accumulates in the tubes on the side with refrigerant up-flow. At low mass fluxes, the liquid phase is not carried up as effectively and therefore accumulates in the tubes. Figure 105 (right) shows the evaporator back in the horizontal orientation. Potentially, some accumulation of refrigerant is still at the bottom of the evaporator and not carried out due to the low mass fluxes. This would explain why the cumulative charge migration is always the highest at 180° and still considerably above 0 g at the end of a completed rotation (as shown in Figure 103 (middle)). It would further explain why the measured pressure drop returns to the initial value (Figure 103 (right)) although the charge migration persists. A transparent evaporator on the inclinable test stand could verify a hypothesis like this.



Figure 104: Schematic of evaporator coil for fin-tube heat exchanger.

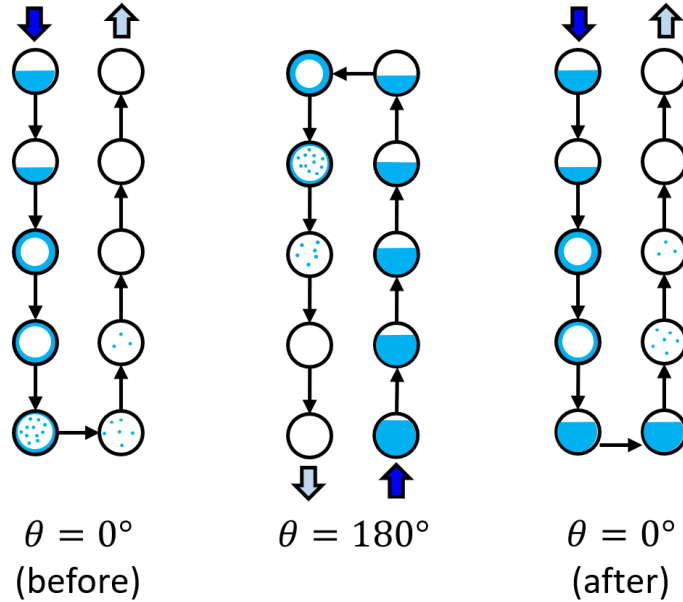


Figure 105: Schematically illustrated charge migration.

8.4 Summary

The orientation dependent heat exchanger model used experimental data from the steady-state testing as inputs. The tuned model predicted the heat transfer, pressure drop and charge accurately for the horizontal position. However, large discrepancies were found for the pressure drop at 180° . The hypothesis to explain this deviation is a charge migration taking place during the experiments which the model cannot predict. The charge migration leads to a different void fraction, thereby changing the pressure drop, heat transfer and evaporation temperature. Conclusions of this chapter can be summarized as follows:

- 1) *A tuning factor for the boiling heat transfer coefficient fitted for each steady-state shows a sinusoidal trend as a function of the inclination angle similar to most measurements (Brendel et al., 2022b).*
- 2) *The pressure drop model does not align with the experimental data in the up-side-down orientation and suggests that a charge migration takes place caused by the inclination changes which is not tracked by the model (Brendel et al., 2022b).*
- 3) *Modeled and measured charge migration have a large discrepancy and also suggest that more refrigerant migrates into the evaporator during the experiments than predicted by the model.*
- 4) *An increased overall liquid fraction (decreased void fraction) in the evaporator is hypothesized for orientations with the inlet at the bottom (section 8.3).*

9. START-UP FLOODING AT NORMAL VERSUS MICROGRAVITY

9.1 Motivation

Liquid slugging from the evaporator into the compressor upon cycle start-up has been suggested as a relevant problem for microgravity. On-off cycling of the refrigerators could repeatedly send liquid into the compressor and eventually lead to a failure. A pump down of the evaporator prior to each off-cycling would be a simple solution for this problem: Before shut down of the cycle, a solenoid valve in the liquid line could close and stop the refrigerant supply to the evaporator. The compressor would operate until there was no more liquid in the low-pressure side. Instead, liquid refrigerant would be stored in the condenser. A check valve in the discharge line would prevent backflow. However, despite this possible workaround, it was decided to investigate liquid flooding in normal and microgravity for a more fundamental understanding (also see reasoning in section 1.4.3).

9.2 Straight-tube testing

During the design of the start-up test rig, shake down experiments with singular, straight and bare (unfinned) tubes instead of an evaporator were conducted. A straight, inclined, transparent tube was filled approximately 50% with liquid refrigerant. It was then closed on the bottom end and the compressor connected to the higher end was started. An example flow visualization from such a test is shown in Figure 106. Image 1 shows the refrigerant before compressor start. Image 2, 3 and 4 show the refrigerant shortly after the compressor started. The decreasing pressure formed vapor bubbles within the liquid phase. The expansion of the bubbles pushed the liquid phase up the tube. If sufficient liquid was in the tube initially, the quickly growing vapor bubbles pushed refrigerant out of the test section and into the compressor. Due to the inclination of the tube, liquid receded backwards against the vapor flow which created waves from surface interactions. It appeared as if much more liquid would have left the tube without the gravity driven backflow of liquid. This increased concerns about liquid flooding in microgravity environments.

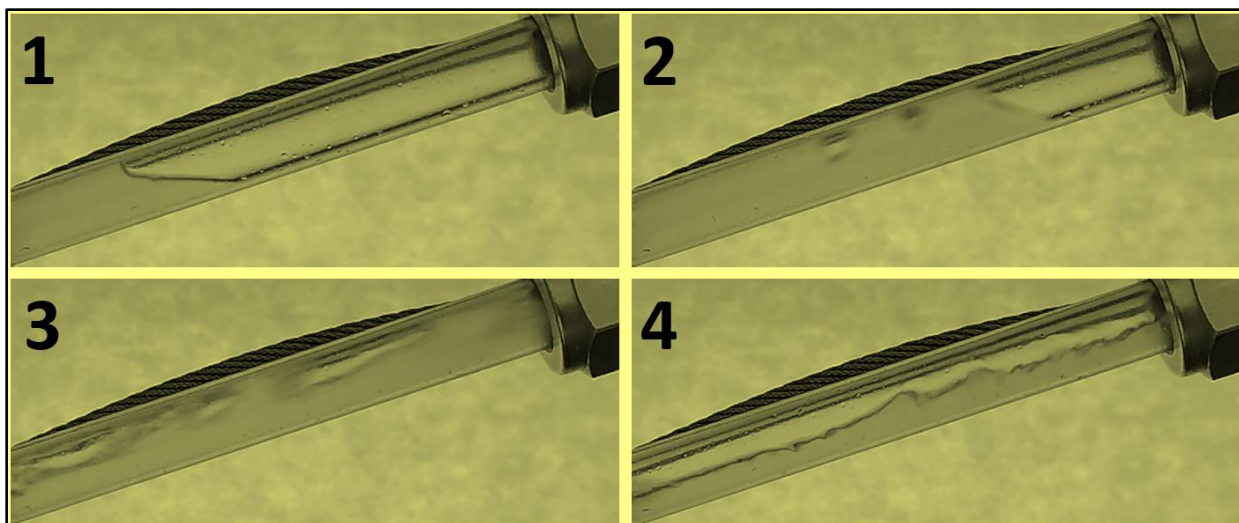


Figure 106: Two-phase flow in straight tube before (image 1) and shortly after compressor start-up (image 2-4) (Brendel et al., 2022a).

9.3 Vertical and horizontal ground-based testing

The parabolic flights were preceded by ground-based testing with the heat exchanger in a vertical and horizontal orientation. Vertical is the orientation shown in Figure 31. Horizontal means the heat exchanger lays on its flat side with the inlet at the bottom and the outlet at the top, albeit the height difference between inlet and outlet is then only approximately 2 centimeters. Beck et al. (2021) summarized findings and described the test setup as it was used for the experiments (not yet in the configuration for parabolic flights, but conceptually equivalent).

As described in section 3.1.1, tests were executed with varying amounts of liquid and a closed inlet. A compressor was started and multiple time-based quantifiers were calculated. Figure 107 shows these results. The left plot shows the time until the start of flooding (test runs where flooding did not occur are not shown). For high charge levels, flooding occurred typically within the first 3 seconds. When the charge was below 55 g, liquid flooding never occurred. At 55 g of charge, flooding was measured to occur anywhere between 7.5 seconds and 17.5 seconds after compressor startup. Overall, for lower charge levels, both the time till start-up and the spread of data increased. No significant difference was found when comparing the horizontal and vertical orientation of the evaporator.

An additional descriptor of the flooding behavior is the elapsed time of liquid flooding (time *elapsed* with liquid at the evaporator outlet). This is shown in Figure 107 (right). Charge

levels < 55 g never led to flooding. For charge levels ≥ 55 g, the elapsed time of liquid flooding increased linearly with the charge. It should be noted that if flooding occurred, it lasted for at least 6 seconds, typically even more than 15 seconds. Like for ΔT_{start} , the horizontal and vertical orientations yielded comparable results.

The last quantifier to observe is $\Delta T_{30\text{ kPa}}$ (the time from starting the compressor until the pressure reached 30 kPa). $\Delta T_{30\text{ kPa}}$ increased linearly from low to high charge levels (Figure 108). The values for the vertical orientation were distinctly higher than for the horizontal orientation. In the vertical orientation, the remaining liquid after initial flooding accumulated in the two bottom tubes and had a relatively small surface area available for heat transfer. This slowed down the evaporation process compared to the horizontal orientation, in which the remaining liquid after the initial flooding was distributed across more tubes and therefore had more surface area available for heat transfer.

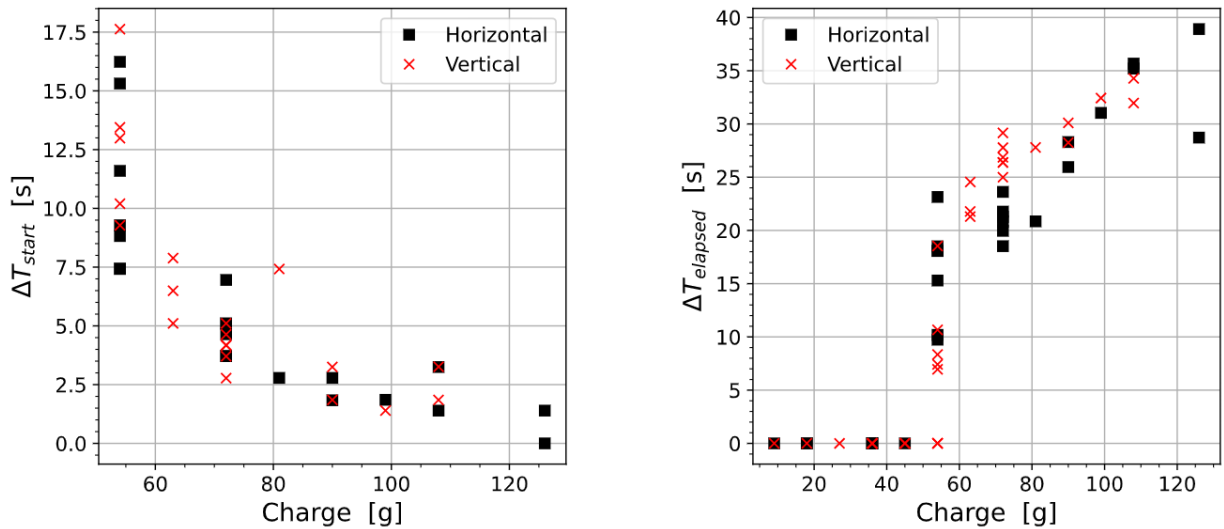


Figure 107: Time till flooding and elapsed time of liquid flooding for standard evaporator in horizontal and vertical orientation (Beck et al., 2021).

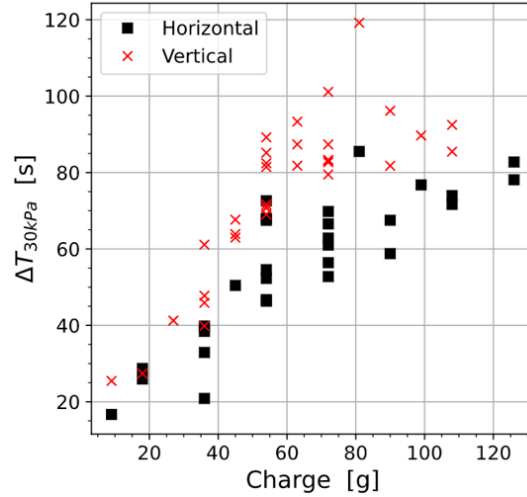


Figure 108: Time till 30 kPa for evaporator in horizontal and vertical orientation (Beck et al., 2021).

9.4 Parabolic flight testing

The preparations for the parabolic flights led to several changes of the test rig. Refrigerant hoses were rerouted, inlet and outlet tubes of the evaporator were adjusted in length and height and a liquid level probe was installed in the refrigerant tank. With the liquid level probe, the charge in the test section was determined much more accurately. Therefore, the results from section 9.3 are not directly comparable to the results from the parabolic flight configuration presented in the following. This section discusses ground-based and parabolic flight results but only using data from the test stand in the parabolic flight configuration.

Figure 109 and Figure 110 show the three quantifiers discussed previously for the standard evaporator (blue) and the transparent evaporator (orange and green). Dots are used for data from ground-based testing at normal gravity and “x”-symbols are used for microgravity data points. A few data points were collected for Lunar and Martian gravity conditions and were plotted in green. For faster testing, the evaporators were emptied only down to a pressure of 70 kPa (previously 30 kPa) so that the third measured quantifier was changed from ΔT_{30kPa} to ΔT_{70kPa} . Figure 109 shows the raw data while Figure 110 shows the data after applying a smoothing algorithm explained in Brendel et al. (2022a) to reduce the scatter. The following conclusions can be drawn:

- Differences between normal gravity and microgravity data were generally small.
- The minimum required charge for flooding decreased from approximately 40 g in normal gravity to 35 g for microgravity.

- $\Delta T_{elapsed}$ was longer for the transparent evaporator in microgravity than for the same evaporator in normal gravity.
- ΔT_{start} was slightly lower in microgravity than in normal gravity for both evaporators.
- The reduced gravity data fit into the general trends of the rest of the data.
- Differences between the two evaporators were most distinct for the quantifier $\Delta T_{70\text{ kPa}}$. The transparent evaporator needed 5 to 10 seconds longer to reach 70 kPa than the standard evaporator. This was probably due to an imperfection in the tube arrangement. A tilted tube in the transparent evaporator created a small liquid pool which always evaporated last. The small pool became very cold and therefore evaporated slowly.
- $\Delta T_{70\text{ kPa}}$ was shorter for the transparent evaporator in microgravity than in normal gravity. In microgravity, the mentioned pool of liquid was smaller or non-existent, thereby allowing a faster rate of evaporation.

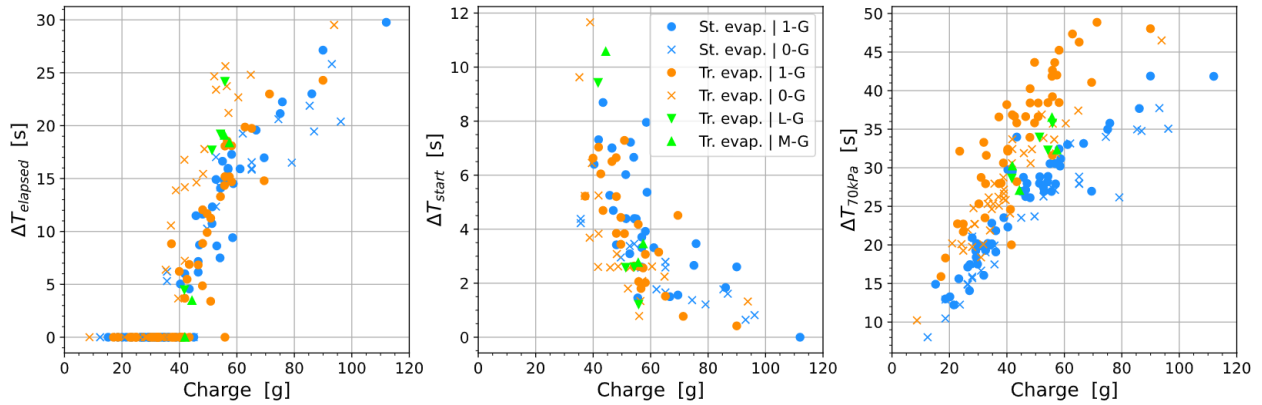


Figure 109: Overlay plot of processed data points for three different quantifiers (Brendel et al., 2022a).

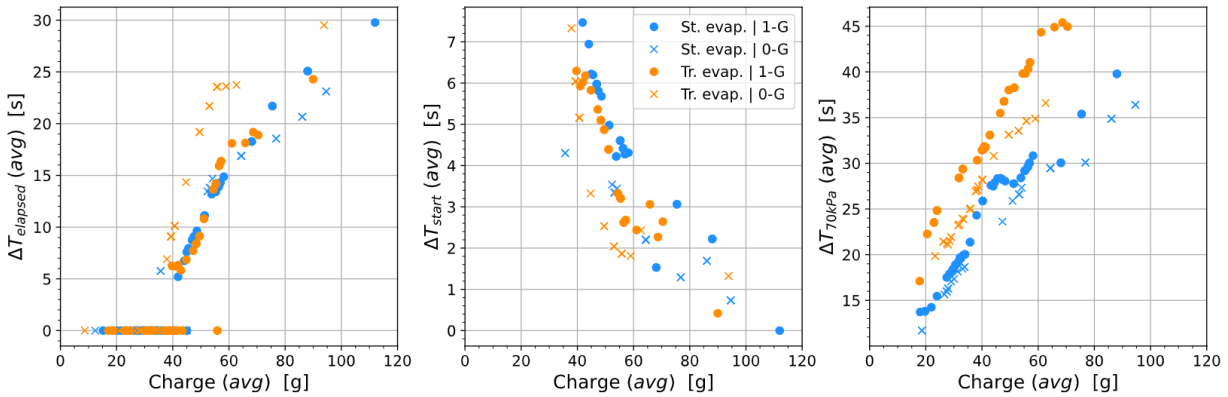


Figure 110: Overlay plot of clustered data points for three different quantifiers (Brendel et al., 2022a).

9.5 Microgravity flow visualizations

The transparent evaporator was recorded with a GoPro camera both in normal gravity and in microgravity. The footage can explain why the differences in the measured quantifiers are so small. Figure 111 shows three tubes shortly after start-up. The middle tube was in the front column where refrigerant flowed down. The other two tubes were in the back column where the refrigerant flowed up and had a lower quality.

In normal gravity, all tubes showed stratified flow regimes. In microgravity, annular flow was observed in two tubes with low quality while a slug flow occurred in the middle tube at a lower quality. Comparing the stratified and annular flow explains why the differences of time-based quantifiers were so small in normal and microgravity: Both flow regimes leave a continuous flow path for any generated vapor. Therefore, the liquid is mostly moved by shear forces between the phases. Hence, the general mechanisms between stratified and annular flow are so similar with respect to flooding, that the overall behavior is comparable. The slug flow in Figure 111 (bottom) is the exception. It can form in the early phase of the start-up when the quality is still low. Then the growing vapor bubbles that fill the tube cross section can indeed push more liquid towards the outlet. This may explain the shorter ΔT_{start} and smaller flooding thresholds measured in microgravity as compared to normal gravity.

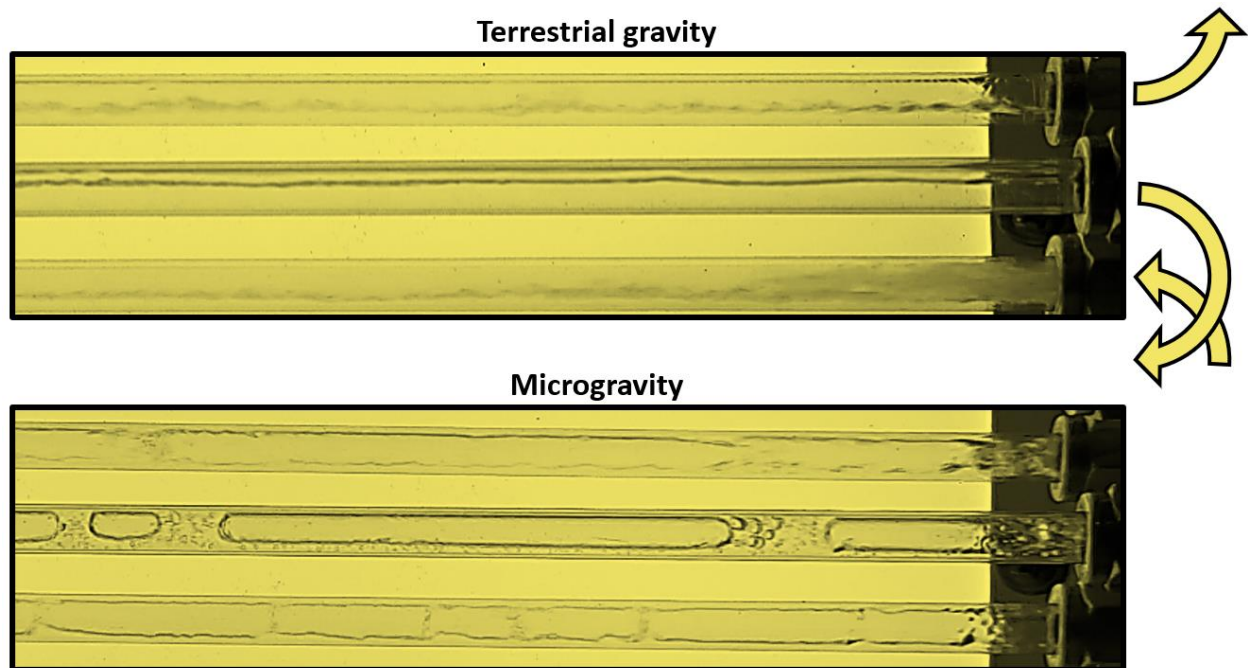


Figure 111: Comparison of flow regimes in terrestrial and microgravity (Brendel et al., 2022a).

9.6 Summary

The experimental investigation of liquid-flooding upon start-up did not confirm the initial hypothesis. The time until liquid flooding started reduced slightly for microgravity but overall, microgravity did not lead to significantly more flooding as compared to normal gravity. Flow visualizations showed that both environments led to a separated flow in which the generated vapor escaped the evaporator with similar interactions with the liquid phase. This does not mean that liquid flooding of the compressor is no concern at all. The experiments investigated start-up where the liquid is in the evaporator but are meaningless for a situation where liquid migrates into the suction line or into the compressor shell in microgravity. Therefore, a pump down approach or another method to prevent liquid from entering the compression chamber is still recommended for space-bound VCCs.

- 1) Flooding behavior in a single straight tube closed on one end upon compressor start-up depends strongly on the inclination angle of the tube. An inclination with accumulation of the liquid phase at the bottom end leads to violent and pulsating liquid movements. A horizontal tube may be emptied without movement of the liquid phase (Beck et al., 2021).*
- 2) Tube insertions can reduce the flooding intensity at start-up by partially obstructing the flow passage (Beck et al., 2021).*
- 3) For an evaporator closed off at the inlet, the time till and the time of liquid flooding upon compressor start-up as a function of the initial charge was similar in the horizontal and vertical orientation. The time until the pressure reached 30 kPa was longer in the vertical orientation (Beck et al., 2021).*
- 4) Flow regimes in the evaporator after compressor start-up are different in microgravity compared to normal gravity (Brendel et al., 2022a).*
- 5) The differences found in the duration of liquid flooding and the time till the first occurrence were negligible when comparing normal gravity and microgravity start-ups. The flow regimes at normal and microgravity both allow vapor to leave the evaporator without pushing large amounts of liquid towards the exit, therefore, the flooding characteristics were similar (Brendel et al., 2022a).*

10. CONCLUSIONS

10.1 Design recommendations for space-bound vapor compression cycles

A number of conclusions were provided at the end of relevant chapters. Those are specific to the chapters and not repeated here. Instead, more comprehensive and practical guidelines from the research are provided. Design recommendations are a topic difficult to navigate, though. After four VCCs operated on orbit, even though with only mediocre success, the fifth failed “*soon after on-orbit operation*” for an unknown reason. Similarly, even though all flight tests were successful with the test rigs described in this dissertation, one should interpret the results carefully and recognize that different systems are not guaranteed to behave equivalently. Nevertheless, an unprecedented dataset as well as broad experience has been accumulated. Ideas and perspectives have formed that should be shared with other researchers. The following subsections are each separated into two parts. The initial *Considerations* part mentions relevant aspects that may require future work to validate or extend. The *Conservative recommendations* part is meant for a hypothetical future engineer wanting to design a reliable vapor compression cycle without additional research and based on results of this dissertation and the open literature.

10.1.1 Liquid ingestion by the compressor

Considerations

Looking at the continuous operation of a vapor compression cycle, liquid flooding is just as unlikely to occur in microgravity as it is in normal gravity. As long as operating conditions or loads are not changed too quickly, there is no risk for flooding. At start-up, liquid is expected to accumulate at the coldest point of the system, which is the evaporator. Microgravity testing showed that liquid flooding from the evaporator upon compressor start-up is as likely to occur in a microgravity environment as in a normal gravity environment.

Conservative recommendation

Since the compressor is the only moving part in the system, its protection is of utmost importance. Combining a pump down approach with a slow ramp-up of the compressor frequency

would minimize the risk of liquid flooding and not penalize the system performance. Valves and control strategies needed for this are simple and widely used in terrestrial applications.

10.1.2 Heat exchanger type

Considerations

Fin-tube heat exchangers, with a long coil and many bends, provide a higher stability for two-phase flow against orientation changes in ground-based testing than flat-plate or helical coil tube-in-tube heat exchangers. However, generally speaking, in the absence of gravity, vapor can push liquid around the circumference of a tube or flow channel more effectively than with gravity. In the evaporator, this enhances the boiling heat transfer. In the condenser, this is expected to have a minor effect. Flat-plate, tube-in-tube and fin-tube heat exchangers should theoretically function well in normal, reduced and microgravity although they show sensitivity to orientation changes at normal gravity.

Conservative recommendation

Flat-plate heat exchangers are extremely orientation sensitive. A tube-in-tube evaporator showed liquid flooding at small inclinations, but a convincing explanation is lacking. Therefore, where easily possible, heat exchangers with long coils and many bends, e.g. fin-tube heat exchangers, are recommended since they showed the highest stability for two-phase flow against inclination changes in the conducted testing.

10.1.3 Heat exchanger sizing

Considerations

Flow boiling and condensation heat transfer coefficients are different when comparing normal gravity and microgravity. However, the change is predicted to be within a range that does not require a different heat exchanger sizing. In particular, with the dominant heat transfer resistance on the secondary fluid side, the heat exchanger can be sized according to terrestrial design tools or testing.

Conservative recommendation

Since a microgravity heat transfer correlation has not been established, the heat exchanger can be designed such that the uncertainty in the heat transfer coefficient has a negligible effect on the overall capacity. Figure 112 shows how a tuning factor for the boiling heat transfer coefficient changes the normalized overall capacity of an evaporator. The curve levels out towards the right. Hence, for sufficiently high heat transfer coefficients, the uncertainty has only a small effect on the overall performance. A heat exchanger should be designed such that the default operating condition lies within this region where the capacity is not diminished much when considering the uncertainty of the heat transfer coefficient.

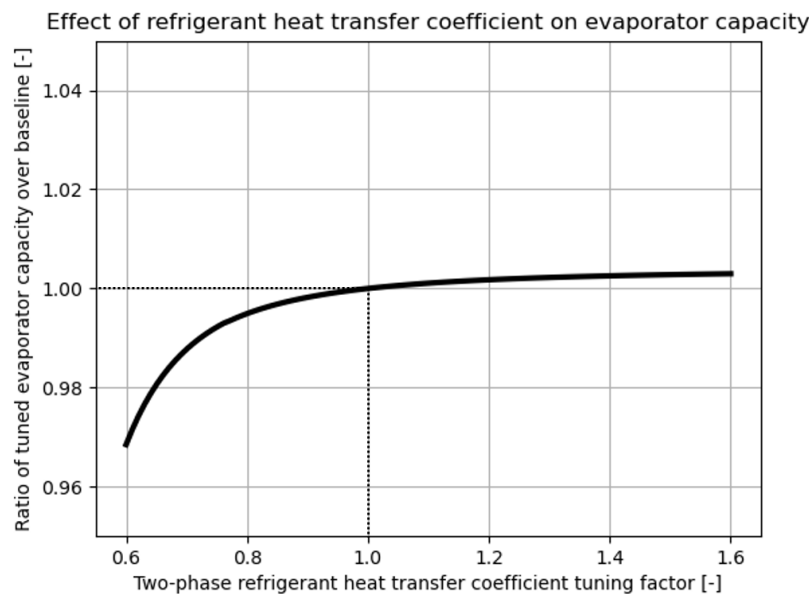


Figure 112: Effect of boiling heat transfer coefficient on heat exchanger capacity.

10.1.4 Compressor type

Considerations

The use of an oil-free compressor removes concerns about proper oil management in microgravity. The concern becomes then the longevity and efficiency of the compressor. Oil lubrication can improve the compressor efficiency and longevity, but most oil-management systems are gravity based. A gravity independent oil-lubrication system for a compressor should be possible but will require prototyping and testing work.

Conservative recommendation

The key for compressor selection should be longevity and efficiency. The compressor must support a complete mission without the need for maintenance by astronauts. If it is not sufficiently efficient, the original motivation for the vapor compression cycle over other cooling technologies is not valid anymore. Prior to being utilized for refrigeration on a multi-year mission without a backup cooling system, any compressor design should have been evaluated for a similar number of years on an orbital spacecraft.

10.1.5 Expansion device

Considerations

No dedicated tests for expansion devices in microgravity have been reported in the open literature. Passive, thermal and electric expansion devices most likely function in microgravity environments like they do in normal gravity environments.

Conservative recommendation

Passive expansion devices (capillary tubes, orifices) cannot support a widely varying range of cooling loads well. Thermal and electronic expansion valve are therefore better suited. An electronic expansion valve is recommended because it could be an additional measure against liquid flooding by closing quickly if there is a risk of liquid flooding according to a simple algorithm.

10.1.6 Inclination testing

Considerations

The inclinable test stand is a very valuable tool. It allows a researcher to become familiar with the gravity sensitivity of a cycle through relatively inexpensive research. Operability through 360 degrees provides the highest possible confidence into seamless microgravity operation available from ground-based testing. Overall, the cycle responses from inclination testing were similar or more intense than the responses from parabolic flight testing.

Conservative recommendation

A vapor compression cycle for space applications should be able to operate at any orientation under normal gravity.

10.1.7 Microgravity testing

Considerations

Different microgravity testing platforms are available to researchers. Parabolic flights offer only 20 seconds of microgravity but can be very useful in understanding the system response. Moreover, the alternating hyper and microgravity provides a good two-phase stability test for a vapor compression cycle. Sounding rockets have severe space and weight constraints and may not be able to facilitate a medium sized vapor compression cycle with a heat source and heat sink. Suborbital testing may therefore be omitted and parabolic flight testing should be a sufficient preparation for usage on an orbital spacecraft.

Conservative recommendation

Generally, the more testing the better. Before operation on an orbital spacecraft, a vapor compression cycle should have been tested at least on parabolic flights.

10.1.8 Gravity independence criteria

Considerations

Gravity independence for a vapor compression cycle is a tempting concept. It initially seems to remove any concerns about the effects of microgravity. However, gravity independence criteria are typically applied to steady-state operation and are not applicable to start-up processes or other transients. Criteria have been only proposed for two-phase flow but not yet for entire systems. Moreover, several criteria would cause excessive pressure drops in the lines and heat exchangers if applied to a VCC, which could have an adverse effect on overall performance. Orientation testing showed that gravity *dependent* systems are not necessarily *negatively* impacted by operation at varying orientations. The findings do not justify the excessive pressure drops that would result from designing for high flow velocities.

Conservative recommendation

Heat exchangers should be designed for a mass flux of $G > 40 \text{ kg}/(\text{m}^2 \cdot \text{s})$. Beyond this threshold, mass flow rate oscillations were unlikely and most instability quantifiers started to level out for the inclinable test stand both for ground-based and parabolic flight testing. The mass flux is not unusually high and not expected to cause unreasonable pressure drops. The threshold of $G > 40 \text{ kg}/(\text{m}^2 \cdot \text{s})$ is based solely on testing with the described setup and may change for other systems.

10.1.9 Thermal gravitational scaling

Considerations

Scaling approaches could be useful tools if they were practical and validated. The design guidelines for reduced and microgravity VCCs could be based on dimensionless numbers and/or inclination testing. The research field is interesting and the goals are very valuable. However, the existence of the promised tools is unclear and may take up disproportionately more resources than other approaches to increase the TRL of space-bound VCCs.

Conservative recommendation

If one is after a conservative recommendation, then thermal gravitational scaling should be avoided. The concept is loaded with uncertainties and pitfalls and design guidelines have not been established.

10.2 Recommendations for future work

Several small ideas came up during the research which were not explored. For example, an *electrical slip ring* could be used instead of the cables currently powering the inclinable test stand. A continuous rotation would then be possible, enabling a new type of experiment, in particular if the rotation was *motorized*. Installing the *transparent evaporator* on the inclinable test stand could verify the hypothesis of charge migration as explained in 8.3. The test stand could also be modified to reach significantly *higher mass fluxes* in search for true system-level gravity independence. Even performing certain inclination procedures backwards could lead to new insights. These ideas

would be interesting but not necessarily impactful. The following is a small collection of only large packages of recommended work which would be a significant contribution to the field.

10.2.1 In depth study of the potential mass savings

Brendel et al. (2021f) presented a quantitative comparison of cooling technologies using the equivalent mass concept. However, the research did not include a detailed comparison of the expected weight of different technologies, as for example a Stirling or Reversed Brayton cooler. Additionally, reliable performance predictions for the different technologies at relevant operating conditions are missing. A literature review that provides better approximations of mass and efficiency would make the comparison more meaningful. Such a study will become important when VCCs with a lower TRL compete against more established cooling technologies.

10.2.2 Insertion of vapor compression cycle into ISS or other orbital spacecraft

One next experimental step for VCCs in microgravity should be operation for an extended period of time in microgravity. This would further increase the confidence into the technology and provide valuable data. In particular, if a VCC were to be used for a multi-year “Mission to Mars” as originally intended, it must have proven itself for a long time in a microgravity environment. The International Space Station is the ideal laboratory for this endeavor. BioServe Space Technologies may act as an important partner in the realization of an ISS testing campaign.

10.2.3 Orientation independent compressor lubrication

Oil lubrication of a refrigeration compressor generally increases the efficiency, reduces the heat generation and increases the longevity. These potential improvements warrant the investigation of a gravity independent oil-management system. Oil could be carried by the refrigerant through the cycle and reach the compressor as a mist in the superheated refrigerant. Alternatively, a compressor shell could be formed tightly such that oil is hit and distributed by rotating parts regardless of its location. Either realization could also be interesting for terrestrial applications.

10.2.4 Pump down approach

A pump down approach has been proposed multiple times to avoid liquid reaching the compressors. It was briefly described in section 7.5.2. However, on the inclinable test stand, the pump down was facilitated with manually operated ball valves and tested only a few times. Systematic research could automate the process and prove a successful start-up of the cycle at any orientation. The research would produce the minimal set of required hardware and control logic and show systematically that the pump-down approach is simple and useful.

10.2.5 Removal of condensed water from heat exchanger

A heat exchanger that condenses water vapor operates successfully on the International Space Station and could be a model for a similar heat exchanger in a VCC. However, several questions are unclear, since the condensing heat exchanger is for air-conditioning and not for a refrigerator/freezer. Can the prototype on the ISS be adapted to serve refrigeration and freezing applications? What if frost builds up? Can it be packaged tightly for a small refrigerator? And last but not least, is there any better way to remove condensed water from the evaporator? Condensed water/ice must be removed from the evaporator coil somehow and it is not as trivial in microgravity as in normal gravity. Hence, this research would make an important contribution to the field.

10.3 Summary

The demand for cooling on spacecraft is expected to increase. In particular, manned missions of long duration would benefit from a large storage capacity for refrigerated or frozen food. A vapor compression cycle outperforms other typically used cooling technologies with respect to the coefficient of performance, and could therefore lead to valuable equivalent mass savings through a reduced energy consumption. However, only very few vapor compression cycles have ever operated in microgravity and the technology readiness level is still low. Two vapor compression cycle test stands were leveraged on parabolic flights and in ground-based orientation testing to increase the understanding of and the confidence in the technology for reduced and microgravity applications.

The first test stand was a heavily instrumented, four component vapor compression refrigeration cycle. Design modifications enabled its continuous operation through 360 degrees of

rotation in ground-based testing. Flat-plate heat exchangers were found to be the most orientation sensitive and fin-tube heat exchangers the least. Adverse orientations created mild oscillations measurable in the evaporation pressure and suction line mass flow rate and led to experimentally determined charge migrations between the heat exchangers. Comparing the steady-state operation at varying angles and for different sets of operating conditions, an increasing mass flux showed an increased absolute impact of the orientation changes judging by the mean deviation (MDV) but a constant relative impact judging by the inclination impact ratio (IIR) when observing the refrigerant side heat transfer rate. A strongly decreasing trend with mass flux was found in dynamic testing for the relative impact of orientation changes on the evaporator heat transfer rate measured on the heat source side. This trend was a smooth function of the mass flux across two different test setup configurations. A minimum mass flux of $40 \text{ kg}/(\text{m}^2 \cdot \text{s})$ is recommended based on these results for a stable operation. Operating beyond this threshold also avoided oscillations which had been observed during steady-state testing.

The same test stand performed robustly through alternating gravity levels during four parabolic flights, totaling 122 parabolas. For example, for any set of 5 parabolas which was recorded with the test stand at steady-state, the evaporation temperature fluctuated within a band of at most 3.4 K due to the different gravity levels. Changes of the evaporator inlet flow regime were recorded clearly through a transparent tube for two different mass flow rates. Stratified flow in normal gravity changed to either slug flow for low flow rates or to annular flow for high flow rates in microgravity. Each onset of microgravity was accompanied by a sharp increase of the condensation pressure by 1 to 3%, probably due to a depreciated heat transfer coefficient in the absence of gravity. Across most conducted tests, inclination testing led to similar or stronger changes compared to parabolic flight testing.

The second test stand quantified liquid flooding from the evaporator into the compressor at cycle start-up with time-based measures. A clear difference of flow regimes was observed in a transparent evaporator, but the overall liquid flooding quantifiers were similar for normal, reduced and microgravity. Hence, given that the liquid phase was in the evaporator at cycle start-up, flooding thresholds were found to be similar with and without gravity. A protection of the compressor against liquid flooding is still recommended, since microgravity will allow liquid refrigerant to migrate in the tubing and could accumulate in the suction line or at the outlet of the evaporator.

Future VCCs for space applications should be built with some liquid slugging protection as for example a pump-down before the cycle is shut down or a slow compressor frequency ramp when starting the cycle. Heat exchangers can be sized to reduce the impact of an altered heat transfer coefficient due to microgravity. Ground-based inclination testing is recommended for space-bound vapor compression cycles but cannot completely replace microgravity testing. Orientation independence is unlikely to be achieved with moderate flow velocities and pressure drops. The compressor as the component with greatest risk of damage should be reliable and of high longevity since repairs will be difficult if not impossible in a spacecraft.

Future work should continue the quantitative evaluation of potential mass savings. A refinement of models and input parameters could be important to correctly prioritize future work. Removing water condensate from the evaporator is a relevant topic not addressed in this dissertation. Future work should add orientation and microgravity testing with different cycle configurations and sizes to confirm the thermodynamic stability presented in this dissertation. While additional parabolic flight testing is seen as valuable, the continuous operation on an orbital spacecraft would be another significant step for the maturity of spaceborne vapor compression cycles.

Selected data, code, pictures and videos were released through an online repository (Brendel, 2021).

REFERENCES

- Anderson, M. S., Ewert, M. K., & Keener, J. F. (2018). *Life Support Baseline Values and Assumptions Document* (Technical Report NASA/TP-2015-218570/REV1).
<https://ntrs.nasa.gov/search.jsp?R=20150002905>
- Azzolin, M., Bortolin, S., Le Nguyen, L. P., Lavieille, P., Glushchuk, A., Queeckers, P., Miscevic, M., Iorio, C. S., & Del Col, D. (2018). Experimental investigation of in-tube condensation in microgravity. *International Communications in Heat and Mass Transfer*, 96, 69–79.
<https://doi.org/10.1016/j.icheatmasstransfer.2018.05.013>
- Baba, S., Sakai, T., Sawada, K., Kubota, C., Wada, Y., Shinmoto, Y., Ohta, H., Asano, H., Kawanami, O., Suzuki, K., Imai, R., Kawasaki, H., Fujii, K., Takayanagi, M., & Yoda, S. (2011). Proposal of experimental setup on boiling two-phase flow on-orbit experiments onboard Japanese experiment module “KIBO.” *Journal of Physics: Conference Series*, 327, 012055. <https://doi.org/10.1088/1742-6596/327/1/012055>
- Balasubramaniam, R., Ramé, E., & Motil, B. J. (2019). *Microgravity Liquid-Gas Two-Phase Flow: Review of Pressure Drop and Heat Transfer Correlations and Guidelines for Equipment Operability*. NASA.
- Balistreri, S. F., Mobley, G. L., & Son, C. H. (2018). *The CDRA Snorkel: Developing a Flow Diversion Device to Protect the Carbon Dioxide Removal Assembly from Liquid Water Ingestion*. 12.
- Beck, P. E., Brendel, L. P. M., Ore, J. P., Braun, J. E., & Groll, E. A. (2021). Investigation of two-phase refrigerant behavior upon cycle startup for compressor protection in microgravity applications. *Purdue Conferences 2020One*.

- Bockel, J.-M. (2018). *The Future of Space Industry* [General Report]. NATO Parliamentary Assembly. <https://www.nato-pa.int/download-file?filename=sites/default/files/2018-12/2018%20-%20THE%20FUTURE%20OF%20SPACE%20INDUSTRY%20-%20BOCKEL%20REPORT%20-%2020173%20ESC%2018%20E%20fin.pdf>
- Bower, J. S., & Klausner, J. F. (2006). Gravity independent subcooled flow boiling heat transfer regime. *Experimental Thermal and Fluid Science*, 31(2), 141–149. <https://doi.org/10.1016/j.expthermflusci.2006.03.024>
- Brauner, N. (1990). On the relations between two-phase flows under reduced gravity and earth experiment. *International Communications in Heat and Mass Transfer*, 17(3), 271–281. [https://doi.org/10.1016/0735-1933\(90\)90092-X](https://doi.org/10.1016/0735-1933(90)90092-X)
- Brendel, L. (2021). *VCC in Zero-G* [Online repository]. Vapor Compression Refrigeration in Microgravity - Supplemental Material for Dissertation. <https://1drv.ms/u/s!Akpdf-IBYb0m3TOkS1KYbpafq0T8?e=3apbop>
- Brendel, L. P. M., Beck, P. E., Ore, J. P., Braun, J. E., & Groll, E. A. (2022a). Liquid Flooding from an Evaporator upon Compressor Start-up in Microgravity. *To Be Determined*, 16.
- Brendel, L. P. M., Braun, J. E., & Groll, E. A. (2019a). Matching Testing Possibilities and Needed Experiments for Successful Vapor Compression Cycles in Microgravity. *3rd International Conference for Refrigeration and Cryogenic Engineering, Air Conditioning and Life Support Systems*.
- Brendel, L. P. M., Braun, J. E., & Groll, E. A. (2020a). Similar Fluids Based on Thermal Gravitational Scaling using Dimensionless Numbers for Three Example Applications. *Thermal & Fluids Analysis Workshop (TFAWS) 2020*.

- Brendel, L. P. M., Braun, J. E., & Groll, E. A. (2020b). Test Stand to Investigate a Vapor Compression Cycle at Varying Orientation and First Experimental Results. *IIR Rankine 2020 Conference - Advances in Cooling, Heating and Power Generation*.
<https://doi.org/10.18462/iir.rankine.2020.1201>
- Brendel, L. P. M., Braun, J. E., & Groll, E. A. (2020c). Unpublished manuscript: Review of Gravity Independence Criteria for Two-Phase Flow. *International Journal of Heat and Mass Transfer*.
- Brendel, L. P. M., Braun, J. E., & Groll, E. A. (2021a). Comparison of Gravity Independence Criteria for Two-Phase Flow. *Journal of Thermophysics and Heat Transfer*, 35(4), 830–842. <https://doi.org/10.2514/1.T6202>
- Brendel, L. P. M., Caskey, S. L., Braun, J. E., & Groll, E. A. (2021b). Characterizing Steady State Compressor Performance by Using Transient Test Data. *Purdue Conferences 2020One*.
- Brendel, L. P. M., Caskey, S. L., Braun, J. E., & Groll, E. A. (2021c). Experimentally Observed Anomalies from Inclining a Vapor Compression Cycle. *Purdue Conferences 2020One*.
- Brendel, L. P. M., Caskey, S. L., Braun, J. E., & Groll, E. A. (2021d). Similarity of Two-phase Cycle Stability Between Ground-Based Inclination and Parabolic Flight Experiments. *Thermal & Fluids Analysis Workshop (TFAWS) 2021*.
- Brendel, L. P. M., Caskey, S. L., Braun, J. E., & Groll, E. A. (2022b). Sinusoidal Response of Vapor Compression Cycle to Lasting Orientation Changes. *International Journal of Refrigeration*.
- Brendel, L. P. M., Caskey, S. L., Braun, J. E., & Groll, E. A. (2022c). Submitted manuscript: Thermodynamic Stability of a Liquid-to-Liquid Vapor Compression Cycle Against Changes of the Inclination Angle. *Journal of Thermal Science and Engineering Progress*.

- Brendel, L. P. M., Caskey, S. L., Braun, J. E., & Groll, E. A. (2021e). Stability Against Orientation Changes of a Vapor Compression Cycle in Two Configurations. *DKV Meeting 2021*, 9.
- Brendel, L. P. M., Caskey, S. L., Braun, J. E., Groll, E. A., Braun, J. E., & Groll, E. A. (2022d). Submitted manuscript: Vapor Compression Refrigeration Cycle Testing on Parabolic Flights: Heat Exchanger Performance. *International Journal of Refrigeration*.
- Brendel, L. P. M., Caskey, S. L., Ewert, M. K., Gomes, A. R., Braun, J. E., & Groll, E. A. (2021f). Equivalent Mass Benefits from Employing Vapor Compression Refrigeration on Spacecraft. *International Conference on Environmental Systems 2021*, 12.
- Brendel, L. P. M., Caskey, S. L., Ewert, M. K., Hengeveld, D., Braun, J. E., & Groll, E. A. (2021g). Review of vapor compression refrigeration in microgravity environments. *International Journal of Refrigeration*, 123, 169–179. <https://doi.org/10.1016/j.ijrefrig.2020.10.006>
- Brendel, L. P. M., Caskey, S. L., Ewert, M. K., Lee, F., Braun, J. E., & Groll, E. A. (2022e). Submitted manuscript: Vapor Compression Refrigeration Cycle Testing on Parabolic Flights: Cycle Performance and Stability. *International Journal of Refrigeration*.
- Brendel, L. P. M., Hengeveld, D., Braun, J. E., & Groll, E. A. (2019b). *Vapor Compression Cycles for High Component Heat Loads on Next-Generation Small Satellites*. 11th International Conference on Compressors and their Systems, London, England. <https://doi.org/10.1088/1757-899X/604/1/012036>
- Brendel, L. P. M., Zhang, X., Braun, J. E., & Groll, E. A. (2019c). *Modelling of a Vapor Compression Cycle Independent of Orientation and Gravity*. 9th International Conference on Compressors and Refrigeration, Xian, China.
- Bryce Space. (2017). *Global Space Industry Dynamics—Research Paper* [Report to Government]. https://brycetechnology.com/downloads/Global_Space_Industry_Dynamics_2017.pdf

- Carter, L. (2017). *Challenges with Operating a Water Recovery System (WRS) in the Microgravity Environment of the International Space Station (ISS)*.
- Churchill, S. W. (1977). Friction Factor Equation Spans All Fluid-Flow Regimes. *Chemical Engineering (New York)*, 84(24), 91–92.
- Cole, G. S., Scaringe, R. P., Grzyll, L. R., & Ewert, M. K. (2006). *Development of a Gravity-Insensitive Heat Pump for Lunar Applications*. Space Technology and Applications Meeting.
- Cooper, M., Perchonok, M., & Douglas, G. L. (2017). Initial assessment of the nutritional quality of the space food system over three years of ambient storage. *Npj Microgravity*, 3(1). <https://doi.org/10.1038/s41526-017-0022-z>
- Crowley, C. J., & Izenson, M. G. (1989). *Design Manual for Microgravity Two-Phase Flow and Heat Transfer (U)* (AD-A214 937; p. 141). Air Force Astronautics Laboratory.
- Crowley, C. J., & Sam, R. G. (1991). Microgravity experiments with a simple two-phase thermal system. *AIP Conference Proceedings*, 217, 1207–1213. <https://doi.org/10.1063/1.40166>
- deFiebre, J., & Guzik, M. (2019, August). *Assembly and Integrated Systems Testing for the Flow Boiling and Condensation Experiment (FBCE)* [Workshop Paper Session]. Thermal & Fluids Analysis Workshop, Hampton, VA.
- Del Col, D., Bortolato, M., Azzolin, M., & Bortolin, S. (2014). Effect of inclination during condensation inside a square cross section minichannel. *International Journal of Heat and Mass Transfer*, 78, 760–777. <https://doi.org/10.1016/j.ijheatmasstransfer.2014.06.078>
- Delil, A. A. M. (1989). Two-Phase Heat Transport Systems for Spacecraft Scaling with Respect to Gravity. *Journal of Aerospace*. <https://doi.org/10.4271/891467>

- Delil, A. A. M. (2001). Fundamentals of gravity level dependent two-phase flow and heat transfer—A tutorial. *AIP Conference Proceedings*, 552, 209–220.
<https://doi.org/10.1063/1.1357927>
- Delil, A. M. M. (1991). *Thermal gravitational modelling and scaling of two-phase heat transport systems similarity considerations and useful equations predictions versus experimental results*. 579–599.
- Domitrovic, R. E., Chen, F. C., Mei, V. C., & Spezia, A. L. (2003). Microgravity heat pump for space station thermal management. *Habitation (Elmsford, N.Y.)*, 9(1–2), 79–88.
- El Fil, B., Boman, D. B., Tambasco, M. J., & Garimella, S. (2021). A comparative assessment of space-conditioning technologies. *Applied Thermal Engineering*, 182, 116105.
<https://doi.org/10.1016/j.applthermaleng.2020.116105>
- European Space Agency. (2014). *ESA User Guide to Low Gravity Platforms* (Issue 3, Revision 0). European Space Agency.
- Foster, T. G. (1967). Compressor Protection. *ASHRAE Journal*, 9(5), 59–62.
- Gaseor, T., Hunter, R., & Hamill, D. (1996). *Advanced Refrigerator/Freezer Technology Development* (Contractor Report OSS Document No. 22100-70001 prepared for NASA Lewis Research Center). Oceaneering Space Systems.
- Gerner, H. J. V., Donk, G. V., Pauw, A., Es, J. V., & Agency, E. S. (2015). A Heat Pump for Space Applications. *45th International Conference on Environmental Systems*. 45th International Conference on Environmental Systems.
- Ginwala, K. (1961). *Engineering study of vapor cycle cooling equipment for zero-gravity environment* (Technical Report TR 60-776; p. 256). Wright-Patterson Air Force Base.
<http://contrails.iit.edu/files/original/WADDTR60-776.pdf>

- Goerig, K. (2001). *Data Book: Service Module (SM), Basic*. NASA/International Liaison Office.
- Goodman, J. R., & Grosveld D.E., F. W. (2015). *Acoustic and noise control in space crew compartments*. NASA.
- Grzyll, L. R., & Cole, G. S. (2000). *A Prototype Oil-Less Compressor for the International Space Station Refrigerated Centrifuge*. International Compressor Engineering Conference, West Lafayette, Indiana.
- Hartley, G. (2018, April). *Cold Stowage: An ISS Project* [Oral/Visual Presentation]. 43rd Payload Operations Interface Working Group (POIWG), Huntsville, AL.
<https://ntrs.nasa.gov/search.jsp?R=20180002941>
- Hurlbert, K. M. (2000). *Flow Dynamics for Two-Phase Flow in Partial Gravities* [PhD Thesis]. University of Houston.
- Hurlbert, K. M., Witte, L. C., Best, F. R., & Kurwitz, C. (2004). Scaling two-phase flows to Mars and Moon gravity conditions. *International Journal of Multiphase Flow*, 30(4), 351–368.
<https://doi.org/10.1016/j.ijmultiphaseflow.2004.01.004>
- Hye, A. (1985, June 19). Use of two-phase flow heat transfer method in spacecraft thermal system. *20th Thermophysics Conference*. 20th Thermophysics Conference, Williamsburg, VA, U.S.A. <https://doi.org/10.2514/6.1985-1050>
- Jimenez, J. (2019). Compressors used for (E)OR/F and LSLE. *Personal Communication, KBRwyle*.
- Johnston, R. S., & Dietlein, L. F. (1977). *Biomedical Results from Skylab* (NASA-SP-377). National Aeronautics and Space Administration.
- Klein, S. A., & Alvarado, F. L. (2002). *Engineering Equation Solver (EES)* (Version V10.643) [Computer software]. F-Chart Software. <http://fchartsoftware.com/ees/>

- Konishi, C., Mudawar, I., & Hasan, M. M. (2013). Criteria for negating the influence of gravity on flow boiling critical heat flux with two-phase inlet conditions. *International Journal of Heat and Mass Transfer*, 65, 203–218. <https://doi.org/10.1016/j.ijheatmasstransfer.2013.05.070>
- Lipson, D. (1982). *STS-4 Postflight Final Report for the Vapor Phase Compression Refrigerator/Freezer* (Technical Information Release DTO No. 467).
- Liu, Z., & Soedel, W. (1995). A Mathematical Model for Simulating Liquid and Vapor Two-Phase Compression Processes and Investigating Slugging Problems in Compressors. *HVAC&R Research*, 1(2), 99–109. <https://doi.org/10.1080/10789669.1995.10391312>
- Manieri, P., Brinckmann, E., & Brillouet, C. (1996). The BIORACK facility and its performance during the IML-2 Spacelab mission. *Journal of Biotechnology*, 47(2–3), 71–82.
- Matney, M. L., Boyd, J. F., Covington, P. A., Leano, H. J., Limero, T. F., & James, J. T. (1993). Air Quality Assessments for Two Recent Space Shuttle Flights. *Aviation, Space and Environmental Medicine*, 64(11).
- Morton, R. D., Bergeron, D., Hurlbert, K. M., Ewert, M., & Cornwell, J. (1998). Proof of Concept High Lift Heat Pump for a Lunar Base. *SAE Transactions*, 107, 678–691. <https://doi.org/10.4271/981683>
- Mudawar, I. (2017). Flow Boiling and Flow Condensation in Reduced Gravity. In *Advances in Heat Transfer* (Vol. 49, pp. 225–306). Elsevier. <https://doi.org/10.1016/bs.aiht.2017.06.002>
- NASA. (2018a). *Life Sciences Laboratory Equipment Refrigerator/Freezer Hardware Information*. Life Sciences Data Archive. <https://lsda.jsc.nasa.gov/Hardware/hardw/18>

- NASA. (2018b). *Orbiter Refrigerator/Freezer Hardware Information Guide*. Life Sciences Data Archive. <https://lsda.jsc.nasa.gov/Hardware/hardw/64>
- NASA. (2019, March 31). *Refrigerated Centrifuge (RC)*. International Space Station. https://www.nasa.gov/mission_pages/station/research/experiments/explorer/Investigation.html?#id=629
- NASA. (2021, July 31). *Technology Readiness Level*. TRL - Technology Readiness Level. https://www.nasa.gov/directorates/heo/scan/engineering/technology/technology_readiness_level
- Niederwieser, T., Anthony, J., Darnell, A., King, G., Koenig, P., Stodieck, L., Wright, J., Gahbler, P., & Hoehn, A. (2015). SABL – An EXPRESS locker-sized incubator for performing biological experiments onboard the ISS. *45th Conference on Environmental Systems*, 17.
- O'Neill, L. E., Park, I., Kharangate, C. R., Devahdhanush, V. S., Ganesan, V., & Mudawar, I. (2017). Assessment of body force effects in flow condensation, part II: Criteria for negating influence of gravity. *International Journal of Heat and Mass Transfer*, 106, 313–328. <https://doi.org/10.1016/j.ijheatmasstransfer.2016.07.019>
- Ore, J. P. (2021, April). *Purdue-DC-Nanogrid-House-Project* [GitHub]. Purdue-DC-Nanogrid-House-Project. <https://github.com/Purdue-DC-Nanogrid-House-Project/eco-iot-daq>
- Pike, J. (2021, August 12). *Purdue-designed heat transfer experiment arrives at International Space Station*. Purdue University News. <https://www.purdue.edu/newsroom/releases/2021/Q3/purdue-designed-heat-transfer-experiment-arrives-at-international-space-station.html>
- Ravex, A., Trollier, T., Sentis, L., Durand, F., & Crespi, P. (2005). Cryocoolers Development and Integration for Space Applications at Air Liquide. *Twentieth International Cryogenic*

- Engineering Conference (ICEC20)*, 427–436. <https://doi.org/10.1016/B978-008044559-5/50101-0>
- Rohleder, C. S., Bansal, K., Shaffer, B., & Groll, E. A. (2018). *Vapor Compression Refrigeration System for Cold Storage on Spacecrafts*. International Refrigeration and Air Conditioning Conference.
- Ross, R. G. (2006). Aerospace Coolers: A 50-Year Quest for Long-Life Cryogenic Cooling in Space. In K. D. Timmerhaus & R. P. Reed (Eds.), *Cryogenic Engineering* (pp. 225–284). Springer New York. https://doi.org/10.1007/0-387-46896-X_11
- Rouleau, R. L. (Uni. of. Alab.). (2019). Features of GLACIER, MERLIN and Polar. *Personal Communication*.
- Sardesai, R. G., Owen, R. G., & Pulling, D. J. (1981). Flow regimes for condensation of a vapour inside a horizontal tube. *Chemical Engineering Science*, 36(7), 1173–1180. [https://doi.org/10.1016/0009-2509\(81\)85065-8](https://doi.org/10.1016/0009-2509(81)85065-8)
- Shah, M. . M. (1982). Chart correlation for saturated boiling heat transfer: Equations and further study. *ASHRAE Tr*, 88(1), 185–196.
- Shah, M. M. (2016). Comprehensive correlations for heat transfer during condensation in conventional and mini/micro channels in all orientations. *International Journal of Refrigeration*, 67, 22–41. <https://doi.org/10.1016/j.ijrefrig.2016.03.014>
- Siewert, H. G. (1972). *Compressor Tolerance to Liquid Refrigerant*. International Compressor Engineering Conference, West Lafayette, IN, USA. <https://docs.lib.purdue.edu/icec/37/>
- Singh, R., Nieter, J. J., & Prater Jr., G. (1986). An Investigation of the Compressor Slugging Phenomenon. *ASHRAE Transactions* 1986, 92.

- Smith, S. M., Zwart, S. R., Kloeris, V., & Heer, M. (2009). *Nutritional Biochemistry of Space Flight*. Nova Science Publishers.
- Sunada, E., Miller, J., Ganapathi, G. B., Birur, G., & Park, C. (2008). Start-Up Characteristics and Gravity Effects on a Medium/High-Lift Heat Pump using Advanced Hybrid Loop Technology. *38th SAE International Conference on Environmental Systems*.
<https://doi.org/10.4271/2008-01-1959>
- Swagelok. (2007). *Valve Sizing Technical Bulletin*. Swagelok Company.
<https://www.swagelok.com/downloads/webcatalogs/EN/MS-06-84.PDF>
- Taitel, Y., & Dukler, A. E. (1976). A model for predicting flow regime transitions in horizontal and near horizontal gas-liquid flow. *American Institute for Chemical Engineering Journal*, 22(1), 47–55. <https://doi.org/10.1002/aic.690220105>
- Ungar, E. K. (1998). Selection of a Gravity Insensitive Ground Test Fluid and Test Configuration to Allow Simulation of Two-Phase Flow in Microgravity. *7th AIAA/ASME Joint Thermophysics and Heat Transfer Conference*, 3, 71–78.
- University of Oxford. (2020, July). *Cryocoolers for space applications*. Cryocoolers for Space Applications. <http://www2.eng.ox.ac.uk/cryogenics/research/cryocoolers-for-space-applications>
- Wagner, E. B. (2019, September 16). *New Shephard—Payloads*. CSF Microgravity Symposium, Tempe, Arizona.
- Wieland, P. O. (1998). *Living Together in Space: The Design and Operation of the Life Support Systems on the International Space Station* (NASA/TM-1998-206956/Volume II). NASA, George C. Marshall Space Flight Center.

- Williams, J. L., Keshock, E. G., & Wiggins, C. L. (1973). Development of a Direct Condensing Radiator for Use in a Spacecraft Vapor Compression Refrigeration System. *Journal of Engineering for Industry*, 95(4).
- ZERO-G. (2020). *ZERO-G Research—Program package*.
- ZERO-G. (2021). *ZERO-G Research Programs*. Zero-G - the Weightless Experience.
https://www.gozerog.com/index.cfm?fuseaction=Research_Programs.welcome
- Zhang, H., Hasan, M. M., & Mudawar, I. (2004). A Method for Assessing the Importance of Body Force on Flow Boiling CHF. *Journal of Heat Transfer*, 126(2), 161–168.
<https://doi.org/10.1115/1.1651532>
- Zhang, Y., Liu, B., Zhao, J., Deng, Y., & Wei, J. (2018). Experimental study of subcooled flow boiling heat transfer on micro-pin-finned surfaces in short-term microgravity. *Experimental Thermal and Fluid Science*, 97, 417–430.
<https://doi.org/10.1016/j.expthermflusci.2018.05.003>
- Zhao, J., Li, H., & Hu, W. (2002). Application of the linear stability theory in the study on fully developed two-phase flow patterns in circular pipes. *Advances in Mechanics*, 32(2), 223–233.
- Zhao, J., Xie, J., Lin, H., Hu, W. R., Ivanov, A. V., & Yu Belyeav, A. (2000, October). *Experimental study on gas/liquid two-phase flow in microgravity*. 51st Int. Astronautical Congress, Rio de Janeiro, Brazil.
- Zivi, S. M. (1964). Estimation of Steady-State Steam Void-Fraction by Means of the Principle of Minimum Entropy Production. *Journal of Heat Transfer*, 86, 247–252.

PUBLICATIONS

The following papers and presentations were published or submitted by the author as part of the research for this dissertation.

Journal Publications

- L. P. M. Brendel, J. E. Braun, and E. A. Groll, “Comparison of Gravity Independence Criteria for Two-Phase Flow,” *Journal of Thermophysics and Heat Transfer*, pp. 1–13, Jun. 2021, doi: 10.2514/1.T6202.
- L. P. M. Brendel, S. L. Caskey, M. K. Ewert, D. Hengeveld, J. E. Braun, and E. A. Groll, “Review of vapor compression refrigeration in microgravity environments,” *International Journal of Refrigeration*, vol. 123, pp. 169–179, Mar. 2021, doi: 10.1016/j.ijrefrig.2020.10.006.

Journal Publications (submitted or to be submitted)

- Effect of Orientation on the Steady-State Performance of Vapor Compression Cycles (Applied Energy)
- Vapor Compression Refrigeration Cycle Testing on Parabolic Flights: Cycle Performance and Stability (International Journal of Refrigeration)
- Vapor Compression Refrigeration Cycle Testing on Parabolic Flights: Heat Exchanger Performance (International Journal of Refrigeration)
- Thermodynamic Stability of a Liquid-to-Liquid Vapor Compression Cycle Against (Thermal Science and Engineering Progress)

Conference Publications

- L. P. M. Brendel, S. L. Caskey, J. E. Braun, and E. A. Groll, “Stability Against Orientation Changes of a Vapor Compression Cycle in Two Configurations”, presented at the DKV meeting 2021, Dresden, Germany.

- L. P. M. Brendel, S. L. Caskey, J. E. Braun, and E. A. Groll, “Similarity of Two-phase Cycle Stability Between Ground-Based Inclination and Parabolic Flight Experiments,” presented at the Thermal and Fluids Analysis Workshop 2021, Virtual, 2021.
- Skipworth, A., Caskey, S. L., Brendel, L. P. M., Gomes, A., Chhajed, R., Phalak, S., Phatak, S., & Groll, E. A. (2021, August). “Zero Gravity Effects on Vapor Compression Cycle Performance for Cold Food Storage with Oil-Free Scroll Compression,” presented at the Thermal and Fluids Analysis Workshop 2021, Virtual, 2021.
- L. P. M. Brendel, S. L. Caskey, M. K. Ewert, A. R. Gomes, J. E. Braun, and E. A. Groll, “Equivalent Mass Benefits from Employing Vapor Compression Refrigeration on Spacecraft,” presented at the International Conference on Environmental Systems 2021, Lisbon, Portugal (Virtual Conference), Jul. 2021.
- L. P. M. Brendel, S. L. Caskey, J. E. Braun, and E. A. Groll, “Experimentally Observed Anomalies from Inclining a Vapor Compression Cycle,” presented at the Purdue Conferences 202One, West Lafayette, IN, USA, 2021.
- L. P. M. Brendel, S. L. Caskey, J. E. Braun, and E. A. Groll, “Characterizing Steady State Compressor Performance by Using Transient Test Data,” presented at the Purdue Conferences 202One, West Lafayette, IN, USA, 2021.
- P. E. Beck, L. P. M. Brendel, J. P. Ore, J. E. Braun, and E. A. Groll, “Investigation of two-phase refrigerant behavior upon cycle startup for compressor protection in microgravity applications,” presented at the Purdue Conferences 202One, West Lafayette, IN, USA, 2021.
- L. P. M. Brendel, J. E. Braun, and E. A. Groll, “Similar Fluids Based on Thermal Gravitational Scaling using Dimensionless Numbers for Three Example Applications,” presented at the Thermal & Fluids Analysis Workshop 2020, Virtual conference hosted in Pasadena, CA, USA, 2020.
- L. P. M. Brendel, J. E. Braun, and E. A. Groll, “Test Stand to Investigate a Vapor Compression Cycle at Varying Orientation and First Experimental Results,” presented at the IIR Rankine 2020 Conference - Advances in Cooling, Heating and Power Generation, Virtual conference hosted in Glasgow, Scotland, 2020, doi: 10.18462/iir.rankine.2020.1201.

- L. P. M. Brendel, J. E. Braun, and E. A. Groll, “Matching Testing Possibilities and Needed Experiments for Successful Vapor Compression Cycles in Microgravity,” presented at the 3rd International Conference for Refrigeration and Cryogenic Engineering, Air Conditioning and Life Support Systems, Moscow, Russia, 2019,
- L. P. M. Brendel, D. Hengeveld, J. E. Braun, and E. A. Groll, “Vapor Compression Cycles for High Component Heat Loads on Next-Generation Small Satellites,” presented at the 11th International Conference on Compressors and their Systems, London, England, 2019.
- L. P. M. Brendel, X. Zhang, J. E. Braun, and E. A. Groll, “Modelling of a Vapor Compression Cycle Independent of Orientation and Gravity,” presented at the 9th International Conference on Compressors and Refrigeration, Xian, China, 2019.

Presentations (without paper)

- L. P. M. Brendel and E. A. Groll, “Stabilität des Kaltdampfprozesses bei Änderung des Neigungswinkels,” presented at the DKV-Tagung, Virtual conference hosted in Marbug, Germany (Virtual), Nov. 2020.
- L. P. M. Brendel, “Besonderheiten in der Konstruktion von Kaltdampfprozessen für die Schwerelosigkeit,” presented at the DKV-Jahrestreffen, Ulm, Germany, 2019.
- L. P. M. Brendel, “Efficient Refrigeration for Space Applications,” presented at the NASA Fluid Physics Workshop, Cleveland, Ohio, 2019.

APPENDIX A. DESIGN OF SECONDARY LOOPS FOR AN INCLINABLE TEST STAND

Figure 113 shows the behavior of the water-glycol and water flowrate and heat exchanger outlet temperature over a range of angles from -180° to 180° . The flow rate of the water was very steady while the flow rate of the water-glycol had strong fluctuations. The difference can be explained by the design of the two secondary loops. The water supply came from the building. The driving pressure differential was constant and since there was no air in the loop, the flow rate was constant disregarding changes in the inclination angle. On the other hand, the water-glycol was driven by a pump which was installed *on* the inclinable test stand. At angles $>170^\circ$, the pump did not provide a steady flow of water-glycol anymore. The reason is probably the changing pressure head on the pump inlet as the pump experienced orientations where the liquid was fed from the top. The problem was solved by placing the water-glycol pump independent of the inclination structure. Then, the pump provided a constant driving pressure differential similar to the building water supply.

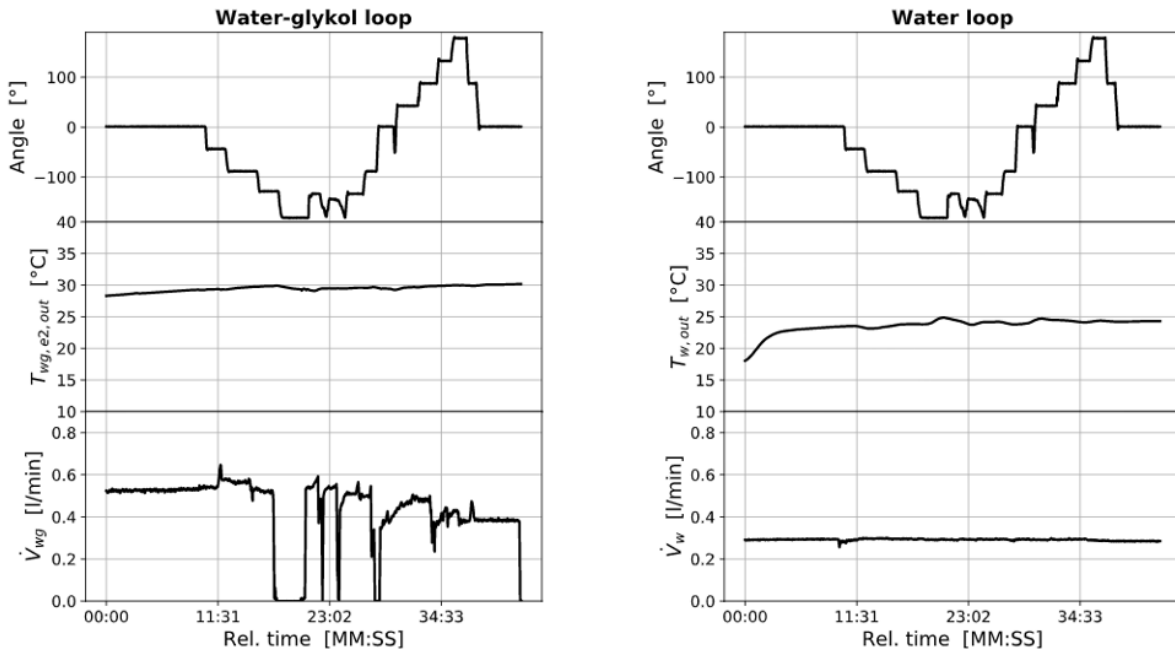


Figure 113: Flow rates at heat exchanger outlet temperatures for secondary loops.

APPENDIX B. MDV AND IIR FOR ARTIFICIAL DATASETS

Figure 114 shows the MDV and IIR for artificially created example datasets, all of which have a duration of 200 time units (for example seconds). The MDV and IIR for each case are indicated in the title of the subplot. The units of the axis are not important, but could be Watts for the y-axis and seconds for the x-axis. The MDV has the unit of the measured property, the IIR has the unit percent. Row 1 shows that different types of excursion can still create the same MDV and IIR values. Row 2 shows the impact of a short (5 time units) spike of different height. Row 3 shows the effect of an unstable steady-state. Row 4 shows that a constant MDV and increasing measured values will lead to smaller IIR values.

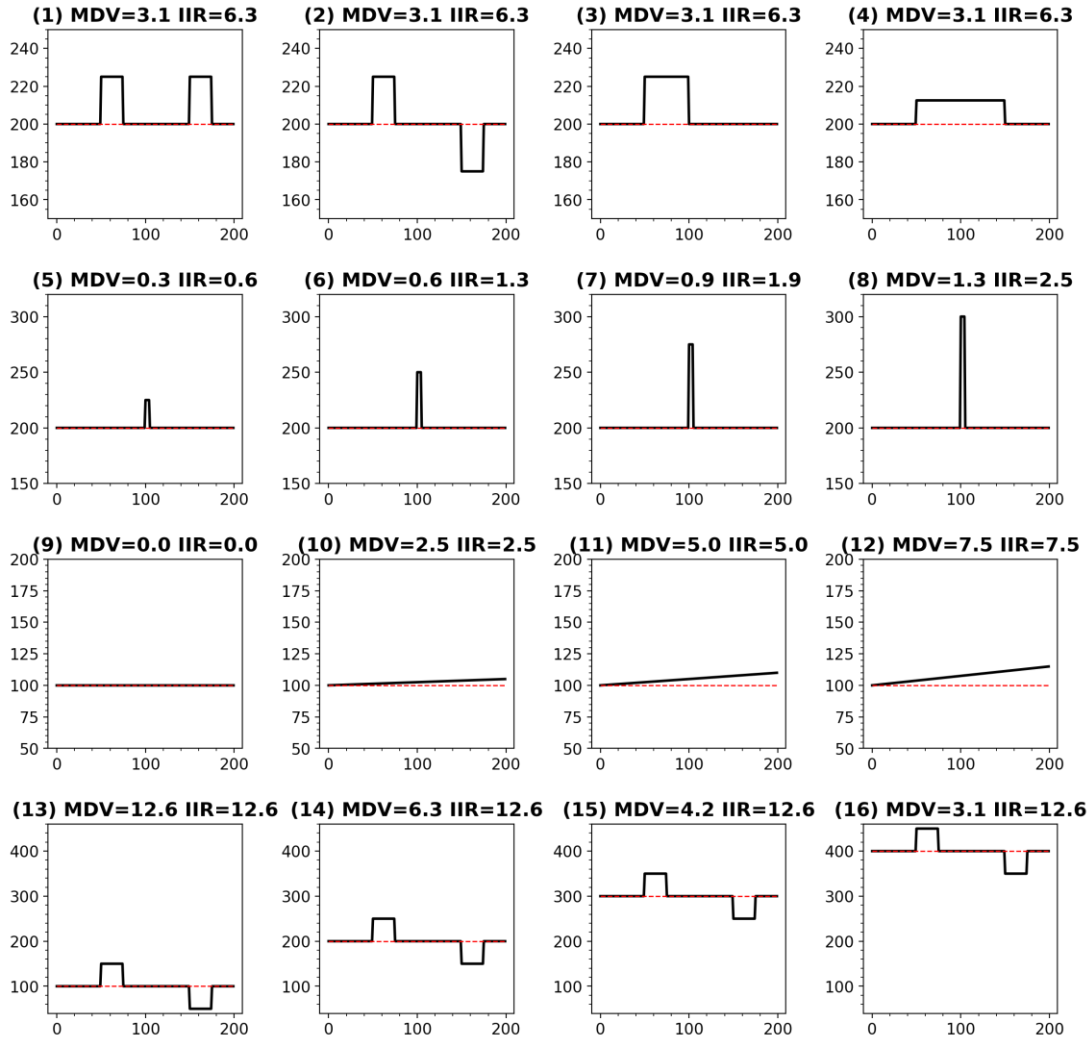


Figure 114: MDV and IIR for artificial datasets.